Chem Soc Rev

Atomically precise alloy nanoclusters: syntheses, structures, and properties

Journal:	*Chemical Society Reviews*
Manuscript ID	CS-SYN-09-2019-000633.R2
Article Type:	Review Article
Date Submitted by the Author:	05-Jun-2020
Complete List of Authors:	Kang, Xi; Anhui University, School of Chemistry and Chemical Engineering Li, Yingwei; Carnegie Mellon University, Chemistry Zhu, Manzhou; Anhui university, Department of Chemistry Jin, Rongchao; Carnegie Mellon University, Chemistry

Journal Name

Review

Atomically precise alloy nanoclusters: syntheses, structures, and properties

Received 00th January 20xx,
Accepted 00th January 20xx

DOI: 10.1039/x0xx00000x

Xi Kang,[‡,a,b] Yingwei Li,[‡,c] Manzhou Zhu,*[,a,b] and Rongchao Jin*[,c]

Metal nanoclusters fill the gap between discrete atoms and plasmonic nanoparticles, providing unique opportunities for investigating the quantum effects and precise structure-property correlations at the atomic level. As a versatile strategy, alloying can largely improve the physicochemical performances compared to corresponding homo-metal nanoclusters, and thus benefit the applications of such nanomaterials. In this Review, we highlight the achievements of atomically precise alloy nanoclusters, and summarize the alloying principles and fundamentals, including the synthetic methods, site-preferences for different heteroatoms in the templates, and alloying-induced structure and property changes. First, based on various Au or Ag nanocluster templates, heteroatom doping modes are presented. The templates with electronic shell-closing configurations tend to maintain their structures during doping, while the others may undergo transformation and give rise to alloy nanoclusters with new structures. Second, alloy nanoclusters of specific magic sizes are reviewed. The arrangement of different atoms is related to the symmetry of the structures, i.e., different atom(s) are symmetrically located in the nanoclusters of smaller sizes, and evolve to the shell-by-shell structure at larger sizes. Then, we elaborate on the alloying effects in terms of optical, electrochemical, electroluminescent, magnetic and chiral properties, as well as the stability and reactivity *via* comparisons between the doped nanoclusters and their homo-metal counterparts. For example, the central heteroatom-induced photoluminescence enhancement is emphasized. The applications of alloy nanoclusters in catalysis, chemical sensing, bio-labeling, and other fields are further discussed. Finally, we provide perspectives on existing issues and future efforts. Overall, this Review provides a comprehensive synthetic toolbox and controllable doping modes so as to achieve more alloy nanoclusters with customized compositions, structures, and properties for applications. This review is based on publications available up to February 2020.

1 Introduction

1.1 Overview of alloying

In retrospect to the development of metallurgy, the material properties of metals have fascinated human beings since the Bronze Age. The new epoch began when mankind discovered that mixing two (or more) different metals could produce an alloy that was much stronger than the individual metals.

It has been more than 5000 years since the ancient work on “alloying”, but this concept is still of critical importance in modern metal industry for enhancing the performance of metals. For instance, iron is prone to be oxidized (or rusted) when exposing to an environment containing oxygen, water, or salts. By contrast, alloying iron with a small amount of carbon and chromium produces steel that exhibits highly oxidation-proof surface; and hybrid steel displays much higher mechanical strength relative to iron. From iron to steel, scientists have demonstrated that the improved oxidation resistance of steel results from the compact film of Cr-based oxide which prevents the exposure of iron surface to the environment, and the enhanced mechanical strength of steel stems from the hardening agents within iron (e.g. carbon) which prevent the movement of dislocations.

1.2 From bulk to nanoscale alloys

Aside from its ubiquitous use in industrial applications such as manufacturing hybrid materials, the alloying strategy is now displaying its indispensable value in nanoscience as well.[1-12] The synergistic effects between metals have been extensively applied in producing alloy nanoparticles with enhanced properties relative to homo-metallic ones.[4-6,13-21] Studies on nanoparticels demonstrate that the size, shape, and composition are the three major factors that are responsible for the controllable properties of nanoparticles.[5-7,22-26]

As for the size effect, Raman spectroscopy is enhanced with the help of nanoparticles in which visible light can be readily absorbed by stimulating LSPR (localized surface plasmon resonance).[27-29] In the case of catalysis, it has been well-established that the catalytic activity of metal nanoparticles can be significantly enhanced by reducing their size.[24,30-32] As for the shape effect, the catalytic selectivity is

[a.] *Department of Chemistry and Centre for Atomic Engineering of Advanced Materials, Anhui Province Key Laboratory of Chemistry for Inorganic/Organic Hybrid Functionalized Materials, Anhui University, Hefei, Anhui 230601, China.*
[b.] *Key Laboratory of Structure and Functional Regulation of Hybrid Materials (Anhui University), Ministry of Education, Hefei, Anhui 230601, China.*
[c.] *Department of Chemistry, Carnegie Mellon University, Pittsburgh, PA 15213, USA.*
**E-mail: zmz@ahu.edu.cn (M.Z.); rongchao@andrew.cmu.edu (R.J.)*
‡ These authors contributed equally to this work.

sensitive to the packing modes of the surface atoms, or the different exposed facets (Miller indices {*hkl*}) of nanoparticles.[22,23,33-35] A prototypical example is the highly active Pt nanoparticles, whose {100} and {210} facets are most active for H_2 or CO production.[36,37] Thus, it is of great importance to control the size and shape so as to endow nanoparticles with favorable facets for better catalytic activity and selectivity. Besides, for metal nanoparticles with fixed size and shape, mastering over the metal composition will enable the manipulation of its physicochemical properties and broaden the practicability in specific applications.[5,38-44] In other words, alloying nanoparticles from homo-composition to bi-metallic or multi-metallic compositions will enrich their physicochemical properties, and make them superior to their homo-metallic counterparts in many cases. Alloying-induced enhancement of properties was discovered back in the Bronze Age. For instance, the platinum group metals (including Pt, Pd, and Ru) are widely used in chemical catalysis as well as in pharmaceutical, pesticide, and polymeric industries;[45] remarkably, a practical catalytic system in these industries often uses alloys of these metals as catalysts to achieve the goal of "killing two birds with one stone," *i.e.* enhancing the catalytic efficiency, and in the meantime reducing the producing costs.[45] As evident from this example, the alloying strategy is a promising approach for preparing novel nanoparticles with enhanced properties for different types of catalysis and many other applications.

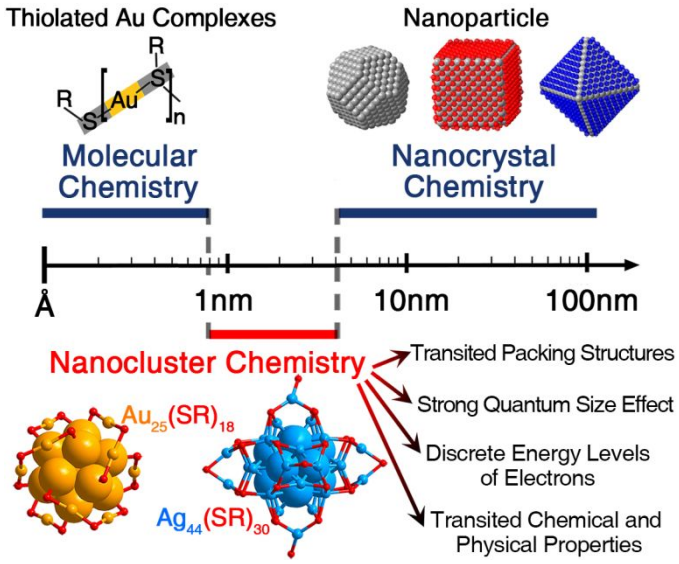

Scheme 1 Illustration of the scope of nanocluster science. Metal nanoclusters bridge the metal complexes and plasmonic metal nanoparticles.

Atomically precise nanoclusters as a special type of nanoparticles provide great opportunities for researchers to relate the properties to the well-defined structures, as single crystals can be grown from such unique nanoparticles and the crystal structure can be solved by X-ray crystallography (SC-XRD).[46-51] Of note, they are titled as atomically precise nanoclusters in order to differentiate them from the conventional alloy nanoparticles.

(A) From the structural point of view, the unknown surface structures and unclear metal-organic bonding modes of nanoparticles limit the fundamental knowledge on the structure-property correlations.[47,48,52] Nanochemists are often frustrated by the notorious fact that no two nanoparticles are the same, which precludes the studies on many fundamental properties of nanoparticles. Benefited from their precisely characterized structures, ultra-small nanoclusters (typically 1-3 nm in diameter, as depicted in Scheme 1) are capable of providing an ideal platform for investigating the detailed mechanism of structure-dependent properties at the atomic level;[47,48,53,54]

(B) From the size point of view, nanoclusters with 1-3 nm diameter can be placed in between metal complexes and plasmonic metal nanoparticles (Scheme 1). Indeed, nanoclusters can serve as perfect models of nanoparticles and establish the bridge from metal complexes to conventional nanoparticles. For simplicity, we take Au-thiolate (SR) complexes, $Au_{25}(SR)_{18}$ and $Ag_{44}(SR)_{30}$ nanoclusters, and large-sized FCC nanoparticles as representatives for molecules, nanoclusters, and nanoparticles, respectively. Compared to conventional nanoparticles of which the surface structures are unclear, nanoclusters can be characterized by single crystal X-ray diffraction (SCXRD) and their surface structures have been determined; for example, the thiolate-protected nanoclusters comprise a polyhedral metal kernel and various protecting metal-thiolate motifs.

(C) From the property point of view, strong quantum size effects in nanoclusters are manifested in their chemical and physical characteristics such as discrete energy levels of electrons, multiple absorption bands because of molecular-like electronic transitions, and so on.[46-49] It has been demonstrated that a slight change in nanoclusters, *e.g.*, adding/subtracting one electron into/from the nanocluster template, will result in a non-negligible disturbance on the electronic and geometric structures, which further influences the properties remarkably.[46-49,55,56] However, in regular nanoparticles, addition or subtraction of a small number of metal atoms might not make discernable differences. In addition, compared with nanoparticles, smaller sizes of nanoclusters endow them with higher specific surface areas, and consequently distinct potential for applications in chemical sensing, biology, energy conversion, catalysis, and so on.[47,48,57-61]

1.3 Atomically precise alloy nanoclusters

It is worth a note on the terminology. Doping was originally used in the semiconductors, whereas alloying is used in metallurgy. If one starts with a homometal nanocluster, introducing one or more heterometal atoms is typically called doping; that is, the starting nanocluster serves as the template, and the doping process leads to one or multiple atoms of the parent nanocluster being replaced by atom(s) of another metal, with the resulting product called a "doped" nanocluster. Alloying refers to the mixing of different metals in one cluster framework. Alloy nanoclusters containing two or more

different types of metal atoms do not necessarily correspond to a parent (i.e. homometal) nanocluster.[62] Thus, all doped nanoclusters belong to alloy nanoclusters, and alloying is a more general concept than doping. Nevertheless, in the following discussions, "alloying" and "doping" are used as interchangeable. "Doping" is more used in specific cases for "one-on-one" replacement by heteroatom(s) in the parent nanocluster.

For nanoclusters, we take advantage of their atomically precise structures to understand the structure-property correlations, which will guide researchers to customize new nanoclusters based on the desired performance. As discussed above, the size, shape, and composition of metal nanoparticles are the three major factors responsible for the physicochemical properties.[5-7,22-26] Nonetheless, mastering over the shape and size of nanoclusters might not be enough for elucidating the relationships between structure and properties. Since adding/subtracting only one metal atom into/out of a nanocluster often alters its properties, the structure-property correlations would better be clarified by specifying the metal and ligand types, the numbers of metal atoms and ligands, and structural anatomy. Furthermore, controlling over the composition of nanoclusters also changes the chemical/physical properties.

Doping the homo-gold and homo-silver nanoclusters with heteroatoms has been demonstrated as a versatile approach to tune their physicochemical performances.[47,48] Generally, doping atom(s) into parent nanoclusters will enhance their thermal stability and catalytic activity.[63,64] In addition, the electronic structure and optical properties of nanoclusters can also be tailored by substituting with heterometals.[65-71] Owing to the homologous structures between the parent nanocluster and its doped ones, insightful correlations between metal compositions and chemical/physical properties can be mapped out. Such a goal is however difficult to achieve for large-sized metal nanoparticles due to the lack of information of atomic sites and inhomogeneity;

It is inadequate to simply consider the "composition" of alloy nanoclusters because their chemical/physical properties are highly dependent on the position(s) that the heteroatom(s) take in the alloy particle. Of note, the doping modes of heteroatoms can differ from metal to metal due to their different electronic and geometric features. Multiple doping modes in the template, including the central doping, kernel's shell doping, and exterior motif doping, pose highly versatile chemistry for the nanocluster materials (Scheme 2).

In the past years, some reviews related to the development of nanoclusters have been published, including those about controllable synthesis and purifications,[50,72-83] atomically precise structures and structural evolution patterns,[55,84-109] structure-based chemical/physical properties,[52,57-61,110-141] and distinct property-dependent applications.[142-157] Besides these reviews, there are also some overviews touching upon specific topics of experimental and theoretical works.[49,158-169]

The main objective of this Review is to summarize the research achievements and extract the fundamental principles of alloying in nanoclusters with a focus on the following aspects.

(A) "Heteroatom doping patterns and structures of alloy nanocluster" (*Sections 2-6*) are divided by different nanocluster templates. Specifically, considering that the doping mode varies by different heteroatoms and different nanocluster templates, we divide alloy nanoclusters into five categories, including alloying in homo-gold nanocluster templates (*Section 2*), alloying in homo-silver nanocluster templates (*Section 3*), alloy nanoclusters of specific magic sizes (*Section 4*), alloy nanoclusters with multi-metallic compositions (*Section 5*), and other alloy nanoclusters without specific homo-metal template (*Section 6*). The alloying principles and fundamentals are discussed in each section.

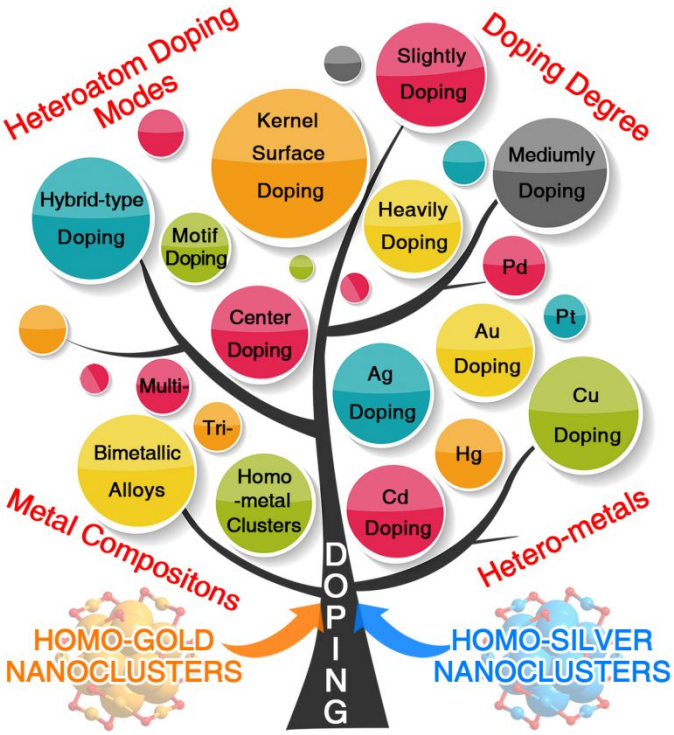

Scheme 2 The doping tree of metal nanoclusters. Doping heteroatom(s) into different templates follows distinct doping modes, which increases the structural/compositional diversity of metal nanoclusters.

(B) As alloying has been proved to be a versatile strategy in improving their chemical and physical performances, alloy nanoclusters constitute a platform for investigating inter-metallic synergism at atomic level. *Section 7* includes an overview of their optical, electrochemical, magnetic, and chiral properties, as well as their stability and reactivity. In addition, atomically precise structure-property correlations are summarized.

(C) Alloy nanoclusters exhibit largely improved physicochemical performances relative to corresponding homo-metallic nanoclusters, which benefit the applications of cluster-based nanomaterials. The *Section 8* discusses catalysis, sensing, bio-labelling, bio-imaging, biomedicine, and energy conversion based on alloy nanoclusters.

In the end, we provide perspectives and highlight the challenges for future researches on alloy nanoclusters (*Section 9*). For instance, precise control over alloying sites, diversity in atomically precise alloying processes, limitation for metal-exchange in nanoclusters, and new applications for alloy nanoclusters.

In summary, this Review summarize research progress in the syntheses of alloy nanoclusters with controllable compositions, X-ray crystallographic determination of doping sites, and effects of doping on the optical, electronic, magnetic, electrochemical and catalytic properties. Besides, the inter-metallic synergies derived from alloy nanocluster systems are discussed, which will guide researchers in designing new alloy nanomaterials with tailored functionality.

2 Alloying in homogold nanocluster templates

The systems of homo-metal nanoclusters and their derivatives, *e.g.* $Au_{25}(SR)_{18}$ and $M_xAu_{25-x}(SR)_{18}$ (M = Ag/Cu/Pt/Pd/Cd/Hg) nanoclusters, make it possible to map out the inter-metal synergisms at the atomic level, which is of great significance in the field of nanoscience. Understanding synergetic effects would instruct the preparation of novel alloy nanoclusters with tailored chemical/physical properties.

The synthetic methods of alloy nanoclusters can be mainly classified into two categories: (i) chemical reduction of a mixture of ligated metal complexes (such as Au-SR/Ag-SR complexes); (ii) doping the homo-metal nanoclusters with hetero-metal salts or complexes. For example, either co-reducing Au-SR/Ag-SR complexes or doping $Au_n(SR)_m$ with Ag-SR generates $Au_{n-x}Ag_x(SR)_m$ alloy nanoclusters.

This section summarizes the alloying of heterometals into gold nanoclusters, mainly including the icosahedral Au_{25}, the bi-icosahedral Au_{38}, the FCC/HCP Au nanoclusters (Au_{18}, Au_{21}, Au_{23}, Au_{36}), the small-sized Au:PPh_3 nanoclusters (Au_{9-13}:PPh_3), the nanoclusters in the form of "cluster of clusters" (rod-like Au_{25}, Au_{37} and Au_{38} capped by PPh_3), and the large-sized Au_{144} nanocluster. Of note, doping based on $Au_{25}(SR)_{18}$, $Au_{38}(SR)_{24}$, and $Au_{25}(PPh)_{10}(SR)_5Cl_2$ templates is reviewed elsewhere when this Review is under preparation.[81]

2.1 Alloying in icosahedral $Au_{25}(SR)_{18}$ template

Since the early synthesis of $Au_{25}(SR)_{18}$ in 1998 and successful structural determination in 2008,[170,171,172] it has stimulated great interest because of its ease of preparation, high yield, thermal stability, and versatile surface functionalization, as well as broad applications.[166,167] $Au_{25}(SR)_{18}$ possesses an icosahedral Au_{13} kernel, which is protected by six SR-Au-SR-Au-SR staple motifs in a *quasi*-octahedral symmetry.[171,172] This nanocluster has acted as a template for diverse alloying works and is perhaps the most widely studied system. So far, rich types of hetero-metals, including Ag, Cu, Pt, Pd, Hg, Cd, Ir, etc., have been successfully doped into the $Au_{25}(SR)_{18}$ template (Table 1), and several synthetic methods were developed, including *in-situ* syntheses (co-reduction), doping of pre-synthesized $Au_{25}(SR)_{18}$ (e.g., metal-exchange/anti-galvanic reduction), inter-cluster reactions, and so on. Interestingly, different alloying outcomes occur from these approaches. For example, the Pd_1Au_{24} or Pt_1Au_{24} nanocluster can only be prepared by *in-situ* synthesis *via* reducing Pd-SR/Au-SR or Pt-SR/Au-SR complexes,[63,64] while $Au_{22}Ir_3(SR)_{18}$ can only be prepared by inter-cluster reaction.[173]

Table 1 Alloy nanoclusters based on the $Au_{25}(SR)_{18}$ template.

Formula	Measurement(s)	Ref(s)
$Au_{25}(SR)_{18}$	SC-XRD	171, 172
$Au_{22}Ir_3(SR)_{18}$	ESI-MS	173
$Au_{25-x}Ag_x(SR)_{18}$ (x ~6)	SC-XRD	66
$Au_{25-x}Ag_x(SR)_{18}$ (x ~20)	SC-XRD	177, 179
$Au_{25-x}Ag_x(SR)_{18}$	MALDI-MS, ESI-MS	54, 65, 180-184, 186-188, 189-195
$Au_{25-x}Ag_x(SR)_{18-y}(SR')_y$	MALDI-MS	185
$Au_{25}Ag_2(SR)_{18}$	SC-XRD	184
$Au_{25-x}Cu_x(SR)_{18}$	MALDI-MS	67, 68, 174, 180, 181, 187, 201, 202
$Pt_1Au_{24}(SR)18$	ESI-MS	63, 196-198
$Pt_1Au_{24}(SR)_{18}$	SC-XRD	207, 216, 222
$Pd_1Au_{24}(SR)_{18}$	MALDI-MS	64, 203, 204
$Pd_1Au_{24}(SR)_{18}$	SC-XRD	210, 216
$Pd_1Au_{24}(SR)_{18-y}(SR')_y$	ESI-MS	205
$Au_{24}Cd_1(SR)_{18}$	ESI-MS, SC-XRD	174, 175, 176
$Au_{24}Hg_1(SR)_{18}$	ESI-MS	71

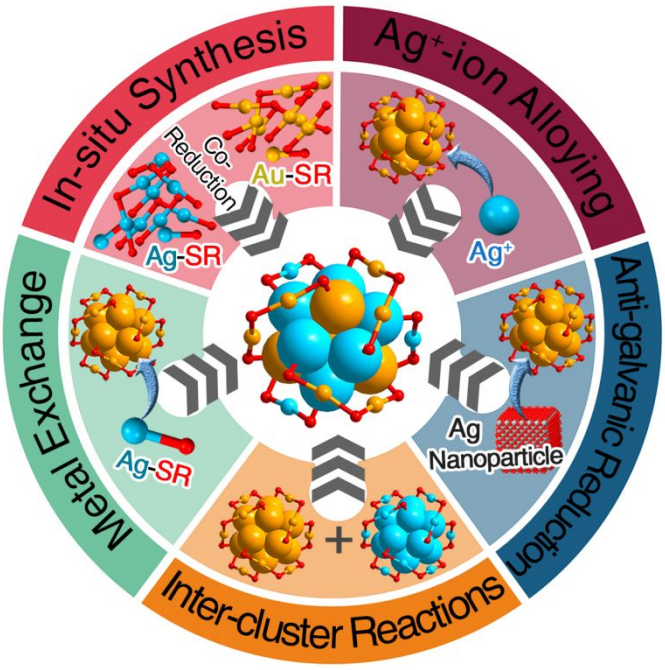

Fig. 1 Different synthetic methods of $Au_{25-x}Ag_x(SR)_{18}$ alloy nanoclusters**,** including *in-situ* synthesis, Ag^+-ion alloying, metal exchange, anti-galvanic reduction, and inter-cluster reaction.

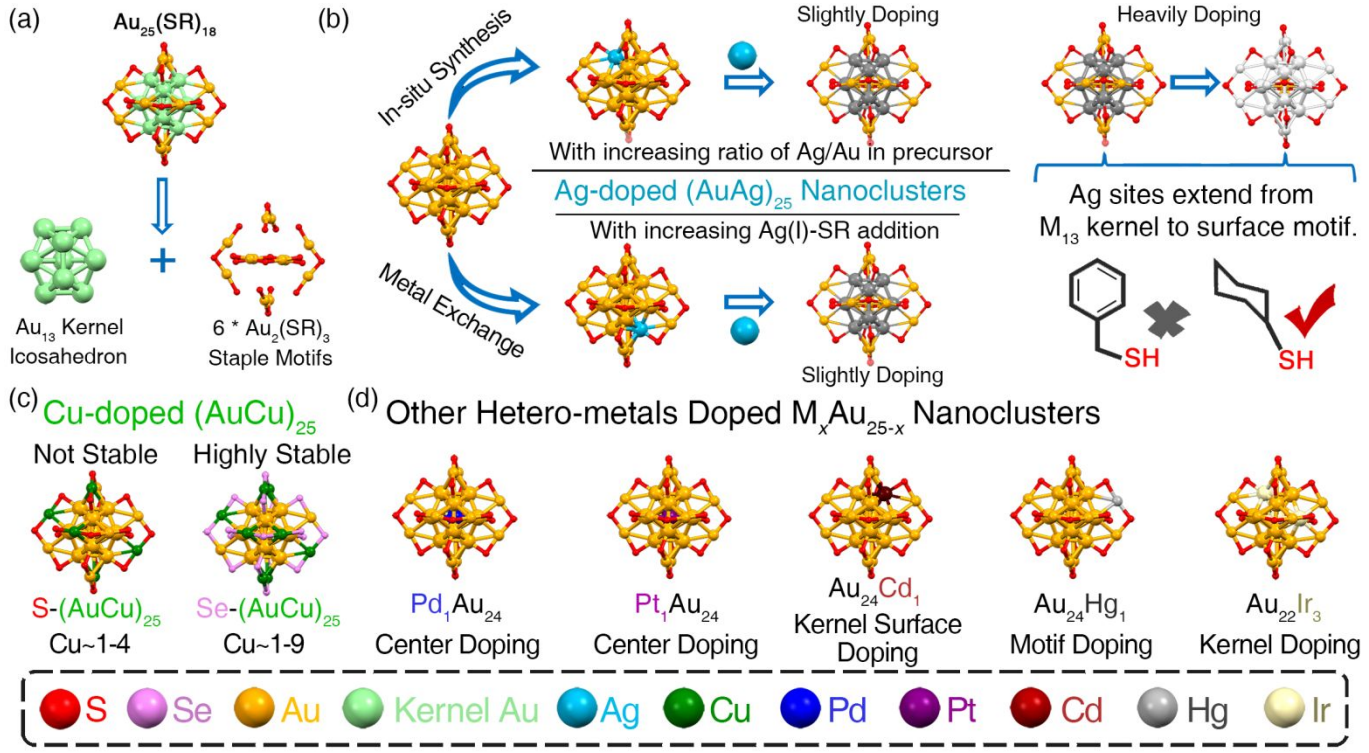

Fig. 2 Doping sites of heteroatom(s) in $Au_{25}(SR)_{18}$ template. (a) Structural anatomy of the $Au_{25}(SR)_{18}$ nanocluster. Structures of (b) $Au_{25-x}Ag_x(SR)_{18}$ nanoclusters with increasing doping degree. Of note, both "in-situ synthesis" (top) and "metal exchange" (bottom) approaches can direct the synthesis of $Au_{25-x}Ag_x(SR)_{18}$ alloy nanoclusters. Structures of (c) $Au_{25-x}Cu_x(SR)_{18}$ and $Au_{25-x}Cu_x(SeR)_{18}$ nanoclusters. (d) Other heteroatom(s)-doped $Au_{25-x}M_x(SR)_{18}$ nanoclusters, including $Pd_1Au_{24}(SR)_{18}$, $Pt_1Au_{24}(SR)_{18}$, $Au_{24}Cd_1(SR)_{18}$ $Au_{24}Hg_1(SR)_{18}$, and $Au_{22}Ir_3(SR)_{18}$.

Because of the different properties of hetero-metals, different doping modes in the $Au_{25}(SR)_{18}$ template are observed, i.e., heterometals in different doping sites and degrees of doping. The mono-heteroatom doping mode is associated with Pt, Pd, Hg, and Cd,[63,64,71,171-176] while three Ir atoms could be introduced into $Au_{25}(SR)_{18}$.[173] The Ag and Cu dopants are more complicated. As for Ag-doped $M_{25}(SR)_{18}$ nanoclusters, (i) the number of Ag heteroatoms in $Au_{25}(SR)_{18}$ can be easily controlled by regulating the Au/Ag ratios in synthetic procedures;[65,66,174,177,178] (ii) the incorporated Ag heteroatoms can go from the icosahedral kernel to the surface structure;[179] that is, only the center Au is non-swappable. As for Cu-doped $M_{25}(SR)_{18}$ nanoclusters, no crystal structure of $Au_{25-x}Cu_x(SR)_{18}$ has been obtained yet, but it is evidenced by extensive experiments that Cu should substitute the Au atom(s) on staple motifs. In this section, doped nanoclusters based on the $Au_{25}(SR)_{18}$ template are reviewed, including the synthetic procedures and doping modes.

$Au_{25-x}Ag_x(SR)_{18}$ alloy nanoclusters have been successfully prepared *via* several methods (Fig. 1), including (i) *in-situ* syntheses by co-reducing Au-SR/Ag-SR complexes;[65,66,177,180-182] (ii) reactions between $Au_{25}(SR)_{18}$ and Ag^+ ions;[183,184] (iii) metal-exchange between $Au_{25}(SR)_{18}$ and Ag(I)-SR complexes;[185] (iv) anti-galvanic reaction (AGR) of thiolate-protected gold and silver nanoparticles;[186-188] (v) inter-cluster reactions between $Au_{25}(SR)_{18}$ and Ag nanoclusters.[189-193]

Methods (i)/(ii): Early in 2010, $Au_{25-x}Ag_x(SR)_{18}$ nanoclusters with continuously modulated *x* were synthesized, albeit with different procedures — *in-situ* synthesis by Negishi et al.,[65] and reacting $Au_{25}(SR)_{18}$ with Ag^+ ions by Murray et al.[183] The structures of $Au_{25-x}Ag_x(SR)_{18}$ nanoclusters prepared by *in-situ* synthesis with increasing doping degrees are shown in Fig. 2b. The Ag-doping process and synergistic effect between Au and Ag enable the doped nanoclusters to display differences and tunability in optical and catalytic properties, as well as the reactivity for ligand-exchange reactions, which are discussed in Section 7.[54,181,194,195] By concomitantly reducing the Au-SR and Ag-SR complexes, the Xie group developed a series of hydrophilic $Au_{25-x}Ag_x$ nanoclusters protected by mono- and bi-thiolate ligands.[182] In their work, the compositions of both the Au/Ag kernel and the ligand shell could be tailored by regulating the feeding ratios of Au/Ag precursors and different ligands, which further enriched the functionalities of alloy nanoclusters.[182]

Methods (iii): Bulk metals display galvanic-replacement performance, which was utilized to prepare metal nanoparticles with controllable sizes, shapes, and configurations.[196-198] For example, typical galvanic reactions are as follow,

Ag NPs + $HAuCl_4$ (or Pt, Pd salts) → Ag/M alloy NPs

However, in the size regime of nanoclusters, different alloying manners emerge due to the molecular behavior of nanoclusters as opposed to bulk-metal behavior. It was

surprisingly found that ions of more active metals (*e.g.* Ag^{I} or Cu^{I}) can replace Au^0 atoms in the cluster to produce M^0 (Ag^0 or Cu^0) atoms.[186] To gain a deeper understanding on this interesting behavior, the Zhu group developed a versatile approach to synthesizing alloy nanoclusters containing both high- and low-activity metals.[174] With this "metal exchange" method, doped M_{25} nanoclusters including $Au_{25-x}Ag_x(SR)_{18}$, $Au_{25-x}Cu_x(SR)_{18}$, $Au_{24}Cd_1(SR)_{18}$ and $Au_{24}Hg_1(SR)_{18}$ were obtained. The structure of $Au_{25-x}Ag_x(SR)_{18}$ nanoclusters prepared by metal-exchange with increasing doping degrees is shown in Fig. 2b. More significantly, "metal exchange" is reversible in these alloy systems: i.e., Ag^{I} can substitute Au^0 atoms in Au_{25}, and Ag^0 in $Au_{25-x}Ag_x$ can be reversibly exchanged back by Au^{I}, with the reaction equilibrium as:

$Au_{25}(SR)_{18} + x$ Ag(I)-SR → $Au_{25-x}Ag_x(SR)_{18} + x$ Au(I)-SR;

$Au_{25-x}Ag_x(SR)_{18} + x$ Au(I)-SR → $Au_{25}(SR)_{18} + x$ Ag(I)-SR.

Considering that all these surviving nanoclusters exhibit delocalized electron shell closing (DESC) of 8e (superatom rule),[199] Wang et al. rationalize that the "metal exchange" method should be associated with electron shell closing and stability of the obtained alloy nanoclusters, but be less related to metal activity.[174] Some follow-up works were performed on simultaneously doping Ag and exchanging foreign-thiolates into the $Au_{25}(SR)_{18}$ nanocluster.[185]

Methods (iv): The Wu group presented an AGR strategy to make alloy nanoclusters.[184,186,187,200] In their works, the reactions between $Au_{25}(SR)_{18}$ nanoclusters and Ag/Cu nanoparticles introduced the heteroatoms into the Au_{25} template, which was an opposite process to the galvanic reaction.[186,187] The concept of AGR is also exploited to synthesize atomically precise $Au_{25}Ag_2(SR)_{18}$ *via* the reaction between $Au_{25}(SR)_{18}$ and $AgNO_3$, where the additional Ag atoms are collocated on Au_{25}.[184]

Methods (v): Inter-cluster reactions were developed for preparing alloy nanoclusters.[173,189-193] The Pradeep group meticulously explored the inter-cluster reactions between $Au_{25}(SR)_{18}$ and a series of Ag nanoclusters, such as $Ag_{25}(SR)_{18}$, $Ag_{44}(SR)_{30}$, and $Ag_{51}(S_2R)_{19}(PPh_3)_3$. For instance, reacting $Au_{25}(SR)_{18}$ with $Ag_{44}(SR)_{30}$ produced $Au_{25-x}Ag_x(SR)_{18}$ and $Ag_{44-y}Au_y(SR)_{30}$ alloy nanoclusters (no exact relationship between x and y).[189] The inter-cluster reaction between $Au_{25}(SR)_{18}$ and $Ag_{25}(SR)_{18}$ not only generated $Au_{25-x}Ag_x(SR)_{18}$ (x = 1-24), but a dianionic adduct—$Au_{25}(SR)_{18}Ag_{25}(SR')_{18}$—was detected as well by the electrospray ionization mass spectrometry (ESI-MS).[190] Of note, regulating the feeding ratios of $Au_{25}(SR)_{18}$ and homo-silver nanoclusters enabled controlling the Ag doping degrees in final products.[191-193] Theoretical results illustrated that (i) the Ag heteroatoms in $Au_{25-x}Ag_x(SR)_{18}$ tended to occupy the sites on the icosahedral kernel's shell, and (ii) the Au heteroatoms in $Ag_{44-y}Au_y(SR)_{30}$ would substitute the Ag atoms in the icosahedral Ag_{12} kernel.[191,192] In the follow-up work, Ir heteroatoms were doped into $Au_{25}(SR)_{18}$ through an inter-cluster reaction between $Au_{25}(SR)_{18}$ and $Ir_9(SR)_6$ nanoclusters.[173] DFT calculations illustrated the optimal structure of $Au_{22}Ir_3(SR)_{18}$ in which three Ir heteroatoms were arranged triangularly with one Ir at the center and the other two on the M_{13} kernel's shell (Fig. 2d).[173]

Ag-doping: The structure of $Au_{25-x}Ag_x(SR)_{18}$ was determined by Dass and co-workers in 2014.[66] Single-crystal X-ray crystallography (SC-XRD) revealed a tri-stratified arrangement—$Au_1@Au_{5.3}Ag_{6.7}@6\times Au_2(SR)_3$ (Fig. 2b, upper-middle). The center and the motifs are exclusively occupied by Au atoms, whereas Ag heteroatoms selectively take the twelve sites of the icosahedral kernel's surface.[66] However, Ag dopants are later discovered not to be limited to the kernel shell. By using cyclohexanethiol (HS-*c*-C_6H_{11}), heavily-doped $Au_{25-x}Ag_x(SR)_{18}$ nanoclusters with average x = 20.45 were prepared.[177,179] The maximum number of Ag dopants was determined to be 24 by ESI-MS analysis.[177,179] SC-XRD results suggested that, except the center Au atom, all the other Au atoms in the parent Au_{25} could be substituted by Ag (Fig. 2b, upper-right).

Both moderately-doped $Ag_{6.7}Au_{18.3}(SR)_{18}$ and heavily-doped $Ag_{20.45}Au_{4.55}(SR)_{18}$ nanoclusters were prepared by an *in-situ* procedure.[66,177] Structurally, when protected by S-C_2H_4Ph or $SC_{12}H_{25}$ ligand, Ag heteroatoms are restricted on the M_{12} kernel shell.[65,66] Even with a large Ag/Au ratio in the precursor, the obtained $Au_{25-x}Ag_x(SR)_{18}$ nanoclusters can hardly support more than twelve silver atoms in the template.[65] By comparison, heavily-doped $Au_1Ag_{24}(SR)_{18}$ nanoclusters can be achieved with the help of HS-*c*-C_6H_{11}.[177] Such a phenomenon was also observed in $Au_{25-x}Ag_x(SR)_{18}$ nanoclusters synthesized by metal-exchange metheds.[174,179] Metal-exchanging of $Au_{25}(S\text{-}C_2H_4Ph)_{18}$ with Ag(I)-(S-C_2H_4Ph) introduced up to 12 Ag atoms into the $M_{25}(S\text{-}C_2H_4Ph)_{18}$ template.[174] By comparison, up to 19 silver atoms were doped into $M_{25}(S\text{-}c\text{-}C_6H_{11})_{18}$ by reacting $Au_{23}(S\text{-}c\text{-}C_6H_{11})_{16}$ with Ag(I)-(S-*c*-C_6H_{11}), and some staple motif sites were exclusively occupied by Ag.[179] All of these results indicate the important effects of ligands on the doping processes.

Cu-doping: $Au_{25-x}Cu_x$ nanoclusters can be synthesized by *in-situ* synthesis,[67,68,180,181,201,202] metal-exchange,[174] and AGR methods.[187] Ligand effects were also observed in $Au_{25-x}Cu_x$ alloy nanoclusters (Fig. 2c).[67,68] The $Au_{25-x}Cu_x(SR)_{18}$ showed a spontaneous de-alloying process over time, and the initially prepared bimetal nanoclusters would convert back to $Au_{25}(SR)_{18}$ (such a phenomenon was not observed in Ag-doped M_{25}).[67,201] For comparison, selenolate-capped $Au_{25-x}Cu_x(SeR)_{18}$ nanoclusters exhibited high stability.[68] Another difference lies in the Cu doping number. As for $Au_{25-x}Cu_x(SR)_{18}$, a maximum of four Cu heteroatoms can be introduced;[67,201] whereas in $Au_{25-x}Cu_x(SeR)_{18}$ with selenolate, up to 9 Cu atoms can be introduced (Fig. 2c).[68] It should be noted that no structure of Cu-doped M_{25} is accessible so far. In order to determine the preferential doping sites of Cu in the $Au_{25}(SR)_{18}$ template, several means have been performed, *e.g.* DFT calculations, and EXAFS (extended X-ray absorption spectroscopy).[201,202] Specifically, DFT calculations suggested that the optimal doping site in $Au_{24}Cu_1(SR)_{18}$ is the icosahedral surface. However, EXAFS results demonstrated that the single Cu should occupy the staple site, i.e. $Au_2(SR)_3$ staple motifs.[202] The discrepancy between DFT and EXAFS

was explained in terms of the difference in the chemical durability of the Cu dopant at various sites against oxidation.[202]

Pt/Pd-doping: Mono-Pt- or Pd-doped $M_1Au_{24}(SR)_{18}$ nanoclusters were well-studied in the last ten years, mainly because of their capability in tuning the electronic/geometrical structures and chemical/physical properties of $Au_{25}(SR)_{18}$.[63,64,203-222] Of note, doping a Pt/Pd heteroatom into the $Au_{25}(SR)_{18}$ template was only achieved by *in-situ* synthesis, and mass spectra demonstrated that only one heteroatom was allowed in M_{25} no matter what Pd/Au or Pt/Au ratio was,[63,203-208,214] which is different from the doping of Ag and Cu. High-performance liquid chromatography (HPLC) was exploited to separate/purify the prepared $M_1Au_{24}(SR)_{18}$ from its mixture with $Au_{25}(SR)_{18}$.[204-208] With the pure $M_1Au_{24}(SR)_{18}$, changes on chemical/physical properties introduced by the Pd/Pt-doping have been thoroughly investigated, including thermal stability,[204] reactivity,[205,206] catalytic performance,[63,64,217-219] magnetism,[216] and excited-state behavior[220,221] (see more details in Section 7). In early studies, several means, *e.g.* DFT calculations and EXAFS measurements, were performed to determine the doping site of Pd/Pt, and all evidence suggested the center occupation.[63,209,211-215] Such results also demonstrated that the doped Pt/Pd would significantly affect the electronic structure of the parent $Au_{25}(SR)_{18}$ nanocluster. Kwak *et al.* presented the interconversion of $Pd_1Au_{24}(SR)_{18}$ or $Pt_1Au_{24}(SR)_{18}$ between superatomic 6-electron and 8-electron configurations ($[M_1Au_{24}(SR)_{18}]^0$ and $[M_1Au_{24}(SR)_{18}]^{2-}$, M = Pd/Pt), and attributed the variations in electronic and geometric structures to Jahn—Teller-like distortion of the 6-electron nanoclusters,[211] which is reminiscent of a similar effect in different-charged $Au_{25}(SR)_{18}^q$ (q = -1, 0, +1).[212] Sels *et al.* investigated the structures of M_1Au_{24} nanoclusters co-stabilized by mono-thiol and di-thiol ligands, indicating the di-thiol would bridge the apex S and one core S of two adjacent $Au_2(SR)_3$ motifs.[213]

The X-ray structures of $Pd_1Au_{24}(SR)_{18}$ and $Pt_1Au_{24}(SR)_{18}$ nanoclusters (both charge-neutral) were reported in 2016,[210,216] further verifying the center-doping mode of Pd/Pt heteroatom in $Au_{25}(SR)_{18}$ (Fig. 2d). SC-XRD suggested slightly oblate M_{13} kernels induced by Pd/Pt doping.[210,216]

In 2019, Tsukuda and co-workers reported the crystal structures of negatively charged $[Pt_1Au_{24}(SR)_{18}]^-$ and $[Pt_1Au_{24}(SR)_{18}]^{2-}$.[222] Specifically, the stoichiometric production of open shell $[Pt_1Au_{24}(SR)_{18}]^-$ (7e) was achieved by reaction between an equal amount of $[Pt_1Au_{24}(SR)_{18}]^0$ and $[Pt_1Au_{24}(SR)_{18}]^{2-}$, that is, electron transfer from $[Pt_1Au_{24}]^{2-}$ to $[Pt_1Au_{24}]^0$:

$[Pt_1Au_{24}]^{2-} + [Pt_1Au_{24}]^0 \rightarrow [Pt_1Au_{24}]^- + [Pt_1Au_{24}]^-$.[222]

The reaction between $[HM_1Au_8(PPh_3)_8]^+$ (M = Pt/Pd) and Au(I)-SC_2H_4Ph or Au(I)-C≡CAr (Ar = 3,5-$(CF_3)_2$Ph) offered $[M_1Au_{24}(SC_2H_4Ph)_{18}]^0$ (with a $(M_1Au_{12})^{6+}$ kernel) or $[M_1Au_{24}(C{\equiv}CAr)_{18}]^{2-}$ (with a $(M_1Au_{12})^{4+}$ kernel) alloy nanoclusters.[221] $[M_1Au_{24}(C{\equiv}CAr)_{18}]^{2-}$ is the doping counterpart of the reported homo-gold $[Au_{25}(C{\equiv}CAr)_{18}]^-$.[222] The larger number of valence electrons in the $(M_1Au_{12})^{4+}$ kernel protected by alkynyl was ascribed to the increase of attractive potential owing to the stronger electron-withdrawing nature of alkynyl relative to thiolates. Of note, reacting $HPt_1Au_8(PPh_3)_8$ with the Au(I)-S-*c*-C_6H_{11} complexs resulted in $Pt_1Au_{24}(S\text{-}c\text{-}C_6H_{11})_{18}$, whereas the addition of Au(I)-S-*c*-C_6H_{11} to $HPd_1Au_8(PPh_3)_8$ yielded new $Pd_1Au_{23}(S\text{-}c\text{-}C_6H_{11})_{17}$ with its structure being composed of a flattened $(Pd_1Au_{12})^{6+}$ kernel, three $Au_1(SR)_2$ staples, one $Au_2(SR)_3$ staple, and two $Au_3(SR)_4$ staples.[223]

Cd/Hg-doping: Aside from Pt- and Pd-doped $M_1Au_{24}(SR)_{18}$ alloys, the single-heteroatom doping mode has also been found in Cd- and Hg-doped $M_{25}(SR)_{18}$ nanoclusters.[71,174,175] The doping site of the single Hg/Cd heteroatom is however still controversial (i.e. staple site, icosahedral center or shell).[71,175] Interestingly, $Au_{24}Cd_1$ can be transformed to $Au_{24}Hg_1$ (within 1 min) after the addition of 1 eq. Hg^{2+}; however, the reversible process was not successful.[175] DFT calculations showed that the reaction $Cd_1Au_{24}(SR)_{18} + Hg^{2+} \rightarrow Hg_1Au_{24}(SR)_{18} + Cd^{2+}$ was favorable (ΔG = -3.5 kcal/mol).[175]

The number and location(s) of foreign-metal atom(s) in the $Au_{25}(SR)_{18}$ template aforementioned were determined by mass spectrometry and SC-XRD. Maran and co-workers used a combination of NMR, isotope analysis, MALDI-MS, electrochemistry, and SC-XRD to analyze the alloying positions and found that Pt or Pd heteroatom is at the center of $Au_{25}(SR)_{18}$, whereas Cd or Hg heteroatom is doped into the icosahedral kernel's surface.[176] The alloying results are not dependent on the thiols, the metal salts/complexes used in the syntheses, or the synthetic methods.[176] Thus, supplementary characterization along with SC-XRD is required when determining the doping position(s) in alloy nanoclusters when the electron-density difference between Au and heteroatom(s), i.e. Pt/Hg, is very small. The X-ray absorption spectroscopy analysis is quite conclusive.[63]

Theoretical calculations: Many theoretical works have been performed to obtain the information of (i) doping sites and (ii) doping effects based on the $Au_{25}(SR)_{18}$ template.[63,71,174,178,190,192, 211,225-231] Early in 2009, Walter and Moseler reported the optimal structures of mono Ag-, Cd-, or Pd-doped $M_{25}(SR)_{18}$ nanoclusters.[225] Considering that $[Au_{25}(SR)_{18}]^-$ features a magic number of 8 free electrons (superatom), Jiang and Dai surveyed many elements as potential central doping atom candidates, and their results indicated that the 8-electron count rule based on superatom concept was powerful for $M@Au_{24}(SR)_{18}^q$ predictions.[226] The Häkkinen group presented that $[Pd_1Au_{24}(SR)_{18}]^{2-}$ was a 8-electron closed-shell species, whereas $[Pd_1Au_{24}(SR)_{18}]^z$ nanoclusters ($-1 \le z \le +3$) held holes in superatom 1P HOMO manifold, indicating that the Pd dopant contributes no electron to the delocalized electron density in the kernel.[227] In the theoretical works based on $Au_{25-x}Ag_x(SR)_{18}$ nanoclusters, it is demonstrated that the Ag dopants tend to maintain an average distribution on the icosahedral surface—which possesses the lowest thermodynamic energy and the highest stability.[178,228,230] In 2018, a "thermodynamic stability model" was proposed to explain the preference in heteroatom

doping position(s) by relating the metal core cohesive energy to the shell-to-core binding energy.[231]

Collectively, a number of heteroatoms can be doped into the $Au_{25}(SR)_{18}$ template with different doping degrees and doping positions: Ag, Cu, or Ir follows a multiple-heteroatom doping mode, whereas Pd, Pt, Cd, or Hg adopts the mono-doping mode. The Pd or Pt takes the central position, and Ag, Cd, or Hg prefers the kernel's surface, whereas Cu might be on the staple motifs. The different preferential doping manners of heteroatoms could be caused by their different electron configurations, atomic sizes, electronegativity, surface energy, etc. Interestingly, different doping approaches enable $Au_{25-x}M_x(SR)_{18}$ alloy nanoclusters with diverse doping degrees and doping sites. In addition, different ligands of –SR might also have some important influences on the doping manners. Another intriguing phenomenon is that Pt- and Pd-doped $M_1Au_{24}(SR)_{18}$ nanoclusters can only be prepared by *in-situ* synthesis procedures. Future works should focus on the root that causes such diversity, and mechanistic understanding on alloying should still be pursued.

2.2 Alloying in bi-icosahedral $Au_{38}(SR)_{24}$ template

As with $Au_{25}(SR)_{18}$, $Au_{38}(SR)_{24}$ is also one of the classical and most researched nanoclusters owing to its high stability, rod-shaped structure and intriguing properties, especially chirality.[232-245] Although several other Au_{38} nanoclusters with different capping ligands and structures have been reported,[246-248] doping has only been accomplished on the classical $Au_{38}(SR)_{24}$ nanocluster (Table 2).

Table 2 Alloy nanoclusters based on the $Au_{38}(SR)_{24}$ template.

Formula	Measurement(s)	Ref(s)
$Au_{38}(SR)_{24}$	SC-XRD	232
$Au_{38-x}Ag_x(SR)_{24}$	MALDI-MS, ESI-MS	250-254
$Au_{38-x}Ag_x(SR)_{24}$ (x ~4)	SC-XRD	249
$Au_{38-x}Cu_x(SR)_{24}$ (x ~1)	SC-XRD	255
$Au_{38}Cu_1(SR)_{24}$	MALDI-MS	257
$Pd_2Au_{36}(SR)_{24}$	MALDI-MS, ESI-MS	258-260,262
$Pt_2Au_{36}(SR)_{24}$	MALDI-MS	262

The homo-gold $Au_{38}(SR)_{24}$ contains a bi-icosahedral Au_{23} kernel, which is capped by three monomeric $Au(SR)_2$ staples and six dimeric $Au_2(SR)_3$ staple motifs, Fig. 3a. Such a bi-icosahedral kernel can be viewed as two icosahedral Au_{13} kernels fused at a common Au_3 plane.

Ag-doping: The structure of $Au_{38-x}Ag_x(SR)_{24}$ (average x = 3.96) is determined to be the same as its parent cluster.[249] Although the MALDI-MS spectra indicated that up to 10 Ag heteroatoms can be incorporated into the $Au_{38}(SR)_{24}$ template, no crystal structures of heavily-Ag-doped $Au_{38-x}Ag_x(SR)_{24}$ are accessible yet,[250-253] which might due to the enhanced nanocluster surface flexibility along with the increased Ag-doping degree.[253] As for the doping modes, the introduced Ag heteroatoms preferentially take the bi-icosahedral kernel's surface sites (Fig. 3a, bottom-left). Specifically, the Au/Ag exchangeable positions are located at the middle three positions (the shared triangular plane), and the top/bottom two triangles of the Au_{23} kernel, resulting in $Au_2@Au_{17.04}Ag_{3.96}@3\times Au(SR)_2\&6\times Au_2(SR)_3$.[249] The kernel shell sites that can be doped with Ag might be related to the different coordination, and Ag atoms tend to take the positions which are more likely to transfer charge to staple Au or S atoms.

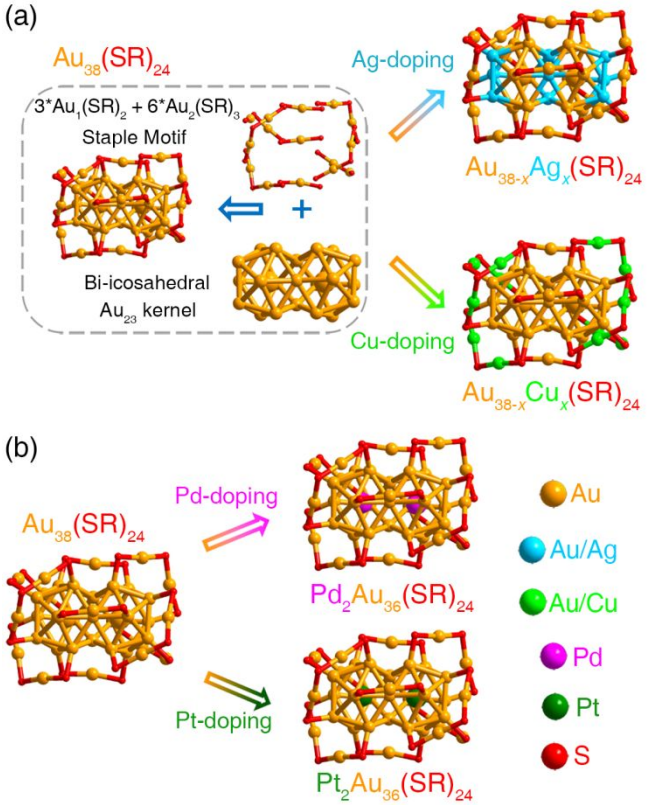

Fig. 3 Doping based on the $Au_{38}(SR)_{24}$ template. (a) Structural anatomy of $Au_{38}(SR)_{24}$, and corresponding $Au_{38-x}M_x(SR)_{24}$ (M = Ag/Cu) nanoclusters. (b) Structures of homo-gold $Au_{38}(SR)_{24}$ and proposed structures of corresponding $Pd_2Au_{36}(SR)_{24}$ and $Pt_2Au_{36}(SR)_{24}$ nanoclusters.

The dynamic behavior for doping $Au_{38}(SR)_{24}$ into $Ag_{38-x}Ag_x(SR)_{24}$ (SR = butanethiolate) in solution *via* adding Ag(I)-SR complexes was investigated by Negishi *et al*.[254] Although ESI-MS spectra suggested that the chemical composition of the doped clusters remains unchanged after $Ag_{38-x}Ag_x(SR)_{18}$ nanoclusters were obtained, continuously undergoing inter-cluster metal exchange was still implied by HPLC results. The frequency of the inter-cluster metal exchange was inversely proportional to the standing time of reaction, while such a phenomenon was absent if $Ag_{38-x}Ag_x(SR)_{24}$ nanoclusters were directly synthesized (co-reducing Au-SR/Ag-SR complexes). The reason for the inter-cluster metal exchange was proposed to be the presence of structural isomers of $Ag_{38-x}Ag_x(SR)_{24}$.[254]

Cu-doping: With an *in-situ* two-phase ligand-exchange approach, $Au_{38-x}Cu_x(SR)_{24}$ (x = 1-6) alloy nanoclusters were prepared and structurally determined.[255] Of note, the

stabilizer in $Au_{38-x}Cu_x(SR)_{24}$ is 2,4-DMBT (2,4-dimethylbenzenethiol), which is different from HS-C_2H_4Ph in $Au_{38-x}Ag_x(SR)_{24}$.[249] Interestingly, Cu heteroatoms are only found in the six dimeric motifs to form -SR-M-SR-M-SR- (M = Au/Cu) units (Fig. 3a, bottom-right). The different doping modes of Ag (exclusively kernel shell doping) and Cu (exclusively dimeric motif doping) probably result from the different electronic structures of these heteroatoms, the much smaller size of Cu compared to Ag and Au, etc. ESI-MS suggested that up to six Cu heteroatoms could be doped into the nanocluster template, with the strongest signal corresponding to $Cu_3Au_{35}(SR)_{24}$. However, SC-XRD demonstrated an average 0.996 of Cu, which was much less than the MS result,[255] which might be due to the less stability of multi-doped nanoclusters as we observed in the case of $Au_{18-x}Ag_x(SR)_{14}$. For the latter system, the initial MS spectrum showed signals for $Au_{14}Ag_4$ and $Au_{13}Ag_5$ co-existent with $Au_{15}Ag_3$, but the former two components slowly faded out during the crystallization process due to their lower stability.[256] Thus, a similar phenomenon might exist in $Au_{38-x}Cu_x(SR)_{24}$ nanoclusters as well. In terms of the doping effect on optical properties, because Cu heteroatoms contribute little to the frontier molecular orbitals of the nanocluster according to DFT calculations, its optical absorption is similar to that of homo-gold $Au_{38}(SR)_{24}$.[255]

Kazan *et al.* found that a Cu heteroatom can be captured by $Au_{38}(SR)_{24}$ onto its surface, producing $Cu_1Au_{38}(SR)_{24}$.[257] HPLC was used to separate Cu_1Au_{38} from the mixture, and the circular dichroism (CD) spectrum of chiral Cu_1Au_{38} was distinctively different from that of its Au_{38} homologue, revealing a variation in electronic structure due to copper addition.[257] Such a metal-ion capture was also found in $Au_{25}Ag_2(SR)_{18}$ as mentioned in Section 2.1 [see the method (iv)].[184]

Pt/Pd-doping: Mono-Pd or Pt can be introduced at the center position of the icosahedral kernel in $Au_{25}(SR)_{18}$ (see section 2.1). Similarly, center-occupation of Pd heteroatoms in the bi-icosahedral kernel is theoretically suggested for the alloyed $Pd_2Au_{36}(SR)_{24}$ nanocluster.[258] Comparative tests between homo-gold Au_{38} and doped Pd_2Au_{36} nanoclusters demonstrated that Pd-doping had significant effects on the electronic structure of M_{38} nanoclusters, which could further enhance the chemical/physical properties, such as thermal stability and surface flexibility.[258-262] Unfortunately, crystal structures of $M_2Au_{36}(SR)_{24}$ (M = Pd/Pt) nanoclusters have not been obtained, and thus, other means have been performed to determine the doping sites of Pt/Pd dopants, including theoretical analysis, XPS (X-ray photoelectron spectroscopy) and EXAFS spectroscopy,[260-262] but all indicate the center-doping mode in $M_2Au_{36}(SR)_{24}$ (Fig. 3b).[260-263]

Collectively, in the doped $M_{38}(SR)_{24}$, the introduced Ag heteroatoms are exclusively doped into the 9 specific sites of bi-icosahedral kernel shell; whereas some of the motif Au atoms can be replaced by Cu with the homo-gold kernel is preserved. However, only slight Ag- or Cu-doping has been achieved in M_{38} nanoclusters. Information on moderately to heavily-doped $Au_{38-x}M_x(SR)_{24}$ nanoclusters is highly desired, which might provide an opportunity to further illustrate (i) the gradual heteroatom doping processes and (ii) structure-property correlations at the atomic level. Furthermore, there are many relationships between $Au_{38}(SR)_{24}$ and $Au_{25}(SR)_{18}$ in terms of kernel configuration, motif structure, and the fusion transformation;[107,264] thus, it would be interesting to see if the doped $M_{25}(SR)_{18}$ can fuse into $M_{38}(SR)_{24}$ in a similar way as their parent clusters do.[264] Moreover, doping other heteroatoms, e.g., Cd and Hg, into the $Au_{38}(SR)_{24}$ template has not been reported yet, and neither has the ligand study been attempted. Considering that $Au_{38}(SR)_{24}$ nanoclusters can be prepared by different stabilizers (e.g., S-C_2H_4Ph, S-Ph, Se-Ph,[232,235,236] it remains unknown whether $Au_{38-x}M_x(SR)_{24}$ alloy nanoclusters display ligand-dependent alloying behavior or not. This deserves to be pursued in future work.

2.3 Alloying based on FCC/HCP Au templates

In sections 2.1 and 2.2, the doping modes in icosahedral nanoclusters have been highlighted, and one would wonder whether alloying based on FCC/HCP (FCC: face-centered cubic; HCP: hexagonal closest packed) templates would be different or not. In this section, alloying based on HCP $Au_{18}(SR)_{14}$, FCC $Au_{21}(SR)_{15}$, FCC $Au_{23}(SR)_{16}$, FCC $Au_{36}(SR)_{24}$ templates are highlighted. The doping mode indeed varies in nanocluster templates of different structure types.

2.3.1 Alloying based on HCP $Au_{18}(SR)_{14}$ nanocluster template

$Au_{18}(SR)_{14}$ contains a bi-octahedral HCP Au_9 kernel, which is protected by three $Au_1(SR)_2$ motifs, one $Au_2(SR)_3$ motif, and one $Au_4(SR)_5$ motif (Fig. 4a).[265,266] So far, two crystal structures of $Au_{18-x}Ag_x(SR)_{14}$ nanoclusters have been reported: $Au_{15}Ag_3(S\text{-}c\text{-}C_6H_{11})_{14}$ and $Au_{15}Ag_3(S\text{-}PhMe_2)_{14}$.[256,267] These two $Au_{15}Ag_3(SR)_{14}$ nanoclusters were obtained by different synthetic methods: (i) $Au_{15}Ag_3(S\text{-}c\text{-}C_6H_{11})_{14}$ was prepared by combining *in-situ* synthetic and ligand-exchange methods. Specifically, $(AuAg)_n(SG)_m$ (H-SG = glutathione) were initially prepared, and then the SG ligands were replaced by S-*c*-C_6H_{11} ligands *via* a two-phase ligand-exchange method;[267] (ii) the $Au_{15}Ag_3(S\text{-}PhMe_2)_{14}$ was produced by a metal-exchange method, in which $Au_{18}(S\text{-}PhMe_2)_{14}$ was first prepared by ligand-exchanging hydrophilic $Au_{18}(SG)_{14}$ with excess HS-$PhMe_2$, and then Ag(I)-S$PhMe_2$ was added to the solution of as-prepared $Au_{18}(S\text{-}PhMe_2)_{14}$ to prepare the alloy.[256]

Crystal structures of both $Au_{15}Ag_3$ nanoclusters (capped by S-*c*-C_6H_{11} or S-$PhMe_2$) demonstrate that the three Ag heteroatoms locate at the center triangle of the M_9 kernel, i.e., the Au_9 kernel with Au_3-Au_3-Au_3 constitution is doped into an Au_3-Ag_3-Au_3 constitution in $Au_{15}Ag_3(SR)_{14}$ (Fig. 4a). Although the final Ag doping numbers in crystal states for both alloy nanoclusters and the kernel structures are the same, some differences are apparent:

(i) The as-prepared products prepared by metal-exchanging $Au_{18}(S\text{-}PhMe_2)_{14}$ with Ag(I)-S$PhMe_2$ included $Au_{15}Ag_3$, $Au_{14}Ag_4$, and $Au_{13}Ag_5$. But only $Au_{15}Ag_3$ survived after repeated crystallization due to its distinctly higher stability.[256]

(ii) The atomic arrangements in the two $Au_{15}Ag_3$ structures are different, including the different kernel orientation and the motif structure orientations. Such differences induce the red-shifted optical absorption (by ~25 nm) and reduced optical gap (by ~0.15 eV) when comparing the UV-vis spectra of $Au_{15}Ag_3(S\text{-}PhMe_2)_{14}$ and $Au_{15}Ag_3(S\text{-}c\text{-}C_6H_{11})_{14}$.[267]
(iii) Enhanced thermal-stability accompanied by Ag doping has been proved in the $Au_{18}(S\text{-}PhMe_2)_{14}$-to-$Au_{15}Ag_3(S\text{-}PhMe_2)_{14}$ doping process,[256] and the enhanced stability might result from the Au-Ag inter-metallic synergism effects. However, in the $S\text{-}c\text{-}C_6H_{11}$ stabilized system, the stability of $Au_{15}Ag_3$ was much lower than the homo-gold Au_{18} nanocluster. DFT calculations were carried out based on the displacement reaction of $Au_{18}(S\text{-}c\text{-}C_6H_{11})_{14}$ + 3 Ag → $Au_{15}Ag_3(S\text{-}c\text{-}C_6H_{11})_{14}$ + 3 Au. The calculated heat of reaction is 0.41 eV, demonstrating that $Au_{15}Ag_3(S\text{-}c\text{-}C_6H_{11})_{14}$ displays relatively lower stability than $Au_{18}(S\text{-}c\text{-}C_6H_{11})_{14}$.[267] Therefore, the different thermal-stability observed in different thiolate-stabilized Au_{18}-$Au_{15}Ag_3$ systems can be understood by the ligand effect, which also induces slight structural changes and optical absorption variations between the two $Au_{15}Ag_3(SR)_{14}$ nanoclusters.[256]

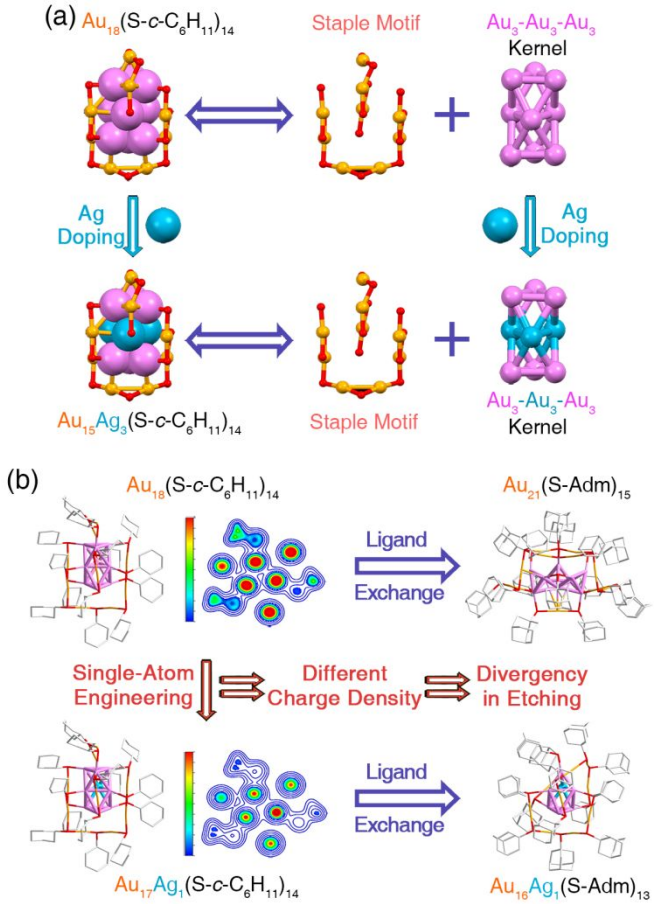

Fig. 4 Alloying based on the $Au_{18}(SR)_{14}$ template. (a) Structural anatomies of $Au_{18}(SR)_{14}$ and $Au_{15}Ag_3(SR)_{14}$ nanoclusters. (b) Ligand-exchanging induced size-growth from $Au_{18}(SR)_{14}$ to $Au_{21}(SR)_{15}$ or size-decrease from $Au_{17}Ag_1(SR)_{14}$ to $Au_{16}Ag_1(SR)_{13}$. Redrawn from ref. 271 with permission from American Chemical Society, copyright 2018.

The Ag doping process in hydrophilic $Au_{18}(SG)_{14}$ nanocluster is remarkably different from that in hydrophobic $Au_{18}(SR)_{14}$. Yu *et al.* reported an efficient synthesis of alloyed $Au_{18-x}Ag_x(SG)_{14}$ nanoclusters by the carbon monoxide (CO) reducing method.[268] The metal compositions of the final doped products could be rationally tuned by adjusting the Ag/Au ratio in the precursor. Specifically, (i) $Au_{18}(SG)_{14}$ was prepared from the Au(I)-SG complex; (ii) up to six Au atoms in the Au_9 kernel could be substituted by incoming Ag heteroatoms when Au/Ag ratio = 0.5, and increasing the Ag/Au ratio would increase the Ag doping number in $Au_{18-x}Ag_x(SG)_{14}$; (iii) when the Ag/Au ratio is over 0.75, no $M_{18}(SG)_{14}$ was generated, and only complexes were detected, such as $Au_1Ag_1(SG)_2$, $Au_1Ag_2(SG)_2$, and $Au_4Ag_3(SG)_5$ complexes. Consequently, Yu *et al.* proposed that the center Au_3 triangle was significant to maintain the $M_{18}(SG)_{14}$ nanoclusters, and the template would collapse when more than six Au atoms were substituted.[268] Moreover, it is proposed that hydrophilic $Au_{18}(SG)_{14}$ should have an Ag_3-Au_3-Ag_3 sequence in the kernel,[268] opposite to the Au_3-Ag_3-Au_3 sequence in hydrophobic $M_{18}(SR)_{14}$. This work demonstrates once again the ligand effect on the doping process.[268]

It is also possible to have $Au_{18-x}Ag_x(SR)_{14}$ ($x \geq 7$). Molina *et al.* theoretically explored the preferred Ag doping sites in $Au_{18-x}Ag_x(SR)_{14}$ ($1 \leq x \leq 10$).[269] Specifically, the first three Ag heteroatoms prefer to substitute the central Au_3 triangle, consistent with the experiments.[256,267] The fourth and fifth Ag heteroatoms tend to occupy the separated locations in the other two Au_3 plates on either side. When the Ag doping number reaches seven, an Ag_3-Ag_3-Ag_1Au_2 kernel is obtained. Then, all of the nine positions in the kernel will be replaced. DFT calculations revealed that the synergistic effects between Au and Ag disturbed the optical and chiroptical properties of $M_{18}(SR)_{14}$ nanoclusters, depending on the number of incorporated Ag heteroatoms.[269]

Doping Ag into $Au_{18}(SR)_{14}$ would remarkably affect the electronic structure of the nanocluster owing to the Au-Ag synergetic effect,[269] which would further affect the performance of nanoclusters in chemical reactions such as the ligand-exchange process. Ligand-exchange on $Au_{18}(S\text{-}C_6H_{11})_{14}$ with 1-adamantanethiol (HS-Adm) produces an $Au_{21}(S\text{-}Adm)_{15}$ nanocluster, following a size-growth mode.[270] Interestingly, Kang *et al.* demonstrated that the single-Ag-doped Au_{18} nanocluster, i.e., $Au_{17}Ag_1(S\text{-}C_6H_{11})_{14}$, would profoundly change the outcomes, giving rise to $Au_{16}Ag_1(S\text{-}Adm)_{13}$ with a decreased size (Fig. 4b).[271] The crystal structure of $Au_{16}Ag_1$ exhibits an Au_6Ag_1 kernel protected by one dimeric and two tetrameric motifs. Such a comparison illustrates that the Au_3-Au_2Ag_1-Au_3 kernel of $Au_{17}Ag_1$ transforms into an Au_1-Au_2Ag_1-Au_3 kernel in $Au_{16}Ag_1$, and the position of Ag atom maintains in this size-transformation process.[271] In order to reveal the fundamental cause of the differences in ligand-exchange processes, Vienna *ab initio* simulation package (VASP) was employed to perform the charge analysis on these two nanoclusters.[271] Results show that the heterogeneous distribution of charge density around

the Ag in $Au_{17}Ag_1$ comparing to that around the corresponding gold in Au_{18} was proposed as the fundamental reason.[270,271]

The Ag heteroatoms can also be used to bridge small Au(I)-thiolate motifs of $Au_{18}(SR)_{14}$, in which no Au atom in $Au_{18}(SR)_{14}$ is substituted.[272,273] Xie and co-workers reported using Ag^+ to link Au(I)-SG staple motifs, producing Au_{18}@Ag nanoclusters.[272] The formation of large Au(I)/Ag(I)-SG staple motif on the surface was suggested as the reason for remarkably enhanced photoluminescence (PL) of Au_{18}@Ag nanoclusters (quantum yield (QY) = 6.8%) *via* aggregation-induced emission (AIE), compared to the weakly emissive $Au_{18}(SG)_{14}$ nanocluster (QY = 0.37%). Such a method was also exploited for tailoring the PL properties of $Au_{15}(SG)_{13}$ and $Au_{25}(SG)_{18}$ nanoclusters.[272] In their latter work, the excited state dynamics of Au@Ag nanoclusters (including Au_{15}@Ag, Au_{18}@Ag, and Au_{25}@Ag) were studied by time-resolved transient absorption and emission,[273] demonstrating longer excited-state lifetimes than homo-gold nanoclusters. Particularly, the 350 nm absorption was more pronounced in Au@Ag nanoclusters, indicating the introduced Ag was on the surface (doping Ag into the kernel would induce a significant shift).[273]

Collectively, there are two alloying modes for Ag heteroatoms to interact with the $Au_{18}(SR)_{14}$ template: doping into the kernel, and alloying with the motifs, which would induce effects on electronic/geometrical structures, and variations in physical/chemical properties (such as PL) of the parent $Au_{18}(SR)_{14}$ nanoclusters. The M_{18} system is interesting because its HCP kernel is rarely observed in metal-thiolate nanoclusters,[90,117] and the unusual structure might bring about very different physicochemical properties which is deviated from other structures (icosahedral, FCC, etc.).[274,275]

2.3.2 Alloying based on FCC $Au_{21}(SR)_{15}$ nanocluster

There are two different structures for homo-gold $Au_{21}(SR)_{15}$, represented by Au_{21}(S-Adm)$_{15}$ and Au_{21}(S-^{t}Bu)$_{15}$ (S-^{t}Bu = *tert*-butyl mercaptan). The Au_{21}(S-Adm)$_{15}$ is obtained by ligand-exchanging $Au_{18}(S\text{-}C_6H_{11})_{14}$ with HS-Adm, where the HCP Au_9 kernel in $Au_{18}(SR)_{14}$ was transformed to an FCC Au_{10} kernel which is protected by a bridging thiolate, an $Au(SR)_2$ monomer, an $Au_2(SR)_3$ monomer, and an $Au_8(SR)_9$ staple motif (Fig. 5a).[270] By comparison, the Au_{21}(S-^{t}Bu)$_{15}$ counterpart comprises an Au_{14} kernel, capped by 5 bridging thiolates, two $Au_2(SR)_3$ dimers, and an $Au_3(SR)_4$ staple motif (Fig. 5b).[276] Alloying has been successfully done on both Au_{21} nanoclusters. Of note, another Au_{21} was also reported, *i.e.*, $Au_{21}S$(S-Adm)$_{15}$, but no alloying has been done yet.[277,278]

So far, only two heteroatoms (Ag, Cu) have been doped into the $Au_{21}(SR)_{15}$ template by *in-situ* synthetic procedures.[277,279] Zhu and co-workers prepared a group of HS-^{t}Bu stabilized $Au_{21-x}M_x(SR)_{15}$ (Fig. 5b), including $Au_{20}Cu_1$(S-^{t}Bu)$_{15}$, Ag_1Au_{20}(S-^{t}Bu)$_{15}$, $Au_{21-x}Ag_x$(S-^{t}Bu)$_{15}$ (x = 4-8), and $Au_{21-x}Cu_x$(S-^{t}Bu)$_{15}$ (x = 2-5). SC-XRD illustrated that the frameworks of these nanoclusters are all alike to Au_{21}(S-^{t}Bu)$_{15}$ except the $Au_{21-x}Cu_x$(S-^{t}Bu)$_{15}$ (x = 2-5) which is alike to Au_{21}(S-Adm)$_{15}$,[270,276] demonstrating that more Cu dopants would alter the structure of Au_{21}(S-^{t}Bu)$_{15}$. As to the slightly Ag-doped Ag_1Au_{20}(S-^{t}Bu)$_{15}$, the single Ag atom binds to $Au_2(SR)_3$ staple motif. As the Ag-doping number increases, more parent Au atoms on the kernel shell can be substituted, and finally, the staple Au can be replaced, too (Fig. 5b, upper-right).[276] The Cu doping is more complicated: (i) when the Cu doping number is 1, the configuration of Au_{21}(S-^{t}Bu)$_{15}$ is preserved, and Cu is arranged on the Au_2(S-^{t}Bu)$_3$ staple motif (Fig. 5b, marked in dark blue); (ii) more Cu dopants would alter the structure of Au_{21}(S-^{t}Bu)$_{15}$ to that of Au_{21}(S-Adm)$_{15}$. Specifically, aside from the central Cu, two Au atoms on the $Au_8(SR)_9$ motif are completely substituted as well, while other Au positions on $Au_8(SR)_9$ are partially doped (Fig. 5b, marked in dark green).[276] Optical absorption spectra of these S-^{t}Bu stabilized nanoclusters show characteristic peaks, demonstrating that alloying remarkably affects the electronic structure and chemical/physical properties of these nanoclusters.[276]

Accessing a series of correlated bi-metallic nanoclusters with different doping degrees and further revealing the successive transformations are of critical importance for gaining fundamental insight into the alloying mechanism. In 2018, Li et al. reported a series of correlated Au/Ag bimetallic nanoclusters.[279] Based on the structures of these alloy nanoclusters and correlations between structures and optical absorption, the effects of alloying on the evolution of size, structure, and optical properties were analyzed.[279] Structurally, the incomplete cuboctahedral FCC kernel of Au_{21}(S-Adm)$_{15}$ first transforms to a complete cuboctahedral $Au_{12}Ag_1$ kernel in the $Au_{20}Ag_1$(S-Adm)$_{15}$, then to an icosahedral $Au_{10}Ag_3$ kernel in $Au_{19}Ag_4$(S-Adm)$_{15}$, $Au_{23-x}Ag_x$(S-Adm)$_{15}$ (x ~5.76), and $Au_{23-x}Ag_x$(S-Adm)$_{15}$ (x ~7.44) nanoclusters (Fig. 5c). Of note, the configuration of $Au_{20}Ag_1$(S-Adm)$_{15}$ is the same as that of $Au_{20}Ag_1$(S-*t*Bu)$_{15}$ nanocluster.[276,279] Significantly, (i) along with the increase of Ag number in the cluster, the cluster size increased from the size of 21-metal (with a 11-metal kernel) to 23-metal (with a 13-metal kernel), and meanwhile, the free electron number increased from 6e to 8e; (ii) such transformations could be controlled by controlling the ratio of Au/Ag in the precursor.[279] Electron density accumulated on the center Au atoms due to the large difference in electronegativity between Au and Ag was rationalized to force an expansion of radial metal-metal bond angles, which triggered the M_{21}-to-M_{23} configuration conversion (or cuboctahedral-to-icosahedral kernel conversion).[279] As for the S-Adm stabilized Ag_4Au_{19}, Ag_xAu_{23-x} (x ~5.76), and Ag_xAu_{23-x} (x ~7.44) adopting the same configurations, the optical gap increased (from 1.31 to 1.37 and 1.46 eV, respectively) along with the number of Ag doping.[279] This trend is consistent with the increased HOMO-LUMO gap of doped $Ag_xAu_{25-x}(SR)_{18}$ nanoclusters relative to that of homo-gold $Au_{25}(SR)_{18}$,[65,177] which is caused by the involvement of silver 5*s* and 5*p* orbitals in electronic states.[177]

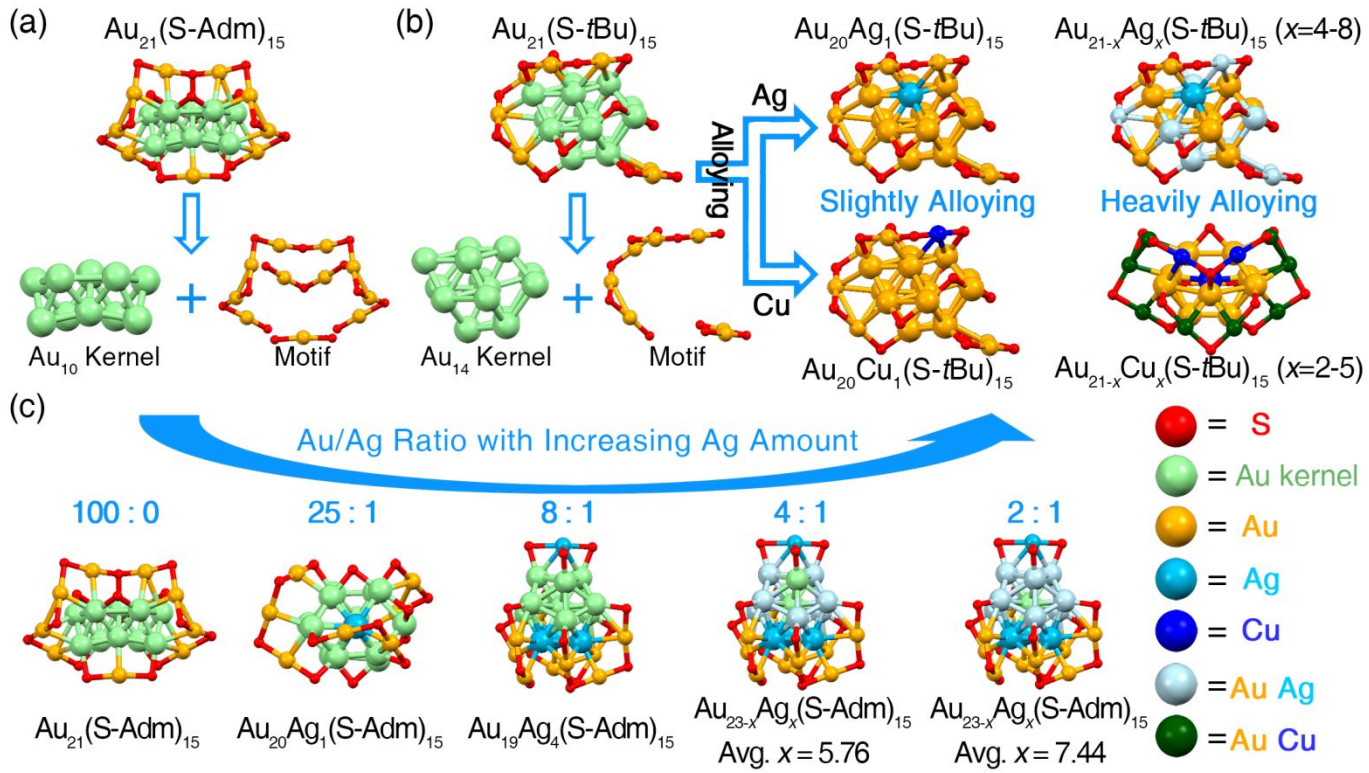

Fig. 5 Alloying based on the $Au_{21}(SR)_{15}$ template. (a) Structural anatomy of $Au_{21}(S\text{-}Adm)_{15}$ nanocluster. (b) Structural anatomy of $Au_{21}(S\text{-}^tBu)_{15}$ nanocluster and its Ag- or Cu-doping counterparts. (c) Evolution of crystal structures in synthesizing a series of Au/Ag nanoclusters, depending on the Au/Ag ratio in precursors.

In summary, the Ag and Cu heterometals have been incorporated into the $Au_{21}(SR)_{15}$ (SR = S-Adm or S-^{t}Bu) templates. The alloying mode varies by the different dopants (Ag *versus* Cu) and ligands (S-Adm *versus* S-^{t}Bu). Series of correlated nanoclusters are achieved, making them different from the simple templated doping mode (with the structure preserved) we discussed in $M_{25}(SR)_{18}$ and $M_{38}(SR)_{24}$. This will pave the way towards controllable synthesis of alloy nanoclusters with atomic-level capabilities.

2.3.3 Alloying based on FCC $Au_{23}(SR)_{16}$ nanocluster

The FCC $Au_{23}(S\text{-}c\text{-}C_6H_{13})_{16}$ contains a cuboctahedron (Au_{13}) kernel, which is capped by two hub-like gold atoms, and further protected by four bridging thiolates, two $Au_1(SR)_2$ monomers, and two $Au_3(SR)_4$ trimers.[280] Up to now, three types of heteroatoms (M = Ag, Cd, Cu) have been doped into the Au_{23} template. The alloying degree (or the doping number) of each heteroatom can be controlled *via* regulating the M/Au ratio in *in-situ* synthetic procedures, or the amount of M-SR complexes reacting with the pre-synthesized $Au_{23}(SR)_{16}$. More than 10 derivatives have been obtained on the basis of $Au_{23}(SR)_{16}$ (Fig. 6),[179,194,200,281-283] including (i) Ag-doping derivatives: slightly-doped $Au_{23-x}Ag_x(SR)_{16}$ (x ~0.87), moderately-doped $Au_{25-x}Ag_x(SR)_{18}$ (x ~4.49), heavily-doped $Au_{25-x}Ag_x(SR)_{18}$ (x ~19.4), Ag-doped/ligand-exchanged $Au_{24-x}Ag_x(SR)_{20}$ (x ~1), and Ag-Au-Cl treated $[Au_{21}(SR)_{12}(P\text{-}C\text{-}P)_2][AgCl_2]$ and $[Au_{21}(SR)_{12}(P\text{-}C\text{-}P)_2][Cl]$; (ii) Cd-doping derivatives: slightly-doped $Au_{23-x}Cd_x(SR)_{16}$ (x ~2.3), Au/Cd alloy $Au_{20}Cd_4(SH)(SR)_{19}$ and $Au_{19}Cd_2(SR)_{16}$, and Cd^{2+} or H_2O_2 oxidization-induced transformation into $Au_{28}(SR)_{20}$; (iii) Cu-doping derivatives: slightly-doped $Au_{23-x}Cu_x(SR)_{16}$ (x ~1.66). Of note, accompanied by the doping process, the cluster constitution can be maintained or altered, depending on the method, the quantity or the ligand of heteroatom complexes.[179,194,200,281-283]

Altering the homo-gold precursor to Au/Ag = 1/0.07 produced slightly-doped $Au_{23-x}Ag_x(SR)_{16}$, in which the $Au_{23}(SR)_{16}$ template was maintained.[281] Structurally, four Au sites, two on the kernel shell and the other two bridging the Au_{13} kernel and motifs, can be substituted. The largest occupancy of Ag at each position is only 31.5%. Based on this alloy nanocluster, Li et al. demonstrated a site-specific "surgery" on the surface motif *via* a two-step metal-exchange process, causing the "resection" of two surface Au atoms without altering the other parts of the initial $Au_{23}(SR)_{16}$ nanocluster.[281] Specifically, the $Au_{23}(SR)_{16}$ was first alloyed into the slightly-doped $Au_{23-x}Ag_x(SR)_{16}$, and then reacted with Au_2Cl_2(P-C-P) complex (P-C-P = $Ph_2PCH_2PPh_2$) to produce homo-gold $[Au_{21}(SR)_{12}(P\text{-}C\text{-}P)_2]^+$ (counterion: $[AgCl_2]^-$).[281] In another work, $[AgCl_2]^-$ was substituted by Cl^-,[194] and these counterions indeed affect the assembly of such nanoclusters and charge-transport properties.[194,281]

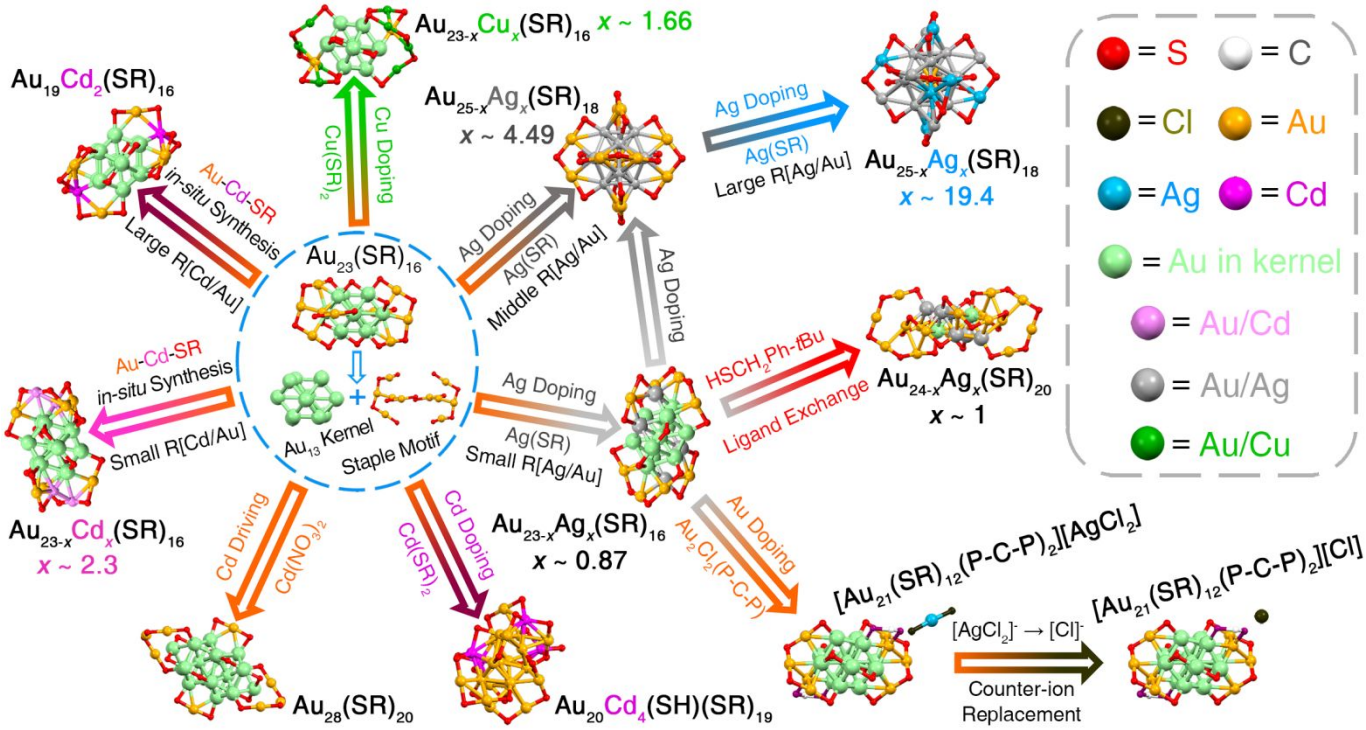

Fig. 6 Alloying based on the $Au_{23}(SR)_{16}$ template. Crystal structures include $Au_{23-x}Ag_x(SR)_{16}$ (x ~0.87), $Au_{25-x}Ag_x(SR)_{18}$ (x ~4.49), $Au_{25-x}Ag_x(SR)_{18}$ (x ~19.4), $[Au_{21}(SR)_{12}(P\text{-}C\text{-}P)_2][AgCl_2]$, $[Au_{21}(SR)_{12}(P\text{-}C\text{-}P)_2][Cl]$, ligand-exchanged $Au_{24-x}Ag_x(SR)_{20}$ (x ~1), $Au_{23-x}Cu_x(SR)_{16}$ (x ~1.66), $Au_{20}Cd_4(SH)(SR)_{19}$, $Au_{28}(SR)_{20}$, $Au_{23-x}Cd_x(SR)_{16}$ (x ~ 2.3), and $Au_{19}Cd_2(SR)_{16}$. Of note, some in this figure are not alloy nanoclusters (e.g., $Au_{28}(SR)_{20}$, $Au_{21}(SR)_{12}(P\text{-}C\text{-}P)_2$), but they were synthesized in the presence of heteroatoms (e.g., Cd, Ag).

In contrast to the slightly-doped $Au_{23-x}Ag_x(SR)_{16}$ (x ~0.87), increasing Ag-doping would transform M_{23} into $Au_{25-x}Ag_x(SR)_{18}$ with moderate doping (x ~4.49), i.e. the size of the nanocluster increased from M_{23} to M_{25}.[281] All Ag heteroatoms were on the icosahedral kernel shell.[281] More Ag doping resulted in heavily-doped $Au_{25-x}Ag_x(SR)_{18}$ (x ~19.4), in which only the center cannot be occupied by Ag heteroatom due to the electronic effect. Collectively, a continuous Ag-doping system is established: $Au_{23}(SR)_{16}$ → slightly-doped $Au_{23-x}Ag_x(SR)_{16}$ (x ~0.87) → moderately-doped $Au_{25-x}Ag_x(SR)_{18}$ (x ~4.49) → heavily-doped $Au_{25-x}Ag_x(SR)_{18}$ (x ~19.4).[179,280,281] A noticeable conversion in cluster size/configuration occurs (*i.e.*, from M_{23} to M_{25}) when the doped Ag increases from ~1 to ~4. This case is also used to support the M_{21} to M_{23} transformation we discussed in section 2.3.2 that partial electron transfer would happen from Ag to Au to cause electron density accumulation on the central Au to trigger the structural transformation.[279]

Ligand-exchange on slightly-doped $Au_{23-x}Ag_x(SR)_{16}$ (x ~0.87) with HS-CH_2Ph-*t*Bu gives rise to $Au_{24-x}Ag_x(SR)_{20}$ (x ~1).[282] Similar to the Ag_{23} → $Au_{25-x}Ag_x$ process, the size-growth process was observed in $Au_{23-x}Ag_x$ → $Au_{24-x}Ag_x$, even if the driving forces in these two reactions are different — doping effect *versus* ligand effect.[179,282] The ligand exchange induced Au_{23} → Au_{24} transformation was reported before.[284] The obtained $Au_{24-x}Ag_x(SR)_{20}$ contains a M_8 kernel that is capped by four $Au_4(SR)_5$ tetramers, and only three special kernel positions can be occupied by Ag atoms.[282]

Controlling the ratio of Au/Cd in the syntheses of Au/Cd alloy nanoclusters enables control of the composition and size. Li *et al.* successfully reconstructed the surface structure of $Au_{23}(SR)_{16}$ by Cd alloying.[283] A low Au/Cd ratio in the precursor only introduced some Cd heteroatoms without altering the $Au_{23}(SR)_{16}$ template, i.e., $Au_{20.7}Cd_{2.3}(SR)_{16}$. At a high Au/Cd ratio, $Au_{19}Cd_2(SR)_{16}$ was obtained, representing a size decrease (M_{23} → M_{21}). Structurally, the cuboctahedral Au_{13} kernel of $Au_{19}Cd_2(SR)_{16}$ is the same as that of $Au_{23}(SR)_{16}$. However, the two adjacent gold atoms on the motif in $Au_{23}(SR)_{16}$ coalesced and were occupied by one introduced Cd heteroatom, creating a "paw-like" $Cd(SR)_3$ motif.[283] In all, the surface reconstruction induced by Cd doping is as follows, $Au_{23}(SR)_{16}$ → slightly-doped $Au_{23-x}Cd_x(SR)_{16}$ (x ~2.3) → $Au_{19}Cd_2(SR)_{16}$.

$Au_{23-x}Cd_x(SR)_{16}$ and $Au_{19}Cd_2(SR)_{16}$ nanoclusters were obtained *via* an *in-situ* synthetic procedure. Interestingly, some unexpected phenomena occurred by reacting $Au_{23}(SR)_{16}$ with $Cd(SR)_2$ complex or $Cd(NO_3)_2$ ions (AGR reaction).[200] Adding $Cd(SR)_2$ to $Au_{23}(SR)_{16}$ solution transformed Au_{23} to $Au_{20}Cd_4(SH)(SR)_{19}$, and the introduced Cd heteroatoms were at specific positions in both staple motifs and kernel.[200] In comparison, the addition of $Cd(NO_3)_2$ ions would transform $Au_{23}(SR)_{16}$ into a larger nanocluster—$Au_{28}(SR)_{20}$—by oxidation.[200] It should be noted that Higaki et al. earlier reported the transformation from $Au_{23}(SR)_{16}$ to $Au_{28}(SR)_{20}$ by H_2O_2 oxidation.[285] Tang *et al.* found that this growth could also be promoted by photons

with energy higher than the HOMO-LUMO energy gap of $Au_{23}(SR)_{16}$.[286] It is worth noting that light was also found to promote the one-electron oxidation of $Au_{25}(SR)_{18}^-$ to $Au_{25}(SR)_{18}^0$.[287] The photoinduction pathway could be exploited in future work.

Aside from Ag and Cd, Cu alloying based on the $Au_{23}(SR)_{16}$ template has also been achieved by the metal-exchange strategy.[283] Very few Cu heteroatoms could be exclusively introduced into the staple motifs of Au_{23} with the composition as $Au_{21.34}Cu_{1.66}(SR)_{16}$. Increasing the quantity of Cu dopants would cause the decomposition of the template.[283]

Overall, $Au_{23}(SR)_{16}$ has emerged as one of the most versatile templates to "absorb", "eliminate" and "accommodate" atoms upon alloying with heteroatoms such as Ag, Cd, and Cu. The number of heteroatoms in these Au_{23}-based alloy nanoclusters is controlled by (i) different M/Au ratios in the *in-situ* synthetic procedures, (ii) different hetero-metal complex/Au_{23} ratio. The structure of Au_{23} maintains in the case of slight-doping; however, overdosing heteroatoms transforms Au_{23} into other sizes/shapes. From this viewpoint, the transformation point (or the extreme that maintains the Au_{23} configuration) is of great significance for thoroughly grasping the alloying mechanism in FCC structures.

2.3.4 Alloying in FCC $Au_{36}(SR)_{24}$ nanocluster template

$Au_{36}(SR)_{24}$ contains an FCC $Au_{28}(SR)_{12}$ kernel, which is capped by four $Au_2(SR)_3$ staple motifs (Fig. 7a).[288-290] Since structural determination in 2012, many works have been reported on Au_{36} nanoclusters, including controllable syntheses,[281-295] structure transformations,[292-294,296,297] property investigations,[298,299] and alloying. Besides, two other types of Au_{36} nanoclusters, i.e., $Au_{36}(SR)_8Cl_{20}$ (with a different structure) and $Au_{36}(PhC{\equiv}C)_{24}$) were also reported.[300,301]

The Ag and Cu have been introduced into the $Au_{36}(SR)_{24}$ (SR = S-Ph-^{t}Bu) template.[302-305] By altering the Au:Ag ratios in the precursor, Dass and co-workers found that up to 8 Ag heteroatoms could be incorporated into $Au_{36}(SR)_{24}$.[302] In 2019, Sakthivel *et al*. reported the X-ray crystal structure of $Au_{36-x}Ag_x$(S-Ph-^{t}Bu)$_{24}$.[303] SC-XRD revealed a composition of $Au_{33.17}Ag_{2.83}$(S-Ph-^{t}Bu)$_{24}$ with 2 Ag heteroatoms doped on the 28-atom FCC kernel and 0.83 Ag distributed over metal atoms on the staple motifs (Fig. 7b).[303]

$Au_{36-x}Cu_x(SR)_{24}$ nanoclusters were prepared and structurally determined.[305] Compared with Ag-doping in the $Au_{36-x}Ag_x(SR)_{24}$ (x = 1-8), the number of doped Cu (x up to 3) is even smaller. Besides, Cu was also observed inside the FCC Au_{28} kernel of the $Au_{36}(SR)_{24}$ template (Fig. 7c), and a total of 14 sites could be substituted.[305]

Ag- and Cu-doping have been accomplished in the $Au_{36}(SR)_{24}$ template. Both Ag and Cu heteroatoms can be doped in staple motifs, and can also substitute the surface atoms in the FCC part of $Au_{36}(SR)_{24}$. General speaking, doping in FCC Au nanoclusters (Au_{23}, Au_{36}, etc.) is quite challenging. This can be understood by their unique electronic structure being very different from the superatom ones such as $M_{25}(SR)_{18}$, $M_{44}(SR)_{30}$, etc. For FCC nanoclusters, a superatom network model is proposed, in which multiple 4-center-2 electron tetrahedral Au_4 units can be found.[306,307] Experimental work also identified Au_4 features.[296] Thus, it might be very hard to break such electronic structures, hence, doping such FCC nanoclusters has met with difficulties; otherwise, structural transformation would be inevitable.

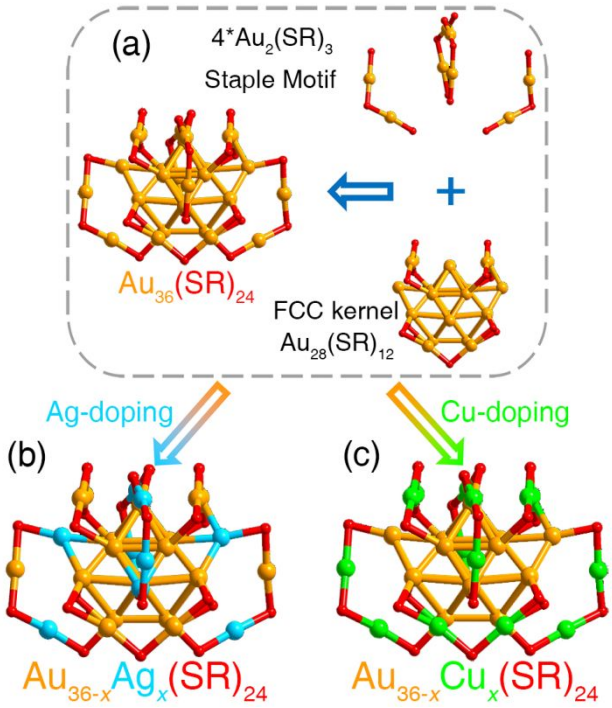

Fig. 7 Doping based on the $Au_{36}(SR)_{24}$ template. Structural anatomy of (a) $Au_{36}(SR)_{24}$ nanocluster, and (b) Ag- or (c) Cu-doped $Au_{36-x}M_x(SR)_{24}$ counterparts.

2.4 Alloying in small-sized Au:PPh_3 nanocluster template

Early research on phosphine-protected gold nanoclusters includes Au_9, Au_{11}, Au_{13}, and other sizes.[47,93,103,308] Typically, these small-sized nanoclusters adopt an incomplete or full icosahedral configuration. Here, we briefly summarize alloys based on Au_9, Au_{11}, and Au_{13} nanoclusters.

$Au_9(PPh_3)_8$ is one of the earliest studied small-sized gold nanoclusters.[309-313] Crystal structures of Au_9 demonstrate the reversible isomerization of this cluster. Specifically, $[Au_9(PPh_3)_8]^{3+}$ with a crown-like structure is crystallized in the presence of $[PMo_{12}O_{40}]^{3-}$ counter-ions; while a butterfly-like configuration can be observed when the Au_9 nanocluster is evaporated in the presence of Cl^- or NO_3^- counter-ions.[312,313] The presence of a Pd source in the synthesis results in $[Pd_1Au_8(PPh_3)_8]^{2+}$.[314-316] The central Au atom in the crown-like Au_9 is substituted; however, whether the Pd_1Au_8 is butterfly-like or not is not known yet (Fig. 8a). The Tsukuda group gave some reasons: First, DFT calculations demonstrated that the energy differences between the crown- and butterfly-like Au_9 nanoclusters were comparable to those between crown- and butterfly-like Pd_1Au_8 counterparts, i.e., the relative stability was not the reason. Second, the temperature-dependent Debye-Waller factors illustrated that the bond strength in

crown-like Pd_1Au_8 was much stiffer than that in crown-like Au_9. Third, the natural bond orbital analysis revealed that the stiffer Pd-Au and Au-Au bonds in crown-like Pd_1Au_8 relative to the corresponding Au-Au bonds in crown-like Au_9 originated from the increase in the ionic nature ($Pd^{\delta-}$-$Au^{\delta+}$) and the decrease in electrostatic repulsion between the surface Au atoms in Pd_1Au_8 nanocluster, respectively.[316]

Besides the enhanced metal-metal bonds in Pd_1Au_8 relative to those in Au_9, the Pd-Au synergetic effects will also regulate the electronic/geometrical structures and chemical/physical properties. Pd doping into Au_9 alters its structure, especially the ligand arrangement;[317] thus, the collision cross section (CCS, evaluated using the ion mobility mass spectrometry) values of these two nanoclusters are different: the CCS value of $Pd_1Au_8(PPh_3)_8$ is 422 Å^2, much smaller than that of the $Au_9(PPh_3)_8$ (442 Å^2).[317]

In 2018, Takano et al. doped a hydride (H^-) into the Au_9 or Pd_1Au_8 cluster surface, and then reacted the H-Au_9 or H-Pd_1Au_8 cluster with Au(I)-Cl (Fig. 8b).[318,319] The $(H\text{-}Au_9)^{2+}$ was converted to superatomic Au_{11}^{3+} in the presence of Au(I)-Cl, *via* the Au_{10}^{2+} superatom.[318] A sharp difference in the same procedure was observed when the interstitially doped H^- survived during the sequential addition of Au(I)-Cl, and the $(H\text{-}Pd_1Au_{10})^{3+}$ was the only product.[320] These opposite Au-addition results between $(H\text{-}Au_9)^{2+}$ and $(H\text{-}Pd_1Au_8)^{+}$ nanoclusters further demonstrate that the doping effect induced by the Pd would significantly affect their behaviors in the bottom-up synthetic procedure (*i.e.*, Au-addition process).

Similar to the Pd doping process, a single Pt atom was doped into the center of the Au_9 cluster.[320,321] Two situations can be observed from Pt/Pd doping: (i) only a single Pt/Pd heteroatom can be doped; (ii) the doped Pt/Pd heteroatom occupies the center in Au_9. Of note, this is exactly the same as what is observed in other mono-Pd/Pt-doped homo-gold or homo-silver nanoclusters (*e.g.*, $Pt_1Au_{24}(SR)_{18}$, $Pd_1Au_{24}(SR)_{18}$ see Section 2.1, and $Pt_1Ag_{24}(SR)_{18}$, and $Pd_1Ag_{24}(SR)_{18}$ see Section 3.1). Such characteristics might originate from the differences in electronic structures (outermost electronic configuration) between Au/Ag and Pd/Pt atoms.

Au_{11} and Au_{13} are the other two small-sized, phosphine-protected nanoclusters that have been successfully alloyed.[322-331] Based on these two templates, alloy nanoclusters of Pd/Au, Pt/Au, Ag/Au, and Cu/Au have been prepared.[332-338] By simultaneously reducing $Au(PPh_3)Cl$ and $Pd(PPh_3)_4$ complexes, Kurashige and Negishi reported $Pd_1Au_{10}(PPh_3)_8Cl_2$ (Fig. 8c).[332] The stability of Pd_1Au_{10} was much higher than Au_{11}, but no structure of Pd_1Au_{10} was obtained. The Pd_1Au_{10} emitted at ~950 nm with a PL QY of 0.15% owing to the synergetic effect between Au and Pd, while Au_{11} was non-emissive.[332] Steggerda and co-workers reported the hydride-containing H-Pt/Ag/Au and H-Pt/Cu/Au tri-metallic nanoclusters, with chemical formulas of $[H\text{-}Pt_1(X)_1(AuPPh_3)_8]^-$ and $[H\text{-}Pt_1(X)_2(AuPPh_3)_8]^-$ (X = $AgNO_3$ or CuCl), corresponding to the Au_{10} and Au_{11}, respectively.[333,334] Structurally, the single Pt atom occupies the center position, and the Au, Ag, and Cu atoms are on the surface.[333,334]

Different from the aforementioned phosphine-protected alloy nanoclusters that were prepared by the *in-situ* synthetic procedure, Copley and Mingos developed a metal-exchange method to synthesize small-sized alloy nanoclusters.[335,336] Specifically, the reaction between $Au_{11}(PPh_3)_{10}$ and Au(I) (or Ag(I), Cu(I)) complexes generate $Au_{13}(PPh_3)_8Cl_4$, $Ag_4Au_9(PPh_3)_8Cl_4$, or $Cu_4Au_9(PPh_3)_8Cl_4$ (Fig. 8d).[336] For these M_{13} nanoclusters, Au atoms (or the introduced Ag/Cu heteroatoms) on the surface could be divided into two categories: (i) the 8 surface Au atoms (from the starting Au_{11}) binding to PPh_3 that were originally on Au_{11}; (ii) the four M atoms (M = Au/Ag/Cu) connecting to Cl ligands that are concomitantly introduced to the Au_{13} system.[336]

Qin et al. obtained the crystal structure of $Ag_3Au_8(PPh_3)_7Cl_3$.[337] The Ag_3Au_8 nanocluster possesses a similar structure as that of Au_{11}, both having an 8e closed shell electronic structure. Three Ag heteroatoms are found to be on the surface and are bonded with the three chlorine ligands.[337]

In 2017, Lv *et al.* theoretically investigated the alloying effects based on the structure of $Au_{13}(PPh_3)_8Cl_4$ nanoclusters.[338] DFT results illustrated that the Ag and Cu heteroatoms prefer the surface sites, whereas the single Pd tends to occupy the central position. By doping different types of heteroatoms, the geometric structure and the frontier orbitals of Au_{13} change in different ways. The Pd doping leads to relatively longer metal-metal distances within the icosahedron, while the bond lengths are significantly shortened when Cu heteroatoms are incorporated. In addition, theoretical energies between the highest occupied molecular orbital (HOMO) and the lowest unoccupied molecular orbital (LUMO) follow the order of Pd_1Au_{12} < Ag_4Au_9 < Au_{13} ≈ Cu_4Au_9.[338]

Based on these phosphine-protected alloy nanoclusters, one can conclude that the Ag/Cu alloying is (i) in multiple number and (ii) surface-doping. By comparison, the Pd and Pt follow a mono-doping and central occupation tendency. The reason might be the difference in outermost electron configurations between Au/Ag/Cu and Pt/Pd atoms, i.e. Au/Ag/Cu ($d^{10}s^1$) vs. Pd ($d^{10}s^0$) vs. Pt (d^{10}) in the doped state. Other alloying works based on small-sized phosphine-protected Au clusters can be found in Ref. 93.

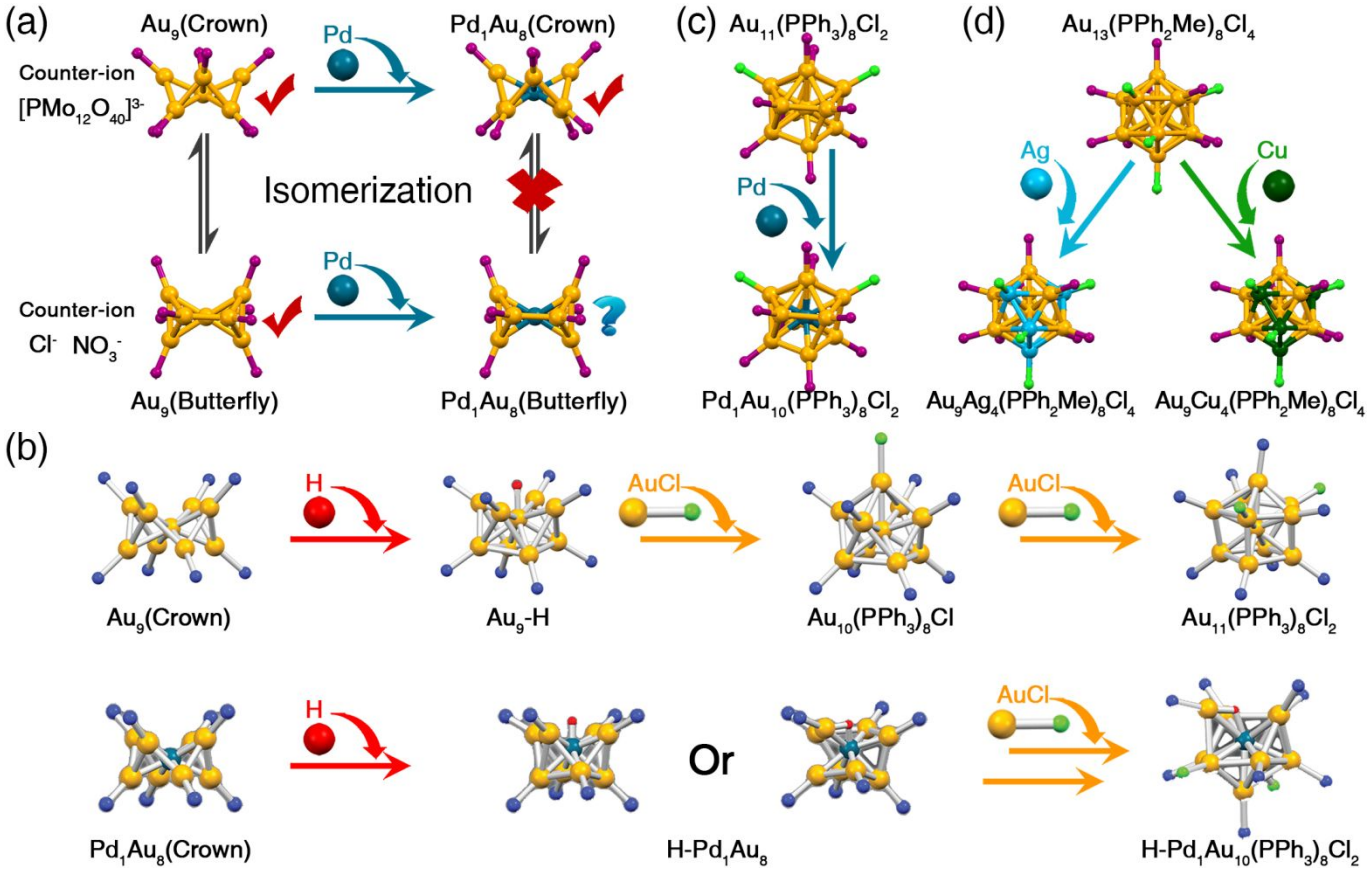

Fig. 8 Alloying in phosphine-stabilized small-sized nanoclusters. (a) $Au_9(PPh_3)_8$ and $Pd_1Au_8(PPh_3)_8$ nanoclusters with butterfly-like or crown-like configurations (the structure of butterfly-like Pd_1Au_8 is proposed). Redrawn from ref. 316 with permission from American Chemical Society, copyright 2017. (b) H-$Au_9(PPh_3)_8$ and H-$Pd_1Au_8(PPh_3)_8$ nanoclusters and the growth induced by the addition of AuCl. Redrawn from ref. 318, 319 with permission from American Chemical Society, copyright 2018. (c) Structure of $Au_{11}(PPh_3)_8Cl_2$ and proposed structure of its $Pd_1Au_{10}(PPh_3)_8Cl_2$ counterpart. (d) $Au_{13}(PPh_2Me)_8Cl_4$, and its $Ag_4Au_9(PPh_2Me)_8Cl_4$ and $Cu_4Au_9(PPh_2Me)_8Cl_4$ alloy counterparts.

2.5 Alloying in cluster of clusters

Before the attainment of rod-like Au_{25} co-protected by phosphine and halogen ligands, Teo and coworkers reported rod-like $Au_{25-x}M_x$ nanoclusters (M = Ag, Pt, Pd) in the 1980s, and they proposed a "cluster of clusters" assembly pattern that generalized the structural- and size-growth mode based on these alloy nanoclusters.[339-345] The follow-up works include the experimental formation of a relatively large $(Au_{13})_{55}$ assembled super-cluster and theoretical investigations on the assembled linear or cyclic $(M_{13})_n$ nanoclusters.[346-348] The synthesis and crystal structure of rod-like $[Au_{25}(SR)_5(PPh_3)_{10}Cl_2]^{2+}$ (Fig. 9a) were reported by Tsukuda's group in 2007.[349] For the M_{25} rod cluster, because the halogen-Ag bond is much stronger than halogen-Au (e.g., Ag-Cl bond energy of 314 ± 21 KJ/mol > Au-Cl bond energy of 289 ± 63 KJ/mol; and so are the M-Br and M-I bonds),[350] the metal atoms that coordinate to the halogen atoms are all Ag atoms. By comparison, Au atoms preferentially take the top and bottom pentagonal positions that bond to the PPh_3 ligands. Similar bonding modes have been observed in halogen/phosphine co-protected M_{37} and M_{38} alloy nanoclusters (*vide infra*). Introducing thiol into the Au_{11} solution successfully assembled the icosahedral building blocks into an Au_{25} nanocluster.[349] Structurally, two icosahedral Au_{13} building blocks are fused together by sharing a vertical gold atom and are also linked by five thiolates (Fig. 9a). On a note, the halogen-protected rod-like Au_{25} counterpart (*i.e.*, halogen replacing thiolate) has not been experimentally available (see the $[Au_{25}(PPh_3)_{10}Cl_7]^{2+}$, Fig. 9a), probably due to the less stable Au-halogen bonds. The alloying nanoclusters for cluster of clusters are summarized in Table 3. Several other works were reported for the rod-like $[Au_{25}(SR)_5(PPh_3)_{10}X_2]^{2+}$ (X = Cl/Br) nanoclusters,[351-355] and the chemical/physical properties were investigated, including the ultrafast dynamics, optical and electrochemical properties.[356-359]

Based on the "cluster of clusters" assembly mode, Teo and co-workers reported a series of structures of $Au_{12}Ag_{13}$ nanoclusters co-protected by phosphine and halogen ligands (Fig. 9b).[360-365] Specifically, Ag atoms are at the top/bottom apexes, the waist, and the shared vertex. By comparison, Au atoms prefer to occupy the sites that are capped by phosphine ligands, and the centers of the two icosahedra. Interestingly, two types of waist-halogen protecting modes are observed, labeled as X_5 and X_6 (Fig. 9b). As for the X_5

mode, the formula is $[Au_{12}Ag_{13}(PPh_3)X_7]^{2+}$, in which the waist-Ag atoms are linked by five halogen atoms, with "one-to-one" linking (Fig. 9b, *upper-right*).[363] When six halogen atoms are introduced to give rise to $[Au_{12}Ag_{13}(PPh_3)X_8]^{+}$, the capping mode at the waist positions is shown in Fig. 9b, bottom-right.[361,362,364,365] Using metal-organic frameworks (MOFs) as size-selection templates, Zhu and co-workers obtained pure $[Au_{12}Ag_{13}(PPh_3)_{10}Cl_8]^{+}$ nanocluster *via* a one-step, *in-situ* reduction method.[366] Nunokawa et al. replaced the halogen ligands with NO_3^- and synthesized a charge-neutral $Au_{12}Ag_7(PPhMe_2)_{10}(NO_3)_9$ (Fig. 9d), whose configuration is a bi-capped pentagonal anti-prismatic cage with staggered-staggered M_5 rings (M = Au/Ag).[367] The $Au_{12}Ag_7$ nanocluster exhibits an interpenetrated biicosahedron mode and provides the missing link between icosahedral M_{13} and bi-icosahedral M_{25} nanoclusters, and hence useful insights into the nanocluster growth.[367]

Table 3 Alloy nanoclusters of the "cluster of clusters" type.

Formula	Ref(s)
$[Au_{25}(SR)_5(PPh_3)_{10}Cl_2]^{2+}$	349
$[Au_{13}Ag_{12}(PPh_3)_{12}X_n]^{m+}$	360-365
$[Au_{25-x}Ag_x(SR)_5(PPh_3)_{10}Cl_2]^{2+}$	368
$[Au_{25-x}Cu_x(SR)_5(PPh_3)_{10}Cl_2]^{2+}$	375
$[Pd_1Au_{24}(SR)_5(PPh_3)_{10}Cl_2]^{+}$	376
$[Pd_2Au_{23}(PPh_3)_{10}Br_7]^{+}$	377
$Pt_2Ag_{23}(PPh_3)_{10}Cl_7$	383
$[Au_{12}Ag_7(PPhMe_2)]^{9+}$	367
$[Cu_3Au_{34}(SR)_6(PPh_3)_{13}S_2]^{3+}$	375
$[Au_{18}Ag_{19}(p\text{-}Tol_3P)_{12}Br_{11}]^{2+}$	386
$Au_{18}Ag_{20}(PPh_3)_{12}Cl_{14}$	391-394

Inspired by the reaction of small-sized phosphine-protected gold nanoclusters with thiols to generate the homo-gold $[Au_{25}(SR)_5(PPh_3)_{10}Cl_2]^{2+}$ nanocluster,[350] Wang *et al.* introduced Ag-SR complexes into this size-growth process, and was able to adjust the number of Ag heteroatoms doped into the rod-like M_{25} template (Fig. 9c).[368] Two approaches were developed: (i) doping the PPh_3-capped gold nanoclusters with Ag-SR complexes to generate $[Au_{25-x}Ag_x(SR)_5(PPh_3)_{10}Cl_2]^{2+}$ nanoclusters with $x \leq 12$; (ii) metal-exchanging the $[Au_{11}(PPh_3)_8Cl_2]^{+}$ with Ag-SR complexes to generate $[Au_{25-x}Ag_x(SR)_5(PPh_3)_{10}Cl_2]^{2+}$ nanoclusters with $x \leq 13$. SC-XRD results demonstrated that the shared vertex, the waist, and the icosahedral centers were randomly occupied by Au or Ag, but with a much higher Ag percentage for the $x \leq 13$ nanocluster.[368] Significantly, in sharp contrast to the non-emissive $[Au_{25}(SR)_5(PPh_3)_{10}Cl_2]^{2+}$, and the weakly-emissive $[Au_{25-x}Ag_x(SR)_5(PPh_3)_{10}Cl_2]^{2+}$ ($x \leq 12$), the $[Au_{25-x}Ag_x(SR)_5(PPh_3)_{10}Cl_2]^{2+}$ ($x \leq 13$) showed a 200-fold QY boost in PL, illustrating the important role of the 13th silver in the nanocluster.[368] Further theoretical work suggested that the origin of PL boost lied in the nature of the first excited state (S_1) and its corresponding HOMO-LUMO transition, which was significantly affected by the doping number and position of Ag heteroatoms in the rod-like Au_{25} template.[369] Ultrafast relaxation dynamics of these M_{25} nanoclusters were also investigated for understanding the mechanism of the PL enhancement,[370] which will be presented in Section 7.

Mattoussi and co-worker reported the synthesis of functionalized Au/Ag alloy nanocluster by reacting the $Au_{11}(PPh_3)_8Cl_2$ with Ag(I)-SR complexes, where SR is short-chain aliphatic monothiols, poly(ethylene glycol)- or zwitterion-appended monothiols.[371] The optical absorption and PL emission of the obtained Au/Ag nanoclusters were very close to those of $[Au_{25-x}Ag_x(SC_2H_4Ph)_5(PPh_3)_{10}Cl_2]^{2+}$.[371]

Because of the similarity in electronic structures of Ag and Cu with Au ($d^{10}s^1$ configuration), the single-heteroatom doping into gold nanoclusters is limited, that is, easily forming a distribution of Cu or Ag dopants in Au_n templates (see section 2.3.1-2.3.4). Wang et al. put forward an alloying strategy to shuttle a single Ag or Cu heteroatom into a centrally hollow, rod-shaped $[Au_{24}(SR)_5(PPh_3)_{10}Cl_2]^{2+}$ nanocluster, transforming it into Ag_1Au_{24} and Cu_1Au_{24} alloy nanoclusters in a highly controllable manner (Fig. 9e/f).[372] The hollow Au_{24} rod (c.f. the center-filled Au_{25} rod) was prepared by etching the $[Au_{25}(SR)_5(PPh_3)_{10}Cl_2]^{2+}$ rod with a large amount of PPh_3,[373] with theoretical insight reported by Goh et al.[374] Furthermore, reacting this hollow Au_{24} with AuCl, AgCl or CuCl salt produced "non-hollow" Au_{25}, Ag_1Au_{24}, and Cu_1Au_{24} rod, respectively.[372] The introduced Ag heteroatom occupies one apex site. Repeating the PPh_3 etching and Ag doping process generated Ag_2Au_{23}, in which both apex sites became Ag (Fig. 9e).

Compared to Ag doping, alloying the hollow Au_{24} with CuCl was different. The mono-Cu heteroatom was selectively doped into two different sites in the template with 30% of apex-doping and 70% of waist-doping (Fig. 9f), that is, a distribution of two configurations. This ligand-induced single-heteroatom shuttling procedure provides a strategy to control the doping number and the site of heteroatoms in M_{25} rods.[372] For comparison, multi-Cu doped $[Au_{25-x}Cu_x(SR)_5(PPh_3)_{10}Cl_2]^{2+}$ (x ~2.75) was later obtained,[375] in which the $Au_{25-x}Cu_x$ rods were prepared by doping PPh_3-stabilized gold nanoparticles with Cu(I)-SR complexes. SC-XRD revealed that both the apex and the waist sites are partially occupied with Cu/Au = 1:3 proportion (Fig. 9g).[375]

An interesting phenomenon in the aforementioned M_{25} rod nanoclusters is that the centers of icosahedrons are always occupied by Au atoms in Ag or Cu doping, which indicates the gold atoms at icosahedral centers are critical to ensure the stability. However, Pd or Pt doping would take the central site of the icosahedron, i.e. a Pt/Pd@Au/Ag mode (Fig. 9h). Negishi and co-workers reacted $Au_{n-x}Pd_x$ (n = 6-12; x = 0-2) with abundant thiol to assemble these small-sized nanoclusters into a bi-icosahedral $[Pd_1Au_{24}(SR)_5(PPh_3)_{10}Cl_2]^{+}$ nanocluster in which one of the two icosahedral centers was substituted by Pd.[376] In another work, substitution of both central Au atoms by Pd was accomplished.[377] Considering that alloying is capable of tailoring the electronic structure of nanoclusters, Kang *et al*. introduced the Pd heteroatom into the M_{25} template and successfully obtained the electroneutral $Pd_2Au_{23}(PPh_3)_{10}Br_7$ possessing unprecedented

Au-halogen linkages.[377] SC-XRD results suggested that the two centers of M_{13} building blocks were occupied by Pd atoms. By comparison, the absence of Pd sources resulted in un-assembled Au_{11} nanoclusters. Hirshfeld charge analyses implied that significantly reduced electronic repulsion between two icosahedral units induced by the synergism between Pd and Au metals promoted the assembly.[377] Such results expand the scope of linkage in rod-like M_{25} nanoclusters.[377] With Pt or Pd heteroatoms in the center(s) of the icosahedron(s), several other M_{25} nanoclusters with tri-metallic compositions were also obtained and structurally determined, including $Pt_1Ag_{12}Au_{12}$, $Pt_2Ag_{13}Au_{10}$ nanoclusters (Fig. 9h),[378-381] which will be discussed in section 5. Besides, based on the rod-like M_{25} template, the alloying effects on geometric structures, electronic structures, optical properties (such as PL and ECL) have been investigated.[382-385]

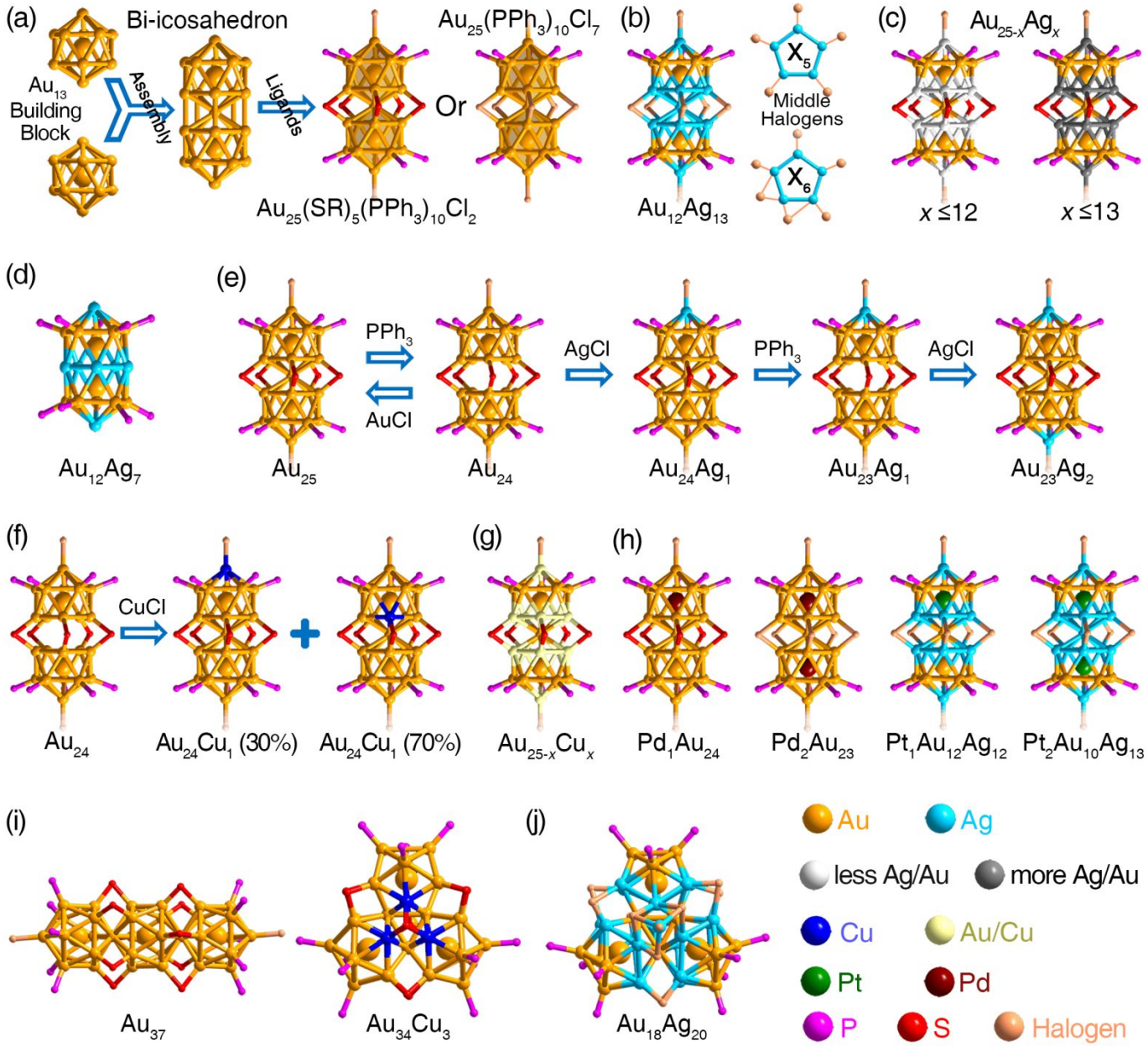

Fig. 9 Alloying based on the rod-like Au_{25} and cyclic/linear $Au_{37/38}$ templates. (a) Structural anatomy of rod-like $Au_{25}(SR)_5(PPh_3)_{10}Cl_2$ and proposed structure of $[Au_{25}(PPh_3)_{10}Cl_7]^{2+}$ nanoclusters. (b) Structures of rod-like $Au_{12}Ag_{13}$ nanoclusters with two types of waist-halogen protecting modes (X_5 and X_6, X = Cl/Br), giving $[Au_{12}Ag_{13}(PPh_3)_{10}X_7]^{2+}$ and $[Au_{12}Ag_{13}(PPh_3)_{10}X_8]^{+}$. (c) Crystal structures of $[Au_{25-x}Ag_x(PPh_3)_{10}(SR)_5Cl_2]^{2+}$ nanoclusters. (d) Crystal structure of $Au_{12}Ag_7(PPhMe_2)_{10}(NO_3)_9$. (e) Mechanism of controllably injecting two Ag heteroatoms into rod-like Au_{25} *via* the hollowing-refilling sequence. (f) Doping a single Cu heteroatom into rod-like Au_{25}. (g) Crystal structure of $[Au_{25-x}Cu_x(PPh_3)_{10}(SR)_5Cl_2]^{2+}$ nanoclusters (x ~2.5). (h) Crystal structures of rod-like Pd_1Au_{24}, Pd_2Au_{23}, $Pt_1Au_{12}Ag_{12}$, $Pt_2Au_{10}Ag_{13}$ nanoclusters. (i) Crystal structures of linear $Ag_{37}(SR)_{10}(PPh_3)_{10}Cl_2$ and cyclic $Cu_3Au_{34}(PPh_3)_{13}(SR)_6S_2$ (M_{37}). (j) Crystal structure of cyclic $Au_{18}Ag_{20}(PPh_3)_{12}Cl_{14}$ (M_{38}).

Nanoclusters with a cyclic M_{37} framework were also reported in early work by Teo and co-workers. The structure of $Au_{18}Ag_{19}(PPh_3)_{12}Br_{11}$ comprises three M_{13} (M = Au/Ag) icosahedral building blocks formed a cyclic assembly *via* vertex-sharing.[386] The Cu-doped M_{37}, i.e. $Cu_3Au_{34}(PPh_3)_{13}(SR)_6S_2$, was also determined structurally,[375] which can be described as three icosahedral M_{13} building blocks sharing three vertex Au atoms in a cyclic fashion (Fig. 9i). The three Cu atoms occupy the internal positions of the cluster core, and interestingly, all Cu atoms are mono-coordinated to the bare S atoms.[375] Compared with Ag-alloying based on the M_{37} template, Cu-alloying follows a slight doping manner. It should be noted that linear $Au_{37}(SR)_{10}(PPh_3)_{10}X_2$ (X = Cl/Br) was also structurally determined,[387] and the related calculations as well as applications were performed;[388,389] however, no alloying work based on this linear nanocluster was reported. The penta-icosahedral Au_{60} is a cyclic assembly of five Au_{13} icosahedral *via* sharing five vertex Au atoms.[390]

Within the "cluster of clusters" frame, M_{38} nanoclusters were structurally determined *via* cyclic assembly of three icosahedral M_{13} building blocks via vertex sharing.[391-394] The metal compositions of these M_{38} are $Au_{18}Ag_{20}$; however, two categories of the peripheral ligands were observed: 12 phosphines and 14 halogen ligands (*i.e.*, $Au_{18}Ag_{20}(PPh_3)_{12}Cl_{14}$), or 14 phosphines and 12 halogen ligands (*i.e.*, $Au_{18}Ag_{20}(PPh_3)_{14}Cl_{12}$). Fig. 9j exhibits the crystal structure of $Au_{18}Ag_{20}(PPh_3)_{12}Cl_{14}$.[392] The metal framework of $Au_{18}Ag_{20}(PPh_3)_{12}Cl_{14}$ contains a triangular tri-icosahedral core plus two capping Ag atoms on the pseudo-3-foId axis. Of note, the centers of three icosahedrons in M_{38} nanoclusters are 100% occupied by Au atoms.[391-394]

Taken together, under the concept of "cluster of clusters", the mono-icosahedral M_{13} unit has been alloyed, and larger nanoclusters were also obtained via fusion growth, with bi-, tri-, and multi-icosahedral structures. Three types of ligands are commonly used for stabilizing the nanocluster: halogens, phosphines, and thiols. Structurally, the rod-like $(AuAg)_{25}$ nanocluster shows that Au atoms preferentially occupy the top/bottom pentagonal sites that bind to the phosphine ligands, whereas the Ag atoms are generally arranged at the apex, the waist positions that link to the halogen or thiolate ligands, and the shared vertex. Such arrangements are proposed to be a result of the stronger bonding of Au-P than Ag-P, so is Ag-Cl (or Ag-Br) vs. Au-Cl (or Au-Br). The center of each icosahedral building block can be replaced by Pt/Pd. Of note, the central Pt/Pd doping is similar as alloy nanoclusters based on $Au_{25}(SR)_{18}$, $Ag_{25}(SR)_{18}$, and $Au_{38}(SR)_{24}$ templates that possess icosahedral M_{13} units. Assembling more icosahedral M_{13} building blocks would generate M_{36}, M_{37}, and M_{38} alloy nanocluster with different assembly patterns (linear or cyclic assembly), or vertex-sharing modes. However, alloying works based on larger-sized templates (e.g. cyclic Au_{60}) are still absent, which requires future efforts. The different size may induce different doping modes and alloy structures.

2.6 Alloying in $Au_{144}(SR)_{60}$ nanocluster template

$Au_{144}(SR)_{60}$ is one of the most important nanoclusters that have long been attractive to researchers. Although its molecular formula was determined by mass spectroscopy a decade ago, the crystal structure remained mysterious for another decade.[395-400] Determination of the precise structure of Au_{144} is of great significance to evaluate the alloying modes as well as the alloying effects. Several approaches including DFT calculations and TEM (transmission electron microscopy) were performed to predict the structure of the $Au_{144}(SR)_{60}$.[401-403] In 2018, Wu and co-workers unraveled the X-ray structure of this long-pursued nanocluster.[404] It was found to exhibit a tetra-stratified arrangement: Au_{12}(kernel, M-L1) @Au_{42}(1^{st}-shell, M-L2) @Au_{60}(2^{nd}-shell, M-L3) @$Au_{30}(SR)_{60}$(surface, M-L4). The average Au-Au bond length in M-L3 is about 2.884 Å, which is close to that of bulk Au, indicating that this nanocluster exhibits some metal character; however, other Au-Au bonds are much shorter, demonstrating the non-metal character of this nanocluster. In this context, the $Au_{144}(SR)_{60}$ nanocluster is in a transition state between nanoclusters and nanoparticles in view of chemical bonding.[404] Of note, at the same time, the Wang group reported the structure of Au_{144} stabilized by C≡C-PhF.[405] The two Au_{144} nanoclusters display a similar core structure but different arrangements of surface ligands.

Prior to the Au_{144} structure determination, three types of hetero-metals have been introduced into the $Au_{144}(SR)_{60}$ template, including Ag, Cu, and Pd. Kumara and Dass obtained a series of $Au_{144-x}Ag_x(SR)_{60}$ nanoclusters by reducing Au/Ag-SR precursors (SR = S-C_2H_4Ph, S-C_6H_{13}, S-$C_{12}H_{25}$).[406] The value of x in $Au_{144-x}Ag_x(SR)_{60}$ could be controlled by regulating the Ag/Au ratios. In general, the larger the Ag/Au ratio, the heavier the Ag doping in the $Au_{144-x}Ag_x$ template. ESI-MS and MALDI-MS results revealed that up to 60 Ag heteroatoms could be introduced to the template.[406] Considering that the maximum Ag-doping number was equal to the Au number in the 2^{nd}-shell (M-L3) of $Au_{144}(SR)_{60}$, it was proposed that doped Ag preferentially substituted the Au atoms in the 2^{nd}-shell.[406] Of note, such a kernel-surface alloying mode of Ag (i.e., Ag are doped to the outermost surface of the kernel) is the same as that in $Au_{25}(SR)_{18}$ (section 2.1). Based on the $Au_{144-x}Ag_x(SR)_{60}$ with different x values, the Ag-doping effects on optical absorption were experimentally and theoretically studied.[406-409] Collectively, although the crystal structure of $Au_{144-x}Ag_x(SR)_{60}$ is not accessible yet, all of the experimental and theoretical results suggest the kernel's surface doping mode.[406-410] The Ag-alloying has also been accomplished in $Au_{130}(SR)_{50}$ and $Au_{329}(SR)_{84}$ nanoclusters, but the structures of the alloying products remain un-determined.[411,412]

In addition to Ag-doping, Cu and Pd are incorporated into the $Au_{144}(SR)_{60}$ template as well.[413-415] ESI-MS results revealed that up to 23 Au atoms could be substituted by Cu. Considering that (i) the occupation of Cu in the inner kernel could avoid lattice mismatch due to the difference between Au and Cu in terms of atomic radii, and (ii) Cu has a higher

surface energy than Au, Dass and co-workers proposed that the Cu heteroatoms were preferentially dispersed into the M-L1 and M-L2 shells, which was also supported by the maximum doping number of ~23.[413] Molola *et al.* theoretically investigated the Cu doping positions in the $M_{144}(SR)_{60}$ template and reached the same conclusion.[414]

The Dass group also introduced Pd heteroatoms into $Au_{144}(SR)_{60}$,[415] in which up to seven Pd could be doped. Compared with the Ag- and Cu-alloying, the Pd-doping degree is much slighter. Of note, except the $Pd_2Au_{36}(SR)_{24}$ and $Pd_2Au_{23}(PPh_3)_{10}X_7$ nanoclusters (sections 2.2 and 2.5) that contain two icosahedral units, $Pd_xAu_{144-x}(SR)_{60}$ is the only nanocluster that can be doped with multiple Pd.[415]

In all, Ag, Cu, and Pd heteroatoms can be introduced into the $Au_{144}(SR)_{60}$ template with different alloying modes: (i) up to 60 Ag heteroatoms could be doped; (ii) 1-23 Cu can be detected in $Au_{144-x}Cu_x(SR)_{60}$; (iii) only slight-doping for Pd is achieved (up to 7). Of note, although some rational predictions have been made on the alloying modes of $Au_{144-x}M_x(SR)_{60}$ (M = Ag/Cu/Pd), their crystal structures are not available yet. Thus, many questions still remain. Besides, alloying $Au_{144}(SR)_{60}$ with Pt, Cd, Hg has not been reported. Finally, $Au_{144-x}Ag_x(SR)_{60}$ with narrow range *x* values might be achievable and would facilitate clear correlation between the Ag-doping extent and effects on the properties.

Studying the alloying phenomena in the nanoclusters is of great significance, which will provide important information for alloying in regular metal nanoparticles (e.g., 5-100 nm). The latter particles display metallic character, and galvanic reduction is widely used for alloying. For instance, Au ions are used to etch Ag nanoparticles (e.g., $Au^+ + Ag^0 \rightarrow Ag^+ + Au^0$), but the reversible process cannot be implemented because Ag is more active than Au.[196-198] However, when the size is reduced, ultrasmall nanoparticles (e.g., nanoclusters) will show non-metal character, thus anti-galvanic reaction seems to occur. For example, Ag^+ can replace some Au^0 atoms in Au nanoclusters (e.g., x Ag^+ + $Au_{25}(SR)_{18}$ → *x* Au^+ + $Ag_xAu_{25-x}(SR)_{18}$).[174] Such non-metal character is proposed to result from the ultra-small sizes of these nanoclusters.

Many cases of large-sized gold- and silver-thiolate nanoclusters with precise compositions, such as Au_{146}, Au_{246}, Au_{279}, Au_{333},[53,416-426] and Ag_{146}, Ag_{152}, Ag_{206}, Ag_{374},[54,427-431] have been reported. Higaki et al. discovered a sharp transition from nonmetallic Au_{246} to metallic Au_{279} with nascent plasmon.[53,417,419] But the case of Ag nanoclusters remains elusive. The multiple bands in the optical spectrum of the Ag_{146} nanocluster indicates a molecular state, while that of $Ag_{\sim 230}$ seems plasmonic,[427] i.e., the transition seems to move to smaller sizes than the gold system. Thus, one may expect that Ag alloying would alter the boundary between nonmetallic and metallic state, which is worth studying further.

3 Alloying in homo-silver nanocluster templates

This section summarizes the alloying based on homo-silver templates, including the icosahedral Ag_{25}, the icosaheral Ag_{29}, the hollow icosahedral Ag_{44}, and $Ag_{20}/_{21}$ stabilized by S/Se donor ligands.

3.1 Alloying in icosahedral $Ag_{25}(SR)_{18}$ template

The $[Ag_{25}(SR)_{18}]^-$ (SR = S-PhMe$_2$) was synthesized and structurally determined in 2015,[432] and this nanocluster could be prepared by either directly reducing Ag-SR complexes, or etching $Ag_{44}(SR)_{30}$ (section 3.4) or $Ag_{59}(SR)_{32}$ with HS-PhMe$_2$.[433,434] Importantly, $Ag_{25}(SR)_{18}$ is analogous to and corresponds well with the $Au_{25}(SR)_{18}$ in terms of formula and structure (Fig. 10). Accordingly, $Ag_{25}(SR)_{18}$, together with its gold analogue, offers the first model to investigate the fundamental differences between Au and Ag in chemical and physical properties, as well as alloying behavior.[432] The average M-M and M-S bond lengths in Ag_{25} are shorter than those in Au_{25}. Some silver atoms on staple motifs show a μ_3-Ag bonding mode, i.e., each Ag atom links three adjacent sulfur atoms on thiolate ligands. By comparison, each staple gold atom in $Au_{25}(SR)_{18}$ displays a μ_2-Au bonding mode (i.e., linking with two S atoms exclusively).

Alloying based on the $Ag_{25}(SR)_{18}$ template is summarized in Table 4. The Pt or Pd heteroatom can be doped into the $Ag_{25}(SR)_{18}$ nanocluster.[435] following the single- and central-doping mode (Fig. 10), similar to the case of Pd/Pt doping into the $Au_{25}(SR)_{18}$ template.[210,216] However, the $M_1Ag_{24}(SR)_{18}$ (M = Pt/Pd) displays a "-2" charge state, which is in contrast with the charge-neutral $M_1Au_{24}(SR)_{18}$.[63,64] Although $[Pt_2Ag_{23}(SR)_{18}]^{2-}$ was detected by ESI-MS spectrometry, the position of the second Pt heteroatom in the template is unclear yet, and $Pt_2Ag_{23}(SR)_{18}$ also exhibited a low stability and would decompose during the crystallization process.

Table 4 Alloy nanoclusters based on $Ag_{25}(SR)_{18}$.

Formula	Measurement(s)	Ref
$Ag_{25}(SR)_{18}$	SC-XRD, ESI-MS	432
$Pd_1Ag_{24}(SR)_{18}$	SC-XRD, ESI-MS	435
$Pt_1Ag_{24}(SR)_{18}$	SC-XRD, ESI-MS	435
$Au_1Ag_{24}(SR)_{18}$	SC-XRD, ESI-MS	69
$Au_xAg_{25-x}(SR)_{18}$	ESI-MS	69
$Pt_1Au_xAg_{24-x}(SR)_{18}$ (*x* = 1,2)	ESI-MS	442
$Pt_1Au_xAg_{24-x}(SR)_{18}$ (*x* = 6.4)	SC-XRD, ESI-MS	378
$Pt_2Au_{10}Ag_{13}(PPh_3)_{10}Br_7$	SC-XRD	378

Both Au_{25} and Ag_{25} fit the superatoms model. The $M@Au_{24}$ can have both "0" and "-2" charge states corresponding to 6e and 8e, respectively.[211,222] However, only "-2" charge state is observed in $M@Ag_{24}$, indicating that the closed electron shell must be fulfilled in the Ag_{25} system. The Jahn-Teller effect is used to explain the drastically changed HOMO-LUMO gaps observed in 6e $M@Au_{24}$, resulting in the splitting of the originally triply degenerated 1P orbitals.[211] We suppose that Pt/Pd doping into Ag_{25} would not interrupt the degeneration of its 1P orbitals, making it hard to remove electron(s) from the closed shell. The difference between

$Au_{25}(SR)_{18}^-$ and $Ag_{25}(SR)_{18}^-$ could be due to the much stronger spin-orbit coupling in gold.

A galvanic metal-exchange strategy has been devised to synthesize mono-Au doped $Au_1Ag_{24}(SR)_{18}$ nanocluster (Fig. 10).[69] Specifically, reacting $Ag_{25}(SR)_{18}$ with $Au(PPh_3)Cl$ leads to one Au in the center of the icosahedral kernel. By comparison, *in-situ* co-reducing the Ag/Au precursors produced a mixture of $Ag_{25-x}Au_x(SR)_{18}$, where x = 1-8.[69] The non-centered Au were proposed to be onto the icosahedral kernel shell, and these M_{25} with more than one Au atoms would decompose in re-crystallization processes, leaving mono-doped $Au_1Ag_{24}(SR)_{18}$. Bakr and co-workers proposed the single Au doping mechanism — the introduced Au^+ ion was first reduced to Au^0 by the Ag^0 (Ag^+ was formed at the same time) and then Au^0 substituted one of the M_{13} kernel-surface silver atoms. The Au heteroatom at the surface site might not be thermodynamically favorable, thus, it diffused into the center of M_{13}, and pushed the central Ag atom to the icosahedral surface concomitantly.[69]

Based on water-soluble $Ag_{25}(MHA)_{18}$ (MHA = 6-mercaptohexanoic acid), Zheng *et al*. reported the real-time monitoring of the dynamic Au-heteroatom diffusion into the $Ag_{25}(MHA)_{18}$ by *in situ* UV-vis absorption spectroscopy, ESI-MS, and MS/MS techniques.[436] Specifically, to the aqueous phase of Ag_{25}, an equimolar of Au-MHA complex was added, producing the mono-Au doped nanocluster; that is, this alloying process is a stoichiometric reaction. Because the hydrophilic $Ag_{25}(MHA)_{18}$ could be directly ionized, it is possible to do real-time monitoring of the alloying process.[436] Besides, real-time MS/MS was performed to monitor the fragmentation patterns of $Au_1Ag_{24}(MHA)_{18}$ during the alloying process. The combination of real-time experiments and DFT calculations demonstrated that the mono Au-alloying process underwent three steps: (i) substituting one Ag atom in the $Ag_2(MHA)_3$ motif by an Au heteroatom; (ii) diffusion of the Au heteroatom into the Ag_{12} kernel shell; (iii) diffusion of the Au heteroatom to the center of the icosahedral kernel.[436]

The combination of $Ag_{25}(SR)_{18}$, $Pt_1Ag_{24}(SR)_{18}$, $Pd_1Ag_{24}(SR)_{18}$, and $Au_1Ag_{24}(SR)_{18}$ nanoclusters (with the same structure but different central atom) is consistent with the common behavior that atoms with higher electronegativity (Au = 2.54, Pt = 2.28, Pd = 2.20 vs. Ag = 1.93) tend to take the inner position(s), which concentrates the electron density in the center and stabilize the structure. Besides, based on the $M_1Ag_{24}(SR)_{18}$, chemical/physical properties have been thoroughly investigated, including thermal-stability,[69] optical absorption and emission,[69,437-439] catalysis,[440] and electrochemical properties,[441] which will be discussed in Section 7.

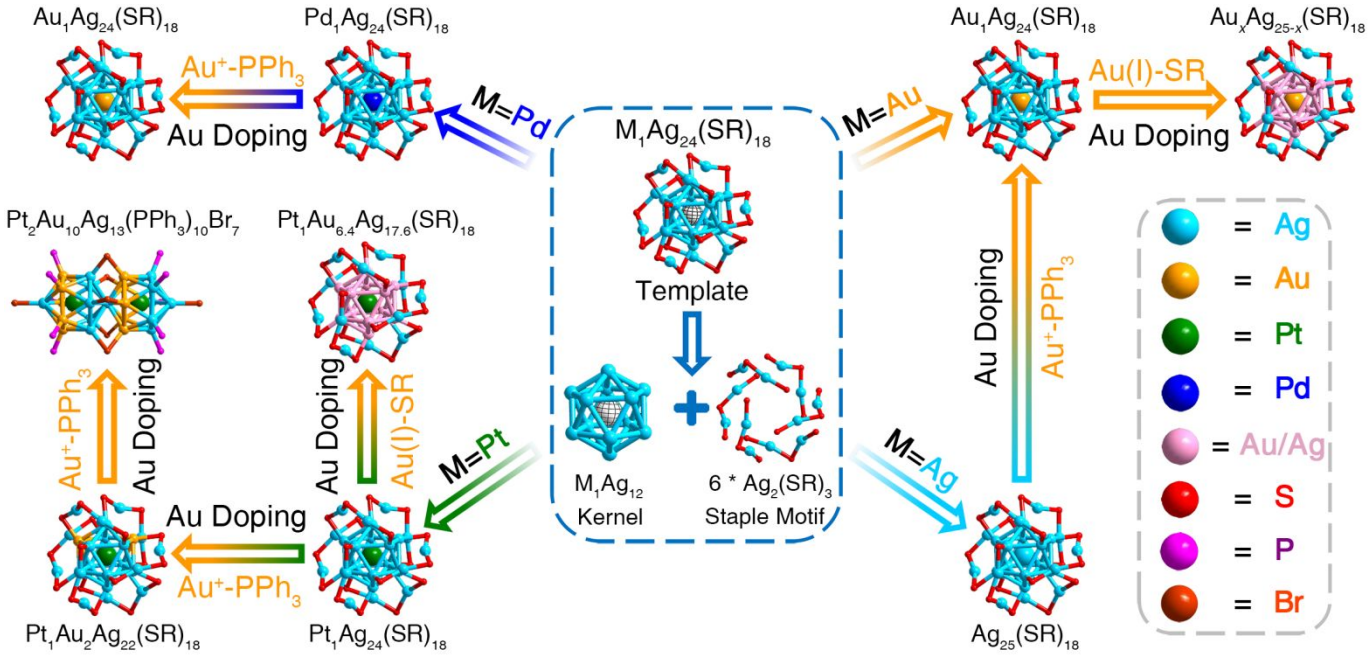

Fig. 10 Alloying based on the $Ag_{25}(SR)_{18}$ template. Nanoclusters obtained based on alloying Ag_{25} include the central-doped $Au_1Ag_{24}(SR)_{18}$, $Pt_1Ag_{24}(SR)_{18}$, and $Pd_1Ag_{24}(SR)_{18}$, the icosahedral kernel shell-doped $Ag_{25-x}Au_x(SR)_{18}$, $Pt_1Au_2Ag_{22}(SR)_{18}$, and $Pt_1Au_{6.4}Ag_{17.6}(SR)_{18}$ nanoclusters, and the shape-altered $Pt_2Au_{10}Ag_{13}(PPh_3)_{10}Br_7$ nanocluster.

Considering that the central Pd/Pt heteroatom in $M_{25}(SR)_{18}$ (or Ag-Pd/Pt inter-metallic synergetism) would remarkably affect chemical/physical reactity in chemical reactions compared to the parent $Ag_{25}(SR)_{18}$ nanocluster, Zhu and Bakr groups have investigated the Au doping process based on $Pt_1Ag_{24}(SR)_{18}$ and $Pd_1Ag_{24}(SR)_{18}$ nanoclusters,[378,442] resulting in tri-metallic nanoclusters, including $Pt_1Au_2Ag_{22}(SR)_{18}$, $Pt_1Au_{6.4}Ag_{17.6}(SR)_{18}$, and $Pt_2Au_{10}Ag_{13}(PPh_3)_{10}Br_7$ (Section 5). When reacting with Au(I)-PPh_3, the central Pd atom in $Pd_1Ag_{24}(SR)_{18}$ will be substituted by Au, and bi-metallic $Au_1Ag_{24}(SR)_{18}$ nanocluster is obtained (Fig. 10, top-left).[442]

In summary, Au, Pt, and Pd heteroatoms have been doped into the $Ag_{25}(SR)_{18}$ template with different modes: (i) Pd and Pt heteroatoms are doped at the center, which is the same as in the $Au_{25}(SR)_{18}$ template; (ii) Au heteroatoms can occupy the central position as well as the sites on the icosahedral kernel shell in the trimetallic system. Of note, the $M_1Ag_{24}(SR)_{18}$ (M = Ag/Au/Pd/Pt) nanoclusters are of great significance in terms of structure-property correlations at the atomic level. Potential future work on alloying based on $Ag_{25}(SR)_{18}$ may include: (i) exploiting other types of heteroatoms, such as Cu, Hg, Cd, Ir, which have been accomplished in $Au_{25}(SR)_{18}$, but not in $Ag_{25}(SR)_{18}$ yet; (ii) the ligand effect requires further understanding as the ligands (e.g., HS-C_2H_4Ph) used to prepare $Au_{25-x}M_x(SR)_{18}$ cannot be used to obtain $Ag_{25-x}M_x(SR)_{18}$, and *vice versa*. The specific "ligand-cluster matching" is quite intriguing and there is much room for future work.

3.2 Alloying in Ag-based cluster of clusters

Rod-like Ag_{25} nanocluster is hard to be prepared due to the relatively low stability. By contrary, a class of Ag nanoclusters co-protected by hydrides and phosphines ligands emerge, such as $Ag_{18}H_{16}(PPh_3)_{10}$, $Ag_{25}H_{22}(DPPE)_8$, and $Ag_{26}H_{22}(TFPP)_{13}$ (DPPE = 1,2-bis(diphenylphosphino)-ethane, TFPP = tris(4-fluorophenyl)phosphine).[443] Bootharaju *et al.* introduced Pt-source to the synthesis of $Ag_{18}H_{16}(PPh_3)_{10}$ nanocluster, and an assembled bi-icosahedral $Pt_2Ag_{23}(PPh_3)_{10}Cl_7$ nanocluster was generated.[383] Structurally, two Pt_1Ag_{12} icosahedrons are connected *via* sharing a vertex Ag atom, and the Pt_2Ag_{23} is capped by five bridging and two terminal Cl and ten PPh_3 ligands. Electronic structure simulations further demonstrated the enhanced stability of center-doped Pt_2Ag_{23} nanoclusters over parent Ag_{25}.[383] Kang *et al.* extracted the single icosahedral Pt_1Ag_{12} structure from the bi-icosahedral Pt_2Ag_{23} nanocluster.[444] Considering the remarkable influence of the size on optical properties (mainly on optical energy gaps), they exploited the concept of de-assembly on Pt_2Ag_{23} nanocluster to render a blue-shift of the PL emission as well as an enhancement in PL QY. The bi-icosahedral Pt_2Ag_{23} was split by a two-step ligand-exchange procedure. Firstly, ligand exchanging Pt_2Ag_{23} with HS-$PhMe_2$ ligands transformed the rod-like nanocluster into spherical $Pt_1Ag_{24}(SR)_{18}$. In this step, the Pt_1Ag_{12} monomer was further capped by six $Ag_2(SR)_3$ staple motifs, resembling Ag_{25}. Then, bis-(diphenylphosphino)-methane (DPPM) was used to etch the Pt_1Ag_{24} and the icosahedral Pt_1Ag_{12} kernel was extracted out, which was finally protected by five DPPM and two thiolate ligands.[444]

Other alloy nanoclusters based on the assembly of icosahedral M_{13} unites (linear/cyclic) are generalized here as well. Yang *et al.* reported the structure of tri-icosahedral Pt_3Ag_{33} nanocluster.[445] The combination of Pt_1Ag_{12}, Pt_2Ag_{25}, and Pt_3Ag_{33} nanoclusters creates an intriguing nanosystem that implying the size-property correlations at the atomic level.[383,444,445] Assembly of two M_{13} icosahedrons generates M_{25} bi-icosahedral nanocluster *via* single vertex sharing. The assembly between three of more icosahedrons rationally gives the corresponding tri-, tetra-, and multi-icosahedral nanoclusters. Of note, two assembled architectures are proposed: linear assembly and cyclic assembly. For instance, self-assembly of three Pt_1Au_{12} (M_{13}) icosahedral building blocks generates cyclic Pt_3Ag_{33}, and the central Pt atom in each icosahedral kernel maintains. With the incorporation of the gold heteroatoms, a tri-metallic $Pt_3Au_{12}Ag_{21}(PPh_3)_{12}Cl_8$ nanocluster maintaining the cyclic M_{36} framework was obtained. Of note, the number of introduced gold atoms was the same as that of the PPh_3 ligands, and SC-XRD demonstrated that Au atoms were at the peripheral sites (linking the PPh_3 ligands) of the cyclic nanocluster.[445]

3.3 Alloying in $Ag_{29}(S_2R)_{12}(PPh_3)_4$ templates

There are two types of Ag-based M_{29} templates—$Ag_{29}(S_2R)_{12}(PPh_3)_4$ and $Ag_{29}(SR)_{18}(PPh_3)_4$ (S_2R = 1,3-benzene dithiol; SR = S-Adm).[446-449] Doping based on the $Ag_{29}(S_2R)_{12}(PPh_3)_4$ template (Fig. 11a) is reviewed in this section; while that on $Ag_{29}(SR)_{18}(PPh_3)_4$ will be discussed in section 4.4.

$Ag_{29}(S_2R)_{12}(PPh_3)_4$ has an icosahedral Ag_{13} kernel, which is protected by an $Ag_{16}(S_2R)_{12}(PPh_3)_4$ cage (Fig. 11a). This $Ag_{16}(S_2R)_{12}(PPh_3)_4$ cage is composed of four $Ag_3(S_2R)_6$ motifs and four Ag-PPh_3 units. Each pair of $Ag_3(S_2R)_6$ motifs shares a S_2R ligand, and thus, the total number of dithiolates is 12. Alloying nanoclusters based on the $Ag_{29}(S_2R)_{12}(PPh_3)_4$ nanocluster template are reviewed in Table 5. Besids, several works have been reported on the geometric/electronic structures and optical properties of $Ag_{29}(S_2R)_{12}(PPh_3)_4$.[450-463]

Table 5 Alloy nanoclusters based on $Ag_{29}(S_2R)_{12}(PPh_3)_4$.

Formula	Measurement(s)	Ref(s)
$Ag_{29}(S_2R)_{12}(PPh_3)_4$	SC-XRD, ESI-MS	446
$Au_1Ag_{28}(S_2R)_{12}(PPh_3)_4$	SC-XRD, ESI-MS	70
$Ag_{29-x}Au_x(S_2R)_{12}(PPh_3)_4$	ESI-MS	70
$Ag_{17}Cu_{12}(S_2R)_{12}(PPh_3)_4$	SC-XRD, ESI-MS	468
$Au_1Ag_{12}Cu_{12}(S_2R)_{12}(PPh_3)_4$	SC-XRD, ESI-MS	468
$Pt_1Ag_{28}(S_2R)_{12}(PPh_3)_4$	SC-XRD, ESI-MS	464,465
$Pd_1Ag_{28}(S_2R)_{12}(PPh_3)_4$	ESI-MS	461
$Ni_1Ag_{28}(S_2R)_{12}(PPh_3)_4$	ESI-MS	461

Mono-Pt-doped $Pt_1Ag_{28}(S_2R)_{12}(PPh_3)_4$ was prepared *via* an *in-situ* or a ligand-exchange approach.[464,465] However, the *in-situ* synthesis produced a mixture of Ag_{29} and Pt_1Ag_{28}, whereas ligand-exchange by etching $Pt_2Ag_{23}(PPh_3)_{10}Cl_2$ with H_2S_2R generates the highly pure $Pt_1Ag_{28}(S_2R)_{12}(PPh_3)_4$ (Fig. 11b).[464] $Pt_1Ag_{28}(S_2R)_{12}(PPh_3)_4$ can be prepared by ligand-exchanging $Pt_1Ag_{28}(SR)_{18}(PPh_3)_4$ with H_2S_2R as well.[465] DFT calculations demonstrated that the central Pt remained in the transformation process, and the corresponding ligand-exchange process just extracted an icosahedral Pt_1Ag_{12} from the bi-icosahedral Pt_2Ag_{23} nanocluster and capped this kernel with new Ag-S_2R-PPh_3 staple motifs.[464] Besides, the crystal structure of $Pt_1Ag_{28}(S_2R)_{12}(PPh_3)_4$ also identified the center-doped Pt heteroatom.[465] The PL intensity of $Pt_1Ag_{28}(S_2R)_{12}(PPh_3)_4$ exhibited a ~2.3-fold enhancement

relative to the parent nanocluster.[464] Besides, the PL QY of $Pt_1Ag_{28}(S_2R)_{12}(PPh_3)_4$ (1.5%) could be further boosted to 17.6% (~11-fold enhancement) when the nanoclusters are wrapped by tetraoctylammonium (TOA) counter-ions.[465] TOA counter-ions are proposed to occupy a large surface volume on the nanocluster and make the ligand shell more rigid, resulting in much higher PL in the $Pt_1Ag_{28}(S_2R)_{12}(PPh_3)_4$@TOA composite material.[465]

Bakr and co-workers changed the mono-metallic Ag-S_2R-PPh_3 precursor to bi-metallic Ag/Au-S_2R-PPh_3 precursor, and obtained the gold-doped $Ag_{29-x}Au_x(S_2R)_{12}(PPh_3)_4$ (x = 1-5) nanoclusters.[70] Of note, accompanied by Au-doping, the PL intensity of $Ag_{29-x}Au_x$ displayed a maximum of 26-fold enhancement (see details in Section 7).[70] Determining the precise positions of the introduced gold heteroatoms within $Ag_{29-x}Au_x(S_2R)_{12}(PPh_3)_4$ is vital to correlate the structure with the changes to the optical properties. MS results demonstrated that the maximum Au-doping number was five; however, only the crystal structure of mono-Au-doped Au_1Ag_{28} was determined, indicating that the Au was at the center of the icosahedral kernel (Fig. 11c). Several means were performed to determine the precise doping positions of the rest Au heteroatoms.[70,466,467] It was found that the ^{31}P NMR (nuclear magnetic resonance) results of $Ag_{29-x}Au_x$ displayed a systematic shift in P signals with an increasing amount of Au-doping.[70]

Theoretical predictions of Au-doping mode based on the $Ag_{29}(S_2R)_{12}(PPh_3)_4$ template were performed to understand the molecular and physical origins of the doping-induced PL enhancement.[466,467] The Häkkinen group theoretically predicted the most favorable doping sites of Au heteroatoms by exploiting DFT and linear-response time-dependent DFT (LR-TDDFT) methods.[466] An enhancement in the electronic transitions at ~450 nm indicated the formation of Au-PPh_3 bond in $Au_xAg_{29-x}(S_2R)_{12}(PPh_3)_4$, which agreed with experiment.[70,466] In addition, the formation of Au-P bonds prevented the nanocluster from degradation, since the Au-PPh_3 bond was stronger by 0.4 eV than Ag-PPh_3 bond.[466] By comparison, Xie et al. computationally explored the electronic and geometric structures of Ag_{29} and $Ag_{29-x}Au_x$ (x = 1-5) nanoclusters in the S_0 and S_1 states.[467] DFT calculations also proved that the enhanced PL intensity and thermal-stability resulted from Au substitution. Specifically, (i) the relativistic effects of the introduced Au played a significant role in enhancing the PL intensity, which was more obvious when increasing the Au number to 3-5; (ii) the newly formed Au-Au bonds resulted in the enhanced thermal-stability of $Ag_{29-x}Au_x$ relative to Ag_{29}.[467]

The Cu-doped $M_{29}(S_2R)_{12}(PPh_3)_4$ nanoclusters were also controllably synthesized and structurally determined.[468] Involving Cu in the precursor during the preparation of $Ag_{29}(S_2R)_{12}(PPh_3)_4$ resulted in the $Ag_{17}Cu_{12}(S_2R)_{12}(PPh_3)_4$ nanocluster, while reducing the Au/Ag/Cu-based precursor gave rise to $Au_1Ag_{16}Cu_{12}(S_2R)_{12}(PPh_3)_4$ (Fig. 11d). Besides, metal-exchanging $Ag_{17}Cu_{12}(S_2R)_{12}(PPh_3)_4$ with $Au^I(PPh_3)Cl$ also produced the same $Au_1Ag_{16}Cu_{12}(S_2R)_{12}(PPh_3)_4$.[468] Structurally, the introduced Au is preferentially incorporated at the center of the icosahedral M_{13} kernel, whereas Cu heteroatoms are arranged in the metal-S_2R motifs, converting the previous $Ag_{12}(S_2R)_{12}(PPh_3)_4$ cage into a novel $Cu_{12}(S_2R)_{12}(PPh_3)_4$ cage (Fig. 11d).[468] All the nanoclusters in the $M_{29}(S_2R)_{12}(PPh_3)_4$ family contain four C_3 axes that all pass through the M-PPh_3 units (Fig. 11d).[468]

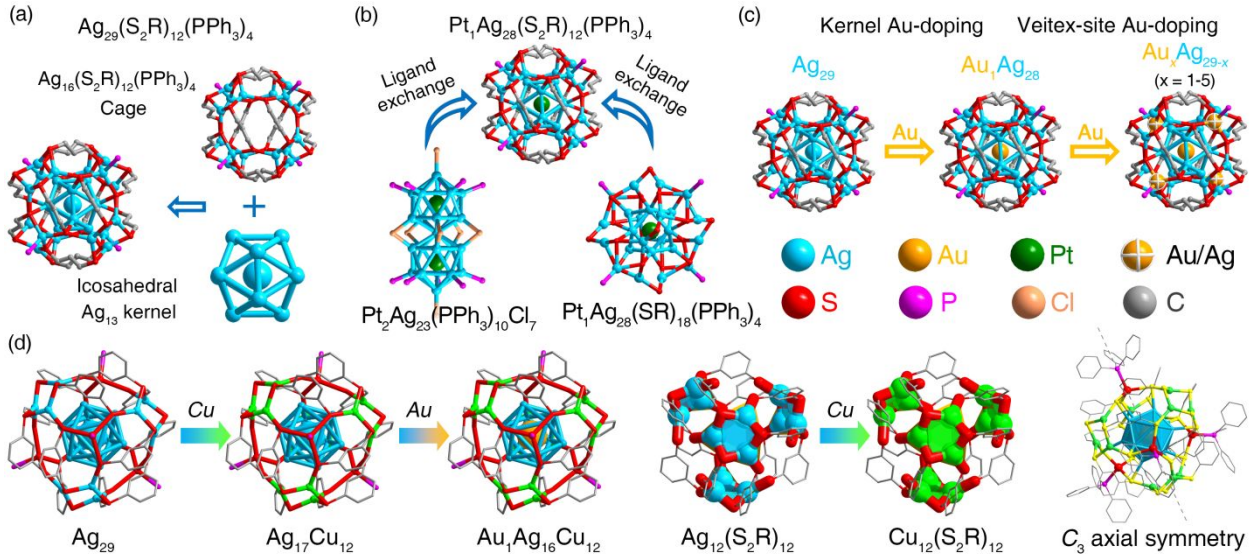

Fig. 11 Alloying based on the $Ag_{29}(S_2R)_{12}(PPh_3)_4$ template. (a) Structural anatomy of $Ag_{29}(S_2R)_{12}(PPh_3)_4$. (b) Nanocluster transformation from $Pt_1Ag_{28}(SR)_{18}(PPh_3)_4$ to $Pt_1Ag_{28}(S_2R)_{12}(PPh_3)_4$, or from $Pt_2Ag_{23}(PPh_3)_{10}Cl_7$ to $Pt_1Ag_{28}(S_2R)_{12}(PPh_3)_4$. (c) Doping 1-5 Au heteroatoms into the $Ag_{29}(S_2R)_{12}(PPh_3)_4$ template. (d) Doping process from $Ag_{29}(S_2R)_{12}(PPh_3)_4$ to $Ag_{17}Cu_{12}(S_2R)_{12}(PPh_3)_4$, then to $Au_1Ag_{16}Cu_{12}(S_2R)_{12}(PPh_3)_4$, corresponding $Ag_{12}(S_2R)_{12}$ and $Cu_{12}(S_2R)_{12}$ cage structures, and the C_3 symmetry of the M_{29} template.

Hydrophilic Ag_{29} nanoclusters are prepared by hydrophilic dithiols. Several works have been reported in terms of preparations (syntheses and purification), properties (isomerism, stability, and luminescence), and applications (antibacterial and antifungal) so far.[469-473] DFT calculations demonstrated that hydrophilic Ag_{29} possessed similar structures as $Ag_{29}(S_2R)_{12}(PPh_3)_4$.[473] In 2018, the Mattoussi group reported $Ag_{29-x}Au_x(DHLA)_{12}$ nanocluster (DHLA = dihydrolipoic acid) with a 6-fold enhancement in PL compared with its Ag_{29} counterpart.[474] Such an Au-doping induced PL enhancement agreed with the phenomena in hydrophobic $Ag_{29-x}Au_x$ nanoclusters.[70] Besides, the hydrophilic $M_{29}(DHLA)_{12}$ is only capped by the dithiolate ligands, which is consistent with $M_{29}(S_2R)_{12}$ obtained by an *in-situ* synthesis in the absence of phosphine source.[70,446] Furthermore, owing to the terminal acid group of the DHLA ligand, further functionalization has been performed on these hydrophilic nanoclusters.[474]

Collectively, Au and Pt has been successfully doped into the icosahedral M_{13} kernel of $Ag_{29}(S_2R)_{12}(PPh_3)_4$, but crystal structures of $Ag_{29-x}Au_x(S_2R)_{12}(PPh_3)_4$ ($x > 1$) are still needed as there is inconsistency in theoretical predictions. The boost in PL based on doping is intriguing and worth further studies, and understanding the significant role of the central heteroatom in the frontier orbitals requires more experimental and theoretical work.

3.4 Alloying based on icosahedral $Ag_{44}(SR)_{30}$ nanocluster

The $Ag_{44}(SR)_{30}$ was first synthesized in 2009,[475] and is one of the most studied silver nanoclusters protected by all thiolates. In the following years, several works were reported focusing on the large-scale synthesis,[476-481] ligand engineering,[476-478,481-485] self-assembly,[483,486-488] and alloying. The structure of $Ag_{44}(SR)_{30}$ was determined in 2013,[476,477] revealing an icosahedral Ag_{12} kernel (hollow, c.f. the centered icosahedral M_{13} kernel discussed before) capped by an $Ag_{32}(SR)_{30}$ cage (composed of a decahedral Ag_{20} and six $Ag_2(SR)_5$ motifs) (Fig. 12a). The Zheng group reported several structures of Ag_{44} and $Au_{12}Ag_{32}$ protected by different thiolate ligands, including S-PhF, S-PhF_2, and S-$PhCF_3$.[477,489] SC-XRD results of $Au_{12}Ag_{32}$ demonstrated that Au heteroatoms formed an Au_{12} kernel shell (Fig. 12a, bottom).[477] Theoretical calculations also demonstrated the preferred kernel occupation by the introduced Au heteroatoms.[477,490,491] Specifically, the relative energy was the lowest when 12 kernel sites were completely occupied by Au.[490] Based on the $Ag_{44}(SR)_{30}$ template (SR = *p*-MBA, *p*-mercaptobenzoic acid ligand), Bigioni and co-workers investigated the full range alloying of $Au_xAg_{44-x}(SR)_{30}$ nanoclusters ($0 \le x \le 12$).[492] DFT calculations also provided insights into the Au/Ag composition-dependent electronic structures and chemical properties (especially reactivity).[492]

Besides doping into the M_{12} icosahedral kernel, Au heteroatoms are also found to substitute the Ag atoms in the six $Ag_2(SR)_5$ motifs.[493] Based on the $[Ag_{44}(SR)_{30-x}Cl_x]^{4-}$ (SR = *p*-MBA) template, Xie and co-workers presented a delicate and well-controlled surface metal-exchange reaction, which used the Au(I)-SR complexes to precisely substitute the initial Ag(I)-SR surface motifs to obtain $Ag_{32}Au_{12}(SR)_{30}$. Different from $[Au_{12}Ag_{32}(SR)_{30}]^{4-}$ with a kernel-doping mode, the configuration of $[Ag_{32}Au_{12}(SR)_{30}]^{4-}$ could be viewed as Ag_{12}(kernel)@Ag_{20}(middle shell)@6×$Au_2(SR)_5$(surface motif) (Fig. 12a, bottom-right).[493] Theoretical calculations suggested that the thermodynamically less favorable Ag@Au core-shell configuration was kinetically stabilized by the decahedral Ag_{20} shell, which further prevented inward diffusion of the surface Au heteroatoms. Owing to the synergism between Au and Ag, $[Ag_{32}Au_{12}(SR)_{30}]^{4-}$ displayed an enhanced thermal-stability relative to $[Ag_{44}(SR)_{30}]^{4-}$, and did not decompose for more than 30 days at room temperature or more than 2 hours at 150°C.[493]

The Xie group reported another inward diffusion process in which a single Au atom goes from the staple motif to the kernel's shell, and finally to the center of Ag_{25}.[436] We also note that both $[Au_{12}@Ag_{32}(SR)_{30}]^{4-}$ and $[Ag_{12}@Ag_{20}Au_{12}(SR)_{30}]^{4-}$ have the same formula but with different configurations as reported,[477,493] and their absorption spectra are very similar to each other. Thus, it is still an open question why the Au atoms would stop moving inside in the case of Ag_{44}.[82]

In summary, based on the $Ag_{44}(SR)_{30}$ nanocluster, several alloying achievements have been reported: (i) $Au_{12}Ag_{32}(SR)_{30}$ nanoclusters (stabilized by different thiolate ligands) are obtained; (ii) the syntheses of full range doped Au_xAg_{44-x}(*p*-MBA)$_{30}$ nanoclusters (x = 1-12) are developed; (iii) two different Au-doping modes are observed: kernel doping mode and motif doping mode; (iv) size-growth from $Ag_{44}(SR)_{30}$ to $Ag_{50}(SR)_{30}(DPPM)_6$ and then metal-exchange led to $Au_xAg_{50-x}(SR)_{30}(DPPM)_6$. The $[Ag_{44}(SR)_{30}]^{4-}$ (18 e) and $[Ag_{25}(SR)_{18}]^-$ (8 e) nanoclusters are both considered to be superatoms.[435,477] The $[Ag_{25}(SR)_{18}]^-$ has a center that can be replaced by group-10 elements when one more electron is trapped on the cluster to maintain the 8 e electron configuration. But $[Ag_{44}(SR)_{30}]^{4-}$ does not have a center and already has a charge state of -4. The 18 e superatom configuration of this template might restrict heteroatoms from doping, especially as they might break the 18e electronic structure. As $[Au_{25}(SR)_{18}]^-$ (8 e) can be altered to 7 e and 6 e with partially occupied superatom orbital by oxidation or Pt/Pd doping,[211,222,494,495] it would be interesting to use alloying to reveal more cases with different superatomic HOMO and LUMO.

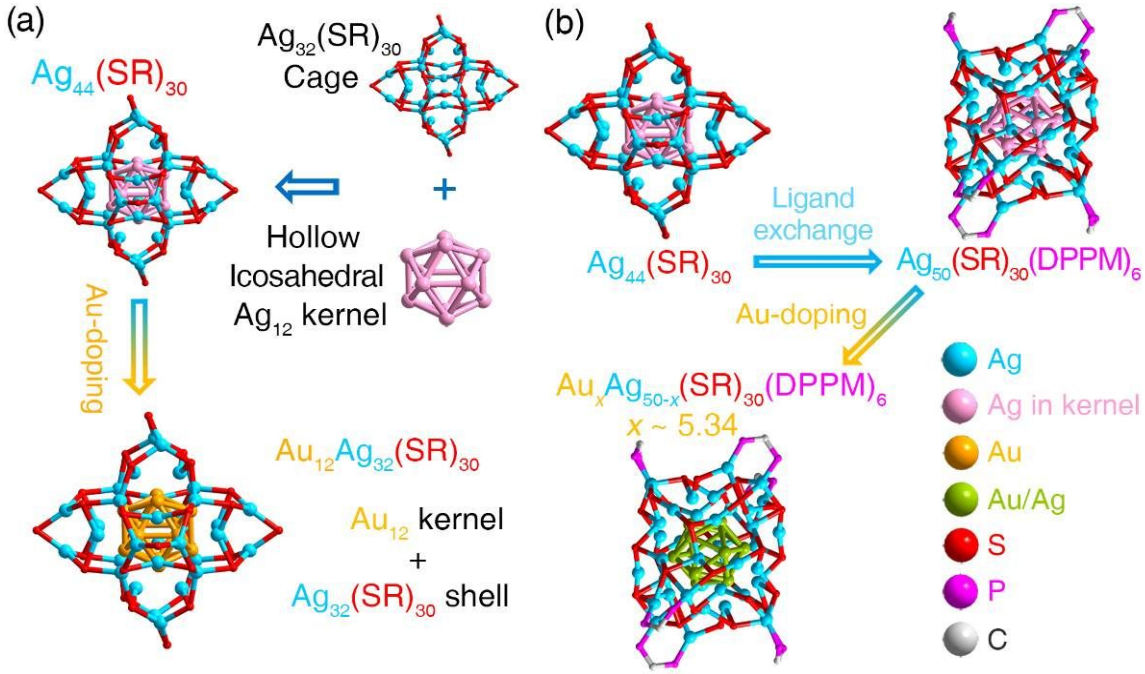

Fig. 12 Alloying based on the $Ag_{44}(SR)_{30}$ template. (a) Structural anatomy of $Ag_{44}(SR)_{30}$, and its Au-doped $Au_{12}Ag_{32}(SR)_{30}$ alloy nanoclusters. (b) Size-growth from $Ag_{44}(SR)_{30}$ to $Ag_{50}(SR)_{30}(DPPM)_6$, and further metal-exchanging to $Au_xAg_{50-x}(SR)_{30}(DPPM)_6$ (x ~5.34).

3.5 Alloying based on icosahedral $Ag_{50}(SR)_{30}(DPPM)_6$ nanocluster

Zhu and co-workers reported the syntheses and crystal structures of $Ag_{50}(SR)_{30}(DPPM)_6$ and its $Au_xAg_{50-x}(SR)_{30}(DPPM)_6$ alloy counterpart.[496] The Ag_{50} was obtained by a seeded growth method based on $Ag_{44}(SR)_{30}$. Structurally, the icosahedral Ag_{12} kernel was retained in the transformation process, and the new Ag_{50} nanocluster shows a structure of an Ag_{12}(kernel)@Ag_{20}(middle shell)@Ag_6(shell linker)@Ag_{12}(surface) configuration (Fig. 12b).[496] Furthermore, the Ag_{50} nanocluster could be alloyed by templated/galvanic metal-exchange to a $Au_xAg_{50-x}(SR)_{30}(DPPM)_6$ homologue. SC-XRD demonstrated that the introduced Au heteroatoms could substitute Ag atoms in the kernel. This kernel-alloying mode is the same as in $Au_{12}Ag_{32}(SR)_{30}$, albeit only partial kernel sites can be replaced.[477,496] The crystal structure and ESI-MS determined the average value of x as 5.34. Owing to Au-doping and Au-Ag intermetallic synergism, the $Au_xAg_{50-x}(SR)_{30}(DPPM)_6$ nanoclusters exhibited enhanced thermal stability and PL intensity compared with that of the parent Ag_{50}.[496]

3.6 Alloying in Ag_{20}/$_{21}$ nanoclusters stabilized by S/Se donor ligands

Liu and co-workers reported Ag_{20} and Ag_{21} nanoclusters and their alloys, all being stabilized by S/Se donor ligands (Fig. 13).[497-502] The $Ag_{21}\{S_2P(O_iPr)_2\}_{12}$ (S-Ag_{21} for short) comprises an icosahedral Ag_{13} kernel capped by eight additional Ag atoms. This Ag_{21} framework is further capped by twelve dithiophosphate ligands.[497] By reducing the S-Ag_{21} with $NaBH_4$, one silver atom could be eliminated, generating $\{Ag_{20}\{S_2P(O_iPr)_2\}_{12}$ (S-Ag_{20} for short) containing an intrinsically chiral kernel.[498] In follow-up works, the initial S donor ligands on S-Ag_{20} and S-Ag_{21} could be replaced by Se donor ligands, and $Ag_{20}\{Se_2P(O_iPr)_2\}_{12}$ (Se-Ag_{20} for short) and $Ag_{21}\{Se_2P(OEt)_2\}_{12}$ (Se-Ag_{21} for short) were prepared and structurally determined.[499] Of note, the structures of Se-Ag_{20} and Se-Ag_{21} display large differences when compared to S-Ag_{20} and S-Ag_{21} (Fig. 13). Thus, these four nanoclusters are closely related: S-Ag_{20}, S-Ag_{21}, Se-Ag_{20}, and Se-Ag_{21}.

Alloying was performed based on these four homo-silver nanoclusters.[499-502] The Au-doping on S-Ag_{21}, Se-Ag_{21}, and S-Ag_{20} produces S-Au_1Ag_{20}, Se-Au_1Ag_{20}, and S-Au_1Ag_{19}, respectively.[499,500] In the alloying process from Se-Ag_{21} to Se-Au_1Ag_{20}, the configuration was maintained with the central Ag substituted by Au. As for the S-Au_1Ag_{20} and S-Au_1Ag_{19} nanoclusters, in addition to the center replacement by Au, slight structural distortions were observed in the motif structures. Such a center-Au doping phenomenon is reminiscent of the Au-doping in other Ag nanoclusters, *e.g.* $Ag_{25}(SR)_{18}$ and $Ag_{29}(S_2R)_{12}(PPh_3)_4$ with icosahedral Ag_{13} kernels.

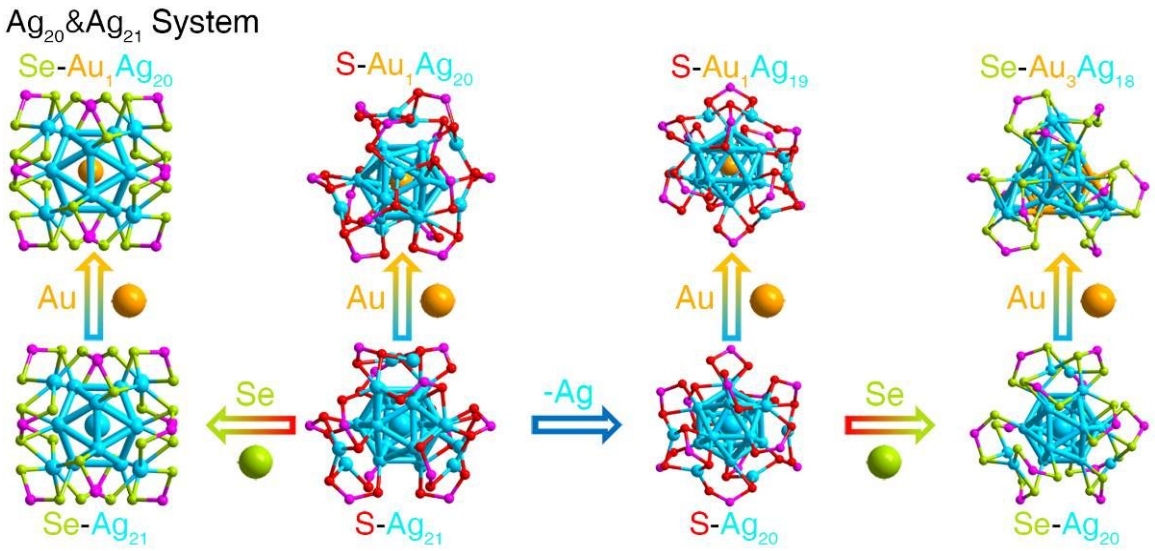

Fig. 13 Au-alloying based on the Ag_{20}/Ag_{21} templates. Structures of Se-Ag_{21}, S-Ag_{21}, S-Ag_{20}, and Se-Ag_{20} nanoclusters, and their corresponding doped Se-Au_1Ag_{20}, S-Au_1Ag_{20}, S-Au_1Ag_{19}, and Se-Au_3Ag_{18} nanoclusters.

By comparison, the Au-alloying mode based on Se-Ag_{20} was different — the result was a multi-Au-doped Se-Au_3Ag_{18} nanocluster.[501] The cluster size increased from M_{20} to M_{21} in this alloying process, and a large structural transformation was found. Specifically, the "spherical" Se-Ag_{20} is altered into a "tetrahedral" shape. The Au atoms were arranged into different sites in the icosahedral M_{13} kernel: one Au occupied the center, and the other two were on the kernel shell.[501] Collectively, the mono-Au-doped counterparts of S-Ag_{20}, S-Ag_{21}, and Se-Au_{21} were successfully prepared without structural transformation, while Au-alloying on Se-Ag_{20} output Se-Au_3Ag_{18} nanocluster. Thus, the mono-doped Se-Au_1Ag_{19} and its structure could be the next synthetic target.

In 2019, the Liu group reported the direct syntheses and structural determinations of two dithiolate-protected Pd/Ag nanoclusters — $Pd_1Ag_{20}\{S_2P(O^nPr)_2\}_{12}$ and $Pd_6Ag_{14}(S)\{S_2P(O^nPr)_2\}_{12}$.[503] The preparations could be controlled by altering the Pd/Ag ratio and reaction times. Structurally, $Pd_1Ag_{20}\{S_2P(O^nPr)_2\}_{12}$ is an 8e superatom isoelectronic to $[Ag_{21}\{S_2P(O^iPr)_2\}_{12}]^+$, and comprises a Pd_1Ag_{12} icosahedral kernel capped by an $Ag_8\{S_2P(O^nPr)_2\}_{12}$ shell. The twelve $S_2P(O^nPr)_2$ ligands are equally distributed in three layers (top, middle and bottom) along a pseudo-C_2 axis.[503] The structure of $Pd_6Ag_{14}(S)\{S_2P(O^nPr)_2\}_{12}$ exhibits a sulfide-centered S-Pd_6Ag_2 rhombohedron surrounded by 12 additional Ag atoms with S_6 symmetry. Of note, $Pd_6Ag_{14}(S)\{S_2P(O^nPr)_2\}_{12}$ is the first reported alloy nanocluster with an octahedral hexa-palladium(0) kernel embodied within a silver(I) cluster.[503]

$Pt_1Ag_{20}\{S_2P(OPr)_2\}_{12}$ has also been reported.[504] The metal framework contains an icosahedral Pt_1Ag_{12} kernel, which is capped by eight Ag atoms, giving rise to a Pt_1Ag_{20} of idealized C_2 symmetry. The Pt_1Ag_{20} is further stabilized by 12 $S_2P(OPr)_2$ ligands.[504] Furthermore, by slightly altering the synthetic route, two "cluster-of-clusters" type Pt/Ag alloys were obtained, namely, $[Pt_2Ag_{33}\{S_2P(OPr)_2\}_{17}]$ and $[Pt_3Ag_{44}\{S_2P(OPr)_2\}_{22}$. The three Pt-alloyed nanoclusters (Pt_1Ag_{20}, Pt_2Ag_{33}, and Pt_3Ag_{44}) contain 8, 16, and 22 free electron counts, respectively.[504] The crystal structures reveal that their inner kernels (Pt_1Ag_{12}, Pt_2Ag_{23}, and Pt_3Ag_{34}) can be visualized as consisting of one, two and three Pt-centered icosahedral Pt_1Ag_{12}, respectively. In Pt_2Ag_{33} and Pt_3Ag_{44} nanoclusters, the Pt_1Ag_{12} units are vertex-shared and assembled linearly, which are isolobal to N_2 and I_3^-, respectively.[504]

Collectively, the Au-alloying has been achieved based on both Ag_{20} and Ag_{21} nanoclusters stabilized by S/Se donor ligands. As for the Ag_{21} template, the central Pd- and Pt-doping processes were accomplished. The surface structure formed by Ag and S/Se donor ligands is different from that in $Ag_{25}(SR)_{18}$ although their superatomic configurations are similar.

4 Alloy nanoclusters of specific sizes

Besides the above-mentioned alloy nanoclusters based on templates, several special alloys have been reported with specific magic-size kernels, such as $Ag_{28}Cu_{12}$ and $Ag_{32}Cd_{12}$ with tetrahedral Ag_{28} kernel; $Au_{13}Cu_2$, $Au_{13}Cu_4$ and $Au_{13}Cu_8$ nanoclusters with icosahedral Au_{13} kernel; $Au_{12}Cu_{32}$, $Au_{14}Cu_{32}$, $Au_{16}Cu_{32}$ and $Au_{18}Cu_{32}$ nanoclusters with icosahedral Au_{12} kernel; Pt-centered Pt_1Ag_{26} and Pt_1Ag_{28} nanoclusters; and M_1Cu_{12} nanoclusters. In this section, these alloy nanoclusters are highlighted. Most of these alloy nanoclusters share one thing in common: the minority atom(s) are symmetrically arranged in the structure, e.g., at the centre, or mounted at equal positions on the surface of the kernel.

4.1 Nanoclusters with tetrahedral Ag_{28} kernel

Yan *et al.* reported the crystal structure of $[Ag_{28}Cu_{12}(SR)_{24}]^{4-}$, which was the first Ag/Cu nanocluster with structure solved (Fig. 14a).[505] The high yield and stability of

this alloy nanocluster were proposed to result from its 20-electron count. Structurally, $Ag_{28}Cu_{12}$ contains a three-concentric shell structure: Ag_4(kernel)@Ag_{24}(shell)@4×$Cu_3(SR)_6$(motifs). The arrangement of Ag(inner)@Cu(surface) is proposed to result from the activities of the two metals, i.e. Ag is more inert and thus goes to the kernel, whereas Cu is more active and thus preferentially resides in surface motifs for wrapping the Ag kernel.[505] Interestingly, $Ag_{28}Cu_{12}(SR)_{24}$ is in a "-4" charge state and has a chiral metal framework with *T* symmetry; thus, the contains an FCC Ag_{28} and HCP Ag-Cu interface. The $Ag_{28}Cu_{12}(SR)_{24}$ prepared using achiral counter-ion, $^nBu_4N$, is a racemic mixture, hence no CD signal. By altering the achiral counter-ion to chiral quaternary ammonium salts, such as N-benzylcinchonidinium chloride (BCDC) or N-benzylcinchoninium chloride (BCNC), counter-ion-pairing enantioseparation and direct asymmetric synthesis have been put forward for *in-situ* preparing chiral nanoclusters.[505]

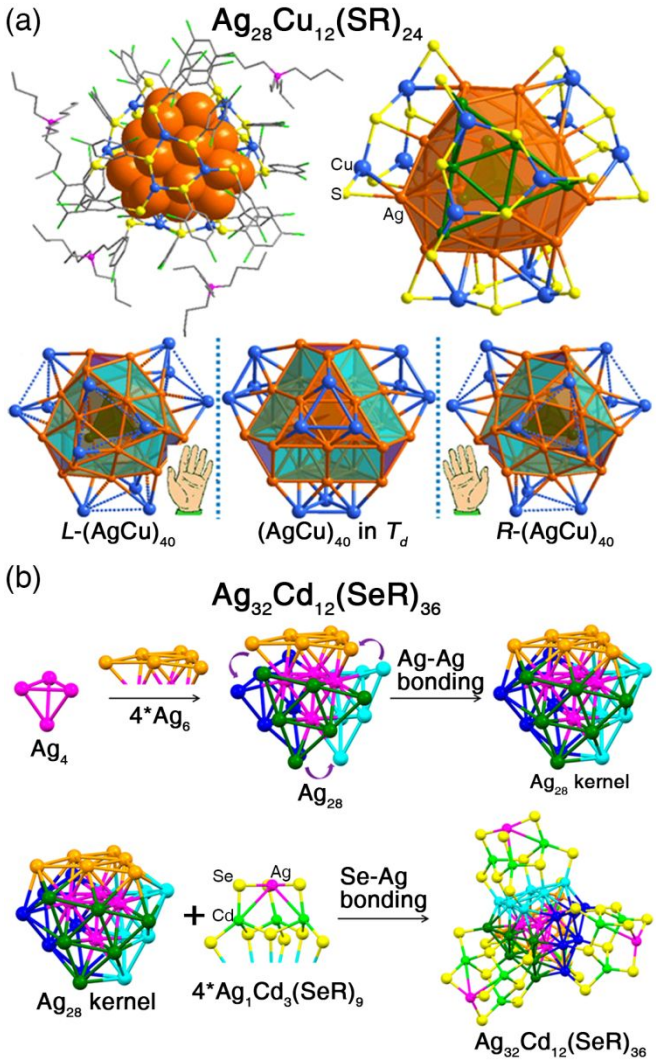

Fig. 14 (a) Structure of $Ag_{28}Cu_{12}(SR)_{24}$ and its twisted kernel structure. Redrawn from ref. 505 with permission from American Chemical Society, copyright 2016. (b) Structural anatomy of $Ag_{32}Cd_{12}(SeR)_{36}$. Redrawn from ref. 506 with permission from American Chemical Society, copyright 2019.

Bootharaju *et al*. reported Cd-alloyed $Ag_{32}Cd_{12}(SePh)_{36}$ — which consists of an Ag_{28} kernel stabilized by four $Ag_1Cd_3(SePh)_9$ motifs (Fig. 14b).[506] The Ag_{28} kernel contains an innermost Ag_4 tetrahedron, which is encapsulated by four Ag_6 facets; and this configuration is the same as that in $Ag_{28}Cu_{12}$.[506] Besides, in the $Ag_1Cd_3(SePh)_9$ motif structure, each Cd atom tetrahedrally coordinates with four SePh ligands, and three of the Se atoms in the $CdSe_4$ tetrahedra bind to the Ag atom on the top to form an $AgSe_3$ cap-like structure, giving rise to $Ag_1Cd_3(SePh)_9$ motif structure. The four $Ag_1Cd_3(SePh)_9$ motifs cap the four Ag_6 kernel facets with a one-on-one mode *via* Se-Ag linkages. The absorption spectrum and electronic structure of this cluster are well consistent with those from DFT calculations.[506]

4.2 Nanoclusters with centered icosahedral Au_{13} kernel

The Zheng group reported a correlated series of Au/Cu alloy nanoclusters with $Au_{13}Cu_x$ (x = 2, 4, 8) compositions.[507] By engineering the peripheral ligands (mainly by introducing the N coordination sites), different numbers of Cu heteroatoms were arranged onto the surface of the icosahedral Au_{13} kernel (Fig. 15a). Specifically, when the Au/Cu nanocluster was co-stabilized by PPh_3 and Spy ligands (Spy = 2-pyridyl), $Au_{13}Cu_2(PPh_3)_6(Spy)_6$ was generated (Fig. 15a, left). The two Cu heteroatoms were at the two ends on the cluster surface. Changing the capped ligands to PPh_2py and SPh^tBu produced $Au_{13}Cu_4(PPh_2py)_4(SPh^tBu)_8$ (Fig. 15a, middle). A regular tetrahedron was formed *via* linking the four Cu atoms, which encircled the icosahedral Au_{13} kernel. In addition, $Au_{13}Cu_8(Spy)_{12}$ emerged with Spy ligand only (Fig. 15a, right) and the overall structure was in an irregular manner with C_1 symmetry.[507] Of note, all of these Cu atoms display a μ_6 binding mode: each Cu atom links to three gold atoms on the icosahedral Au_{13} kernel shell and another three atoms in the ligands (N or S).[507]

Due to the different Cu alloying modes and Cu numbers among these Au/Cu alloy nanoclusters, each nanocluster shows different optical absorption although they share the same Au_{13} kernel.[507] This is can be understood by the fact that the Cu atoms or Cu-containing motifs are directly mounted on the Au_{13} kernel *via* Cu-Au bonds (2.75-3.05 Å), thus, Cu would be more significantly involved in the frontier orbitals and accordingly change the electronic states. A similar phenomenon is also observed in other Au/Cu alloy nanoclusters with Au_{13} kernels (*vide infra*), but the change in motifs far away from the kernel would have less influences (see section 4.3).

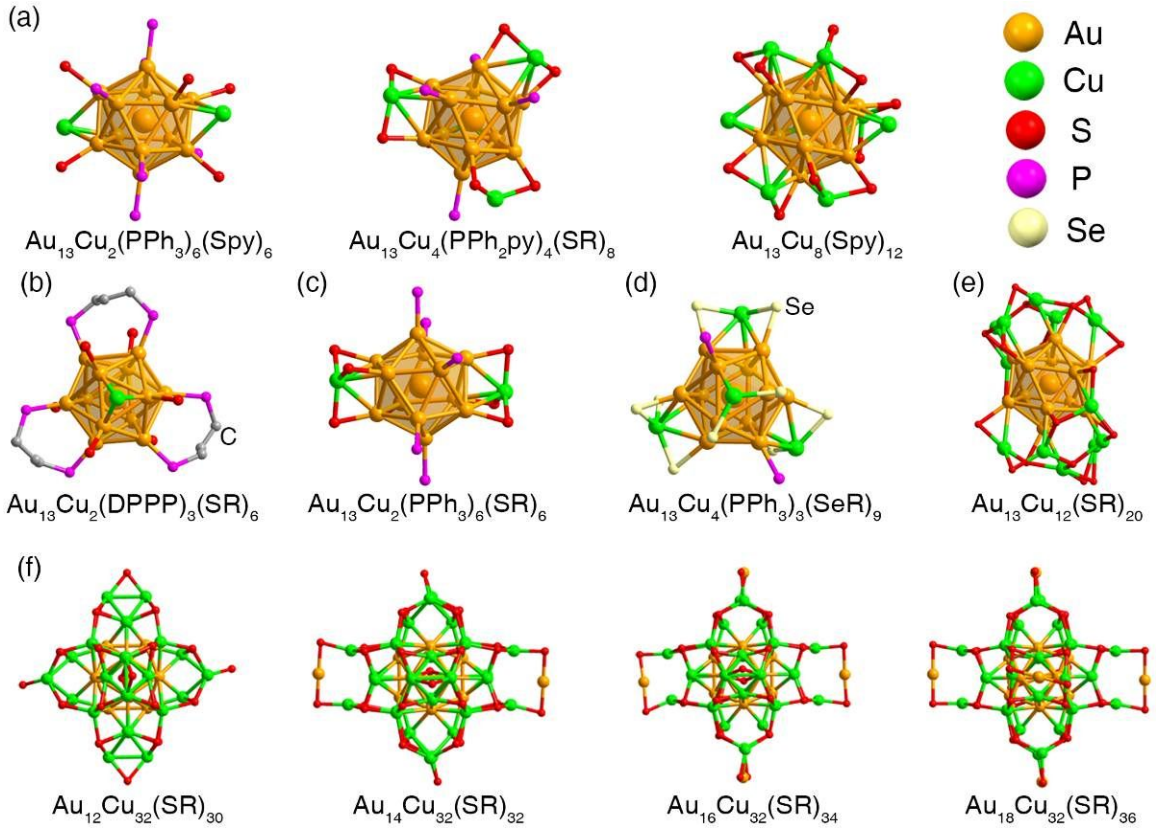

Fig. 15 Structures of Au/Cu alloy nanoclusters with icosahedral Au_{13}/Au_{12} kernels. Crystal structures of (a) $Au_{13}Cu_x$ (x = 2, 4, 8), (b) $Au_{13}Cu_2(DPPP)_3(Spy)_6$, (c) $Au_{13}Cu_2(PPh_3)_6(S\text{-}C_2H_4Ph)_6$, (d) $Au_{13}Cu_4(PPh_2py)_3(SePh)_9$, (e) $Au_{13}Cu_{12}(SR)_{20}$, and (f) $Au_{12+n}Cu_{32}(SR)_{30+2n}$ (n = 0, 2, 4, 6) nanoclusters.

Deng *et al.* changed the PPh_3 ligands in the preparation of $Au_{13}Cu_2(PPh_3)_6(Spy)_6$ nanocluster to 1,3-bis(diphenyphosphino)propane (DPPP), and obtained $Au_{13}Cu_2(DPPP)_3(Spy)_6$ (Fig. 15b).[508] The phosphine coordination sites on these two nanoclusters were the same (6 total). When the achiral DPPP ligands were replaced by chiral (2*r*,4*r*)/(2*s*,4*s*)-2,4-bis(diphenylphosphino)pentane (BDPP) ligands, two optically pure enantiomers $Au_{13}Cu_2(2r,4r\text{-}BDPP)_3(SPy)_6$ and $Au_{13}Cu_2(2s,4s\text{-}BDPP)_3(SPy)_6$ were synthesized.[508]

In 2019, Zhou et al. reported a new $Au_{13}Cu_2$ nanocluster co-protected by PhC_2H_4-SH and PPh_3 ligands, formulated as $Au_{13}Cu_2(PPh_3)_6(S\text{-}C_2H_4Ph)_6$ (Fig. 15c).[509] Although the Cu heteroatoms are fixed by Cu-S interactions in $Au_{13}Cu_2(PPh_3)_6(S\text{-}C_2H_4Ph)_6$, rather than Cu-N interactions in $Au_{13}Cu_2(PPh_3)_6(Spy)_6$, both $Au_{13}Cu_2$ nanoclusters contain the same icosahedral Au_{13} kernel.[507,509] Such surface differences between the two nanoclusters induce tremendous changes in optical absorption.[509]

Based on the $Au_{13}Cu_4(PPh_2py)_4(SR)_8$ nanocluster, Song *et al.* altered the thiol to selenol ligands.[510] An $Au_{13}Cu_4(PPh_2py)_3(SePh)_9$ nanocluster was obtained with a configuration of Au_{13}(kernel)@3×Cu(SePh)$_2$PPh$_2$py&Cu(SePh)$_3$(motifs) (Fig. 15d) with remarkable differences in terms of motif structure compared with $Au_{13}Cu_4(PPh_2py)_4(SR)_8$. ESI-MS results demonstrated a reaction intermediate formulated as $Au_{13}Cu_4(PPh_2py)_4(SeR)_8$, with the same metal-ligand composition as the $Au_{13}Cu_4(PPh_2py)_4(SR)_8$. However, probably due to the low thermal-stability of this reaction intermediate, an additional SePh ligand would further substitute one PPh_2py ligand on the surface to generate the final product—$Au_{13}Cu_4(PPh_2py)_3(SePh)_9$.[510]

4.3 Nanocluster with hollow icosahedral Au_{12} kernel

Through controlling the feeding material in the synthesis, Yang *et al.* obtained a series of all-thiolate stabilized nanoclusters — $Au_{12+n}Cu_{32}(SR)_{30+2n}$ (n = 0, 2, 4, 6) (Fig. 15f).[511] First of all, the configuration of $Au_{12}Cu_{32}(SR)_{30}$ (n = 0) is almost the same as that of $Au_{12}Ag_{32}(SR)_{30}$,[477] in which the icosahedral Au_{12} kernel is capped by a Cu_{20} shell and further protected by three pairs of $Cu_2(SR)_5$ motifs.[511] Of note, each pair of $Cu_2(SR)_5$ motifs can be replaced by a pair of $Cu_2Au_1(SR)_6$ motifs (at contrapuntal sites); alternatively, the $Cu_2Au_1(SR)_6$ motif can be considered as inserting an $Au_1(SR)$ unit into the $Cu_2(SR)_5$ motif, and consequently, a correlated series of nanoclusters — $Au_{12}Cu_{32}(SR)_{30}$, $Au_{14}Cu_{32}(SR)_{32}$, $Au_{16}Cu_{32}(SR)_{34}$, and $Au_{18}Cu_{32}(SR)_{36}$ — was obtained. Different metal compositions and surface structures hardly changed the optical absorption in this series, but there is a large difference in thermal stability, *i.e.* $Au_{12}Cu_{32}(SR)_{30}$ and $Au_{14}Cu_{32}(SR)_{32}$ are much thermally stable than the other two nanoclusters. Zheng and co-workers analyzed the oxidation process based on $Au_{16}Cu_{32}(SR)_{34}$, and obtained the crystal

structure of its decomposed product—$Au_{13}Cu_{12}(SR)_{20}$, which contained an icosahedral Au_{13} kernel capped by two $Cu_6(SR)_{10}$ triangle-like motifs (Fig. 15e).[511]

4.4 Pt-centered nanoclusters

Controllably tuning the structures of nanoclusters with atomic precision is important for tailoring their chemical/physical properties and developing their practical applications. Wu and co-workers altered the capping ligand in the synthesis of $Pt_1Ag_{24}(SR)_{18}$ and obtained a larger Pt-centered, Ag-based alloy nanocluster, *i.e.* $Pt_1Ag_{26}(SR)_{18}(PPh_3)_4$ (Fig. 16a).[512] Structurally, the Pt_1Ag_{12} kernel in $Pt_1Ag_{24}(SR)_{18}$ grew into a Pt_1Ag_{14} kernel and the structures of peripheral motifs also changed. Interestingly, dissimilar optical and electrochemical gaps were found for these two nanoclusters. Both Pt_1Ag_{24} and Pt_1Ag_{26} nanoclusters are 8e superatoms and exhibit highly similar electronic structures illustrated by their almost superimposable optical absorption and similar HOMO/LUMO locations. However, largely different electrochemical gaps were observed: Pt_1Ag_{28} (1.89 eV) vs. Pt_1Ag_{24} (1.48 eV), which was probably resulted from the differences in charges of the Pt_1Ag_{12}/Pt_1Ag_{14} kernels.[512]

In 2019, Wu and co-workers obtained the structures of co-crystallized $Au_1Ag_{24}(SR)_{18}$ and $Au_1Ag_{26}(SR)_{18}(PPh_3)_6$ nanoclusters in one crystal lattice,[513] and the co-crystallization was induced by weak electrostatic interactions between cationic $[Au_1Ag_{26}(SR)_{18}(PPh_3)_6]^+$ and anionic $[Au_1Ag_{24}(SR)_{18}]^-$ nanoclusters as well as the C-H$\cdots\pi$ and $\pi\cdots\pi$ interactions.[513] The $Au_1Ag_{26}(SR)_{18}(PPh_3)_6$ with Au center is a structural analogue of $Pt_1Ag_{26}(SR)_{18}(PPh_3)_4$ (Fig. 16a, right).[512,513]

Among the nanoclusters in the $M_{29}(SR)_{18}(PPh_3)_4$ library (where SR = S-Adm), the Pt-centered Pt_1Ag_{28} are the most researched, and the multi-metallic M_{29} will be discussed in Section 5.2. $Pt_1Ag_{28}(SR)_{18}(PPh_3)_4$ was firstly obtained by ligand-exchange on $Pt_1Ag_{24}(SPhMe_2)_{18}$, and the Pt_1Ag_{12} kernel of $Pt_1Ag_{28}(SR)_{18}(PPh_3)_4$ was a distorted FCC configuration (Fig. 16b).[447] Lin *et al.* prepared the $Pt_1Ag_{28}(SR)_{18}(PPh_3)_4$ nanocluster by *in-situ* reducing Pt/Ag-SR-PPh_3 complexes. Interestingly, the nanocluster contains a Pt_1Ag_{12} kernel with standard FCC configuration (Fig. 16b, right).[449] Although the two $Pt_1Ag_{28}(SR)_{18}(PPh_3)_4$ nanoclusters showed the same composition, the different kernel structures endowed them with different optical properties.[447,449]

Kang *et al.* reported another Pt_1Ag_{28} nanocluster that was co-stabilized by HS-*c*-C_6H_{11} and PPh_3 ligands, Pt_1Ag_{28}(S-*c*-$C_6H_{11})_{18}(PPh_3)_4$, by ligand-exchanging the Pt_1Ag_{28}(S-Adm)$_{18}(PPh_3)_4$ with excess HS-*c*-C_6H_{11} ligands.[514] Of note, the reversible process (*i.e.*, from Pt_1Ag_{28}(S-*c*-$C_6H_{11})_{18}(PPh_3)_4$ to Pt_1Ag_{28}(S-Adm)$_{18}(PPh_3)_4$) was also feasible. Interestingly, although both $Pt_1Ag_{28}(SR)_{18}(PPh_3)_4$ nanoclusters contain similar $Ag_{16}(SR)_{18}(PPh_3)_4$ cages, their Pt_1Ag_{12} kernel are different — Pt_1Ag_{28}(S-Adm)$_{18}(PPh_3)_4$ contains an FCC Pt_1Ag_{12} kernel, whereas the Pt_1Ag_{28}(S-*c*-$C_6H_{11})_{18}(PPh_3)_4$ contains an icosahedral Pt_1Ag_{12} kernel.[514] Such a reversible kernel structure (FCC and icosahedral isomers) is new (Fig. 16c). A combination of UV-vis, ESI-MS, PL, and XAFS unambiguously identified that the FCC-to-icosahedral transformation of the Pt_1Ag_{28} kernel involves two distinct stages: (i) the ligand-exchange induced motif change, and (ii) the abrupt kernel transformation.[514] Such a structural transformation (FCC vs. icosahedron) results in significant differences in both optical absorption and PL emission.[514]

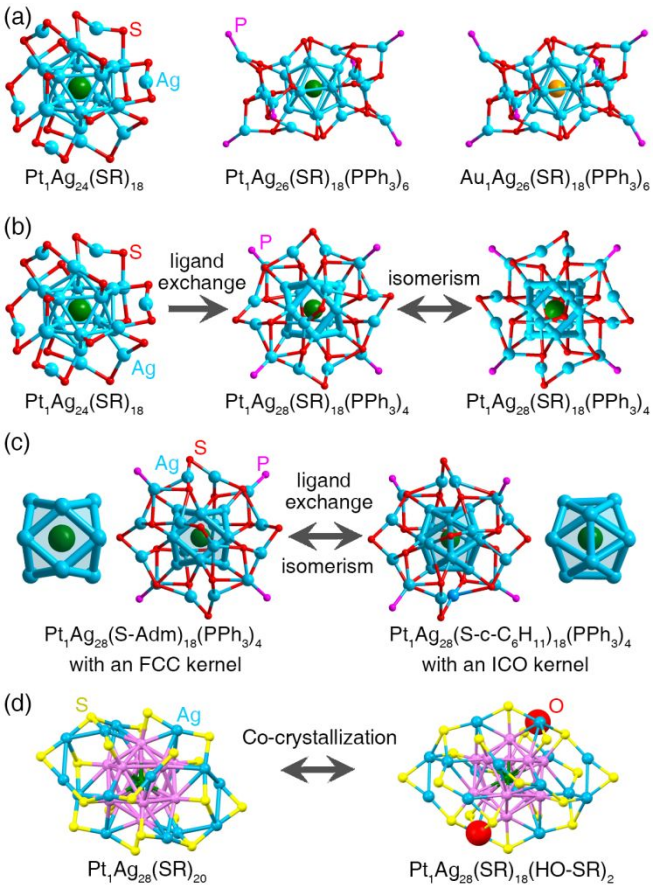

Fig. 16 Structures of Pt-centered Ag nanoclusters. (a) Structural comparison among $Pt_1Ag_{24}(SR)_{18}$, $Pt_1Ag_{26}(SR)_{18}(PPh_3)_6$ and $Au_1Ag_{26}(SR)_{18}(PPh_3)_6$ nanoclusters. (b) Conversion from icosahedral $Pt_1Ag_{24}(SR)_{18}$ to Pt_1Ag_{28}(S-Adm)$_{18}(PPh_3)_4$, and standard FCC Pt_1Ag_{28}(S-Adm)$_{18}(PPh_3)_4$. (c) Inter-conversion between Pt_1Ag_{28}(S-Adm)$_{18}(PPh_3)_4$ with an FCC Pt_1Ag_{12} kernel and Pt_1Ag_{28}(S-*c*-$C_6H_{11})_{18}(PPh_3)_4$ with an icosahedral Pt_1Ag_{12} kernel. (d) Structural anatomy of Pt_1Ag_{28}(S-2-Adm)$_{20}$ and Pt_1Ag_{28}(S-2-Adm)$_{18}$(HO-SR)$_2$ nanoclusters.

Starting from Pt_1Ag_{28}(S-Adm)$_{18}(PPh_3)_4$, the addition of Ag_2(DPPM)Cl_2 was exploited to re-construct the surface structure of the nanocluster, which produced a larger size nanocluster — $Pt_1Ag_{31}(SR)_{16}$(DPPM)$_3Cl_3$.[515] Structurally, the size growth was induced by the substitution of Ag-PPh_3 terminals in Pt_1Ag_{28}(S-Adm)$_{18}(PPh_3)_4$ with Ag_2(DPPM)Cl terminals.[515] The substitution of cluster terminals induces direct changes to the surface structure (size-growth, structure transformation, and surface rotation) as well as indirect changes to the kernel structure (from a FCC configuration to an icosahedral configuration).[515]

Altering HS-Adm to HS-2-Adm (2-adamantanethiol) in the synthesis of $Pt_1Ag_{28}(S\text{-}Adm)_{18}(PPh_3)_4$ gives rise to both $Pt_1Ag_{28}(S\text{-}2\text{-}Adm)_{20}$ and $Pt_1Ag_{28}(S\text{-}2\text{-}Adm)_{18}(HO\text{-}SR)_2$ (Fig. 16d).[516] For the latter, the valence self-regulation of sulfur from "-2" valence state in thiols (*i.e.*, Ag-SR) to the "-1" valence state in hydroxylated thiolates (*i.e.*, HO-SR-Ag) has been accomplished; this is the first time that the "-1" valent sulfur, i.e. "S^{-1}" is detected. Both nanoclusters have icosahedral Pt_1Ag_{12} kernels, whereas the Ag-SR cages of them are different — the cage of $Pt_1Ag_{28}(S\text{-}2\text{-}Adm)_{20}$ comprises an $Ag_{10}(SR)_{10}$ ring motif, two $Ag_2(SR)_3$ and two $Ag_1(SR)_1$ staple motifs, while that of $Pt_1Ag_{28}(S\text{-}2\text{-}Adm)_{18}(HO\text{-}SR)_2$ is composed of an $Ag_8(SR)_{10}$ ring motif plus two $Ag_2(SR)_3$ and two $Ag_2(SR)_1(HO\text{-}SR)_1$ staple motifs.[516] SC-XRD revealed that these two nanoclusters were lamellar co-crystallized (with a 1:1 ratio) in the crystal lattice with an interlayer distance of 33.978 Å (calculated from the distance between two Pt planes). ESI-MS analysis was performed to verify their co-crystallization, as well as the presence of the hydroxyl on the nanocluster surface.[516]

4.5 M_1Cu_{12} nanoclusters

In 2016, Liu and co-workers reported a two-electron homo-copper nanocluster superatom with a chemical formula of $Cu_{13}(S_2CN^nBu_2)_6(C{\equiv}CR)_4$ (R = C(O)OMe or C_6H_4F).[517] Structurally, the cuboctahedral Cu_{13} contains eight triangular faces (capped by acetylide groups) and six square faces (protected by di-thiolate ligands) (Fig. 17). DFT calculations demonstrated that the a_1 HOMO contains two 1S jellium electrons, which is a two-electron superatom.[517] Silalahi *et al.* found that the central Cu atom could be substituted by Ag or Au heteroatom *via* reacting the Cu_{13} solution with M^+ ions, giving $M_1@Cu_{12}(S_2CN^nBu_2)_6(C{\equiv}CR)_4$ (M = Au/Ag) (Fig. 17).[518] However, mainly because the atomic radii of Au and Ag are larger than that of Cu, the Ag-Cu and Cu-Cu (or the Au-Cu and Cu-Cu) bond lengths in Ag_1Cu_{12} (or Au_1Cu_{12}) are slightly longer than those in homo-copper Cu_{13} nanocluster. These experimental and theoretical results revealed that the Au and Ag dopants (i) enhance the stability, (ii) alter the optical absorption, and (iii) significantly improve the PL performance in Au_1Cu_{12} and Ag_1Cu_{12} relative to the Cu_{13}.[518] Specifically, the PL QY of Au_1Cu_{12} at 77 K is about 59%.[518] Chakrahari *et al.* expanded the scope of the central atom to S, Br and Cl atoms.[519]

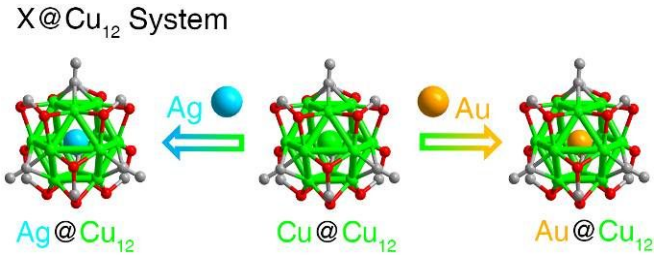

Fig. 17 Structures of the $M_1@Cu_{12}$ nanoclusters including Cu_{13}, Ag_1Cu_{12}, and Au_1Cu_{12}.

5 Multi-metallic nanoclusters

Doping has been considered as a versatile approach to control the compositions, regulate the electronic and geometric structures, and tune the chemical and physical properties of nanoclusters. Doping more than one type of hetero-metal into homo-gold or homo-silver nanoclusters is more challenging but has met with some successes. Here we review the literature progress in multi-metallic nanoclusters containing ≥3 types of metals.

5.1 Spherical and Rod M_{25} systems

The most studied templates for multi-metallic alloying are spherical M_{25} and rod-like M_{25} (M = Au/Ag) nanoclusters (Table 6; and see the bi-metallic systems in sections 2.1 and 2.5).[378-381,442,520-524] Negishi et al. has an excellent review on these systems (mainly on Au-based M_{25} nanoclusters).[82] Here we only briefly highlight some results on Ag-based M_{25} systems.

Table 6 Multi-metallic nanoclusters with spherical or rod-like M_{25} templates.

Formula	Measurement(s)	Ref(s)
$Pt_2Au_{10}Ag_{13}(PPh_3)_{10}Br_7$	SCXRD	378
$Pt_1Au_{12}Ag_{12}(PPh_3)_{10}Cl_7$	SCXRD	379,380
$Ni_1Au_{12}Ag_{12}(PPh_3)_{10}Cl_7$	SCXRD	380
$Pt_2Au_{10}Ag_{13}(PPh_3)_{10}Cl_7$	SCXRD	381
$Pt_1Ag_{24-x}Au_x(SR)_{18}$ (x ~ 6.4)	ESI-MS, SCXRD	378
$Pt_1Ag_{23}Au_1(SR)_{18}$ & $Pt_1Ag_{22}Au_2(SR)_{18}$	ESI-MS	442
$Cd_1Ag_xAu_{24-x}(SR)_{18}$ (x = 2-6)	MALDI-MS	520
$Hg_1Ag_xAu_{24-x}(SR)_{18}$ (x = 1-3)	MALDI-MS	520
$Hg_1Ag_xAu_{24-x}(SR)_{18}$ (x ~ 7.2)	MALDI-MS, SCXRD	521
$Pd_1Cu_xAu_{24-x}(SR)_{18}$ (x = 1-3)	MALDI-MS	522
$Pd_1Ag_xAu_{24-x}(SR)_{18}$ (x = 1-5)	MALDI-MS	523
$Pd_1Ag_xCu_yAu_{24-x-y}(SR)_{18}$ (x = 1-3, y = 1-2)	MALDI-MS	523
$Pd_1Ag_{\sim4}Au_{\sim20}(SR)_{18}$	MALDI-MS, SCXRD	524
$Pt_1Ag_{\sim4}Au_{\sim20}(SR)_{18}$	MALDI-MS, SCXRD	524

As the icosahedral M_{13} kernels can easily be center-doped by Pt/Pd, tri-metallic nanoclusters could be prepared by further doping the Pd/Pt-centered icosahedral kernel shell with Au/Ag dopants. In addition, due to the improved stability by the central Pt heteroatom, the tri-metallic nanoclusters are generally stable and follow a stratified configuration—Pt(center)@Ag/Au(kernel shell). Based on this consideration, several phosphine/halogen co-protected tri-metallic nanoclusters have been prepared, such as $Pt_1Au_{12}Ag_{12}(PPh_3)_{10}Cl_7$, $Ni_1Au_{12}Ag_{12}(PPh_3)_{10}Cl_7$, $Pt_2Au_{10}Ag_{13}(PPh_3)_{10}Cl_7$, etc.[379-381]

Based on the center-Pt-doped $Pt_1Ag_{24}(SR)_{18}$, Kang *et al.* exploited the metal-exchange strategy to prepare Pt/Au/Ag tri-metallic nanoclusters with different structures.[378] Reacting spherical $Pt_1Ag_{24}(SR)_{18}$ with Au-SR complexes generated $Pt_1Ag_{24-x}Au_x(SR)_{18}$ with the maintained structure, i.e. the Pt(center)@Au/Ag(kernel shell)@Ag(motif) tri-stratified

arrangement. Both SC-XRD and ESI-MS results demonstrated that the average Au doping number in $Pt_1Ag_{24-x}Au_x(SR)_{18}$ was 6.4.[378] However, reacting $Pt_1Ag_{24}(SR)_{18}$ with a large amount of $Au(PPh_3)Br$ complexes altered the spherical shape to rod-like shape, *i.e.* a bi-icosahedral $Pt_2Au_{10}Ag_{13}(PPh_3)_{10}Br_7$ nanocluster, with a multi-layered configuration of Ag-Au_5-Pt_1-Ag_5-Ag_1-Ag_5-Pt_1-Au_5-Ag_1.[378] The different metal-exchanging results (structure-maintained vs. structure-altered) might be caused by the different ligand effects between thiol and phosphine.[378]

Adding only a small amount of $Au(PPh_3)Cl$ to $Pt_1Ag_{24}(SR)_{18}$ did not cause structural transformation, but one or two Au heteroatoms were doped into the Pt_1Ag_{12} icosahedral kernel shell, giving rise to $Pt_1Ag_{23}Au_1(SR)_{18}$ or $Pt_1Ag_{22}Au_2(SR)_{18}$ nanoclusters.[442] Thus, there should be a threshold for the $M_{25}(SR)_{18}$ nanocluster to maintain its spherical shape under the attack by $Au(PPh_3)Cl$.[378,442]

The phenomenon in reacting $Pd_1Ag_{24}(SR)_{18}$ with $Au(PPh_3)Cl$ complex is different.[442] ESI-MS identified the products as bi-metallic $Au_1Ag_{24}(SR)_{18}$ and $Au_2Ag_{23}(SR)_{18}$ nanoclusters instead of the tri-metallic ones; that is, the central Pd atom was substituted by the introduced Au heteroatom. Bootharaju *et al.* proposed that such a replacement process was similar to the "$Ag_{25}(SR)_{18}$ → $Au_1Ag_{24}(SR)_{18}$" doping process.[442] Specifically, the introduced Au heteroatom was first arranged onto the icosahedral kernel shell, and then exchanged with the center Pd atom.[442] The differences in Au doping processes for Pt_1Ag_{24} and Pd_1Ag_{24} nanoclusters could be explained in terms of variations in the stability of the Pt/Pd center against the attack from the incoming Au.[442]

5.2 M_{29} system

As for the $Ag_{29}(S\text{-}Adm)_{18}(PPh_3)_4$ nanocluster (of note, its structure remains undetermined, but is predicted from the structures of other $M_{29}(S\text{-}Adm)_{18}(PPh_3)_4$ nanoclusters), the FCC Ag_{13} kernel is capped by an $Ag_{16}(SR)_{18}(PPh_3)_4$ cage. Kang *et al*. constructed a library of $M_{29}(S\text{-}Adm)_{18}(PPh_3)_4$ (M = Au/Ag/Pd/Pt/Cu) nanoclusters with composition ranging from mono-metallic to tetra-metallic (Fig. 18), and atomically precise manipulation on each site.[448] These nanoclusters were prepared step by step with *in-situ* synthesis, target metal-exchange and forced metal-exchange methods, and this stepwise procedure guaranteed the mono-dispersity of these nanoclusters, resulting in Ag_{29}, Pt_1Ag_{28}, $Pt_1Ag_{12}Cu_{16}$, $Pt_1Ag_{12}Cu_{12}Au_4$, etc.[448] Specifically, the $M_{29}(S\text{-}Adm)_{18}(PPh_3)_4$ template possesses a tetra-stratified configuration: M_1(center)@M_{12}(1st-shell)@$M_{12}(SR)_{18}$(2nd-shell)@(Ag-$PPh_3)_4$(vertex), and owing to the accessibility of each site with multi-choices of metals, a rich library of 21 species of M_{29} clusters was successfully prepared: the occupation by Ag/Au/Pt/Pd at the center, and the occupation by Ag/Cu on the cuboctahedral kernel shell (2nd-shell) can be both controlled by *in-situ* syntheses, while the control over the vertex atom (the four sites linking to PPh_3 in the $Ag_{16}(SR)_{18}(PPh_3)_4$ cage) occupation by Ag/Cu/Au is achieved *via* the target metal-exchange and the forced metal-exchange methods. Among these 21 M_{29} nanoclusters, $Pt_1Ag_{12}Cu_{12}Au_4(SR)_{18}(PPh_3)_4$ and $Pd_1Ag_{12}Cu_{12}Au_4(SR)_{18}(PPh_3)_4$ are indeed the first reports of tetra-metallic nanoclusters of atomic precision. The atomic mono-dispersity of each nanocluster has been confirmed by ESI-MS analysis. Based on this M_{29} library, the synergetic effects on optical properties and thermal stability have been mapped out, which will be discussed in Section 7.[448]

Of note, there are great differences in doping modes between $Ag_{29}(S_2R)_{12}(PPh_3)_4$ and $Ag_{29}(SR)_{18}(PPh_3)_4$) due to the different kernel configurations (FCC vs. icosahedron) and the surface structures. Future alloying work based upon these two M_{29} templates will give more insights into the kernel configuration effects and ligand effects in the doping process.

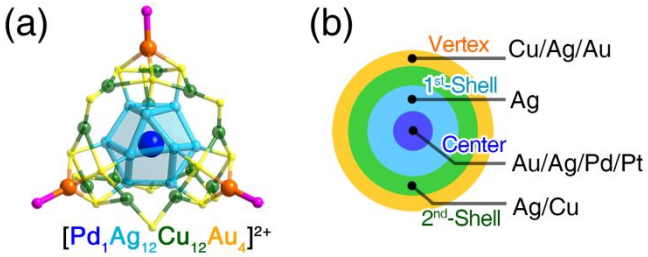

Fig. 18 Alloying based on the $Ag_{29}(S\text{-}Adm)_{18}(PPh_3)_4$ template. (a) Proposed structure of tetra-metallic $Pd_1Ag_{12}Cu_{12}Au_4(S\text{-}Adm)_{18}(PPh_3)_4$ nanocluster. (B) Structural anatomy of the center, 1st-shell, 2nd-shell, and vertex of the $M_{29}(S\text{-}Adm)_{18}(PPh_3)_4$ cluster template. Redrawn from ref. 448 with permission from National Academy of Sciences, copyright 2019.

5.3 Other systems

Except the M_{25} and M_{29} systems, other tri-metallic nanoclusters have been studied as well.[525-527] Puls *et al.* reported the structure of $Ni_1(AuPPh_3)_{(8-2n)}(AuCl)_3(AlCp^*)_n$ (Cp^* = C_5Me_5 and n = 1, 2) based on the icosahedral Au_{13} template.[525] This tri-metallic nanocluster was prepared by the transmetalation of $Ni(AlCp^*)_4$ with $Au(PPh_3)Cl$. In the structure of $Ni_1Au_9Al_1$, the Ni or Al heteroatom is incorporated at the center or on the surface of an incomplete icosahedral kernel. When two Al heteroatoms are doped into the template, the icosahedral configuration of $Ni_1Au_7Al_2$ becomes more defective. By similar synthetic procedures, the central and surface Au atoms can be substituted by the introduced Mo and Ga atoms, respectively, resulting in a tri-metallic nanocluster with a Mo(center)@$Au_8(PMe_3)_8Ga_4Cl_7$ configuration.[525]

Zheng and co-workers reported an alkynyl-protected $Ag_8Au_7(C{\equiv}C^tBu)_{12}$ nanocluster, which follows a three-layer $Au_1@Ag_8@Au_6(C{\equiv}C^tBu)_{12}$ configuration.[526] When copper was added during the synthesis, some of the peripheral Au could be substituted by Cu, producing tri-metallic $Ag_8Au_{7-x}Cu_x(C{\equiv}C^tBu)_{12}$ nanoclusters (x up to 6).[526]

The reaction between H-$Pd_1Au_8(PPh_3)_8$ and Au(I)Cl generated bi-metallic $HPd_1Au_{10}(PPh_3)_8Cl_2$ nanocluster.[319] Hirai

et al. introduced Ag(I)Cl or Cu(I)Cl to the solution of $HPd_1Au_8(PPh_3)_8$, and obtained tri-metallic $HPd_1Ag_2Au_8(PPh_3)_8Cl_2$ or $HPd_1Cu_2Au_8(PPh_3)_8Cl_2$.[527] SC-XRD results found that Ag or Cd heteroatoms were region-selectively incorporated. Besides, DFT calculations suggested that the hydrogen in $HPd_1M_2Au_8(PPh_3)_8Cl_2$ (M = Au, Ag, Cu) occupy the same bridging site between the central Pd and the surface Au atom.[527]

6 Other alloy nanoclusters

Aside from the aforementioned nanocluster systems, alloy nanoclusters with specific structures have been synthesized and determined. In this section, we select some works of recently published alloy nanoclusters. Together with those discussed in previous sections, the combination will provide readers with a comprehensive view on the alloying modes of different metals, novel structures and properties that alloying can bring about.

Similar to section 4, atoms of the same kind tend to arrange according to the symmetry of the nanocluster structure. For smaller sizes, central occupation and symmetrically sparse surface distribution for minor atom(s) are observed, whereas for larger sizes, different atoms prefer to form a shell-by-shell autonomy.

6.1 Au/Ag alloy nanoclusters

In addition to the aforementioned Au/Ag alloy nanoclusters (section 2-5), there are many more of them with specific alloying modes and overall structures, which are reviewed herein and divided into three categories according to their sizes—small size (nanoclusters contain up to 25 metal atoms), medium size (nanoclusters contain 25-50 metal atoms), and large size (nanoclusters contain more than 50 metal atoms). These Au/Ag alloy nanoclusters are summarized in Table 7.

Table 7 Au/Ag alloy nanoclusters reviewed in Section 6.1 (sorted by metal kernel size, from small to large).

Formula	Ref
$Au_6Ag_2(PPh_2py)_6$	529
$Au_4Ag_5(DPPM)_2(S\text{-}Adm)_6$	528
$Au_{10}Ag_2(2\text{-}py\text{-}C{\equiv}C)_3(PPh_2py)_6$	529
$Au_7Ag_8(DPPF)_3(CF_3CO_2)_7$	530
$Au_1Ag_{16}(S\text{-}Ph\text{-}^tBu)_{12}$	532
$Au_4Ag_{13}(DPPM)_3(2,5\text{-}SPhMe_2)_9$	533
$Au_{18-x}Ag_x(DPPM)_6Br_4$ (x = 1, 2)	536
$Au_9Ag_{12}(SR)_4(DPPM)_6X_6$ (SR = S-Adm or S-*t*Bu; X = Br or Cl)	537
$Au_1Ag_{24}(DPPM)_3(S\text{-}c\text{-}C_6H_{11})_{17}$	538
$Au_4Ag_{23}(C{\equiv}C\text{-}^tBu)(DPPF)_4Cl_7$	539
$Au_5Ag_{24}(C{\equiv}C\text{-}C_6H_4\text{-}p\text{-}^tBu)_{16}(DPPF)_4Cl_4$	539
$Au_1Ag_{33}S_2(S\text{-}Ch_2Ph)_{18}(CF_3COO)_9(DMF)_6$	540
$Au_1Ag_{33}(BTCA)_3(C{\equiv}C^tBu)_9(tfa)_4(CH_3OH)_3$	541
$Au_1Ag_{39}(S\text{-}CH_2Ph\text{-}^tBu)_{21}(CH_3COO)_{11}$	542
$Au_1Ag_{39}(S\text{-}CH_2Ph\text{-}^tBu)_{20}(CH_3COO)_{12}$	542
$Au_3Ag_{38}(S\text{-}CH_2Ph)_{24}X_5$ (X = Cl/Br)	543
$Au_{24}Ag_{20}(Spy)_4(C{\equiv}CPh)_{20}Cl_{12}$	544
$Au_2Ag_{42}(S\text{-}Adm)_{27}$	547
$Au_9Ag_{36}(S\text{-}PhCl_2)_{27}(PPh_3)_6$	545
$Au_{26}Ag_{22}(S\text{-}Ph\text{-}^tBu)_{30}$	546
$Au_2Ag_{48}(S\text{-}^tBu)_{20}(DPPM)_6Br_{11}$	547
$Au_{34}Ag_{28}(PhC{\equiv}C)_{34}$	548
$Au_{24}Ag_{46}(S^tBu)_{32}$	549
$Au_{80}Ag_{30}(C{\equiv}CPh)_{42}Cl_9$	550
$Au_{57}Ag_{53}(C{\equiv}CPh)_{40}Br_{12}$	551
$Au_{130-x}Ag_x(S\text{-}Ph^tBu)_{55}$ (x ~ 98)	552
$Ag_{267-x}Au_x(2,4\text{-}SPhMe_2)_{80}$ (x ~93.8)	553

6.1.1 Au/Ag alloy nanoclusters of up to 25 metal atoms

Jin *et al.* reported a small-sized Au/Ag nanocluster co-protected by DPPM and S-Adm ligands with a chemical formula of $Au_4Ag_5(DPPM)_2(S\text{-}Adm)_6$.[528] In the Au_4Ag_5, an Ag_5 central plane is penetrated by an Au_2 unit which is further linked by the other two Au atoms (Fig. 19a). SC-XRD identified two chiral isomers in the unit cell. Interestingly, although Au_4Ag_5 in the solution phase is non-emissive, strong PL is induced when Au_4Ag_5 nanoclusters are in solid state (amorphous or crystals). Such an AIE phenomenon could be attributed to the tight combination of left- and right-handed enantiomers in solid state, which induces a strong restriction on intramolecular motions (RIM).[528]

The Wang group obtained two small-sized Au/Ag alloy nanoclusters—$Au_6Ag_2(PPh_2py)_6$ and $Au_{10}Ag_2(2\text{-}py\text{-}C{\equiv}C)_3(PPh_2py)_6$.[529] As shown in Fig. 19b, Au_6Ag_2 adopts the μ_6-Ag binding mode, *i.e*. each Ag is linked to three N donors in PPh_2py ligand and three Au atoms. As for $Au_{10}Ag_2$, two Ag heteroatoms are anchored to the two terminals of Au_{10}, and the integrate structure of $Au_{10}Ag_2$ displays C_{3h} symmetry. Three 2-py-C≡C ligands encircle the central Au_{10}, whereas the PPh_2py ligands are only at the terminal positions to anchor the Ag heteroatoms (Fig. 19c).[529] Of note, $Au_{10}Ag_2$ shows intense red-NIR dual emissions at 653 nm and 971 nm in solution. The emission at 653 nm is proposed to originate from the process of metal-to-ligand charge transfer (MLCT) from Ag to phosphine ligands, whereas the NIR emission (971 nm) is associated with the participation of PPh_2py ligands in the frontier orbitals of $Au_{10}Ag_2$.[529]

Wen *et al.* reported a linear cluster-based polymer by assembling $Au_7Ag_8(DPPF)_3(CF_3CO_2)_7$ (DPPF = 1,1'-bis(diphenylphosphino)ferrocene) entities *via* covalent Ag-O bonds, resulting in $[Au_7Ag_9(DPPF)_3(CF_3CO_2)_7BF_4]_n$.[530] In the building block of Au_7Ag_8, the icosahedral $Au@Au_6Ag_6$ kernel following an Ag_3-Au_7-Ag_3 three-layer fashion is further capped by two Ag atoms. Two adjacent Au_7Ag_8 building blocks are connected by an additional Ag atom, and thus, a cluster-based, one-dimensional chain is produced.[530]

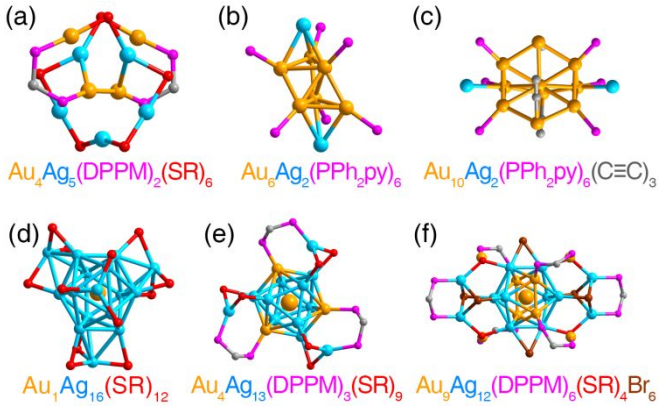

Fig. 19 Structures of Au/Ag alloy nanoclusters with metal atom number up to 25, including (a) $Au_4Ag_5(DPPM)_2(S\text{-}Adm)_6$; (b) $Au_6Ag_2(PPh_2py)_6$; (c) $Au_{10}Ag_2(2\text{-}py\text{-}C\equiv C)_3(PPh_2py)_6$; (d) $Au_1Ag_{16}(S\text{-}Ph\text{-}^tBu)_{12}$; (e) $Au_4Ag_{13}(DPPM)_3(SR)_9$; and (f) $Au_9Ag_{12}(SR)_4(DPPM)_6Br_6$.

Bigioni and co-workers characterized $Ag_{17}(S\text{-}Ph\text{-}^tBu)_{12}$, and DFT predicted that the homo-silver nanocluster contained an icosahedral Ag_{13} kernel capped by four tetrahedrally arranged $Ag_1(SR)_3$ staple motifs.[531] In their follow-up work, $Au_1Ag_{16}(SR)_{12}$ was prepared and facilitated the determination of the structure,[532] in which the mono-Au heteroatom was doped into the center of the icosahedral kernel (Fig. 19d). Of note, such a center-doping mode is the same as doping a single Au atom into $Ag_{25}(SR)_{18}$ that bears an icosahedral Ag_{13} kernel as well. So far, $Ag_{17}(SR)_{12}$ is the smallest homo-silver nanocluster protected by thiolates.[532]

Chen *et al.* reported the first alloy nanocluster ($Au_4Ag_{13}(DPPM)_3(SR)_9$) that bearing the crystallization-induced emission enhancement (CIEE) performance.[533] CIEE is a PL variation phenomenon that a non-emissive or weak-emissive compound (in solution or amorphous state) shows high fluorescence when in crystal state.[533-535] The structure of Au_4Ag_{13} exhibits an icosahedral Au_4Ag_9 kernel: one Au atom at the center, and three Au atoms are on the icosahedral kernel shell with triangular arrangement (Fig. 19e). Three $Ag_1(DPPM)_1(SR)_3$ units cap the Au_4Ag_9 kernel along the C_3 axis. Interestingly, the non-emissive Au_4Ag_{13} (in solution and amorphous state) exhibited high PL (QY = 2.7%) in the crystal state owing to the inter-nanocluster C-H$\cdots\pi$ interactions.[533]

By exploiting the thiol-etching synthetic procedure, Jin *et al.* reported three small phosphine-protected nanoclusters: $Au_{13}(DPPM)_6$, $Au_{18}(DPPM)_6Br_4$, and $Au_{20}(DPPM)_6(CN)_6$.[536] Based on $Au_{18}(DPPM)_6Br_4$, the authors doped up to 2 Ag heteroatoms at the position(s) linked to Br due to the stronger binding capability of Ag-Br, and produced $Au_{18-x}Ag_x(DPPM)_6Br_4$ (x = 1, 2).[536]

Zhu and co-workers reported $Au_9Ag_{12}(SR)_4(DPPM)_6X_6$ (SR = S-Adm or S-*t*Bu; X = Br or Cl) nanoclusters which contained an icosahedral Au_5Ag_8 kernel, and an $Au_4(DPPM)_4@Ag_4(SR)_4(DPPM)_2@X_6$ peripheral structure (Fig. 19f).[537] With different arrangements of the surface Au atoms, a pair of structural isomers was observed in the unit cell: chiral-Au_9Ag_{12} and achiral-Au_9Ag_{12}. As for the chiral Au_9Ag_{12}, the changeable $Au_4Ag_9@Au_4$ kernel-surface inter-linking modes led to the configurational transformation, responsible for the structural isomerism of this nanocluster. Furthermore, HPLC was used to separate the two enantiomers of the chiral-Au_9Ag_{12} nanocluster, and CD signals were observed.[537]

6.1.2 Au/Ag alloy nanoclusters of 25-50 metal atoms

In addition to $Au_1Ag_{24}(SR)_{18}$ containing an Au_1Ag_{12} kernel, Li *et al.* reported another Au_1Ag_{24} nanocluster that is co-protected by DPPM and S-*c*-C_6H_{11} ligands, namely, $Au_1Ag_{24}(DPPM)_3(SR)_{17}$ (Fig. 20a).[538] Compared with the standard icosahedral Au_1Ag_{12} kernel in $Au_1Ag_{24}(SR)_{18}$, $Au_1Ag_{24}(DPPM)_3(SR)_{17}$ has a distorted icosahedral Au_1Ag_{12} kernel (6 e), which is surrounded by an $Ag_{12}(DPPM)_3(SR)_{15}$ ring motif, and two μ_3 bridging thiolates.[538]

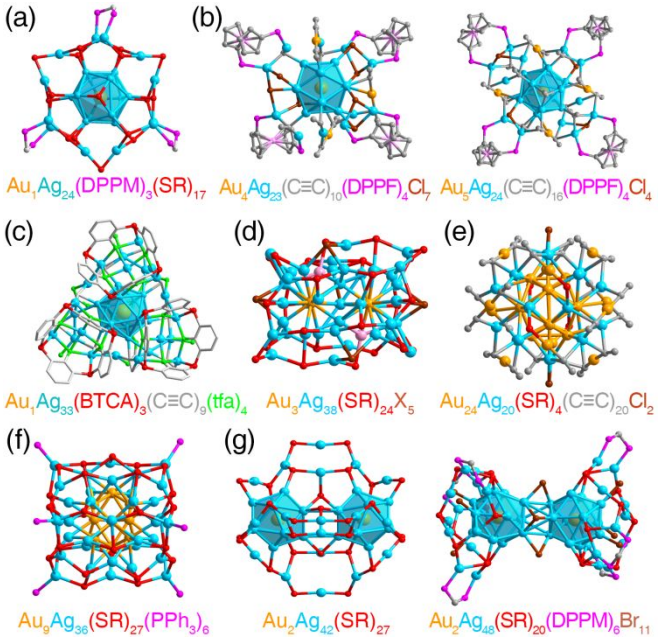

Fig. 20 Structures of Au/Ag alloy nanoclusters with metal atom number between 25 and 50, including (a) $Au_1Ag_{24}(DPPM)_3(SR)_{17}$; (b) $Au_4Ag_{23}(C\equiv C\text{-}^tBu)(DPPF)_4Cl_7$ and $Au_5Ag_{24}(C\equiv C\text{-}C_6H_4\text{-}p\text{-}^tBu)_{16}(DPPF)_4Cl_4$; (c) $Au_1Ag_{33}(BTCA)_3(C\equiv C^tBu)_9(tfa)_4(CH_3OH)_3$; (d) $Au_3Ag_{38}(S\text{-}CH_2Ph)_{24}X_5$; (e) $Au_{24}Ag_{20}(Spy)_4(C\equiv CPh)_{20}Cl_{12}$; (f) $Au_9Ag_{36}(S\text{-}PhCl_2)_{27}(PPh_3)_6$; (g) $Au_2Ag_{42}(S\text{-}Adm)_{27}$ and $Au_2Ag_{48}(S\text{-}^tBu)_{20}(DPPM)_6Br_{11}$.

The ligand effect on the alloying process has been investigated as well. Du *et al.* reported different alloying patterns of Au/Ag-C≡C-R nanoclusters bearing different R groups.[539] Two related nanoclusters with different sizes were synthesized by the same procedure, formulated as $Au_4Ag_{23}(C\equiv C\text{-}^tBu)(DPPF)_4Cl_7$ and $Au_5Ag_{24}(C\equiv C\text{-}C_6H_4\text{-}p\text{-}^tBu)_{16}(DPPF)_4Cl_4$.[539] Au_4Ag_{23} contains an icosahedral Au_1Ag_{12} kernel surrounded by an Au_3Ag_{11} shell, which is further capped by three types of ligands (Fig. 20b, left). As for Au_5Ag_{24}, the icosahedral Au_1Ag_{12} kernel is encircled by four Ag atoms, and further protected by an Au_4Ag_{12} shell (Fig. 20b, right).[539] The $Au_1@Ag_{12}$ kernels in these two nanoclusters agree again with the alloying mode in other silver-based nanoclusters that contain icosahedral M_{13} kernels.[69,70]

Zang and co-workers obtained crystal structures of $Ag_{34}S_2(S\text{-}Ch_2Ph)_{18}(CF_3COO)_9(DMF)_6$, which contained an $Ag_{13}@Ag_{21}$ core-shell configuration.[540] Doping this homo-silver nanocluster with $Au(PPh_3)Cl$ would substitute the central Ag atom with Au, whereas the other parts of the parent nanocluster were retained. In other words, the doped Au_1Ag_{33} nanocluster showed an Au_1Ag_{12}(kernel)@Ag_{21}(shell) configuration.[540]

Guan *et al*. reported the syntheses and structures of $Ag_{34}(BTCA)_3(C{\equiv}C^tBu)_9(tfa)_4(CH_3OH)_3$ and $Au_1Ag_{33}(BTCA)_3(C{\equiv}C^tBu)_9(tfa)_4(CH_3OH)_3$ (BTCA = *p*-tertbutylthiacalixarene; tfa = trifluoroacetate).[541] Both nanoclusters contain icosahedral M_{13} kernels (i.e., Ag_{13} kernel in Ag_{34} and Au_1Ag_{12} kernel in Au_1Ag_{33} with the Au heteroatom at the center), and the doping Au at the center provided an enhancement of stability to the nanocluster (Fig. 20c).[541]

Based on the $Ag_{40}(S\text{-}CH_2Ph\text{-}^tBu)_{22}(CH_3COO)_{10}$ nanocluster, two mono-Au-doped alloy nanoclusters, $Au_1Ag_{39}(S\text{-}CH_2Ph\text{-}^tBu)_{21}(CH_3COO)_{11}$ and $Au_1Ag_{39}(S\text{-}CH_2Ph\text{-}^tBu)_{20}(CH_3COO)_{12}$, have been synthesized and structurally determined.[542] These three nanoclusters possess a similar metal framework, albeit some of the thiolate ligands of Ag_{40} have been replaced by the introduced acetate ligand(s) in both Au_1Ag_{39} nanoclusters.[542] The thiolate-acetate exchangeable sites are located at the two poles of the nanocluster framework.[542]

$Au_3Ag_{38}(S\text{-}CH_2Ph)_{24}X_5$ (X = Cl/Br) features a face-fused bi-icosahedral rod-like $Au_2@Au_1Ag_{20}$ kernel, an $Ag_{18}(S\text{-}CH_2Ph)_{24}X_5$ shell, and two bare X atoms (Fig. 20d).[543] The bi-icosahedral Au_3Ag_{20} kernel is constituted by fusing two Au_2Ag_{11} icosahedral units at the M_3 plane, and the two centers of both icosahedrons are occupied by Au. In addition, the $Ag_{18}(S\text{-}CH_2Ph)_{24}X_5$ shell is formed by aggregating two $Ag_6(SR)_6$ units from two poles and one $Ag_6(SR)_2X_3$ unit at the equator.[543]

Wang *et al.* reported 2-Spy, PhC≡C, and Cl ligands co-protected $Au_{24}Ag_{20}$ with a concentric tri-stratified arrangement: Au_{12}(kernel)@Ag_{20}(shell)@Au_{12}(surface) (Fig. 20e).[544] On the surface, two types of motif structures are observed: Ag_5(shell)@$Au_1(PhC{\equiv}C)_2$(surface) and Ag_5(shell)@$Au_1(PhC{\equiv}C)_1(Spy)_1$(surface). The peripheral PhC≡C ligands were labile and thus, easy to be removed upon thermal treatments or be exchanged by other types of ligands; of note, in the ligand exchange processes, the metallic part was retained, rendering new derivatives with the same metallic configuration but different surface functionality.[544]

A 45-atom trigonal-prismatic Au/Ag nanocluster is reported by Huang *et al.*, formulated as $Au_9Ag_{36}(S\text{-}PhCl_2)_{27}(PPh_3)_6$, which follows an Au(kernel)@Ag(shell) configuration; in other words, the Au atoms make up a trigonal prismatic Au_9 kernel (Fig. 20f).[545] The Ag surface is comprised of a tricapped trigonal prismatic $Ag_{30}(SR)_{27}$ and six Ag-PPh_3 terminals. The distorted square face containing 13 Ag atoms is similar to a "FCC" structure, and within this FCC plane, all edges are bridged by thiol ligands except for three Ag-Ag edges; that is, three vacancies are generated. Two reasons are proposed to explain these "vacancies": (i) the steric hindrance of the peripheral thiolate ligands; (ii) the superatom electronic shell closing of $1S^21P^61D^{10}$.[545]

The $Au_{26}Ag_{22}(S\text{-}Ph\text{-}^tBu)_{30}$ nanocluster displays a Au_{12}(kernel)@Au_1Ag_{19}(1^{st} shell)@$Au_{13}(SR)_{26}$(2^{nd} shell)@$Ag_3(SR)_4$(surface) configuration.[546] The overall structure of $Au_{26}Ag_{22}$ exhibits a basket-like construction with a handle-like $Ag_3(SR)_4$ motif, and the $Au_{13}(SR)_{26}$ shell is comprised of 13 $Au_1(SR)_2$ monomeric staple motifs. The free valence electron of $Au_{26}Ag_{22}$ is 18e (26 + 22 - 30), following the closed-shell electronic structure.[546]

Ligand-protected nanoclusters bearing closed electronic shells have been considered as superatoms due to their noble-gas-atom-like valence electron configurations. Several nanoclusters with icosahedral kernels possess 8 free valence electrons, such as $[Au_{13}(PPh_3)_{10}Cl_2]^{3+}$, $[Au_{25}(SR)_{18}]^-$, $[Ag_{25}(SR)_{18}]^-$, and so on. Jin *et al.* reported two alloy nanoclusters bearing a dimer of 8-electron superatom units—$Au_2Ag_{42}(S\text{-}Adm)_{27}$ and $Au_2Ag_{48}(S\text{-}^tBu)_{20}(DPPM)_6Br_{11}$ (Fig. 20g).[547] Both nanoclusters show two independent icosahedral Au_1Ag_{12} kernels binding to each other. Specifically, Au_2Ag_{42} contains two Au_1Ag_{12} icosahedrons wrapped by an $Ag_{18}(S\text{-}Adm)_{27}$ shell consisting of three independent $Ag_6(S\text{-}Adm)_9$ motifs; as for Au_2Ag_{48}, the two independent Au_1Ag_{12} icosahedrons are central-enwrapped by five Br atoms, and each Au_1Ag_{12} unit is also capped by an $Ag_{12}(S\text{-}^tBu)_{10}(DPPM)_3Br_3$ integrate motif structure as well.[547] The free electron count of each nanocluster is 16, which doubles that of the single icosahedron. DFT calculations suggested that these icosahedral units (Au_1Ag_{12}) still retained the superatom feature after the superatom-superatom assembly. Consequently, the electronic structures of both Au_2Ag_{42} and Au_2Ag_{48} could be interpreted in terms of the dimerization of two 8-electron superatoms.[547]

6.1.3 Au/Ag alloy nanoclusters of more than 50 metal atoms

Wang *et al.* reported all-alkynyl-capped intermetallic $Au_{34}Ag_{28}$ nanocluster stabilized by 34 PhC≡C ligands.[548] The structure of $Au_{34}Ag_{28}$ follows a four-concentric configuration: Ag_1(center)@Au_{17}(1^{st}-shell)@Ag_{17}(2^{nd}-shell)@Au_{17}(motif) (Fig. 21a). The Au_{17} is stabilized by PhC≡C ligands, forming Ag-PhC≡C-Au-PhC≡C-Ag motifs. Similar to the $Au_{24}Ag_{20}(SPy)_4(PhC{\equiv}C)_{20}Cl_2$ alloy nanocluster, the PhC≡C ligands could be easily removed upon thermal treatments.[544,548] Thus, the catalytic activity of $Au_{34}Ag_{28}$ with or without ligands for hydrolytic oxidation of organosilanes to silanols were compared. Interestingly, it was observed for the first time that the nanoclusters with whole ligands were much higher in catalysis than those with surface ligands partially or completely removed.[548]

To investigate the function of different metals in specific positions, a series of correlated nanoclusters (*e.g.*, homo-gold, homo-silver, and Au/Ag alloy nanoclusters with abundant configurations) should be prepared and compared. Zhu and co-workers obtained $Au_{24}Ag_{46}(SR)_{32}$ and compared its catalytic performance with $Au_{25}(SR)_{18}$, $Ag_{44}(SR)_{30}$, and $Au_{12}Ag_{32}(SR)_{30}$.[549] The $Au_{24}Ag_{46}$ alloy nanocluster shows a multi-shell configuration: Ag_2(center)@Au_{18}(1^{st}-

shell)@Ag_{20}(2^{nd}-shell)@$Ag_{24}Au_6(SR)_{32}$(motifs) (Fig. 21b). Four types of motifs were observed on the surface, including $Ag_4(SR)_1$, $Ag_3(SR)_1$, $Ag_2Au_1(SR)_1$, and $Au_1(SR)_2$.[549] As the integrate structure has one C_3 and three C_2 symmetric axes as well as three σ_d planes, the point group of $Au_{24}Ag_{46}(SR)_{32}$ is D_{3d}. Interestingly, in terms of the styrene oxidization, surface Au atoms were determined to be capable of enhancing the conversions of the catalysis, while surface Ag atoms could enhance the selectivity of benzaldehyde.[549]

A large $Au_{80}Ag_{30}(C{\equiv}CPh)_{42}Cl_9$ alloy nanocluster with a concentric four-shell Russian doll arrangement is reported as well.[550] The innermost kernel is an octahedral Au_6, which is wrapped by the Au_{35} shell. The Au_6@Au_{35} is further surrounded by two more shells, forming the Au_6@Au_{35}@$Ag_{30}Au_{18}$@Au_{21} metal configuration (Fig. 21c). A total of 42 -C≡C-Ph and 9 μ_2-Cl ligands are clamping on the nanocluster surface, and three types of staple motifs, including Au_2Ag_2@Ph-C≡C-Au-C≡C-Ph, Au_2Ag_3@Ph-C≡C-Au-C≡C-Ph, and Au_1Ag_4@Ph-C≡C-Au-C≡C-Ph, are found. In a control experiment that no halide sources were added, only some small-sized nanoclusters could be detected, which proved the critical effect of chloride in the preparation of this large-sized alloy nanocluster. The point group of $Au_{80}Ag_{30}$ is D_{3d} (one C_3 symmetric axis, three C_2 symmetric axes, and three σ_d symmetric planes).[550] In their follow-up works, by changing the Ag precursors in the synthetic procedure of $Au_{80}Ag_{30}$, another large-sized $Au_{57}Ag_{53}(C{\equiv}CPh)_{40}Br_{12}$ nanocluster with different metal and ligand compositions was obtained.[551] Although the metal atom numbers in these two nanoclusters are the same, the metal arrangement of $Au_{57}Ag_{53}$ exhibits an Au_3Ag_2@Au_{34}@Ag_{51}@Au_{20} architecture. As the surface motifs in $Au_{57}Ag_{53}$ are much more complicated, the nanocluster displays an irregular structure with C_1 symmetry (Fig. 21d).[551]

The synthesis and the structure of $Au_{130-x}Ag_x(SR)_{55}$ (x ~ 98; SR = SPh^{t}Bu) have been reported.[552] The overall structure of $Au_{130-x}Ag_x$ comprises a decahedral M_{54} (M = Au/Ag) core. In this regular M_{54} decahedron, all of the ~32 Au atoms are localized in the truncated M_{49} Marks decahedron, whereas the five corners of the M_{54} decahedron comprise 100% Ag atoms. The truncated M_{49} Marks decahedron contains an Ag-rich $Au_{5.8}Ag_{11.2}$ tetrahedral core that is capped by an Au-rich $Au_{26.8}Ag_{5.2}$ hollow cage. The obtained M_{49} decahedron is further capped by a shell of Ag_{65} with overall D_{5h} symmetry and 16 outermost Ag. In this context, the overall structure of $Au_{130-x}Ag_x(SR)_{55}$ follows an $(AuAg)_{49}$@$Ag_{81}(SR)_{55}$ core-shell configuration.[552]

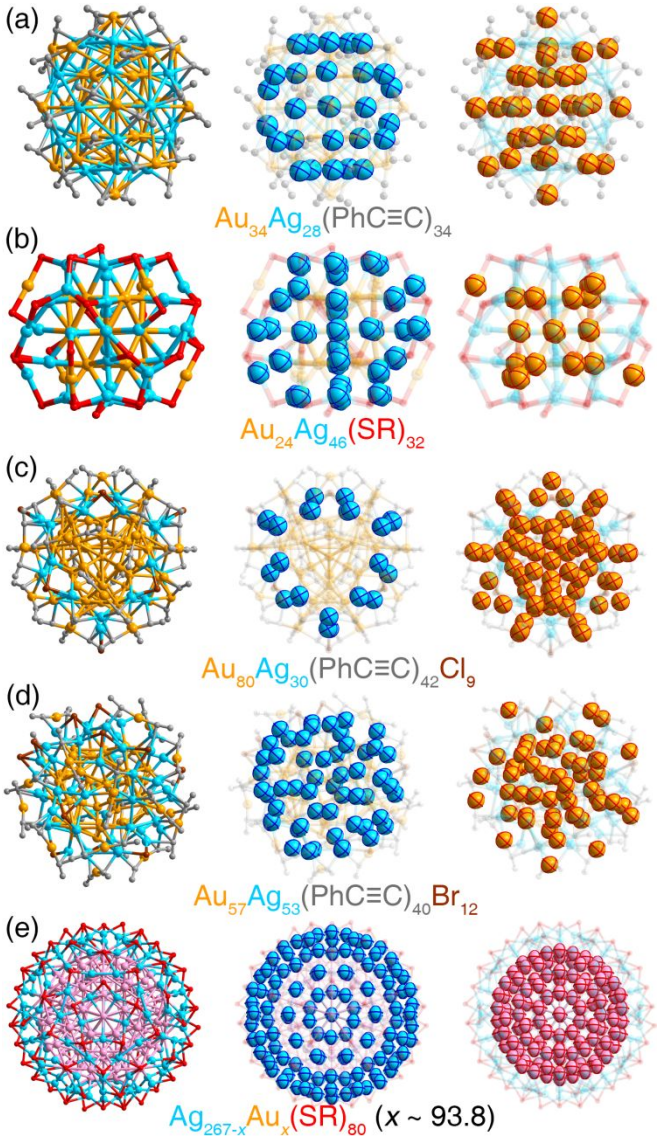

Fig. 21 Structure of Au/Ag Alloy nanoclusters with metal atom number larger than 50, inlcuding (a) $Au_{34}Ag_{28}(PhC{\equiv}C)_{34}$ and its Au and Ag arrangements; (b) $Au_{24}Ag_{46}(S^tBu)_{32}$ and its Au and Ag arrangements; (c) $Au_{80}Ag_{30}(C{\equiv}CPh)_{42}Cl_9$ nanocluster and its Au and Ag arrangements; (d) $Au_{57}Ag_{53}(C{\equiv}CPh)_{40}Br_{12}$ nanocluster and its Au and Ag arrangements; (e) $Ag_{267-x}Au_x(SPhMe_2)_{80}$ (x ~93.8) and its mixed Au/Ag and Ag arrangements.

In 2018, Yan *et al.* reported $Ag_{267-x}Au_x(SR)_{80}$ (x ~93.8), which is the largest alloy nanocluster to date.[553] Owing to its large size, $Ag_{267-x}Au_x$ displays metallic behavior (e.g. plasmon excitation). It contains a concentric icosahedral structure — Ag_1(center)@M_{12}(1^{st}-shell)@M_{42}(2^{nd}-shell)@M_{92}(3^{rd}-shell)@$Ag_{120}(SR)_{80}$(cage) (M = Au or Ag, see Fig. 21e). Of note, the Ag_1@M_{12}@M_{42}@M_{92} kernel is a M_{147} icosahedron, which is similar to the kernel in the $Pd_{165-x}Pt_x(CO)_{72}(PPh_3)_{20}$ nanocluster.[554] In addition, a regular triangle-tetragon-pentagon interlaced arrangement is observed on the surface. The surface Ag atoms are anchored with thiolates *via* two modes, i.e. Ag_3 triangle@SR and Ag_4 tetragon@SR.[553] Of note,

in the unit cell, another medium-sized $Au_9Ag_{36}(SR)_{27}(PPh_3)_6$ is observed (Fig. 21f), of which the structure is similar to that of previously reported Au_9Ag_{36}, albeit with some difference in peripheral ligands.[545,553] Compared with $Ag_{267-x}Au_x(SR)_{80}$, Au_9Ag_{36} has an 18-electron shell closing, a notable HOMO-LUMO energy gap, and molecule-like optical absorption. Such a co-crystallization is meaningful (Fig. 21g), and the interactions between the methyl group on $Ag_{267-x}Au_x(SR)_{80}$ and the benzene ring of PPh_3 ligands o $Au_9Ag_{36}(SR)_{27}(PPh_3)_6$ are proposed to play a predominant role in the nanocluster assembly in crystals.[553]

6.2 Au/Cu alloy nanoclusters

Introduing heterometals into the nanocluster is of importance to prepare new nanoclusters with novel structures and intriguing properties. For example, comparing the M-SR bonding modes between $Au_{25}(SR)_{18}$ and $Ag_{25}(SR)_{18}$, the Au-SR bonding in $Au_{25}(SR)_{18}$ is a linear type for $Au_2(SR)_3$ motifs, whereas the μ_3-Ag (one Ag binds to three thiolates) is observed in $Ag_{25}(SR)_{18}$. One may wonder what binding mode of Cu-ligand will be, similar or different with those of Au-ligand or Ag-ligand binding? Consequently, Au/Cu and Ag/Cu alloy nanoclusters would hopefully show novel structures comparing to homo-Au, homo-Ag, and bi-metallic Au/Ag nanoclusters. In the following two sections, selective Au/Cu and Ag/Cu nanoclusters with specific structures are reviewed (and also see Table 8 for a summary of Au/Cu alloy nanoclusters), as a supplement to sections 4.2 and 4.3.

Table 8 Au/Cu alloy nanoclusters (sorted by metal kernel size, from small to large).

Formula	Ref(s)
Au_2Cu_6(S-Adm)$_6(PPh_3)_2$	555,556
Au_4Cu_4(S-Adm)$_5$(DPPM)$_2$	557
$Au_1Cu_{12}(S_2CN^nBu_2)_6(C{\equiv}CPh)_4$	518
$Au_{13}Cu_2(PPh_3)_6(Spy)_6$	507
$Au_{13}Cu_2(DPPP)_3(Spy)_6$	508
$Au_{13}Cu_2(PPh_3)_6(SC_2H_4Ph)_6$	509
$Au_{13}Cu_4(PPh_2py)_4(SPh^tBu)_8$	507
$Au_{13}Cu_4(PPh_2py)_3(SePh)_9$	510
$Au_7Cu_{12}(PPh_2py)_6(SPh^tBu)_6Br_4$	558
$Au_{20}Cu_1(S^tBu)_{15}$	276
$Au_{21-x}Cu_x(S^tBu)_{15}$	276
$Au_{13}Cu_8(Spy)_{12}$	507
$Au_{23-x}Cu_x(S\text{-}c\text{-}C_6H_{11})_{16}$	283
$Au_1Cu_{24}H_{22}(PPh_3)_{12}$	560
$Au_1Cu_{24}H_{22}(P(p\text{-}FPh)_3)_{12}$	560
$Au_{24}Cu_6(SPh^tBu)_{22}$	561
$Au_{12}Cu_{32}(SPhCF_3)_{30}$	511
$Au_{14}Cu_{32}(SPhCF_3)_{32}$	511
$Au_{16}Cu_{32}(SPhCF_3)_{34}$	511
$Au_{19}Cu_{30}(C{\equiv}C\text{-}3\text{-}S\text{-}C_4H_3)_{22}(Ph_3P)_6Cl_2$	562
$Au_{18}Cu_{32}(SPhCF_3)_{36}$	511
$Au_{52}Cu_{72}(SPh^pMe)_{55}$	646

By exploiting the aggregation-induced emission (AIE) concept, non-luminescent Cu(I)-SR complexes are self-assembled by Au(0) to produce highly luminescent $Au_2Cu_6(SR)_6(PPh_3)_2$ nanocluster (Fig. 22a).[555,556] Au_2Cu_6 contains two free electrons and is indeed the smallest Au/Cu nanocluster. Structurally, a total of six Cu(I)-SR complexes are assembled into a hexagon with two gold atoms, and these two Au(0) are further stabilized by PPh_3 ligands. One C_3, three C_2 axes, three mirror planes (σ_d), and one symmetric center (i) can be found in the nanocluster, giving D_{3d} symmetry.[555,556] Using DPPM instead of PPh_3 in the synthesis could give rise to $Au_4Cu_4(SR)_5(DPPM)_2$ (Fig. 22b), which comprises an Au_4P_4 kernel, and a perpendicular $Cu_4(SR)_5$ ring.[557] Significantly, there are four isomers in the crystal lattice of Au_4Cu_4.[557]

By reducing the Au/Cu-SR-PPh_2py complexes (SR = S-Ph^{t}Bu) with $NaBH_4$, Song *et al*. obtained an alloyed $Au_7Cu_{12}(PPh_2py)_6(SR)_6Br_4$ nanocluster (Fig. 22c), containing a ring-like Au_7Cu_6 kernel in the middle, and two "hat-like" Cu_3-based motifs with four Br atoms from top and bottom.[558]

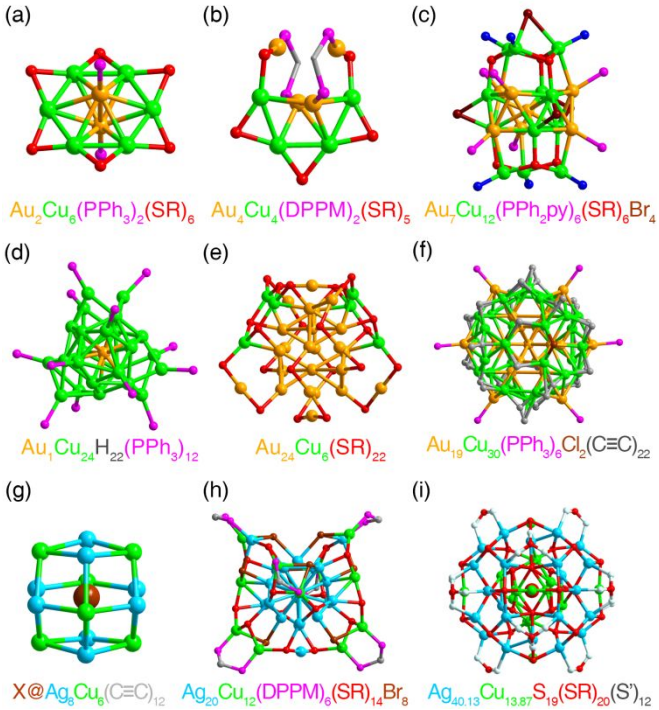

Fig. 22 Structures of Au/Cu and Ag/Cu alloy nanoclusters. (a) Au_2Cu_6(S-Adm)$_6(PPh_3)_4$; (b) Au_4Cu_4(S-Adm)$_5$(DPPM)$_2$; (c) $Au_7Cu_{12}(PPh_2py)_6(SPh^tBu)_6Br_4$; (d) $Au_1Cu_{24}H_{22}(PPh_3)_{12}$; (e) $Au_{24}Cu_6(SPh^tBu)_{22}$; (f) $Au_{19}Cu_{30}(C{\equiv}CR)_{22}(Ph_3P)_6Cl_2$; (g) $X@Cu_6Ag_8(C{\equiv}CR)_{12}$; (h) $Ag_{20}Cu_{12}$(S-Adm)$_{14}$(DPPM)$_6Br_8$; (i) $Ag_{40.13}Cu_{13.87}S_{19}(S^tBu)_{20}(^tBuSO_3)_{12}$.

Hayton and co-workers reported $Cu_{25}H_{22}(PPh_3)_{12}$ with partial Cu(0) character, containing an icosahedral Cu_{13} kernel stabilized by four $[Cu(PPh_3)]_3$ capping motifs and 22 hydride ligands.[559] In 2019, Chen *et al*. successfully substituted the center with Au heteroatom, producing $Au_1Cu_{24}H_{22}(PPh_3)_{12}$ with a maintained overall structure (Fig. 22d).[560] The peripheral PPh_3 ligands of the nanoclusters can be altered to

(p-FPh)$_3$P ligand, yielding $Cu_{25}H_{22}(P(p\text{-}FPh)_3)_{12}$ and $Au_1Cu_{24}H_{22}(P(p\text{-}FPh)_3)_{12}$, respectively.[560]

Chai *et al*. synthesized and structurally determined a 30-nuclei Au/Cu bi-metallic $Au_{24}Cu_6(SPh^tBu)_{22}$ (Fig. 22e).[561] Six copper atoms are found to exclusively occupy the surface shoulder sites to form two planar $Cu_3(SR)_3$ motifs reminiscent of benzene rings on each side. Indeed, the π conjugation within this planar motif plays a pivotal role in catalyzing the ring-opening reaction.[561]

Larger Au/Cu alloy nanocluster—$Au_{19}Cu_{30}(C{\equiv}CR)_{22}(Ph_3P)_6Cl_2$ (Fig. 22f) was reported by the Wang group in 2017.[562] Alkynyl ligands are arranged on the surface, mainly protecting the exposed Cu atoms, and the $Au_{19}Cu_{30}$ shows a multi-shell structure as $Au_1@Au_{12}@Cu_{30}@Au_6$. The outermost six Au atoms constitute a chair-like hexagonal configuration, which is further stabilized by the PPh_3 ligands. Moreover, interfacial structure between Cu and alkynyl ligands follows the μ_3 bridging modes, which is distinctly different from those in Au-alkynyl and Au/Ag-alkynyl nanoclusters.[562]

6.3 Ag/Cu alloy nanoclusters

Early in 2011, Williams and co-workers reported the synthesis of $Cl@Ag_{14}$ cluster compound (all metals are with +1 charge state) and its Cu-doped $Cl@Ag_{14-x}Cu_x$ (x up to six) counterparts. A reversible process between $Cl@Ag_{14}$ and $Cl@Ag_{14-x}Cu_x$ could be expressed as $Cl@Ag_{14} + x\ Cu^+ \rightarrow Cl@Cu_xAg_{14-x} + x\ Ag^+$ and $Cl@Cu_xAg_{14-x} + x\ Ag^+ \rightarrow Cl@Ag_{14} + x\ Cu^+$.[563] The crystal structure of $Cl@Cu_6Ag_8$ was determined two years later,[564] in which the metallic kernel featured a rhombic dodecahedron (Fig. 22g).

$[Ag_{20}Cu_{12}(SR)_{14}(DPPM)_6Br_8]^{2+}$ (where SR = S-Adm) is reported by Zou *et al.*, which consists an Ag_{17} kernel capped by an $Ag_3Cu_{12}(SR)_{14}(DPPM)_6Br_8$ cage (Fig. 22h).[565] The cage is assembled by two $Ag_1Cu_6(SR)_7(DPPM)_3Br_4$ *via* an Ag atom, and each $Ag_1Cu_6(SR)_7(DPPM)_3Br_4$ is composed of a $Cu_2(SR)_3(DPPM)Br$ and an $Ag_1Cu_3(SR)_4(DPPM)_2Br_3$ linked by a Cu atom. Similar to $Ag_{28}Cu_{12}$, all Cu atoms are selectively incorporated on the surface. By comparing the structures of $Ag_{20}Cu_{12}$, $Ag_{32}(DPPE)_5(SR)_{24}$ and $Ag_{32}(DPPM)_5(S\text{-}Adm)_{13}Cl_8$, the authors investigated the ligand and metal effects on the structures of nanoclusters.[565-567]

By using multiple types of protected ligands including bare S atom, *tert*-butyl thiolate, and *tert*-butyl sulfonate, Yang *et al.* obtained $Ag_{40.13}Cu_{13.87}S_{19}(t\text{BuS})_{20}(t\text{BuSO}_3)_{12}$ which exhibited a $Cu_{10}Ag_2S_7$ kernel capped by a $M_{42}(t\text{BuS})_{20}(t\text{BuSO}_3)_{12}$ (M_{42} contained 3.87 Cu and 38.13 Ag atoms) cage and twelve bare S atoms (Fig. 22i).[568] There are several symmetric elements based on the structure of $(AgCu)_{54}$, demonstrating the high symmetry of this alloy nanocluster.[568]

In conclusion, several Au/Cu and Ag/Cu alloy nanoclusters have been reported, reflecting different metal arrangements and metal-ligand interface structures, and structure-determined properties compared to the homo-gold, homo-silver, and bi-metallic Au/Ag nanoclusters. However, compared with Au/Ag alloy nanoclusters that have been extensively investigated, the research on Au/Cu is less, and Ag/Cu is even less. Future work may pay more attention to such alloys.

6.4 Alloy nanoclusters with other metals (Pd/Pt/Cd)

In addition to the alloy nanoclusters composed of Au/Ag/Cu (elements of group 11), other metals from 10 and 12 groups, e.g. Pd/Pt/Cd, can be alloyed with these 11 group elements as well, forming new structures based on different alloying modes. In this section, we highlight some literature works, with a focus on the similarities and differences in structures and other characteristics.

Yang *et al.* obtained the crystal structures $Cd_1Au_{14}(SR)_{12}$ (SR = S^{t}Bu) and predicted the structure of $Au_{15}(SR)_{12}^-$ and $Au_{15}(SR)_{13}$ nanoclusters by DFT calculation.[569] So far, the structure of this small Au-SR nanocluster—$Au_{15}(SR)_{13}$ with 2-electron—is still not accessible.[570-573] As for Cd_1Au_{14}, its Cd_1Au_5 kernel, which is constituted by combining two Cd_1Au_3 tetrahedrons at the Cd-Au edge, is capped by two $Au_4(SR)_5$ tetrameric staple motifs and one $Au_1(SR)_2$ monomeric staple motif (Fig. 23b).[569]

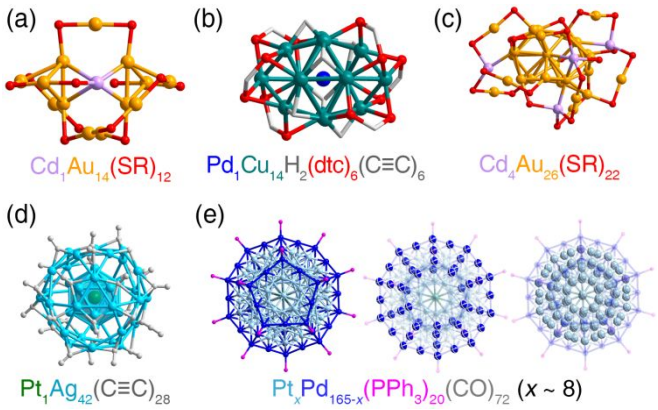

Fig. 23 Structures of Pd/Pt/Cd-contained alloy nanoclusters. (a) $Cd_1Au_{14}(S^tBu)_{12}$; (b) $Pd_1Cu_{14}H_2(dtc/dtp)_6(C{\equiv}CPh)_6$; (c) $Au_{26}Cd_4(S\text{-}c\text{-}C_6H_{11})_{22}$; (d) $Pt_1Ag_{42}(C{\equiv}C\text{-}C_6H_4CH_3)_{28}$; (e) $Pd_{165-x}Pt_x(CO)_{72}(PPh_3)_{20}$ and its Pt and Pd arrangements.

By reacting poly-hydrido copper clusters $Cu_{28}H_{15}(dtc)_{12}$ or $Cu_{20}H_{11}(dtp)_9$ with phenyl acetylene in the presence of $Pd(PPh_3)_2Cl_2$, Chakrahari *et al*. obtained two Cu-rich bi-metallic nanoclusters—$Pd_1Cu_{14}H_2(dtc/dtp)_6(C{\equiv}CPh)_6$ (dtc = $S_2CN^nBu_2$; dtp = $S_2P(O^iPr)_2$).[574] SC-XRD demonstrated that the introduced Pd heteroatom was at the center of the $Pd_1H_2Cu_{14}$ kernel in both nanoclusters, displaying the highest coordination number (14) so far recorded (Fig. 23c). Each H atom in the nanocluster was connected to one Pd^0 and four Cu^I atoms in a slightly distorted trigonal bipyramidal geometry.[574]

Alloying the $Au_{34}(SR)_{22}$ nanocluster (SR = S-c-C_6H_{11}) with $Cd(NO_3)_2$ produces $Au_{26}Cd_4(SR)_{22}$, which comprises a distorted FCC Au_{16} kernel capped by two "paw-like" $Cd_1(SR\text{-}Au\text{-}SR)_3$ motifs, one pentameric $Au_3Cd_2(SR)_8$ motif and one monomeric $Au_1(SR)_2$ motif (Fig. 23d).[575] Owing to the presence of Cd heteroatoms, one monomeric $Au_1(SR)_2$ motif and one trimeric $Au_3(SR)_4$ motif merge into a new pentameric

$Au_3Cd_2(SR)_8$ motif.[575] A dealloying process was observed in $Au_{26}Cd_4(SR)_{22}$ — the addition of Au(I)-SR induced a reversible process and $Au_{26}Cd_4(SR)_{22}$ transformed back to the parent $Au_{34}(SR)_{22}$ nanocluster, while $Au_{18}(SR)_{14}$ was obtained in the presence of Pd(II)-$(SR)_2$.[575]

By changing the feeding Pt/Ag procedures in the synthesis of Pt_5Ag_{22}, Shen and Mizuta obtained $Pt_1Ag_{42}(C{\equiv}C\text{-}C_6H_4CH_3)_{28}$ nanocluster (8e), containing an icosahedral Pt_1Ag_{12} kernel and an $Ag_{30}(C{\equiv}CR)_{28}$ shell (Fig. 23e).[576] Such a Pt_1Ag_{12} kernel is the same as that in other Pt-alloyed Ag nanoclusters, such as $Pt_1Ag_{24}(SR)_{18}$, $Pt_1Ag_{28}(S_2R)_{12}(PPh_3)_4$, and $Pt_2Ag_{23}(PPh_3)_{10}Cl_7$. Among the 28 alkynyl ligands, 12 of them are not only linked to the Ag on the shell but also bonded to Ag on the icosahedron. In addition, SC-XRD also demonstrated the interactions between SbF_6^- ions and Ag atoms on the kernel shell (*via* Ag-F bonds), representing a unique penetrability of the Ag_{30} shell. All these unique interactions result in the high stability of this Pt/Ag alloy nanocluster.[576]

Early in 2007, a large Pt/Pd alloy nanocluster co-protected by CO and PPh_3 ligands was reported, formulated as $Pd_{165-x}Pt_x(CO)_{72}(PPh_3)_{20}$ (x ~8).[554] The innermost kernel is an icosahedral μ_{12}-Pt@$Pd_{12-x}Pt_x$ (x ~1.2), which is wrapped by an icosahedral $Pd_{42-x}Pt_x$ (x ~3.5) shell, and then a 60-atom semi-regular icosahedral $Pd_{60-x}Pt_x$ shell (x ~2.2) (Fig. 23f). The outermost part is a dodecahedral Pd_{50} cage with 20 PPh_3 ligands attached onto it, and the CO ligands bonding to $Pd_{60-x}Pt_x$ and Pd_{50} are symmetrically arranged.[554] Of note, except for the M_{165} nanocluster, several other alloy nanoclusters co-stabilized by phosphine and C-based ligands have been reported, including $Au_4Pd_{32}(CO)_{28}(PMe_3)_{14}$ and $Cu_{43}Al_{12}(C_5Me_5)_{12}$.[577,578] Thus, the combination of C-based and phosphine ligands may generate new alloy nanoclusters that exhibit novel structures and compositions compared with those protected by thiolate ligands.

6.5 Alloy nanoclusters with predicted structures

The aforementioned alloy nanoclusters exhibit explicit atomically precise structures. Besides, there are some more alloy nanoclusters without solved structures, albeit their structures are proposed by DFT calculations. Sarkar *et al.* identified $[Ag_5Pd_4(Se\text{-}Ph)_{12}]^-$ by ESI-MS and MS-MS measurements.[579] Based on the previously reported Ag_7 and Ag_8 clusters, Pradeep and co-workers added Au into the solution of such homo-silver clusters and obtained a 13-atom Au_6Ag_7 cluster according to ESI-MS analysis.[580,581] Hasegawa *et al.* reported the poly(*N*-vinyl-2-pyrrolidone) (PVP) stabilized homo-gold Au nanoclusters and alloyed them with Pd or Rh heteroatoms, such as $Au_{43}Pd_1$, $Au_{33}Pd_1$, $Au_{19}Pd_1$, and $Au_{34}Rh_1$, which all displayed enhanced catalytic activities relative to homo-gold nanoclusters.[582,583]

In 2019, Aikens and co-workers investigated the optimal structures of mono-doped M_1Au_{24}, M_1Ag_{24} and M_1Au_{37} (M = Ni, Pd, Pt, Cu, Ag/Au, Zn, Cd, Hg, Ga, In and Tl) nanoclusters.[584] For all clusters, the group 10 dopants (Ni, Pd, and Pt) prefer to occupy the center due to the relative stability of d electrons in these dopants. For dopants from groups 11-13, doping on the kernel shell or in the staple motifs becomes thermodynamically more preferable as a result of symmetry-dictated coupling between dopant atomic orbitals and super-atomic levels as well as because of the relativistic contraction of s and p orbitals.[584] These calculations indicate that alloy nanoclusters have higher stability and intriguing chemical/physical properties, which might guide the experimental syntheses of alloy nanoclusters with enhanced performances.

6.6 Alloying on phosphine-stabilized cluster compounds with hyper-coordinated carbon

Most of the alloy nanoclusters summarized above contain free electrons (electron count $n^* = N - M - z$, where N is the number metal atoms, M is the number of electron-localizing ligands, and z is nanocluster overall charge).[199] Besides, Wang *et al*. reported several alloy cluster compounds based on the C@Au_6 nanoclusters — these complexes contain no free electrons, but are composed of metal cores and peripheral ligands, and thus described as metal cluster compounds.[585-594] In this section, these cluster compounds are reviewed. Of note, along with the coordination of such heteroatoms (Ag or Cu), the parent (C@Au_6) displays significant changes in luminescence, which will be discussed in Section 7.1.2.

By altering the PPh_3 ligands to PPh_2py, a total of six N coordination sites are introduced in C-PPh_2py@Au_6 template, and consequently, the introduced Ag^+ ions will bond to the surface, generating C-PPh_2py@Au_6Ag_2 (Fig. 24, upper-right).[586] Due to the high emission, C-PPh_2py@Au_6Ag_2 has been used to light up the nucleolus of living cells (see Section 8.3 for more details).[587-589] Wang and co-workers further introduced aldehydes or carboxyls into the ligands of C@Au_6Ag_2, and obtained several new C-Au_6Ag_2 with different surface structures.[590,591] Besides, adding Cu^I salts into the solution of C-PPh_2py@Au_6 produces C-PPh_2py@Au_6Cu_2 alloy, and the coordination situation of Cu is the same as that of Ag in Au_6Ag_2 (i.e., each Cu links to three N atoms on ligands and three Au atoms; see Fig. 24, bottom-right).[592]

Lei *et al.* assembled these nanoclusters *via* intra-connection mode into cluster-based MOFs.[593] By using mdppz ligand (2-(3-methylpyrazinyl)-diphenylphosphine) in place of PPh_2py in C-PPh_2py@Au_6Ag_2, C-mdppz@Au_6Ag_6 emerged. Of note, each mdppz ligand contains two N donors: one inward and one outward. As for C-mdppz@Au_6Ag_6, the inward N donors are employed by the two Ag heteroatoms, whereas the outward N donors are "free" (Fig. 24, upper-left).[593] In the follow-up work, Lei *et al.* introduced more inward N donors on the phosphine ligand by altering PPh_2py into $PPhpy_2$, and then anchored more Ag heteroatoms on the nanocluster surface.[594] By stepwise anchoring Ag heteroatoms on the C-$PPhpy_2$@Au_6 surface, C-$PPhpy_2$@Au_6Ag_4 and C-$PPhpy_2$@Au_6Ag_6 alloy cluster compounds were generated.[594] SC-XRD demonstrated that the surface structure of $PPhpy_2$@Au_6Ag_6 was extremely compact, indicating the high rigidity of this nanocluster, and the rigidity further resulted in the strong PL of $PPhpy_2$@Au_6Ag_6 (PL QY of 92%).[594]

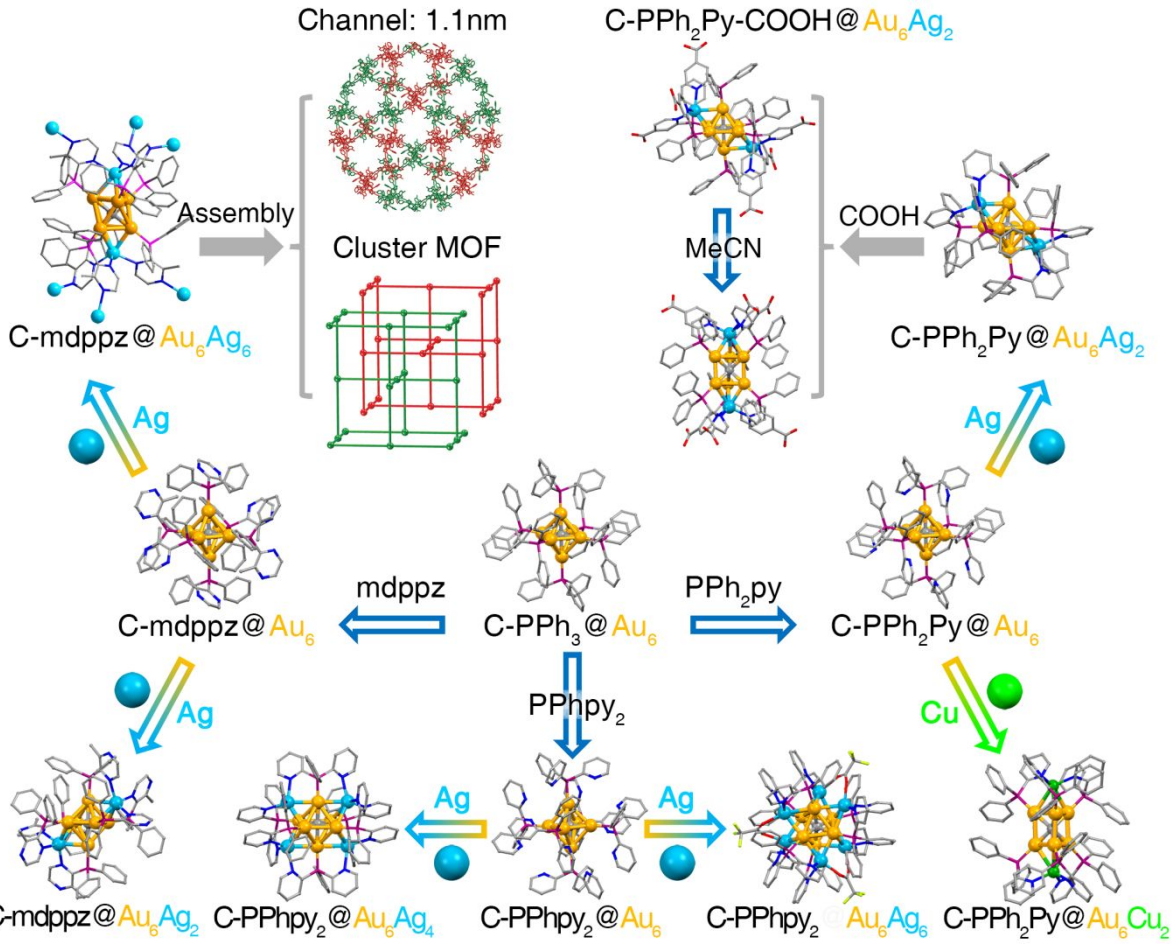

Fig. 24 Alloying based on gold(I) cluster compounds with hyper-coordinated carbon. Crystal structures include C@Au_6, C@Au_6Ag_2, C@Au_6Cu_2, C@Au_6Ag_4, and C@Au_6Ag_6 cluster compounds.

7 Properties of Alloy Nanoclusters

Compared with nanoparticles of large sizes, metal nanoclusters display several glamorous characteristics: atomically precise structures, quantum size effects, and discrete electronic states. The first characteristic enables us to grasp the structural evolution from metal complexes to plasmonic metal nanoparticles. The latter two characteristics endow the nanoclusters with size- or structure-dependent properties. The combination of the these characteristics pinpoint the precise correlations between the structures and properties of nanoclusters, which are of great significance not only because they can help us to figure out the mechanisms/originates of the intriguing properties, but can also be served as guidelines in customizing the nanoclusters (or other nanomaterials) with desired performances. Alloying has been served as a versatile method in tailoring the chemical and physical properties of nanoclusters. Based on the atomically precise structures of these alloy nanoclusters, several efforts have been made to figure out the alloying effects (so-called synergistic effects) on the properties of nanoclusters. In this section, the reported alloying-induced property variations are classified into five aspects, including (i) optical properties (optical absorptions and photoluminescence), (ii) electrochemical properties, (iii) electroluminescence properties, (iv) magnetic properties, (v) chiral properties, and (vi) stability and reactivity. Of note, the catalytic properties and the corresponding works will be reviewed in Section 8.1 (applications of alloy nanoclusters).

7.1 Optical properties

The structure and composition of nanoclusters are decisive to their physical/chemical properties. The optical properties are the most studied due to their significance in applications such as chemical sensing and biological imaging. Alloying alters the metal composition of nanoclusters, and may further affect their geometric/electronic structures, as reflected in the different optical properties. In this section, the alloying effects on the optical properties are reviewed.

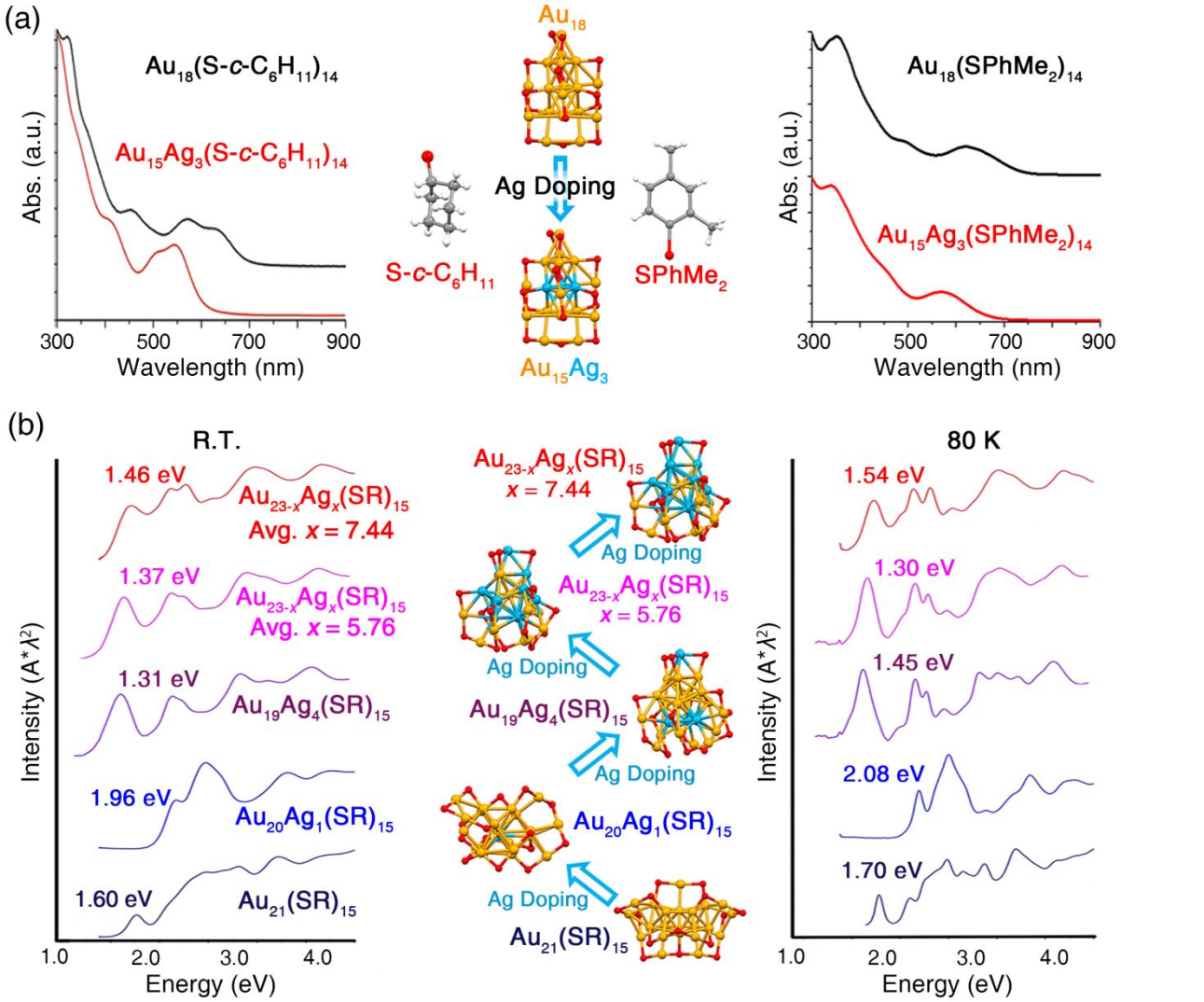

Fig. 25 Doping-induced variations in optical absorptions of Au_{18} and Au_{23} nanoclusters. (a) Optical absorptions of $Au_{18}(SR)_{14}$ and $Au_{15}Ag_3(SR)_{14}$. Redrawn from ref. 267 with permission from The Royal Society of Chemistry, copyright 2015. Redrawn from ref. 256 with permission from Wiley-VCH, copyright 2017. (b) Optical absorptions of $Au_{21}(SR)_{15}$, $Au_{20}Ag_1(SR)_{15}$, $Au_{19}Ag_4(SR)_{15}$, $Au_{23-x}Ag_x(SR)_{15}$ (avg. x = 5.76) and $Au_{23-x}Ag_x(SR)_{15}$ (avg. x = 7.44) at room temperature or 80 K. Redrawn from ref. 279 with permission from American Chemical Society, copyright 2018.

7.1.1 Optical absorption

The absorption spectrum of $Au_{18}(S\text{-}C_6H_{11})_{14}$ shows three bands at 445, 570, and 630 nm, whereas that of doped $Au_{15}Ag_3(S\text{-}C_6H_{11})_{14}$ centers at 400, 505, and 545 nm (Fig. 25a, left).[267] As for S-$PhMe_2$ capped Au_{18} nanocluster, Ag-doping also blue-shifts the absorption peak from 625 nm of $Au_{18}(S\text{-}PhMe_2)_{14}$ to 566 nm of $Au_{15}Ag_3(S\text{-}PhMe_2)_{14}$ (Fig. 25a, right).[256] These blue-shifts illustrate that the incorporation of Ag heteroatoms can interfere with the electronic structure and affect the overall optical absorption of $Au_{18}(SR)_{14}$ nanoclusters.[256,267] Based on the precise system, the correlations between structure and properties are investigated.[256,267] Optically, the remarkable blue-shifts (cal. 70 nm in HS-C_6H_{11} stabilized system, and 60 nm in HS-$PhMe_2$ stabilized system) are observed,[256,267] and accompanied by Ag doping, the HOMO-LUMO gap of Au_{18} nanoclusters significantly decreases.

Similar to $M_{18}(SR)_{14}$, Ag-alloying induced structure transformation is responsible for the energy gap (E_g) enlargement in $Ag_1Au_{20}(SR)_{15}$ (1.60 eV at room temperature and 1.96 eV at 80 K) compared to $Au_{21}(SR)_{15}$ (1.70 eV at room temperature and 2.08 eV at 80 K).[279] As for the $Au_{23-x}Ag_x(SR)_{15}$ nanoclusters, E_g continues to increase with higher Ag-doping extent (Fig. 25b): at room temperature, the 1.31 eV E_g of $Au_{19}Ag_4(SR)_{15}$ increases to 1.37 eV of $Au_{23-x}Ag_x(SR)_{15}$ (avg. x = 5.76), then to 1.46 eV of $Au_{23-x}Ag_x(SR)_{15}$ (avg. x = 7.44); while at 80 K, the 1.45 eV E_g of $Au_{19}Ag_4(SR)_{15}$ increases to 1.50 eV of $Au_{23-x}Ag_x(SR)_{15}$ (avg. x = 5.76), then to 1.54 eV of $Au_{23-x}Ag_x(SR)_{15}$ (avg. x = 7.44).[279]

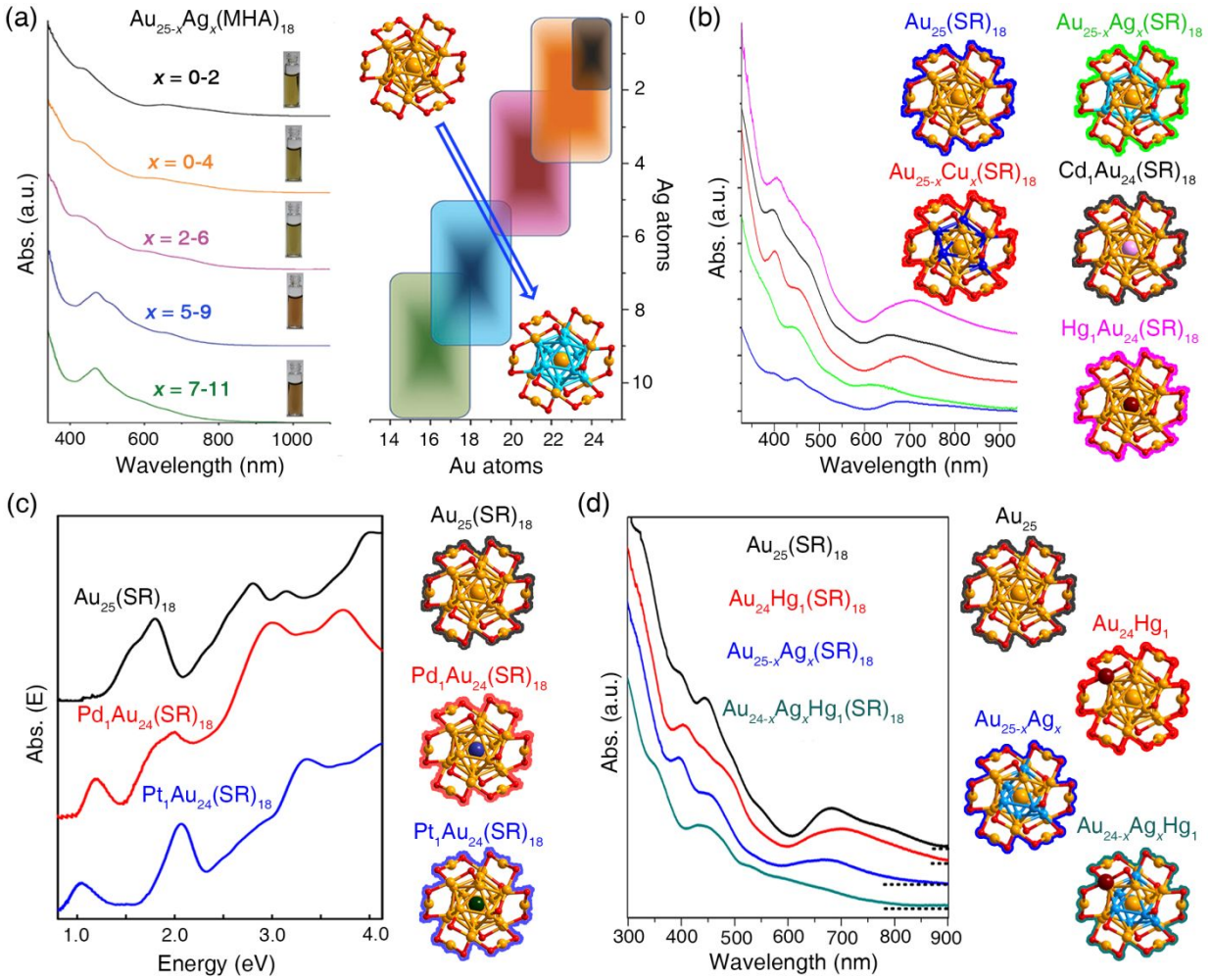

Fig. 26 Doping-induced variations in optical absorptions of spherical Au_{25} nanoclusters. (a) Optical absorptions of $Au_{25-x}Ag_x(MHA)_{18}$. Redrawn from ref. 182 with permission from The Royal Society of Chemistry, copyright 2014. (b) Optical absorptions of $Au_{25}(SC_2H_4\text{-}Ph)_{18}$ and its Ag-, Cu-, Cd-, Hg-doped nanoclusters. Redrawn from ref. 174 with permission from American Chemical Society, copyright 2015. (c) Optical absorptions of $Au_{25}(SC_2H_4\text{-}Ph)_{18}$ and its Pd- and Pt-doped nanoclusters. Redrawn from ref. 211 with permission from American Chemical Society, copyright 2015. (d) Optical absorptions of mono-metallic $Au_{25}(SC_2H_4\text{-}Ph)_{18}$, bi-metallic $Au_{25-x}Ag_x(SC_2H_4\text{-}Ph)_{18}$ and $Au_{24}Hg_1(SC_2H_4\text{-}Ph)_{18}$, and tri-metallic $Au_{24-x}Ag_xHg_1(SC_2H_4\text{-}Ph)_{18}$ nanoclusters. Redrawn from ref. 521 with permission from American Chemical Society, copyright 2016.

Xie and co-workers controlled the Ag-doping extent based on the $Au_{25}(MHA)_{18}$ nanocluster and systematically studied the doping effects on optical absorption.[182] The slightly-doped $Au_{25-x}Ag_x(MHA)_{18}$ (x = 0-2) shows four distinct absorption peaks at 440, 552, 670, and 760 nm (Fig. 26a); further Ag-doping induces the blue-shifts and disappearance of these peaks, and a gradually increased peak at 470 nm; finally, the 470 nm peak evolves into the most obvious peak when 7-11 Ag heteroatoms are doped into the template (Fig. 26a). The optical evolution is also reflected in the changes in solution colors of these nanoclusters (insets of Fig. 26a).[182]

Doping different heteroatoms into the $Au_{25}(SR)_{18}$ template influences the optical absorption in different ways.[174,211,522] Wang *et al.* compared the optical absorption of $Au_{25}(S\text{-}C_2H_4Ph)_{18}$ and its Ag-, Cu-, Cd-, and Hg-doped derivatives.[174] As shown in Fig. 26b, $Au_{25}(S\text{-}C_2H_4Ph)_{18}$ shows absorption at 400, 450, 670, and 780 nm; while Ag-doping blue-shifts the 400 and 670 nm peaks to 380 and 615 nm, respectively, and the peak at 780 nm fades away. Cu-doping red-shifts the initial 670 nm peak to 690 nm and eliminates the peak at 780 nm. Mono-Cd doping ($Au_{24}Cd_1(S\text{-}C_2H_4Ph)_{18}$) blue-shifts the 670 and 780 nm peaks of Au_{25} to 650 and 770 nm, respectively. As for $Au_{24}Hg_1(S\text{-}C_2H_4Ph)_{18}$, two main peaks are observed at 405 and 710 nm (Fig. 26b).[174]

Lee and co-workers analyze the Pd- and Pt-doping effects on optical absorption: in the low energy region (< 2.5 eV), Au_{25} shows an intense absorption band at 1.80 eV, while upon Pd doping, the 1.80 eV band becomes weak, but other two intense bands (1.2 and 2.0 eV) emerge.[211] As for $Pt_1Au_{24}(S\text{-}C_2H_4Ph)_{18}$, two absorption peaks are observed at 1.1 and 2.1 eV (Fig. 26c).[211] The large difference in optical gaps (~0.3 eV for Pt/Pd doped M_1Au_{24} vs. ~1.3 eV for Au_{25}) is associated with the change in superatomic configuration, *i.e.* $1S^21P^4$ for Pt/Pd doped M_1Au_{24} vs. $1S^21P^6$ for Au_{25}.[211]

Based on the $Au_{25}(SR)_{18}$ template, Wu *et al.* reported the stepwise doping process from mono-metallic $Au_{25}(SR)_{18}$ to bi-metallic $Au_{25-x}Ag_x(SR)_{18}$ and $Au_{24}Hg_1(SR)_{18}$, then to tri-metallic $Au_{24-x}Ag_xHg_1(SR)_{18}$, and the evolution of optical absorption was studied.[521] The Ag- and Hg-doping effects are similar to those summarized in Fig. 26b, whereas the tri-metallic $Au_{24-x}Ag_xHg_1(SR)_{18}$ nanoclusters show two intense peaks at 435 and 530 nm, and two shoulder bands at 350 and 580 nm (Fig. 26d).[521]

Rod-like $Au_{25}(PPh_3)_{10}(SR)_5Cl_2$ shows several absorption bands at 380, 415, 430, and 670 nm.[349] When the template is doped to $Au_{25-x}Ag_x(PPh_3)_{10}(SR)_5Cl_2$ (x = 1-12), the peaks in low wavelength range (< 500 nm) become flat, and the initial 670 nm peak blue-shifts to 663 nm. By comparison, when the doping number is even higher, i.e. x = 1-13, the 670 nm peak in Au_{25} significantly blue-shifts to 635 nm, whereas the other peaks are almost unchanged (Fig. 27a).[369,370] TDDFT analysis shows that increasing Ag doping will shift the lowest-energy excited states to higher energy, and for $Au_{12}Ag_{13}$, the transitions have a significant (>70%) HOMO to LUMO (localized on the central atom) contribution, different from other $Au_{25-x}Ag_x$ species.[369]

$Au_{38}(S\text{-}C_2H_4Ph)_{24}$ displays distinct bands at 1050, 750, 630, 478 nm and shoulder bands at 517 and 400 nm.[232] Upon the Ag-doping, the bands at 750 and 1050 nm fade away, and other bands gradually blue-shift and become broad (Fig. 27b).[250] It is suggested that the optical broadening originates from the mixed-characteristics of these doped nanoclusters (for example, the heavily-doped $Au_{38-x}Ag_x$ nanoclusters contain $Au_{28}Ag_{10}$, $Au_{29}Ag_9$, $Au_{30}Ag_8$, and $Au_{31}Ag_7$).[250] Cu-doping on $Au_{38}(SR)_{24}$ blue-shifts the initial 1050 nm peak to 1000 nm, and red-shifts the initial 750 nm peak to 790 nm.[255] The Pd- and Pt-doping effects on optical absorption of $Au_{38}(SR)_{24}$ are also investigated.[262] As shown in Fig. 27c, although the peaks observed at 1.2 and 2.0 eV for $Pd_2Au_{36}(SR)_{24}$ are almost the same as those in $Au_{38}(SR)_{24}$ except for less intenseness, the absorption spectrum of $Pt_2Au_{36}(SR)$ shows higher energy peaks at 1.5 and 2.2 eV.[262]

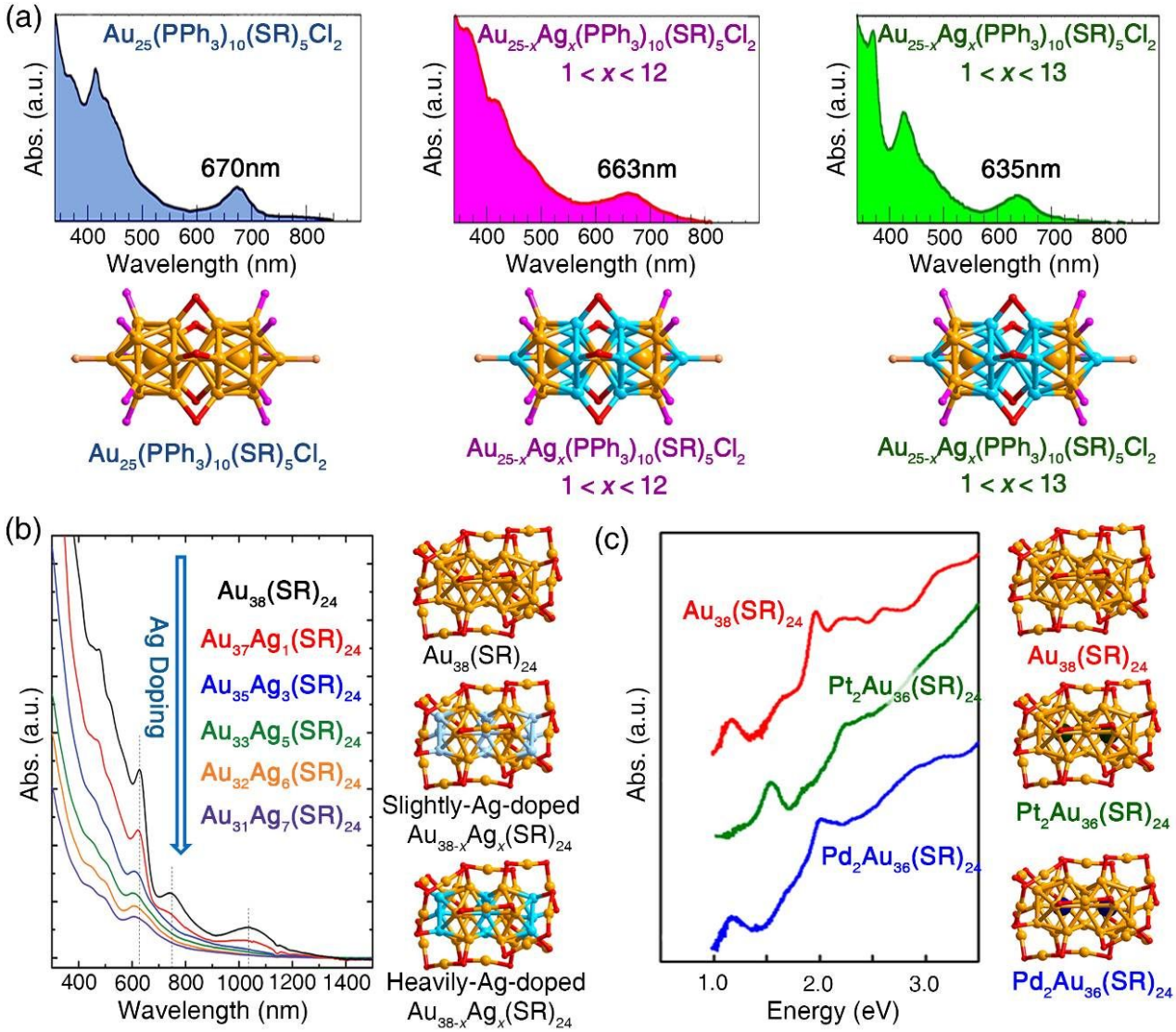

Fig. 27 Doping-induced variations in optical absorptions of rod-like Au_{25} and Au_{38} nanoclusters. (a) Optical absorptions of rod-like $Au_{25}(PPh_3)_{10}(SR)_5Cl_2$ and Ag-doped $Ag_xAu_{25-x}(PPh_3)_{10}(SR)_5Cl_2$ nanoclusters. Redrawn from ref. 369 with permission from American

Chemical Society, copyright 2015. (b) Optical absorptions of $Au_{38}(SR)_{24}$ and Ag-doped $Au_{38-x}Ag_x(SR)_{24}$ nanoclusters. Redrawn from ref. 250 with permission from The Royal Society of Chemistry, copyright 2012. (c) Optical absorptions of $Au_{38}(SR)_{24}$ and Pd- and Pt-doped $Pd_2Au_{36}(SR)_{18}$ and $Pt_2Au_{36}(SR)_{18}$ nanoclusters. Redrawn from ref. 262 with permission from American Chemical Society, copyright 2018.

Based on $M_1Ag_{24}(SR)_{18}$ (M = Ag/Au/Pd/Pt) nanosystem, the alloying effects on optical absorption are evaluated.[378,437,440,441] As shown in Fig. 28a, $Ag_{25}(SR)_{18}$ shows four intense absorption peaks at 334, 390, 490, and 678 nm. Substituting the central Ag atom with Pd hardly changes these bands, which might be due to the same period of Ag and Pd in Ag_{25}.[69,441] Doping a single Au heteroatom into $Ag_{25}(SR)_{18}$ blue-shifts the bands of $Ag_{25}(SR)_{18}$ to 325, 375, 467, and 625 nm, respectively, and upon Pt doping, the absorption bands of $Ag_{25}(SR)_{18}$ are blue-shifted to 333, 390, 455, and 600 nm, respectively (Fig. 28a). The absorption spectra of $Au_1Ag_{24}(SR)_{18}$ and $Pt_1Ag_{24}(SR)_{18}$ are similar, for that Au and Pt are in the same period.[441] Based on the bi-metallic $Pt_1Ag_{24}(SR)_{18}$, two tri-metallic nanoclusters—spherical $Pt_1Ag_{24-x}Au_x(SR)_{18}$ and rod-like $Pt_2Au_{10}Ag_{13}(PPh_3)_{10}Br_7$—are synthesized, and their optical absorption spectra are compared (Fig. 28b).[378] The optical energy gap of $Ag_{25}(SR)_{18}$ (1.57 eV) increases to 1.72 eV upon Pt-doping. A further shape-maintained, Au-alloying process on bi-metallic $Pt_1Ag_{24}(SR)_{18}$ generates tri-metallic $Pt_1Ag_{24-x}Au_x(SR)_{18}$ which shows a slightly reduced optical energy gap (1.62 eV).[378] By comparison, a shape-transformed, Au-alloying process generates rod-like, tri-metallic $Pt_2Au_{10}Ag_{13}(PPh_3)_{10}Br_7$, which exhibits a remarkably enlarged energy gap (1.93 eV).[378]

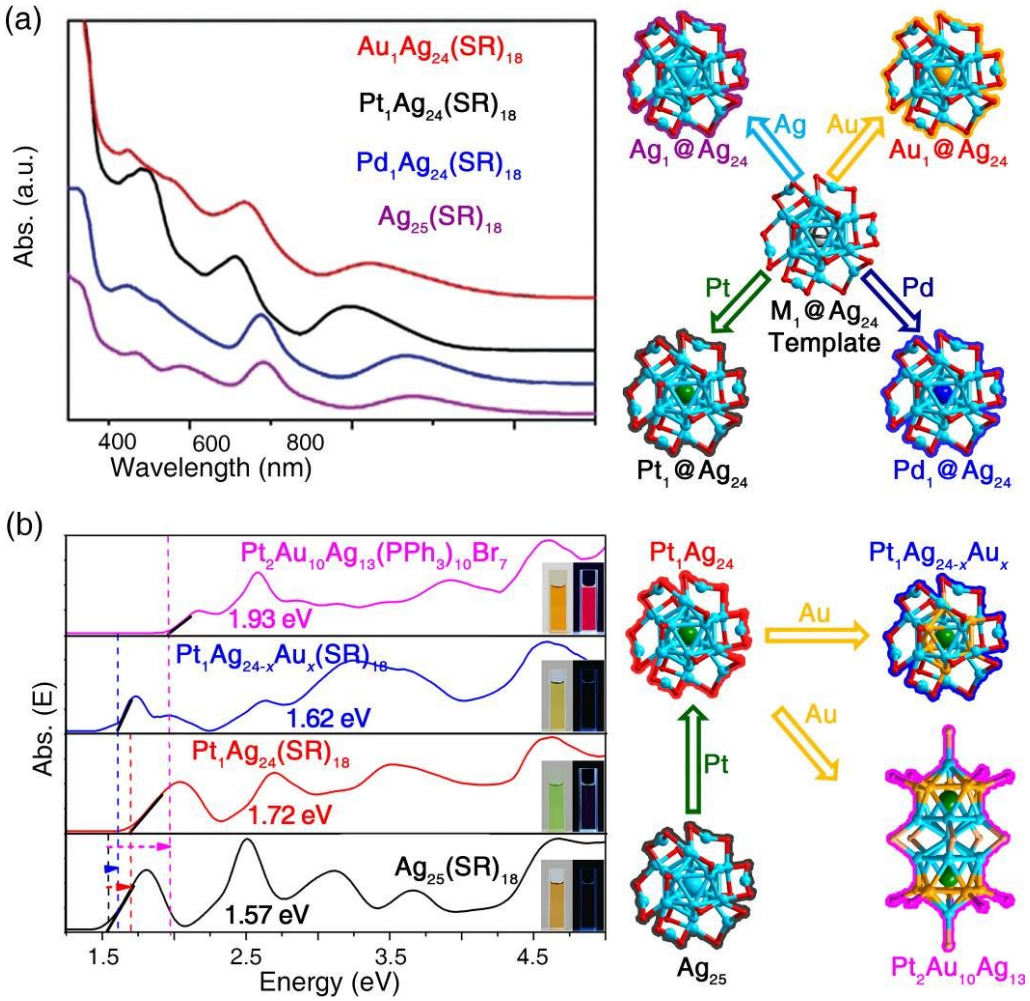

Fig. 28 Doping-induced variations in optical absorptions of Ag_{25}-based nanoclusters. (a) Optical absorptions of $Ag_{25}(SR)_{18}$ and doped $Au_1Ag_{24}(SR)_{18}$, $Pt_1Ag_{24}(SR)_{18}$, and $Pd_1Ag_{24}(SR)_{18}$ nanoclusters. Redrawn from ref. 440 with permission from Wiley-VCH, copyright 2018. (b) Optical absorptions of mono-metallic $Ag_{25}(SR)_{18}$, bi-metallic $Pt_1Ag_{24}(SR)_{18}$, and tri-metallic $Pt_1Ag_{24-x}Au_x(SR)_{18}$ and $Pt_2Au_{10}Ag_{13}(PPh_3)_{10}Br_7$ nanoclusters. Redrawn from ref. 378 with permission from Wiley-VCH, copyright 2016.

Optical absorption of $M_1Ag_{24}(SR)_{18}$ nanoclusters reveal the effect of mono-heteroatom doping on their electronic structures.[378,437,440,441] Kim *et al*. answered the question of how and why the energy levels of the superatomic orbitals

were shifted upon doping by gas-phase photoelectron spectroscopy (PES).[595] The PE spectrum of $[Au_1Ag_{24}(SR)_{18}]^-$ was similar to that of $[Ag_{25}(SR)_{18}]^-$, whereas those of $[Pt_1/Pd_1Ag_{24}(SR)_{18}]^{2-}$ were shifted by about 1.4 eV toward lower binding energy relative to that of $[Ag_{25}(SR)_{18}]^-$, without any large change in spectral profiles. These PES results together with the DFT calculations demonstrated that the superatomic orbitals in $(X@Ag_{12})^{5+}$ (X = Ag, Au) kernels shifted to higher energy by replacing the central X atom by Pt or Pd heteroatom.[595] Such an upward shift of superatomic orbitals resulted from (i) the weaker binding of valence electrons in $(Y@Ag_{12})^{4+}$ (Y = Pd, Pt) relative to those in $(X@Ag_{12})^{5+}$ (X = Ag, Au) because of the reduction in formal charge of the kernel potential, and (ii) the upward shift of the apparent vacuum level by the presence of a repulsive Coulomb barrier for $(Y@Ag_{12})^{4+}$.[595]

The hydrophilic $Ag_{29}(DHLA)_{12}$ nanocluster shows three shoulder bands at 335, 430, and 500 nm.[474] Slight Au-doping blue-shifts these bands to 320, 400, and 485 nm, respectively, and the 400 nm peak becomes intense (Fig. 29a). Further Au-doping will not alter the positions of these absorption peaks, but make them flattened (Fig. 29a).[474] The doping effects on optical absorption have also been investigated on the basis of hydrophobic $Ag_{29}(S_2R)_{12}(PPh_3)_4$ and its Au-doped nanoclusters.[70] $Ag_{29}(S_2R)_{12}(PPh_3)_4$ shows an intense band at 447 nm and a shoulder at 510nm, while $Ag_{29-x}Au_x(S_2R)_{12}(PPh_3)_4$ nanoclusters only have one intense peak at 435 nm. In addition, this peak broadens with the increasing amount of Au dopant (Fig. 29b).[70]

Based on $M_{29}(S\text{-}Adm)_{18}(PPh_3)_4$ nanoclusters with a tetra-stratified configuration of $M_1(center)@M_{12}(1^{st}\text{-}shell)@M_{12}(SR)_{18}(2^{nd}\text{-}shell)@(M\text{-}PPh_3)_4(vertex)$, the structure-optical property correlations have been mapped out:[448] (i) as for the central position (Ag/Au/Pd/Pt), substituting the Ag center by Pd heteroatom can hardly change the optical absorption, while doping mono Pt/Au into the kernel remarkably red-shifts the peak; (ii) as for the 2nd shell (Ag/Cu), exchanging the $Ag_{12}(SR)_{18}$ shell to $Cu_{12}(SR)_{18}$ blue-shifts the optical absorption while maintaining the overall profiles; (iii) as for the vertex positions (Ag/Cu/Au), the characteristic absorption profiles are almost retained when the vertex Ag atoms are substituted by Cu; by contrast, metal-exchanging these vertex atoms by Au not only red-shifts the initial absorption, but generates a new peak at higher wavelength as well.[448]

The optical absorption of $Ag_{44}(SR)_{30}$ (SR = $SPhF_2$, SPhF, or $SPhCF_3$) displays six peaks at 374, 411, 483, 535, 641 and 833 nm and two shoulders at 590 and 689 nm (Fig. 29c, left).[477] Upon Au-doping, the obtained $Au_{12}Ag_{32}(SR)_{30}$ only displays two apparent peaks at 390 and 500 nm and a shoulder at 750 nm (Fig. 29c, right). Considering that these Au heteroatoms are all incorporated into the icosahedral kernel of $Ag_{44}(SR)_{30}$, Yang *et al.* suggested a significant contribution of the kernel metal atoms on the overall optical absorption of these $M_{12}@Ag_{32}(SR)_{30}$ nanoclusters.[477]

The UV-vis spectrum of $Cu_{13}(S_2CN^nBu_2)_6(C{\equiv}CR)_4$ shows broad multi-optical absorption bands at 337, 513, 540, 571 nm and an intense one at 287 nm; by comparison, the doped derivative, Ag_1Cu_{12}, shows optical absorption at 276, 348 and 580 nm peaks, while Au_1Cu_{12} shows optical absorption at 310, 508 and 561 nm.[518] Consequently, Cu_{13} solution is pink, whereas the solutions of Ag_1Cu_{12} and Au_1Cu_{12} nanoclusters are violet and orange, respectively.[518]

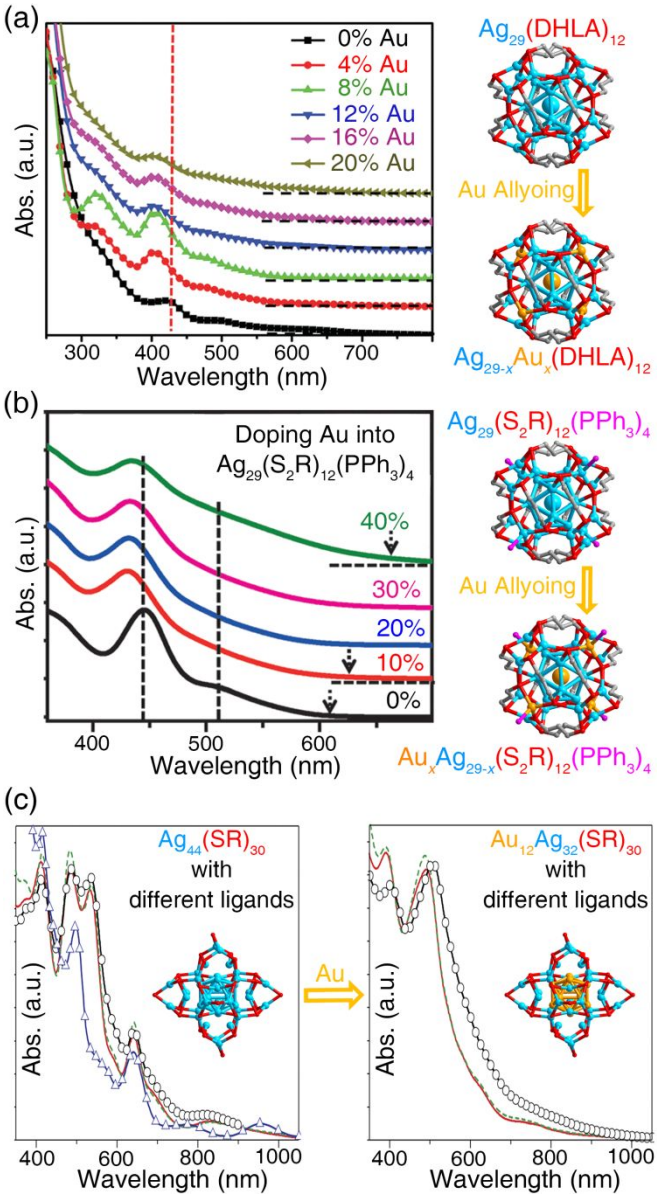

Fig. 29 Doping-induced variations in optical absorptions of Ag_{29}- and Ag_{44}-based nanoclusters. (a) Optical absorptions of DHLA protected Ag_{29} and Au-doped $Ag_{29-x}Au_x$ nanoclusters. Redrawn from ref. 474 with permission from The Royal Society of Chemistry, copyright 2018. (b) Optical absorptions of $Ag_{29}(S_2R)_{12}(PPh_3)_4$ and Au-doped $Ag_{29-x}Au_x(S_2R)_{12}(PPh_3)_4$ (x = 1-5) nanoclusters. Redrawn from ref. 70 with permission from Wiley-VCH, copyright 2016. (c) Optical absorptions of $Ag_{44}(SR)_{30}$ and $Au_{12}Ag_{32}(SR)_{30}$ nanoclusters. Redrawn from ref. 477 with permission from Nature Publishing Group, copyright 2013.

7.1.2 Photoluminescence

Next, we summarize the heteroatom effects on PL characteristics. Rod-shaped $Au_{25}(PPh_3)_{10}(SR)_5Cl_2$ possesses a low PL intensity (QY = 0.1%), however, as shown in Fig. 30a, substituting some Au atoms with Ag can drastically enhance the PL intensity. The obtained $Au_{25-x}Ag_x$ (x = 1-13) nanoclusters exhibit high PL intensity of QY = 40%, which is in striking contrast to the weakly emissive $Au_{25-x}Ag_x$ (x = 1-12, QY = 0.2%).[368] Further theoretical works suggest that the origin of PL enhancement lies in the nature of the first excited state (S1) and the corresponding HOMO-LUMO transition, which are significantly affected by the doping extents of Ag.[369] Ultrafast relaxation dynamics of Au_{25} and $Au_{25-x}Ag_x$ demonstrate the importance of the vertex Ag heteroatom in stabilizing the charges on LUMO and enhancing the rigidity of $Au_{25-x}Ag_x$ nanoclusters, which further leads to the stronger PL.[370]

The alloying effects on PL characteristics is also investigated based on a continuous doping process from mono-metallic $Ag_{25}(SR)_{18}$, to bi-metallic $Pt_1Ag_{24}(SR)_{18}$, then to tri-metallic $Pt_1Ag_{24-x}Au_x(SR)_{18}$ (x = 6.4) and $Pt_2Au_{10}Ag_{13}(PPh_3)_{10}Br_7$ nanoclusters.[378] $Ag_{25}(SR)_{18}$ displays neglectable PL (centered at 809 nm), and $Pt_1Ag_{24}(SR)_{18}$ shows an enhanced PL (QY = 0.1%) at 728 nm (Fig. 30b). However, further Au-alloying generates two tri-metallic nanoclusters, in which rod-like $Pt_2Au_{10}Ag_{13}$ exhibits a significantly enhanced PL intensity at 648 nm with PL QY = 14.7%, representing a 150-fold enhancement relative to $Pt_1Ag_{24}(SR)_{18}$. As a contrast, the spherical tri-metallic $Pt_1Au_xAg_{24-x}(SR)_{18}$ is non-emissive (Fig. 30b).[378]

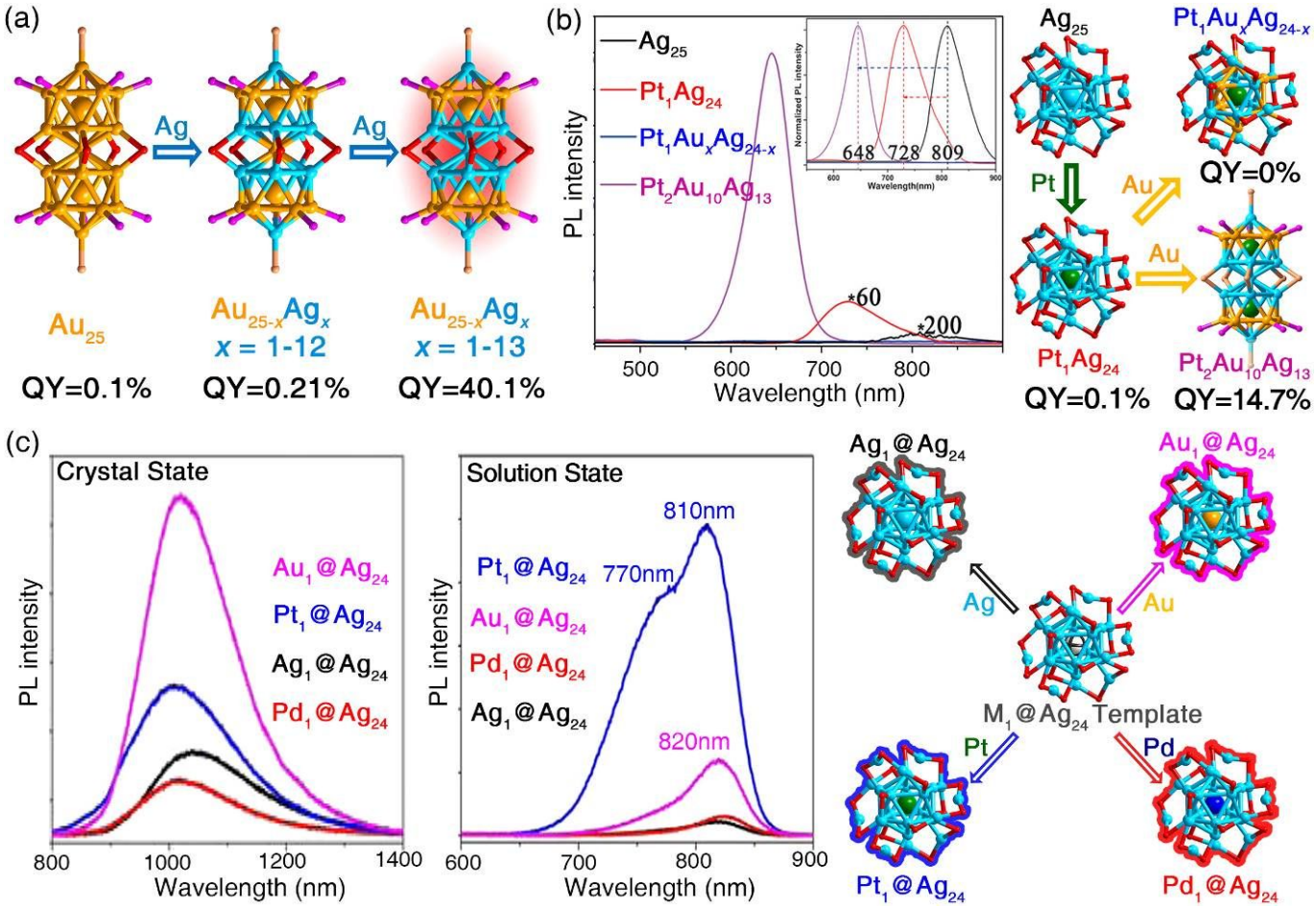

Fig. 30 PL characteristics of alloy M_{25} nanoclusters. (a) Schematic illustration of Ag-induced PL enhancement from rod-like $Au_{25}(PPh_3)_{10}(SR)_5Cl_2$ (PL QY 0.1%) to $Au_{25-x}Ag_x(PPh_3)_{10}(SR)_5Cl_2$ (x = 1-12, PL QY 0.21%), then to $Au_{25-x}Ag_x(PPh_3)_{10}(SR)_5Cl_2$ (x = 1-13, PL QY 40.1%). Redrawn from ref. 368 with permission from Wiley-VCH, copyright 2014. (b) PL variation from mono-metallic $Ag_{25}(SR)_{18}$, to bi-metallic $Pt_1Ag_{24}(SR)_{18}$, then to tri-metallic $Pt_1Ag_{24-x}Au_x(SR)_{18}$ (x = 6.4) and $Pt_2Au_{10}Ag_{13}(PPh_3)_{10}Br_7$. Redrawn from ref. 378 with permission from Wiley-VCH, copyright 2016. (c) PL spectra of $M_1Ag_{24}(SR)_{18}$ (M = Ag/Au/Pd/Pt) nanoclusters in crystal or solution states. Redrawn from ref. 437 with permission from American Chemical Society, copyright 2017.

Bakr and co-workers substitute the central Ag atom in $Ag_{25}(SR)_{18}$ with Au,[69] and the emission of the doped Au_1Ag_{24} (810 nm) is blue-shifted relative to that of Ag_{25} (830 nm), resulting from the modulation in the HOMO-LUMO gap after Au-doping. Moreover, the emission intensity of $Au_1Ag_{24}(SR)_{18}$ is enhanced by a factor of >25 compared to $Ag_{25}(SR)_{18}$.

Conversely, only a little change is observed by comparing the PL characteristics between $Ag_{25}(SR)_{18}$ and Pd-doped $Pd_1Ag_{24}(SR)_{18}$ nanoclusters.[69]

Liu *et al.* investigated the PL characteristics of $M_1Ag_{24}(SR)_{18}$ nanoclusters in crystal or solution state (Fig. 30c).[437] In the crystal state, the PL intensities of these nanoclusters follow the subsequence of $Pd_1Ag_{24}(SR)_{18}$ < $Ag_{25}(SR)_{18}$ < $Pt_1Ag_{24}(SR)_{18}$ < $Au_1Ag_{24}(SR)_{18}$. Besides, the emission wavelengths of $Ag_{25}(SR)_{18}$ locates at 1042 nm, while the M-doping by Au/Pd/Pt heteroatom leads to blue-shifts in emission by 20/21/28 nm, respectively.[437] When in acetonitrile solution, the PL intensities of these nanoclusters follow another subsequence of $Ag_{25}(SR)_{18}$ < $Pd_1Ag_{24}(SR)_{18}$ < $Au_1Ag_{24}(SR)_{18}$ < $Pt_1Ag_{24}(SR)_{18}$. In addition, $Ag_{25}(SR)_{18}$, $Pd_1Ag_{24}(SR)_{18}$ and $Au_1Ag_{24}(SR)_{18}$ all emit at 820 nm, whereas $Pt_1Ag_{24}(SR)_{18}$ emits at both 770 and 810 nm (Fig. 30c).[437]

Based on the $M_1Ag_{24}(SPhMe_2)_{18}$ template, Yuan *et al.* also investigated the synergistic effect introduced by doping on PL properties.[439] Significantly, when the central Ag atom of $Ag_{25}(SR)_{18}$ was exchanged by Au/Pt heteroatom, the free electrons were concentrated toward the interior of the nanocluster, and PL enhancement was observed.[439] By comparison, when the Ag atoms on the kernel shell of $M_1Ag_{24}(SR)_{18}$ (M = Au/Pt) was further exchanged by Au, free valence electrons would expand to the kernel shell, resulting in the attenuation of the PL intensity. The relationship between the free valence electrons and PL properties provides new insight into the origin of PL in nanoclusters.[439]

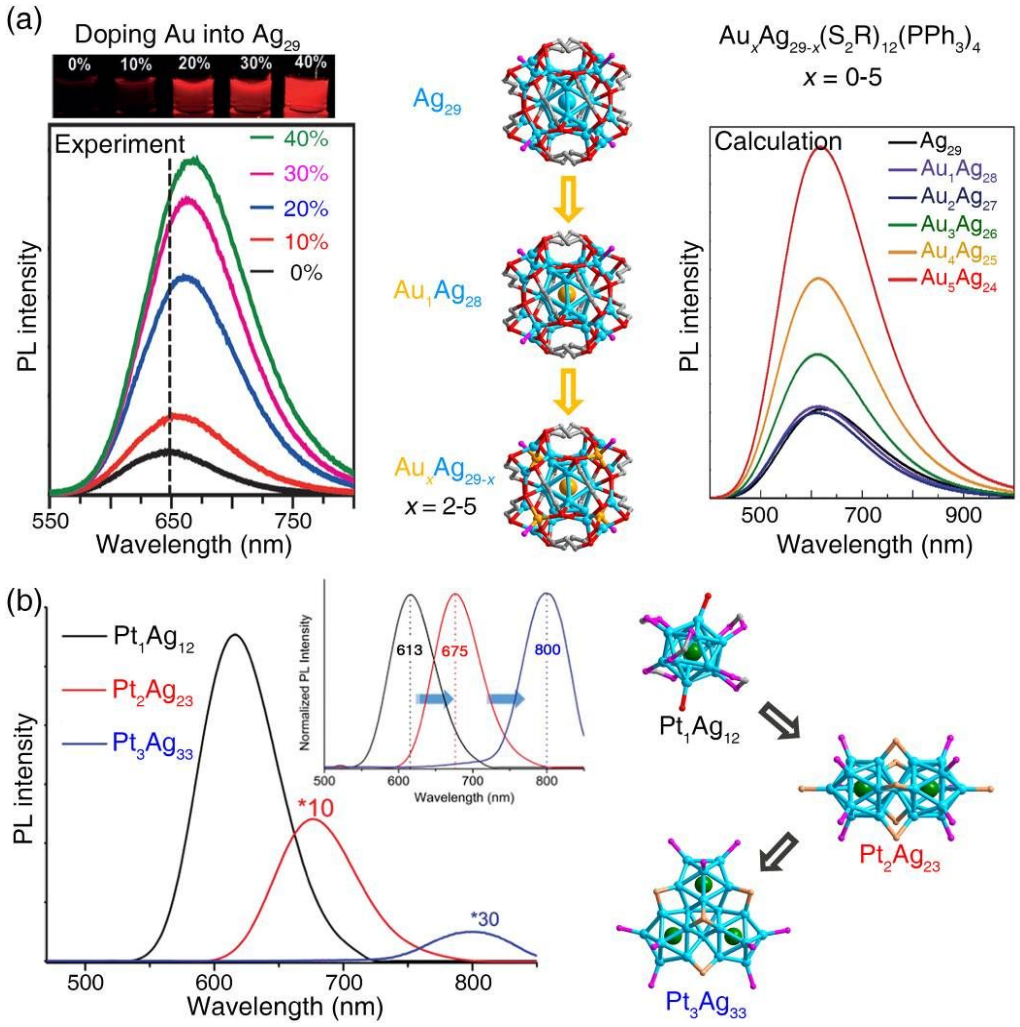

Fig. 31 PL characteristics of alloy M_{29} or $(Pt_1Ag_{12})_m$ nanoclusters. (a) Experimental and theoretical PL spectra of $Ag_{29}(S_2R)_{12}(PPh_3)_4$ and Au-doped nanoclusters. Redrawn from ref. 70 and ref. 467 with permission from Wiley-VCH, copyright 2016 and 2018, respectively. (b) PL variations from mono-icosahedral Pt_1Ag_{12} to bi-icosahedral Pt_2Ag_{23}, then to tri-icosahedral Pt_3Ag_{33}. Redrawn from ref. 445 with permission from The Royal Society of Chemistry, copyright 2018.

In the case of $Ag_{29}(S_2R)_{12}(PPh_3)_4$, Au-doping led to a 26-fold enhancement of PL; that is, the QY of Ag_{29} (~0.9%) was increased to 24% when up to five Au heteroatoms were introduced.[70] Along with this PL enhancement, the emission red-shifts from 649 nm of Ag_{29} to 668 nm of 40%-doped $Ag_{29-x}Au_x$ (Fig. 31a, left). By DFT calculations, Xie *et al.* explored the PL enhancement in Au-doped $Ag_{29-x}Au_x$ nanoclusters (Fig. 31a, right), suggesting that the relativistic effects introduced by Au heteroatoms played a significant role, especially for Au_3Ag_{26}, Au_4Ag_{25}, and Au_5Ag_{24} nanoclusters.[467] Besides hydrophobic

Ag_{29}, hydrophilic Ag_{29} also displays enhanced PL upon Au-doping.[467,596] However, upon Cu-doping, alloying of $Ag_{29}(S_2R)_{12}(PPh_3)_4$ to form $Ag_{17}Cu_{12}(S_2R)_{12}(PPh_3)_4$ results in a remarkable attenuation of the PL intensity.[468]

All M_{29}(S-Adm)$_{18}(PPh_3)_4$ (M = Ag/Au/Pt/Pd/Cu) nanoclusters fluoresce when being illuminated at 445 nm, constituting a series of nanoclusters to analyze the structure-PL correlations at the atomic level.[448] By comparing the PL of M_{29}(S-Adm)$_{18}(PPh_3)_4$, the synergy effects on PL characteristics in terms of PL intensity and emission wavelength are investigated: (i) As for the M_{13} kernel (M = Ag/Au/Pt/Pd), doping Pd heteroatom into the center weakens the PL intensity and blue-shifts the emission; on the contrary, enhanced PL intensity as well as red-shifted emission are observed when substituting the center-Ag with Pt or Au atom; (ii) As for the $M_{12}(SR)_{18}$ shell (M = Ag/Cu), altering $Ag_{12}(SR)_{18}$ into $Cu_{12}(SR)_{18}$ blue-shifts the emission wavelength and slightly reduces the PL intensity; (iii) substituting Ag atoms by Au in the (M-$PPh_3)_4$ vertex (M = Ag/Au/Cu), not only red-shifts the emission, but also remarkably enhances the PL intensity; an opposite phenomenon is observed when replacing Ag with Cu.[448] According to the above observations, the configuration of $Au_1@Ag_{12}@Ag_{12}(SR)_{18}@(Au\text{-}PPh_3)_4$ displays the highest PL intensity and maximum emission wavelength (QY = 11.6% and emission at 715 nm) among all the 21 nanoclusters of M_{29}(S-Adm)$_{18}(PPh_3)_4$. Based on these structure-PL correlations, Kang *et al*. demonstrate that doping the kernel or vertex atoms with metals of large electron affinity (note: metal electron affinity subsequence Au(2.309) > Pt(2.128) > Ag(1.302) > Cu(1.228) > Pd(0.562)) is in favor of generating emissive nanoclusters with higher PL intensity.[448] Overall, the observed trends of PL with different doping modes will provide guidelines in the synthesis of fluorescent alloy nanoclusters.[448]

The PL characteristic of Pt_1Ag_{12}, Pt_2Ag_{23}, and Pt_3Ag_{33} nanoclusters are compared as well. Among them, the mono-icosahedral Pt_1Ag_{12} shows the strongest PL with QY = 5.5%, and the emission locates at 613 nm (Fig. 31b).[445] Assembly of two Pt_1Ag_{12} units into Pt_2Ag_{23} red-shifts the emission to 675 nm, but the PL QY drops to 0.2%. Further assembly results in tri-icosahedral Pt_3Ag_{33} which emits at 800 nm with a neglectable PL QY of 0.013% (Fig. 31b).[445]

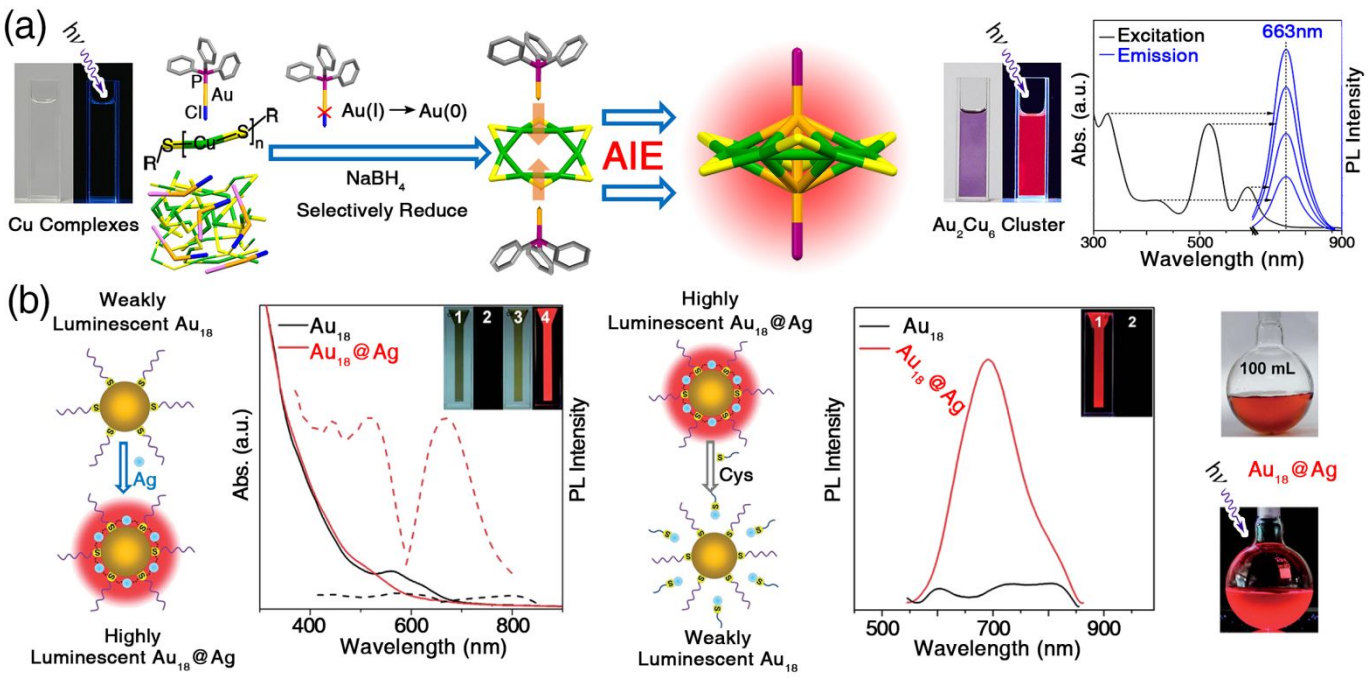

Fig. 32 PL enhancement in alloy nanoclusters induced by AIE process. (a) Schematic illustration of AIE process induced by introducing Au(0) kernel into Cu(I) complexes. Redrawn from ref. 555 with permission from Wiley-VCH, copyright 2016. (b) AIE-induced PL enhancement of $Au_{18}(SG)_{14}$ caused by the introduction of Ag^+ ions, and the cysteine-induced PL quenching of Au_{18}@Ag nanoclusters. Redrawn from ref. 272 with permission from The Royal Society of Chemistry, copyright 2014.

In order to study the PL characteristics of alloy clusters based on C@Au_6, alloyed C@Au_6Cu_2, C@Au_6Ag_2, C@Au_6Ag_4, and C@Au_6Ag_6 clusters were obtained.[586,591-594] C@Au_6M_x (M = Ag/Cu) alloy clusters exhibit ligand-dependent, metal-dependent, and solvent-dependent PL performances — (i) C@Au_6M_x cluster compounds with different peripheral phosphine ligands or metal compositions display diverse metal-ligand coordinations and geometric/electronic structures, and thus show distinguishable PL properties, such as fluorescent colors;[586,592-294] (ii) crystals of C@Au_6M_x clusters have porous structures, and show solvatochromic performance because of the specific interactions between the poles/channels and the solvent molecules.[586,593]

The introduction of heteroatoms can also enhance the PL intensity of metal complexes or nanoclusters *via* aggregation-induced emission (AIE).[272,555] Although the Cu^I-SR complex is

non-emissive, they undergo controlled aggregation with the addition of Au^0, and the aggregated product (Au_2Cu_6) displays high PL at 663 nm with a QY of 11.7% (Fig. 32a).[555]

The weakly luminescent $Au_{18}(SG)_{14}$ emits high PL in the presence of Ag^I ions (Fig. 32b).[272] It is proposed that the introduced Ag^I ions bridge the Au^I-SG motifs on the surface of $Au_{18}(SG)_{14}$, leading to the formation of rigid Au^I/Ag^I-SG motifs, which exhibit strong, red emission (PL QY = 6.8%) *via* AIE (Fig. 32b, right).[272] The anchored Ag^I ions on $Au_{18}(SG)_{14}$ surface can be removed upon the addition of cysteine, and as a result, the Au_{18}@Ag alloy nanocluster reverts to the weakly emissive $Au_{18}(SG)_{14}$ (Fig. 32b, middle).[272]

Pal and co-workers modified the PL of dopamine-protected Au nanoclusters *via* Ag alloying, and a blue-shift of the emission peak, as well as an enhancement in PL intensity for the Au/Ag alloy in comparison to homo-gold nanocluster in aqueous solution, are observed.[597] Besides, the increment of emission intensity is found to be silver concentration-dependent and a maximum 5-fold increase is obtained at Ag:Au ratio = 0.25:0.60.[597]

7.1.3 Ultrafast electron dynamics

Alloying may exhibit effects on the electronic excited-state properties of nanoclusters, including the transient absorption spectral features and ultrafast electron dynamics.[220] By using femtosecond visible and near-infrared transient absorption (TA) spectroscopies, Zhou *et al.* investigated the heteroatom effects on ultrafast electron relaxation dynamics of $Pd_1Au_{24}(SR)_{18}$ and $Pt_1Au_{24}(SR)_{18}$.[220] Three relaxation components were identified for both nanoclusters: (i) sub-picosecond relaxation within the icosahedral M_1Au_{12} (M = Pd/Pt) kernel states (~0.6 ps); (2) kernel to shell relaxation in a few picoseconds (3-5 ps); and (3) relaxation to the ground state in more than one nanosecond. Despite similar relaxation pathways for the two doped nanoclusters, the coupling between the metal kernel and surface motifs was found to be accelerated by about 30% in the case of Pt dopant with ~3.8 ps compared with Pd dopant with ~5 ps (Fig. 33a).[220] The different excited state and ground state behaviors between $Pd_1Au_{24}(SR)_{18}$ and $Pt_1Au_{24}(SR)_{18}$ could be attributed to the different hybridization of Pd 4d (or Pt 5d) orbitals with Au 5d and 6s orbitals in the icosahedral M_{13} kernel.[220] Later, Zhou et al. continued to explore more $M_1Au_{24}(SR)_{18}$ (M = Cd, Hg, Pt, Pd) nanoclusters, and the excited-state behaviors of these nanoclusters demonstrated that the number of valence electrons in $M_1Au_{24}(SR)_{18}$ determined the photodynamics.[221] The $Cd_1Au_{24}(SR)_{18}$ and $Hg_1Au_{24}(SR)_{18}$ with 8 electrons showed long excited-state lifetimes (50-200 ns) and weak picosecond relaxations, similar to the case of $[Au_{25}(SR)_{18}]^-$ (8 e) (Fig. 33b). In contrast, $Pd_1Au_{24}(SR)_{18}$ and $Pt_1Au_{24}(SR)_{18}$ with 6 e showed much more significant picosecond relaxation and thus much shorter excited-state lifetimes (> 1 ns), reminiscent of the 7-electron $[Au_{25}(SR)_{18}]^0$ nanocluster.[221]

Thanthirige *et al.* carried out femtosecond TA measurements on $Au_{25}(SR)_{18}$, $Hg_1Au_{24}(SR)_{18}$ and $Pt_1Au_{24}(SR)_{18}$ nanoclusters after exciting them at 370 nm, to gain a better understanding on the influence of the central metal atom on the optical properties.[598] Compared with $Au_{25}(SR)_{18}$, Pt-doping led to a faster excited state relaxation, where more than 70% of the created electron-hole pairs recombined within 20 ps. By comparison, Hg_1Au_{24} took a much longer time for relaxing exciton to the shell gold before recombination, similar to the case of $Au_{25}(SR)_{18}$ (over 100 ns in exciton relaxation).[598] These results are consistent with the energy gaps of these nanoclusters, in which the smaller energy gap for $Pt_1Au_{24}(SR)_{18}$ leads to a faster exciton relaxation.[598]

Aside from $Au_{25}(SR)_{18}$, alloying effects on ultrafast electron dynamics were also investigated in other nanoclusters.[370,407] The ultrafast relaxation dynamics of rod-shaped $Au_{25}(PPh_3)_{10}(SR)_5Cl_2$ and $Au_{25-x}Ag_x(PPh_3)_{10}(SR)_5Cl_2$ were compared: the excited state relaxation in Au_{25} proceeded with an ultrafast (0.82 ps) internal conversion and a subsequent nuclear relaxation (52 ps), followed by a slow (2.3 μs) decay back to the ground state.[370] Upon Ag-doping, $Au_{25-x}Ag_x$ showed a 0.58 ps internal conversion, a 20.7 ps nuclear relaxation, and a 7.4 μs final decay to the ground state.[370] Zheng *et al.* researched the composition-dependent electronic energy relaxation dynamics of doped $Au_{144-x}Ag_x(SR)_{60}$, and demonstrated a trend of greater electron-phonon coupling efficiency with increasing Ag content in $Au_{144-x}Ag_x$.[410]

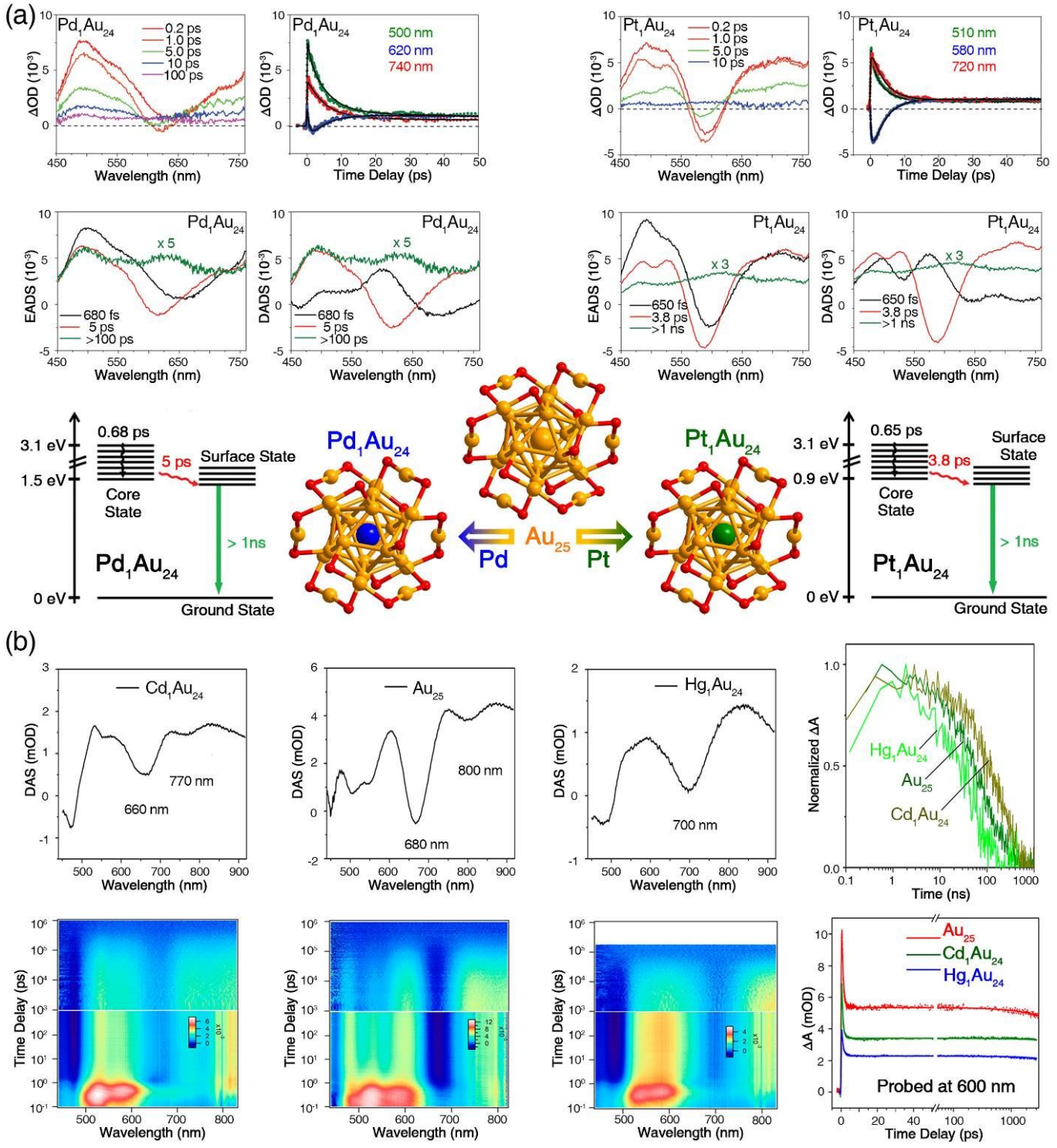

Fig. 33 Ultrafast electron dynamics of alloy nanoclusters. (a) *Top*: transient absorption spectra, transient kinetic traces, evolution associated difference spectra, and decay associated difference spectra of $Pd_1Au_{24}(SR)_{18}$ and $Pt_1Au_{24}(SR)_{18}$. Bottom: proposed relaxation schemes of $Pd_1Au_{24}(SR)_{18}$ and $Pt_1Au_{24}(SR)_{18}$. Redrawn from ref. 220 with permission from The Royal Society of Chemistry, copyright 2016. (b) *Top*: decay associated spectra obtained from global fitting on the nanosecond transient absorptions of $Au_{25}(SR)_{18}$ and doped $Cd_1Au_{24}(SR)_{18}$ and $Hg_1Au_{24}(SR)_{18}$ (normalized kinetic traces monitored at ~600 nm). Bottom: femtosecond and nanosecond transient absorption maps of $Au_{25}(SR)_{18}$ and doped $Cd_1Au_{24}(SR)_{18}$ and $Hg_1Au_{24}(SR)_{18}$ nanoclusters pumped at 360 nm at all time delays; kinetic traces from transient absorption measurements probed at 600 nm and the corresponding fits for $Au_{25}(SR)_{18}$, $Cd_1Au_{24}(SR)_{18}$ and $Hg_1Au_{24}(SR)_{18}$. Redrawn from ref. 221 with permission from American Chemical Society, copyright 2018.

7.2 Electrochemical properties

Electrochemistry reveals the energies of the HOMO and LUMO (associated with the energy gap), and represents one of the important properties of nanoclusters.[599-604] The alloying effects on electrochemical properties have been investigated based on several nanocluster models, which are reviewed in this section.

Differential pulse voltammetry (DPV) was used to compare the electrochemical properties of $Au_{18}(SR)_{14}$ and doped $Au_{15}Ag_3(SR)_{14}$ nanoclusters (in 0.1 M Bu_4NPF_6-CH_2Cl_2 solution, room temperature).[267] The $Au_{18}(SR)_{14}$ exhibited three oxidation peaks at 0.660 (O1), 0.949 (O2), and 1.292 V (O3), and one reduction peak at -1.253 V (R1). Upon Ag-doping, $Au_{15}Ag_3(SR)_{14}$ had three oxidation peaks at 0.837 (O1), 1.087 (O2), and 1.483 V (O3), and two reduction peaks at -1.273 (R1) and -1.591 V (R2). Based on the peaks, the HOMO-LUMO energy gap (*i.e.*, the difference between O1 and R1) of $Au_{15}Ag_3(SR)_{14}$ was calculated as 2.110 eV, larger than that of $Au_{18}(SR)_{14}$ (1.913 eV).[267]

The square wave voltammetry (SWV) analysis was conducted on $Au_{25}(SR)_{18}$, $Pd_1Au_{24}(SR)_{18}$ and $Pt_1Au_{24}(SR)_{18}$ nanoclusters to investigate the doping effects on electrochemical properties.[211] For $Au_{25}(SR)_{18}$, there were three oxidation peaks at -0.39 (O1), -0.04 (O2), and 0.69 (O3), and one reduction peak at -2.06 V (R1). By comparison, $Pd_1Au_{24}(SR)_{18}$ exhibited a doublet of oxidation at -0.03 (O1) and 0.40 (O2), and a doublet of reduction at -0.78 (R1) and -1.10 V (R2); similarly, $Pt_1Au_{24}(SR)_{18}$ also exhibited a doublet of oxidation at -0.03 (O1) and 0.41 (O2) and a doublet of reduction at -0.76 (R1) and -1.10 V (R2) (Fig. 34a).[211] Accordingly, upon Pd- and Pt-doping, the HOMO-LUMO gap was remarkably reduced from 1.32 V of $Au_{25}(SR)_{18}$ to 0.32 V of $Pd_1Au_{24}(SR)_{18}$ and 0.29 V of $Pt_1Au_{24}(SR)_{18}$, respectively.[211]

In the comparison of DPV spectra between $Au_{25}(SR)_{18}$ and mono-Hg-doped $Hg_1Au_{24}(SR)_{18}$, the O1 and R1 potential bands of Au_{25} located at -0.15 and -1.78 V, respectively, while those of $Hg_1Au_{24}(SR)_{18}$ red-shifted to 0.38 and -1.14 V, respectively. In this context, the O1-R1 potential spacing was reduced from 1.63 V of $Au_{25}(SR)_{18}$ to 1.52 V of $Hg_1Au_{24}(SR)_{18}$.[71]

Electrochemical properties of $Au_{38}(SR)_{24}$ and Pt- and Pd-doped $M_2Au_{36}(SR)_{24}$ nanoclusters were compared as well (Fig. 34b).[262] The SWV spectra of $Au_{38}(SR)_{24}$ showed three oxidation peaks at -0.10 (O1), 0.25 (O2), and 0.47 V (O3), and two reduction peaks at -1.31 (R1) and -1.52 V (R2). Upon Pt-doping, $Pt_2Au_{36}(SR)_{24}$ exhibited three oxidation peaks at -0.40 (O1), -0.08 (O2), and 0.30 (O3), and one reduction peak at -1.67 V (R1). As for $Pd_2Au_{36}(SR)_{24}$, a doublet of oxidation at -0.15 (O1) and 0.17 (O2), and a doublet of reduction at -0.73 (R1) and -1.02 V (R2) were observed (Fig. 34b). From these potential bands, the HOMO-LUMO energy gaps of $Au_{38}(SR)_{24}$, $Pt_2Au_{36}(SR)_{24}$, and $Pd_2Au_{36}(SR)_{24}$ nanoclusters were determined as 0.86, 0.95, and 0.26 V, respectively.[262] Lee and co-workers proposed that the similar voltammograms between $[Au_{38}(SR)_{24}]^0$ and $[Pt_2Au_{36}(SR)_{24}]^{2-}$ resulted from similar electronic structures with 14-electron configurations of these two nanoclusters; while $[Pd_2Au_{36}(SR)_{24}]^0$ displayed a drastically reduced HOMO-LUMO energy gap due to its 12-electron configuration.[262]

Doping effects on the electrochemical properties were also evaluated on $M_1Ag_{24}(SR)_{18}$ (M = Ag/Au/Pd/Pt) nanoclusters.[441] From the DPV spectra, the HOMO-LUMO energy gaps of $Ag_{25}(SR)_{18}$, $Au_1Ag_{24}(SR)_{18}$, $Pd_1Ag_{24}(SR)_{18}$, and $Pt_1Ag_{24}(SR)_{18}$ were determined to be 1.82, 1.76, 1.71, and 1.96 V, respectively (Fig. 34c), consistent with the corresponding optical gaps of these nanoclusters.[441]

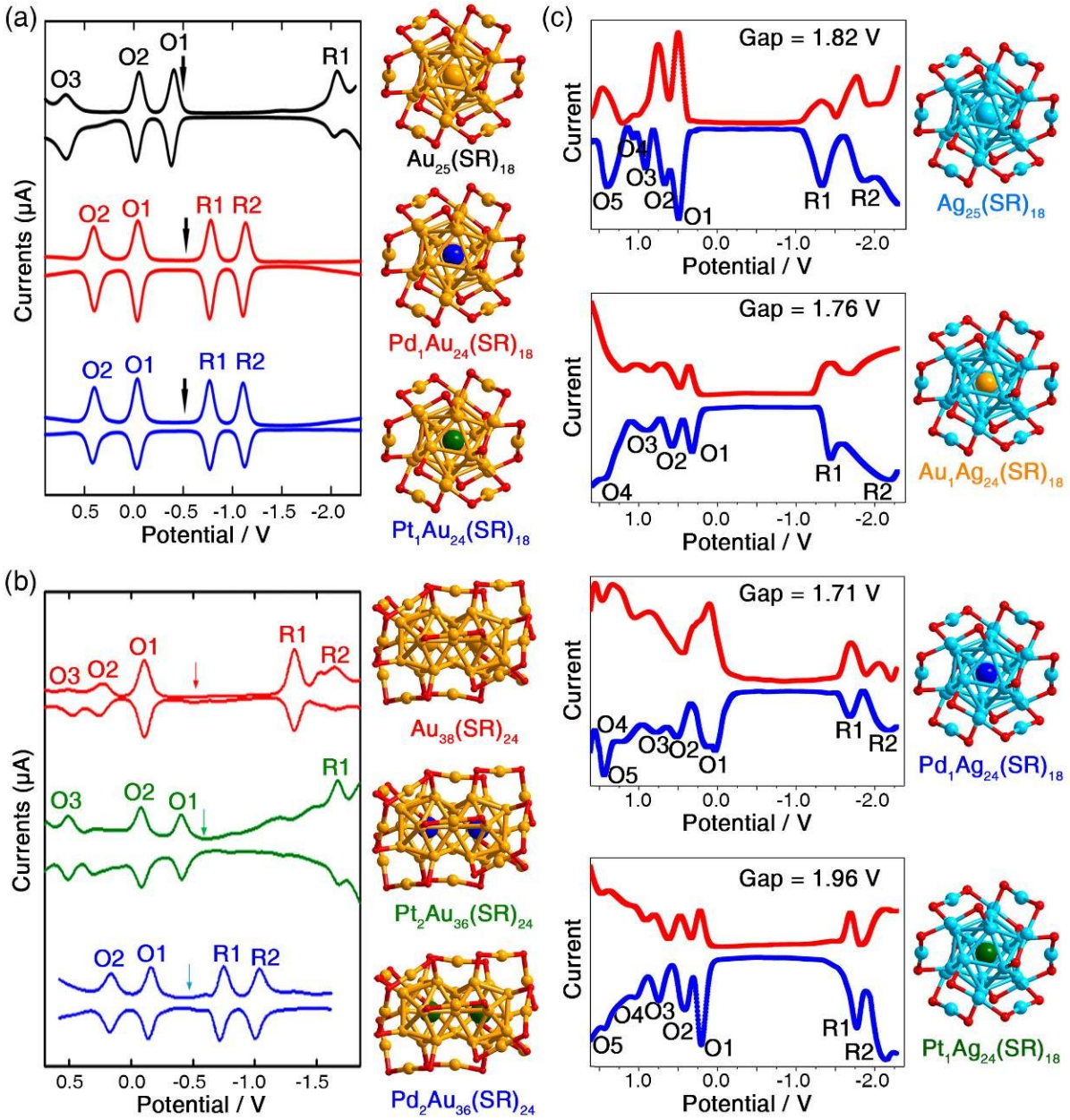

Fig. 34 Alloying effects on electrochemical properties of nanoclusters. (a) The SWV spectra of $Au_{25}(SR)_{18}$, doped $Pd_1Au_{24}(SR)_{18}$ and $Pt_1Au_{24}(SR)_{18}$ nanoclusters. Redrawn from ref. 211 with permission from American Chemical Society, copyright 2015. (b) Electrochemical spectra of $Au_{38}(SR)_{24}$, doped $Pt_2Au_{36}(SR)_{24}$ and $Pd_2Au_{36}(SR)_{24}$ (proposed structures) nanoclusters. Redrawn from ref. 262 with permission from American Chemical Society, copyright 2018. (c) Electrochemical spectra of $M_1Ag_{24}(SR)_{18}$ (M = Ag/Au/Pd/Pt) nanoclusters. Redrawn from ref. 441 with permission from Wiley-VCH, copyright 2016.

7.3 Electroluminescence properties

Electrogenerated chemiluminescence (ECL) or electrochemiluminescence received great interest in these years. Generally, the electroactive nanoclusters are oxidized or reduced at the electrode under appropriate potentials to form active species which will relax to the ground state and emit light. Scheme 3 shows the mechanism of ECL of nanoclusters.[385] Scheme 3a represents the transient oxidative ECL of nanoclusters (at the electrode surface vicinity from negative potential to positive potential): an electron is first injected into the LUMO of [cluster] to generate $[cluster]^{-\bullet}$; then the cathodically produced radicals are oxidized once the electrode potential is stepped below HOMO, producing the excited species [cluster]*, which relaxes to the ground state and emits light. Scheme 3b represents the transient reductive ECL of nanoclusters (from negative potential to positive potential) and the generation of excited species [cluster]* is contrary to the oxidative process. By comparison, Scheme 3c represents the self-annihilation ECL, wherein the diffusive reaction between two types of radical intermediates generates excited [cluster]*, which then releases the energy via photon emission.[385]

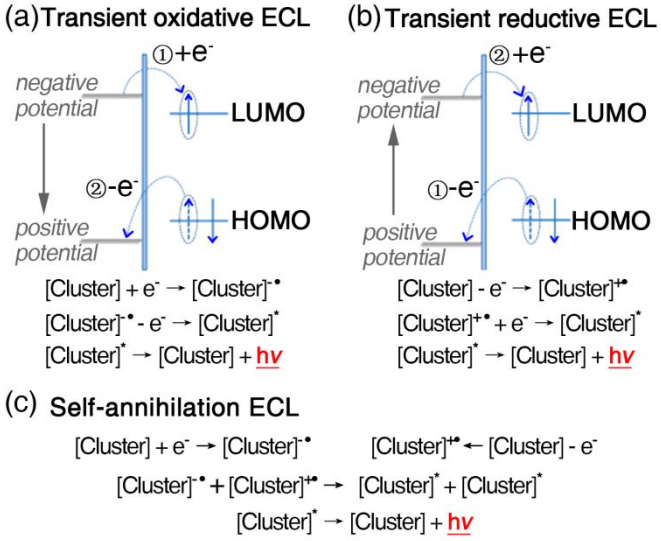

Scheme 3 Illustration of the mechanism of ECL of nanoclusters. Redrawn from ref. 385 with permission from American Chemical Society, copyright 2019.

ECL has been studied on $Au_{25}(SR)_{18}$, $Au_{38}(SR)_{24}$, and $Au_{144}(SR)_{60}$ nanoclusters under co-reactant pathways.[241,605-610] Besides, ECL analysis has been applied to some alloy nanoclusters, which are reviewed in this section.

In 2019, intense NIR ECL from rod-like bimetallic $Au_{12}Ag_{13}(PPh_3)_{10}(SR)_5Cl_2$ was reported by Chen *et al*. (Fig. 35a).[385] With the ECL standard $Ru(bpy)_3$ (bpy: bipyridine) as a reference, the self-annihilation ECL of $Au_{12}Ag_{13}$ was ~10 times higher. More significantly, the co-reactant ECL of $Au_{12}Ag_{13}$ with 1 mM tripropylamine as a co-reactant was ~400 times stronger than $Ru(bpy)_3$. Potential step experiments were performed to capture the transient ECL signals (tens of milliseconds) and decay profiles.[385] A strong and transient self-annihilation ECL of $Au_{12}Ag_{13}$ was detected by activating LUMO and HOMO states sequentially *via* electrode reactions. Besides, based on the key anodic and cathodic activities arising from the energetics of $Au_{12}Ag_{13}$, the ECL generation pathways and mechanism were proposed—the origin of strong ECL in $Au_{12}Ag_{13}$ was attributed to the 13th Ag atom at the sharing vertex position that stabilized the electron on the LUMO orbital and made the rod-like nanocluster more rigid.[385] The insights, elucidated from both femtosecond spectroscopy and DFT calculations, suggested reduced nonradiative decays and thus, enhanced PL and ECL.[370,385] Of note, the ECL intensity of rod-like $Au_{12}Ag_{13}$ is the record-high among all reports.[385]

Wang *et al*. analyzed the ECL of Au/Ag and Pt/Ag nanoclusters.[611] By controlling the pH of the buffer solution to 8.5, the ECL intensity of Au/Ag nanoclusters showed a ~20-fold enhancement. The ECL was remarkably affected by oxygen and hydrogen peroxide, which was attributed to the accelerated production of reactive oxygen species on the nanoclusters. Besides, the ECL was also affected by phenolic artificial estrogens, which in turn, determined their detection limits as low as 700 pg L^{-1} for Au/Ag nanoclusters, and 1.6 ng L^{-1} for Pt/Ag nanoclusters, respectively.[611]

The low ECL efficiency of mono-metallic, GSH-Au nanoclusters limits their applications in ECL sensing. Thus, Xiao and co-workers pursued an alloying strategy to obtain bi-metallic GSH-Au/Ag nanoclusters, finding that the ECL efficiency of the Au/Ag nanocluster/$S_2O_8^{2-}$ system was much higher than that of the homo-gold system.[612] Based on this high ECL property of Au/Ag nanoclusters, an ultrasensitive ECL sensor was constructed for the detection of dopamine (Fig. 35b) as the presence of dopamine would significantly quench the ECL of Au/Ag nanoclusters.[612] The quenching reactions brought by dopamine were proposed as: (i) Au/Ag cluster$^{•}$ + $SO_4^{•}$ → Au/Ag cluster* + SO_4^{2-} and (ii) Au/Ag cluster* → Au/Ag cluster + *hv*. The cluster-based ECL sensor exhibited excellent sensitivity, selectivity, and stability, and had a wide linear range from 10 nM to 1 mM with a low detection limit of 2.3 nM.[612]

A series of GSH-stabilized, Au/Ag nanoclusters *via* controlling the molar ratios of $HAuCl_4/AgNO_3$ precursors were synthesized, and their ECL were analyzed using the trimethylamine (TEA) as a co-reactant.[613] Compared with the mono-metallic Au nanoclusters, Au/Ag nanoclusters exhibited significantly enhanced ECL with decreased peak potential and onset potential, and thus, could be used for sensing Hg^{2+} metal ions. Specifically, as depicted in Fig. 35c, the electron transfer between Au/Ag nanoclusters and TEA resulted in ECL; by comparison, the presence of Hg^{2+} ions would stop the electron transfer, and thus quench ECL. This cluster-based Hg^{2+} sensor exhibited a low detection limit, broad linear range, and good sensitivity and stability.[613]

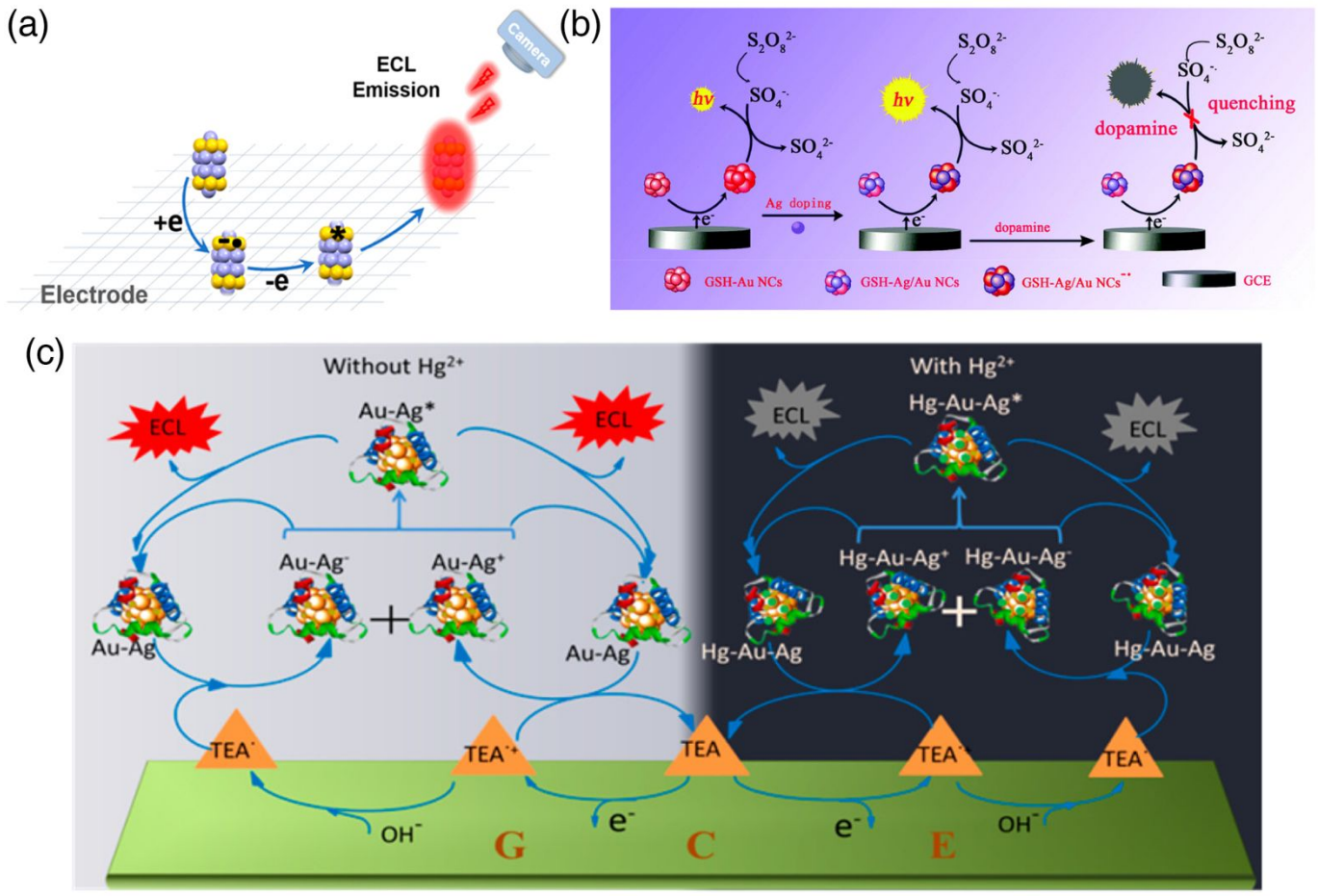

Fig. 35 ECL of alloy nanoclusters. (a) Experimental setup and self-annihilation ECL generation from $Au_{12}Ag_{13}(PPh_3)_{10}(SR)_5Cl_2$. Redrawn from ref. 385 with permission from American Chemical Society, copyright 2019. (b) ECL mechanisms of the Au/Ag nanoclusters/$S_2O_8^{2-}$ system and proposed ECL sensor for dopamine detection. Redrawn from ref. 612 with permission from The Royal Society of Chemistry, copyright 2019. (c) ECL mechanisms of Au/Ag nanoclusters and proposed ECL sensor for Hg^{2+} detection. Redrawn from ref. 613 with permission from American Chemical Society, copyright 2017.

7.4 Magnetic properties

Magnetism in nanoclusters is intriguing, as the number of free electrons in atomically precise nanoclusters can be precisely counted.[614-617] $[Au_{25}(SR)_{18}]^{-1}$ has a superatomic 8-electron configuration, whereas $[Au_{25}(SR)_{18}]^0$ bears 7 electrons, and thus, contains an unpaired electron.[618] Accordingly, the magnetic properties turned from diamagnetism in $[Au_{25}(SR)_{18}]^{-1}$ to paramagnetism in $[Au_{25}(SR)_{18}]^0$.[495,618-620] The Pt- or Pt-doping in $[Au_{25}(SR)_{18}]^0$ is capable of altering the electronic configuration, and further change the magnetic properties of this nanocluster.[216] As shown in Fig. 36, electron paramagnetic resonance (EPR) spectroscopy demonstrates that both $[Pd_1Au_{24}(SR)_{18}]^0$ and $[Pt_1Au_{24}(SR)_{18}]^0$ are diamagnetic, in contrast to the paramagnetic $[Au_{25}(SR)_{18}]^0$.[216] It is suggested that the transformation of the superatom electronic structure from 7-electron of $[Au_{25}(SR)_{18}]^0$ to 6-electron of $[Pd_1Au_{24}(SR)_{18}]^0$ and $[Pt_1Au_{24}(SR)_{18}]^0$ turns the magnetism from paramagnetism to diamagnetism.[216]

Although there is no unpaired electron in the electronic structure of $[Pt_1Au_{24}(SR)_{18}]^0$, the monoanion $[Pt_1Au_{24}(SR)_{18}]^{-1}$ contains an unpaired electron, and is thus EPR active.[222] The EPR signal of $[Pt_1Au_{24}(SR)_{18}]^{-1}$ (g = (2.572, 2.366, 1.749)) is very similar to that of $[Au_{25}(SR)_{18}]^0$ (g = (2.56, 2.36, 1.82)),[618] suggesting that the contribution of spin densities to the 1P superatomic orbitals are comparable between the central Pt in $Pt_1Au_{24}(SR)_{18}$ and the central Au in $Au_{25}(SR)_{18}$.[222]

It is suggested that the most characteristic feature for the planar π-aromatics is its ability to sustain a long-range shielding cone under the magnetic fields oriented in a specific direction.[621] Fedik *et al.* analyzed the aromatic character of $[Au_{13}]^{5+}$ and $[M_1Au_{12}]^{4+/6+}$ (M = Pd, Pt) kernels in $M_1Au_{24}(SR)_{18}$ (M = Au, Pd, Pt) nanoclusters, finding that both $[Au_{25}(SR)_{18}]^-$ and $[M_1Au_{24}(SR)_{18}]^{2-}$ presented inherent spherical aromatic properties ascribed to their icosahedral $[Au_{13}]^{5+}$ and $[M_1Au_{12}]^{4+}$ kernels.[621] However, the $[M_1Au_{12}]^{6+}$ kernels in $[M_1Au_{24}(SR)_{18}]^0$ (M = Pd, Pt) nanoclusters represented a 6e superatom structure, which exhibited characteristics for planar σ-aromatics, totally different from the spherical one in 8e nanoclusters. Accordingly, similar magnetic responses

could be observed in both planar aromatic and spherical aromatic systems of the corresponding M_{25} nanoclusters.[621]

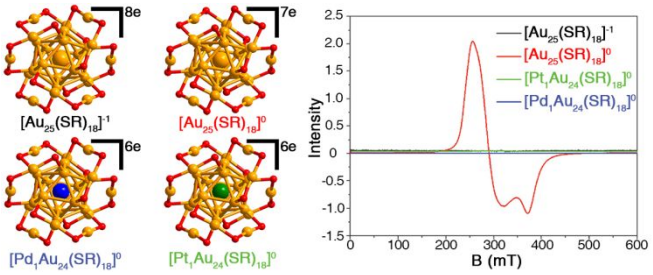

Fig. 36 Magnetism of $Au_{25}(SR)_{18}$-based nanoclusters. Structures and EPR signals of $[Au_{25}(S\text{-}C_2H_4Ph)_{18}]^-$, $[Au_{25}(S\text{-}C_2H_4Ph)_{18}]^0$, $[Pt_1Au_{24}(S\text{-}C_2H_4Ph)_{18}]^0$ and $[Pd_1Au_{24}(S\text{-}C_2H_4Ph)_{18}]^0$ nanoclusters. Redrawn from ref. 216 with permission from The Royal Society of Chemistry, copyright 2016.

7.5 Chiral properties

A chiral nanocluster is non-superimposable with its mirror image, and the chirality in nanoclusters is endowed by their asymmetric structures. Alloying can serve as an effective means to alter the structures of nanoclusters; thus, alloying can be utilized to control the chiral properties.

Yao and co-workers measured the circular dichroism (CD) spectra of –SG protected $Au_{15}(SG)_{13}$, $Au_{18}(SG)_{14}$, and $Au_{25}(SG)_{18}$ nanoclusters.[622,623] All three homo-gold nanoclusters display CD signals in the metal-based electronic transition region (300-600 nm). Upon Ag-doping, the CD responses exhibit quite a difference: (i) the CD signals of $Au_{15}(SG)_{13}$ disappear in $Au_{12.2}Ag_{2.8}(SR)_{13}$; (ii) the non-obvious CD response in $Au_{18}(SG)_{14}$ is enhanced in $Au_{14.4}Ag_{3.6}(SG)_{14}$, with distinct signals at ~280, 310, 340 and 410 nm; (iii) as for $Au_{25}(SG)_{18}$, their CD signals are nearly reversed after Ag-doping.[623]

$Au_{38}(SR)_{24}$ exhibits intense CD responses at 350, 400, 450, 480, 570 and 630 nm.[244] Pd-doping into $Au_{38}(SR)_{24}$ leads to a significant change in CD responses, although the anisotropy factors of $Au_{38}(SR)_{24}$ and $Pd_2Au_{36}(SR)_{24}$ are of similar magnitude.[259] Specifically, the CD signals of $Pd_2Au_{36}(SR)_{24}$ are broader and not as distinct as those of $Au_{38}(SR)_{24}$ (Fig. 37a). In addition, racemization of chiral $Pd_2Au_{36}(SR)_{24}$ occurs at a significantly lower temperature than does the parent $Au_{38}(SR)_{24}$ nanocluster, reflecting in different activation parameters.[259] Bürgi and co-workers proposed that Pd-doping would increase the flexibility of the nanocluster surface, which resulted in weakened CD signals of $Pd_2Au_{36}(SR)_{24}$ compared to $Au_{38}(SR)_{24}$.[259] Similar doping effects are also observed in $Au_{38-x}Ag_x(SR)_{24}$ nanoclusters.[253] As shown in Fig. 37b/c, the more Ag heteroatoms are doped in $Au_{38}(SR)_{24}$, the broader the CD peaks are. Besides, the temperature required for complete racemization follow an order (high to low): $Au_{38}(SR)_{24}$ > $Au_{38-x}Ag_x(SR)_{24}$ (x = 6.5) > $Au_{38-x}Ag_x(SR)_{24}$ (x = 7.9). Significantly, racemization of $Ag_xAu_{38-x}(SR)_{24}$ (x =7.9) occurs even at 20 °C.[253] Therefore, the chiral properties of $Au_{38-x}Ag_x(SR)_{24}$ nanoclusters demonstrate increased flexibility of the surface structure with increasing silver content.[253] The $Cu_1Au_{38}(SR)_{24}$ alloy nanocluster also shows different CD responses with respect to the parent $Au_{38}(SR)_{24}$ nanocluster.[253]

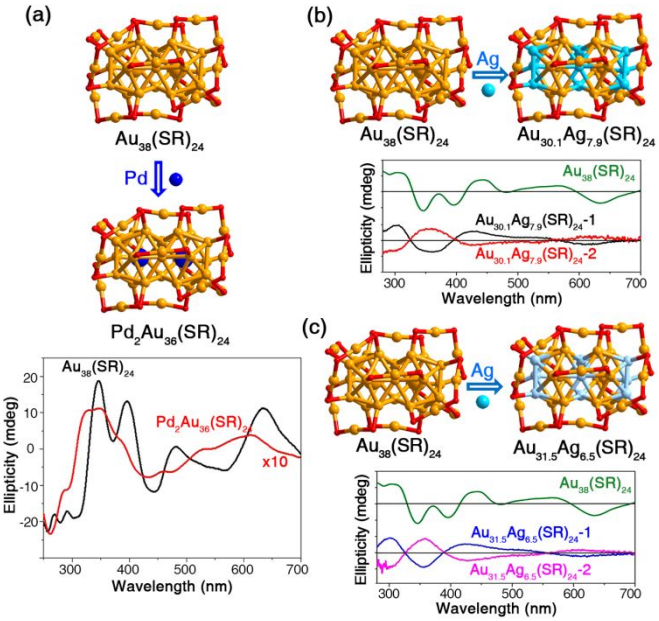

Fig. 37 Doping-induced variations in the chiral properties of nanoclusters. (a) CD spectra of $Au_{38}(SR)_{24}$ and doped $Pd_2Au_{36}(SR)_{24}$ nanoclusters. Redrawn from ref. 259 with permission from American Chemical Society, copyright 2014. (b) CD spectra of $Au_{38}(SR)_{24}$ and doped $Au_{30.1}Ag_{7.9}(SR)_{24}$ nanoclusters. (c) CD spectra of $Au_{38}(SR)_{24}$ and doped $Au_{31.5}Ag_{6.5}(SR)_{24}$ nanoclusters. Redrawn from ref. 253 with permission from American Chemical Society, copyright 2016.

Based on DFT calculations on $Au_{38}(SR)_{24}$ and its Pd- and Ag-doped derivatives, Häkkinen and co-workers proposed a mechanism for chiral inversion that did not require the breaking of Au-S bonds at the metal-ligand interface, but featured a collective rotation of the kernel.[624] The calculated energy barriers of kernel rotation for $Au_{38}(SR)_{24}$ and $Pd_2Au_{36}(SR)_{24}$ are in the range of 1-1.5 eV, significantly lower than the barriers involving breakage of Au-S bonds (2.5 eV). On the other hand, for Ag-doped Au_{38}, the barriers for both mechanisms (kernel rotation and Au-S bond breakage) are similar (1.3-1.5 eV).[624] Such results are in a good agreement with the racemization barriers estimated from the experiments.[624]

7.6 Stability and reactivity

Stability and reactivity are of great significance in the applications of nanoclusters.[14] Alloying serves as a frequently used method to enhance the stability or reactivity of nanoclusters.

Generally speaking, the alloying strategy can be used to enhance the thermal stability of nanoclusters, such as the $Au_{15}Ag_3(SR)_{14}$ nanocluster, which showed no change in its optical absorption spectrum after 24 hours at 60 °C; for comparison, $Au_{18}(SR)_{14}$ showed a decrease in absorption

intensity after 2 hrs and the peaks completely disappeared in ~6 hrs.[256] These results show that the stability of $Au_{18}(SR)_{14}$ was drastically enhanced upon Ag-doping. For $M_{25}(SR)_{18}$, Negishi *et al.* mixed $Au_{25}(SR)_{18}$ and $Pd_1Au_{24}(SR)_{18}$ nanoclusters at 50 °C, and after 30 days, only $Pd_1Au_{24}(SR)_{18}$ survived.[204] Compared to Ag_{44}(*p*-MBA)$_{30}$, the Au-doped $Au_{12}Ag_{32}$(*p*-MBA)$_{30}$ showed enhanced stability at room temperature, with unchanged optical absorption over 30 days (Fig. 38a, middle). Besides, $Au_{12}Ag_{32}$(*p*-MBA)$_{30}$ could sustain at 150 °C for 2 hrs (Fig. 38a, left).[493] However, alloying does not always enhance the thermal stability of nanoclusters. By substituting the central Cu with Au in $Cu_{13}(S_2CN^nBu_2)_6(C{\equiv}CR)_4$, the stability can be enhanced, whereas doping with Ag acts in an opposite way.[518]

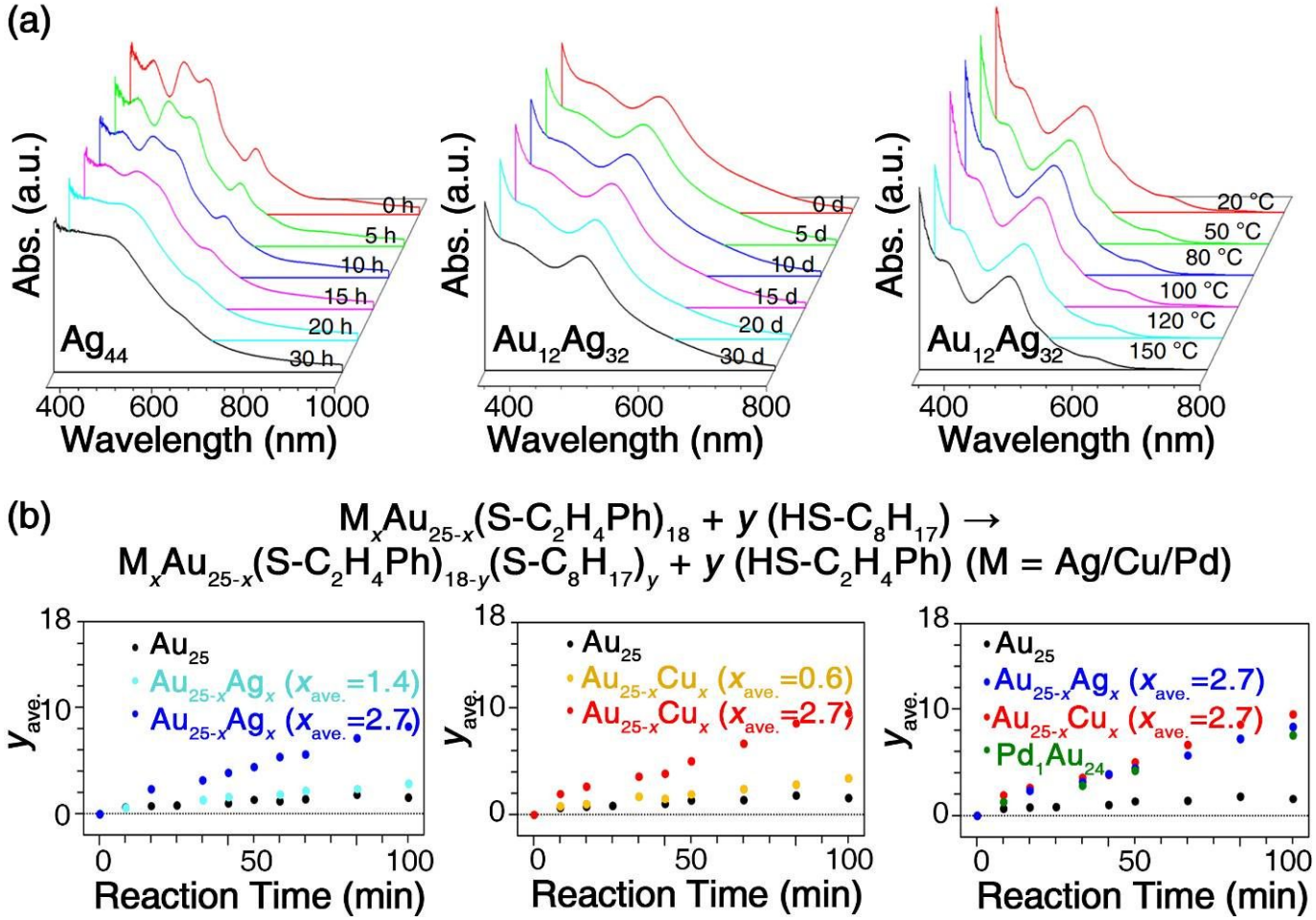

Fig. 38 Doping-induced variations on stability and reactivity of nanoclusters. (a) Doping-induced enhancement in thermal stability from $Ag_{44}(SR)_{30}$ to Au-doped $Au_{12}Ag_{32}(SR)_{30}$ nanoclusters. Redrawn from ref. 493 with permission from Nature Publishing Group, copyright 2017. (b) Comparisons on time-dependent ligand-exchange extents between $Au_{25}(S\text{-}C_2H_4Ph)_{18}$ and its Ag-, Cu-, and Pd-doped nanoclusters upon etching by HS-C_8H_{17}. Redrawn from ref. 180 with permission from American Chemical Society, copyright 2016.

Doping can also tune the reactivity of nanoclusters. Negishi and co-workers investigated the ligand-exchange reactivity of $Au_{25}(SR)_{18}$ and its Pd-, Ag-, and Cu-doped nanoclusters.[180,205] They found that the doped $M_{25}(SR)_{18}$ nanoclusters exhibited remarkably enhanced ligand-exchange reactivity.[180,205] As shown in Fig. 38b, when $Au_{25}(S\text{-}C_2H_4Ph)_{18}$ reacted with HS-C_8H_{17}, only an average of 1.58 S-C_2H_4Ph ligands could be exchanged, while for $Pd_1Au_{24}(SR)_{18}$, ~7.54 S-C_2H_4Ph ligands were exchanged. The Ag- and Cu-doping can also enhance the efficiency in ligand exchange reactions, and the enhancement is more obvious for $Au_{25-x}Cu_x(SR)_{18}$ (Fig. 38b).[180] Besides, the more Ag or Cu heteroatoms are introduced into $Au_{25-x}M_x(SR)_{18}$ (M = Ag/Cu), the more efficient ligand-exchange the nanoclusters exhibit.[180]

By exploiting the free valence electron centralization strategy, Kang *et al.* rendered the moderately stable $Ag_{29}(S_2R)_{12}(PPh_3)_4$ with ultra-stability *via* heteroatom doping.[468] Specifically, the thermal stability of mono-metallic $Ag_{29}(S_2R)_{12}(PPh_3)_4$ (stable at 80 °C) was significantly enhanced in bi-metallic $Ag_{17}Cu_{12}(S_2R)_{12}(PPh_3)_4$ (stable at 110 °C), and even more improved in tri-metallic $Au_1Ag_{16}Cu_{12}(S_2R)_{12}(PPh_3)_4$ (stable at 155 °C, boiling DMF).[468] Due to the differences of metal activity in these alloyed M_{29} nanoclusters, substituting the parent kernel Ag atoms with more inert Au (or exchanging the parent shell Ag atoms with more active Cu)

would concentrate the free electrons from the outer shell to the inner kernel. Thus, the kernel metals would more likely present a M^0 state, while the shell metals will be in more oxidized states (i.e., $M^{\delta+}$). This phenomenon can also be understood by the different electronegativity of group 11 atoms (i.e., Cu < Ag < Au), as atoms of lower electronegativity tend to transfer partial charge to those of higher electronegativity.[279] Consequently, the obtained alloy nanoclusters possess a surface that is harder to be oxidized and thus, higher thermo-stability relative to the parent Ag_{29} nanocluster.[468]

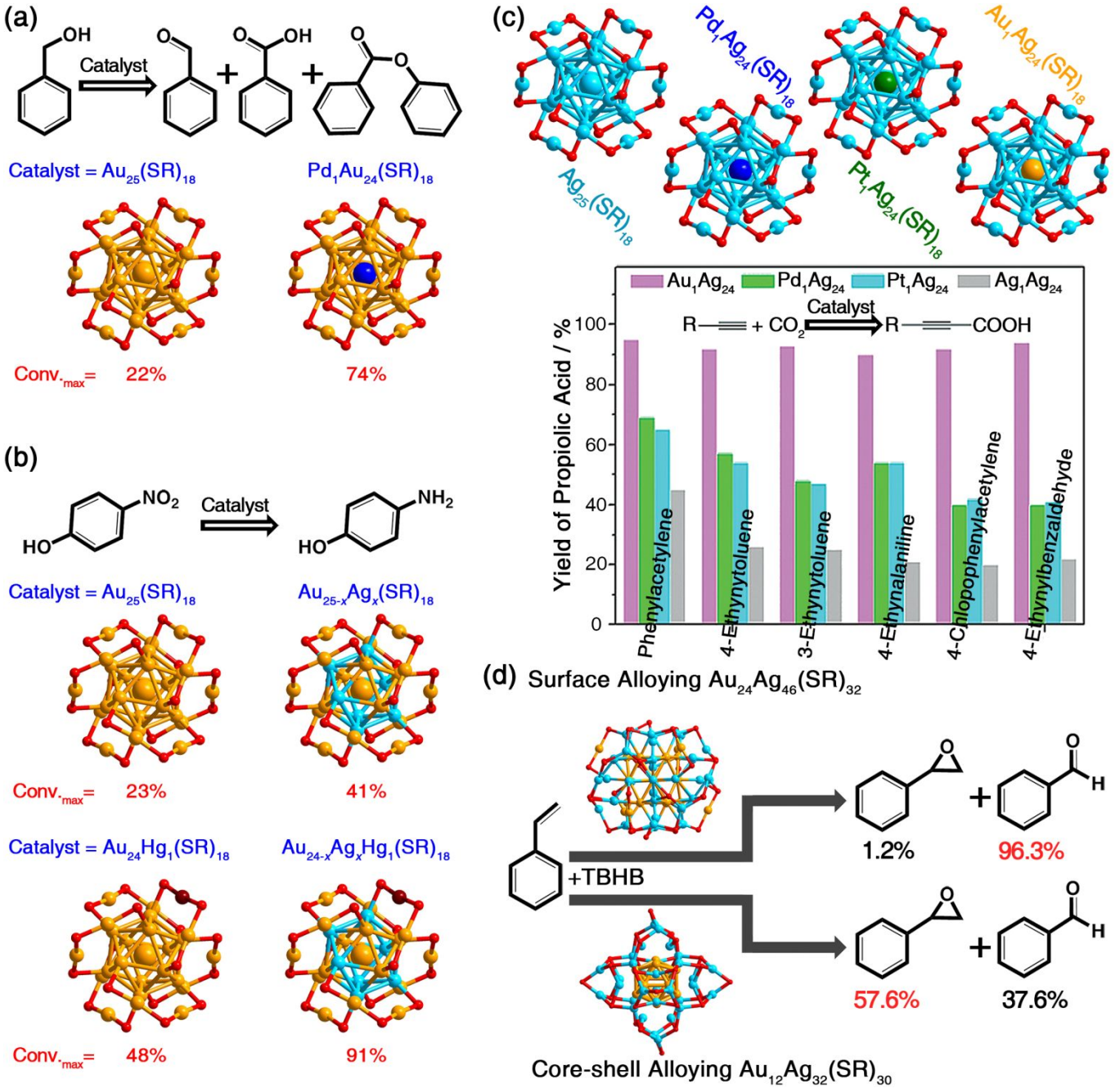

Fig. 39 Catalysis by alloy nanoclusters. (a) Enhancement in aerobic alcohol oxidation catalyzed by mono-Pd doped $Pd_1Au_{24}(SR)_{18}$. Data are from ref. 64. (b) Catalytic activities of the mono-metallic $Au_{25}(SR)_{18}$, bi-metallic $Au_{25-x}Ag_x(SR)_{18}$ and $Au_{24}Hg_1(SR)_{18}$, and tri-metallic $Au_{24-x}Ag_xHg_1(SR)_{18}$ nanoclusters in reducing 4-nitrophenol to 4-aminophenol. Data are from ref. 521. (c) Catalytic carboxylation of terminal alkynes with CO_2 over $Ag_{25}(SR)_{18}$ or $Au_1Ag_{24}(SR)_{18}$, $Pt_1Ag_{24}(SR)_{18}$, $Pd_1Ag_{24}(SR)_{18}$ nanoclusters. Redrawn from ref. 440 with permission from Wiley-VCH, copyright 2018. (d) Catalytic activities and selectivities in styrene oxidation over surface-alloyed $Au_{24}Ag_{46}(SR)_{32}$ and core-shell alloyed $Au_{12}Ag_{32}(SR)_{30}$. Data are from ref. 549.

Based on $M_{29}(S\text{-}Adm)_{18}(PPh_3)_4$ (M = Ag/Au/Pt/Pd/Cu) nanoclusters, Kang *et al*. investigated the inter-metallic synergy effects on their thermal stability by monitoring the time-dependent optical absorption of these nanoclusters.[448] Some structure-stability correlations were obtained: (i) for the kernel (M = Ag/Au/Pt/Pd), the stability sequence is $Pd_1M_{28} < Ag_1M_{28} < Au_1M_{28} \approx Pt_1M_{28}$; (ii) for the 2nd-shell (M = Ag/Cu), substituting the $Ag_{12}(SR)_{18}$ shell with $Cu_{12}(SR)_{18}$ enhances the stability; and (iii) for the vertex position (M = Ag/Cu/Au), the stability sequence is $M_{25}Cu_4 > M_{25}Ag_4 >> M_{25}Au_4$. These correlations between the metal positions and the stability of nanoclusters agree with the energy changes of nanoclusters derived from DFT calculations.[448]

8 Applications of Alloy Nanoclusters

Alloying is able to endow nanoclusters with enhanced chemical/physical properties (*e.g.*, PL properties), which have been reviewed in Section 7. Furthermore, such enhanced properties provide alloy nanoclusters with more potential in applications. In this section, the applications of alloy nanoclusters are reviewed, including catalysis and optical applications.

8.1 Catalysis by alloy nanoclusters

Compared to mono-metallic nanoclusters, alloy nanoclusters have shown great potential for many important chemical transformation reactions owing to their enhanced activity and selectivity induced by intermetallic synergies.[625]

Tsukuda and co-workers loaded $Au_{25}(SR)_{18}$ or $Pd_1Au_{24}(SR)_{18}$ nanoclusters onto multiwalled carbon nanotubes, and compared the catalytic performance of these composites in aerobic oxidation of benzyl alcohol.[64] The mono-Pd doped nanocluster remarkably improved the conversion from 22% for $Au_{25}(SR)_{18}$ to 74% (Fig. 39a).[64] Yao *et al*. incorporated two additional Ag heteroatoms onto the surface of $Au_{25}(SR)_{18}$, and the alloyed $Ag_2Au_{25}(SR)_{18}$ nanocluster displayed enhanced catalytic conversion to 52% for hydrolysis of 1,3-diphenyl-2-propynyl acetate (c.f. only 11% conversion over $Au_{25}(SR)_{18}$).[184] Yan *et al*. obtained a correlated series of nanoclusters from mono-metallic $Au_{25}(SR)_{18}$ to bi-metallic $Au_{25-x}Ag_x(SR)_{18}$ and $Au_{24}Hg_1(SR)_{18}$, and tri-metallic $Au_{24-x}Ag_xHg_1(SR)_{18}$, and compared their catalytic activities in reducing 4-nitrophenol.[521] As shown in Fig. 39b, the catalytic yields over Au_{25}, $Au_{25-x}Ag_x$, $Au_{24}Hg_1$, and $Au_{24-x}Ag_xHg_1$ nanoclusters are 23%, 41%, 48%, and 91%, respectively.[521] Alloying the DNA-stabilized Ag nanoclusters with Pd, Au, or Pt heteroatoms can enhance the catalytic efficiency in reducing 4-nitrophenol to 4-aminophenol.[626] Li and co-workers enhanced the CO oxidation performance of $Au_{25}(SR)_{18}$ by Ag- or Cu-doping, and DFT calculations suggested that the enhanced adsorption of CO on the nanocluster surface induced by Cu or Ag heteroatoms resulted in the enhancement of catalytic activity.[181] Wu and co-workers alloyed $Au_{25}(SR)_{18}$ with $Cd(PPh_3)_2(NO_3)_2$, and obtained a Cd_5Au_{26} alloy nanocluster.[627] For comparison, $Au_{25}(SR)_{18}$ exhibited no catalytic activity toward A^3-coupling reaction between phenylacetylene, benzaldehyde, and pyrrolidine, but Cd_5Au_{26} showed a high catalytic activity (up to 92% conversion) as well as good recyclability and substrate tolerance. The remarkably enhanced catalytic activity was attributed to the cooperation between Cd and adjacent Au atoms in the nanocluster.[627] The PVP-stabilized Au_{34} nanoclusters displayed a relatively low conversion (< 1%) for the hydrogenation of C=C bonds in 1-dodecene, styrene, and cyclooctene, while upon Pd- or Rh-alloying, the catalytic activities were significantly enhanced.[583] For example, the catalytic conversion over PVP-Au_{34} in hydrogenating styrene was only 1%, whereas PVP-Pd_1Au_{33} and PVP-Rh_1Au_{33} showed remarkably enhanced conversions of 33% and 95%, respectively.[583]

Based on $Ag_{25}(SR)_{18}$ and doped $Au_1Ag_{24}(SR)_{18}$, $Pt_1Ag_{24}(SR)_{18}$, $Pd_1Ag_{24}(SR)_{18}$ nanoclusters, the doping effects on catalytic performance were investigated in the carboxylation reaction of CO_2 with terminal alkyne through C-C bond formation to produce propiolic acid.[440] As shown in Fig. 39c, Au-, Pd-, and Pt-doping are all able to enhance the catalytic activity of $Ag_{25}(SR)_{18}$ in carboxylation reactions. The order of catalytic activity is $Au_1Ag_{24}(SR)_{18} > Pd_1Ag_{24}(SR)_{18} \approx Pt_1Ag_{24}(SR)_{18} > Ag_{25}(SR)_{18}$.[440]

The ultra-stable $Au_1Ag_{16}Cu_{12}(S_2R)_{12}(PPh_3)_4$ was obtained by doping $Ag_{29}(S_2R)_{12}(PPh_3)_4$ with Au and Cu heteroatoms.[468] Owing to its high stability, $Au_1Ag_{16}Cu_{12}(S_2R)_{12}(PPh_3)_4$ enabled the multicomponent A^3 coupling reaction at high temperatures, which remarkably shortened the catalytic reaction time from ~24 h in previous works to 3 min, with high conversion, good selectivity, and excellent recyclability.[468]

Wang *et al*. explored the alloying effects of surface-alloying in $Au_{24}Ag_{46}(SR)_{32}$ and core-shell alloying in $Au_{12}Ag_{32}(SR)_{30}$ for the reaction of styrene oxidization.[549] As shown in Fig. 39d, epoxide and benzaldehyde are the major products in the styrene oxidation. The surface-alloying in the $Au_{24}Ag_{46}(SR)_{32}$/CNT (*i.e.*, nanoclusters loaded on multi-walled carbon nanotubes) catalyst displayed high selectivity for benzaldehyde (96.3%), whereas the core-shell alloying in the $Au_{12}Ag_{32}(SR)_{30}$/CNT composite showed a much higher epoxide selectivity (57.6%).[549] In follow-up works, styrene oxidation was used for evaluating the catalytic conversion and selectivity over $Au_{25}(SR)_{18}$, $Ag_{44}(SR)_{30}$, $Au_{25-x}Ag_x(SR)_{18}$, and $Au_{12}Ag_{32}(SR)_{30}$ nanoclusters.[628] The catalytic results demonstrated that the silver atoms in alloy nanoclusters were responsible for the high selectivity for benzaldehyde and the gold atoms were responsible for the high conversion.[628]

The Au/Ag synergistic effect in the alkynylation of CF_3-ketone was evaluated over bi-metallic $Au_1Ag_{24}(SR)_{18}$ and $Au_{25-x}Ag_x(SR)_{18}$ (x = 2-6) nanoclusters, and their corresponding mono-metallic counterparts ($Ag_{25}(SR)_{18}$ and $Au_{25}(SR)_{18}$) were used as reference catalysts.[629] By a combination of experimental and theoretical analyses, Sun *et al*.

demonstrated that the Au@Ag kernel (*i.e.*, M_{13} icosahedral kernel) was essential for high activity and stability in the cluster-catalyzed alkynylation of CF_3-ketone. Besides, such a structure-property correlation was extended to other Au/Ag bi-metallic nanoclusters such as $Au_{12}Ag_{32}(SR)_{30}$, which brought more opportunities for designing alloy catalysts with high reactivity and stability.[629]

Du *et al*. compared the photocatalytic activities of $Ag_{25}(SR)_{18}$ and $Pt_1Ag_{24}(SR)_{18}$ nanoclusters (loaded on graphitic carbon nitride ($g\text{-}C_3N_4$)) in hydrogen evolution, and $Pt_1Ag_{24}(SR)_{18}/g\text{-}C_3N_4$ displayed the highest photocatalytic activity, which was ~330 times and ~4 times higher than bare $g\text{-}C_3N_4$ and $Ag_{25}(SR)_{18}/g\text{-}C_3N_4$, respectively (Fig. 40a).[630] Such catalysts were further compared *via* various photo-electrochemical characterizations to investigate the detailed alloying effects. Unlike bare $g\text{-}C_3N_4$ and $Ag_{25}(SR)_{18}/g\text{-}C_3N_4$, $Pt_1Ag_{24}(SR)_{18}/g\text{-}C_3N_4$ showed a remarkably reduced semicircle in the Nyquist plot (Fig. 40a, bottom-left), demonstrating that a small barrier of photocarrier transfer could be achieved based on the $Pt_1Ag_{24}(SR)_{18}/g\text{-}C_3N_4$ composite. In addition, photocurrent *versus* time curves of these catalysts were compared (Fig. 40a, bottom-right), and $Pt_1Ag_{24}(SR)_{18}/g\text{-}C_3N_4$ displayed a significant photocurrent enhancement compared to $Ag_{25}(SR)_{18}/g\text{-}C_3N_4$, not to mention the pristine $g\text{-}C_3N_4$.[630]

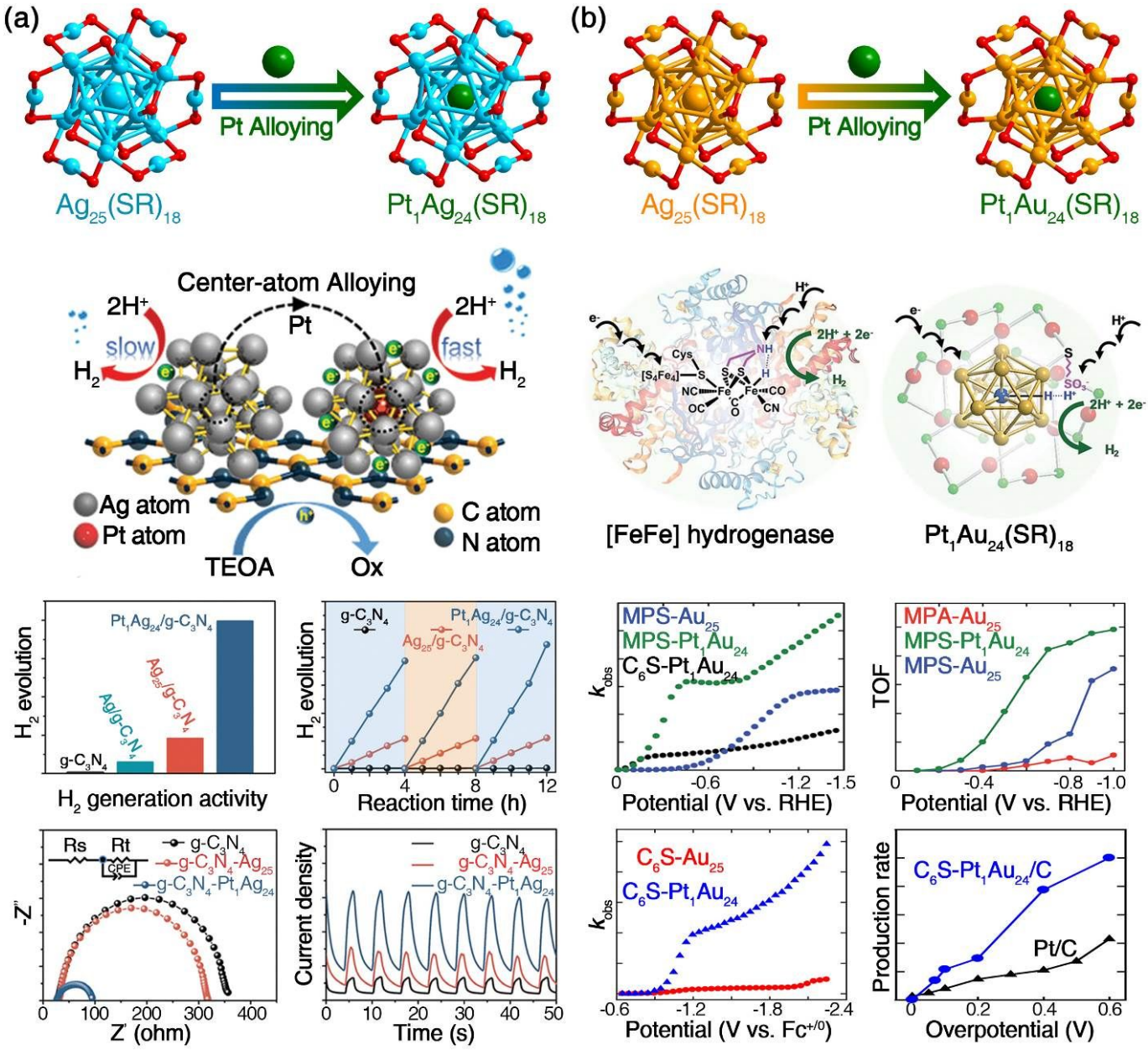

Fig. 40 Alloy nanoclusters for photocatalytic/electrocatalytic hydrogen production. (a) Enhanced efficiency of $Pt_1Ag_{24}(SR)_{18}$ over $Ag_{25}(SR)_{18}$ in photocatalytic hydrogen evolution. Redrawn from ref. 630 with permission from The Royal Society of Chemistry, copyright 2017. (b) Enhanced efficiency of $Pt_1Au_{24}(SR)_{18}$ over $Au_{25}(SR)_{18}$ in electrocatalytic hydrogen production. Redrawn from

ref. 217 with permission from the Nature Publishing Group, copyright 2017. Redrawn from ref. 219 with permission from The Royal Society of Chemistry, copyright 2018.

The visible-light-induced catalytic denitrification coupling of benzylamine by nanoclusters was investigated on the $Au_{25}(SR)_{18}$, $Ag_{25}(SR)_{18}$, and $Au_{25-x}Ag_x(SR)_{18}$ nanoclusters.[631] Basically, two products were observed in the oxidation of benzylamine — *N*-benzylidenebenzylamine and aldimine — the former was the desired product. The $Ag_{25}(SR)_{18}$ gave a complete conversion (100%), but with a relatively low selectivity for *N*-benzylidenebenzylamine (29.1%). The $Au_{25}(SR)_{18}$ showed a higher selectivity (~70%) and a conversion of ~80%. Significantly, the bi-metallic $Au_{25-x}Ag_x(SR)_{18}$ nanoclusters were found to be the best among these catalysts, exhibiting a complete conversion (> 99%) and an exclusive selectivity (100%).[631]

Lee's group investigated the alloying effects on hydrogen evolution reaction (HER) catalyzed by Pt- and Pd-doped $M_1Au_{24}(SR)_{18}$ and $M_2Au_{36}(SR)_{24}$ nanoclusters.[217-219,632] Similar to the hydrogenase enzymes that showed active sites at the intersection of an electron-transport chain and a proton-transport chain (*e.g.*, [FeFe] hydrogenase, shown in Fig. 40b, middle-left),[633-635] the nanoclusters possessed similar configurations containing several intersected $M_x(SR)_y$ staple motifs (shown in Fig. 40b, middle-right), and thus, these nanoclusters showed high electrocatalytic activity in HER.[217-219] The k_{obs} was used to define the efficiency of HER, and $Pt_1Au_{24}(SR)_{18}$ (SR = 3-mercapto-1-propanesulfonic acid, MPS, or 1-hexanethiolate, C_6S) nanoclusters showed remarkably enhanced k_{obs} values relative to their homo-gold counterparts (Fig. 40b, bottom-left).[217,219] Significantly, the HER efficiency of the $Pt_1Au_{24}(SR)_{18}$-based catalysts was determined as 25 mol g^{-1} h^{-1}, which was more than two times higher than that of the benchmarking Pt/C-based catalyst (11 mol g^{-1} h^{-1}) at the same overpotential of 0.6 V.[217] Lee and co-workers also demonstrated that Pt- and Pd-doping were able to enhance the catalytic efficiencies of $Au_{38}(SR)_{24}$ in HER.[632] DFT calculations reveal that the hydrogen adsorption free energy (ΔG_H) is significantly reduced in doped nanoclusters, with the order of $Au_{25}(SR)_{18}$ > $Pd_1Au_{24}(SR)_{18}$ > $Pt_1Au_{24}(SR)_{18}$ and similarly, $Au_{38}(SR)_{24}$ > $Pd_2Au_{36}(SR)_{24}$ > $Pt_2Au_{36}(SR)_{24}$, indicating that hydrogen adsorption on active sites is thermodynamically favored by Pd- or Pt-doping.[632] The doped metals, albeit buried in the kernel of $Au_{25}(SR)_{18}$ and $Au_{38}(SR)_{24}$, have a profound impact on the HER activity by altering the reduction potentials and hydrogen adsorption free energies of the corresponding nanoclusters.[632]

The electrocatalytic activities of $Au_{25}(SR)_{18}$ and $Pt_1Au_{24}(SR)_{18}$ were compared in direct oxidation of formic acid into carbon dioxide.[636] It was observed that $Au_{25}(SR)_{18}$ was inactive in this catalytic reaction, but $Pt_1Au_{24}(SR)_{18}$ exhibited a relatively high activity of 3.7 A mg_{Pt+Au}^{-1}, which was 12 and 34 times greater than Pt nanoclusters and commercial Pt/C catalysts, respectively. DFT calculations also demonstrated the importance of Pt-doping in reducing the energy barrier of formic acid oxidation.[636]

Negishi and co-workers studied the heteroatom doping effect of the co-catalyst on water-splitting activity by loading $Pd_1Au_{24}(SR)_{18}$ or $Pt_1Ag_{24}(SR)_{18}$ nanoclusters on $BaLa_4Ti_4O_{15}$ (one of the most advanced photocatalysts).[637] Experimental results of these photocatalysts revealed the following three features of heteroatom doping on cocatalysts: (i) Pd was located on the surface of the cluster cocatalyst, whereas Pt was at the interface between the cluster cocatalyst and the photocatalyst; (ii) Pd doping decreased the water-splitting activity, whereas Pt doping improved it; and (iii) the doping position of the heteroatom considerably contributed to the doping effect.[637]

In parallel with the experimental results, DFT calculations were performed to investigate the mechanisms of (i) alloying-induced enhancement in catalytic activities, and (ii) atomically precise processes of catalysis based on alloy nanoclusters.[217,218,632,636-640] Based on these DFT calculations, alloying can promote the catalytic processes because of its capability in changing the adsorption energy of substrates (i.e. reactants), helping the stabilization of catalytic intermediates, and reducing the energy barrier of the reactions.[217,218,632,636-640]

8.2 Nanocluster-based, fluorescent sensors for detection of toxic ions

Fluorescent alloy nanoclusters have been developed as highly sensitive and selective sensors for detecting metal ions. In this section, nanocluster-based sensors for detecting various ions are reviewed.

Jiang *et al.* prepared red fluorescent BSA-Au nanoclusters that emitted at 620 nm,[641] and the presence of Ag^+ ions would not only blue-shift the emission to 585 nm, but also enhance the PL intensity significantly. By contrast, all other metal ions (such as Au^{3+}, Ca^{2+}, Mn^{2+}, *etc*.) induced comparable emission intensities of this nanocluster, while Hg^{2+} completely quenched the emission. Besides, based on PL-enhanced BSA-Au/Ag alloy nanoclusters, the addition of Hg^{2+} ions also quenched the emission (Fig. 41a). Accordingly, the fluorescent BSA-Au nanoclusters could serve as a versatile sensor for selectively detecting both Ag^+ and Hg^{2+} ions.[641]

Chen and co-workers prepared a mercaptosuccinic acid (MSA) stabilized fluorescent Au/Ag alloy nanocluster, and further capped it with methoxy-poly(ethylene glycol)-NH_2 (m-PEG-NH_2).[642] The as-prepared alloy nanocluster emitted at 637 nm, and as the presence of Al^{3+} ions significantly enhanced the fluorescence, the PEGylated MSA-Ag/Au nanocluster could serve as a highly selective and sensitive sensor for detecting Al^{3+} ions in aqueous solution, with a detection limit of 0.8 μM (Fig. 41b).[642]

Sannigrahi *et al*. prepared a series of SG-protected Au/Ag alloy nanoclusters with tunable NIR fluorescence, and the PL intensity of such clusters could be significantly enhanced by the addition of Pb^{2+} ions.[643]

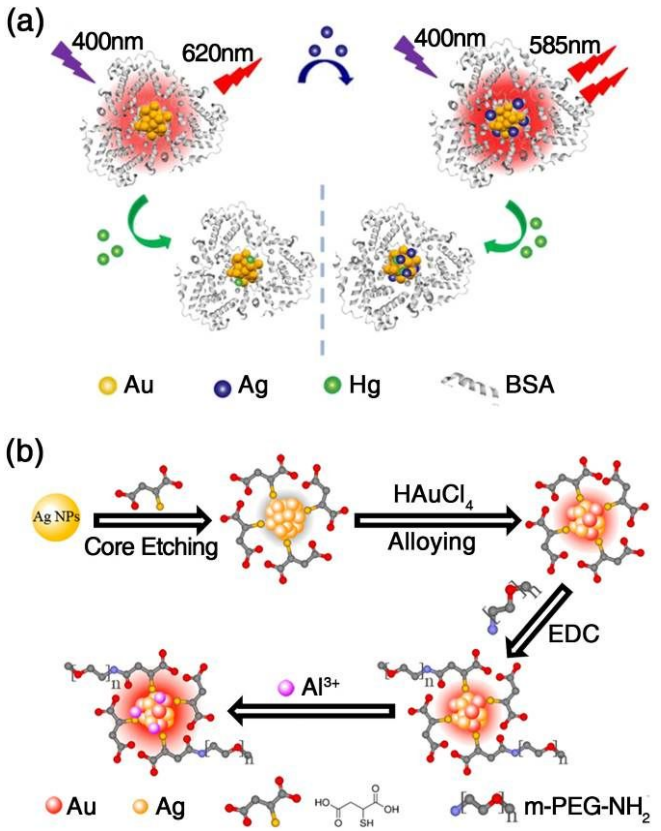

Fig. 41 Metal-ion detection based on fluorescent alloy nanoclusters. (a) Schematic illustration of the Ag^+ and Hg^{2+} effects on the fluorescent BSA-Au and BSA-AuAg nanoclusters. Redrawn from ref. 641 with permission from The Royal Society of Chemistry, copyright 2018. (b) AuAg alloy nanoclusters as a fluorescence-enhanced probe for Al^{3+} sensing. Redrawn from ref. 642 with permission from American Chemical Society, copyright 2013.

8.3 Other applications of alloy nanoclusters

Some alloy nanoclusters have been used for labeling cells owing to their (i) strong luminescence, (ii) ultra-small size, (iii) ability to easily enter cells, (iv) good biocompatibility, and (v) good photo-stability.[368,587] Wang *et al*. prepared $Au_{25-x}Ag_x(PPh_3)_{10}(SC_2H_4OH)_5Cl_2$ (x < 13) alloy nanoclusters with red-emission at 633 nm, displaying good water solubility and capability in labeling the living cells (e.g., human cancer cell 7402, Fig. 42a). The wide excitation range and the red emission make these nanoclusters feasible for simultaneous use with other dyes having emissions shorter than 600 nm (*e.g.*, the most MitoTracker and LysoTracker) without any interference (Fig. 42a). Further cytotoxicity test demonstrated that these nanoclusters showed no cytotoxicity after a long period of incubation in cells.[368] Li and co-workers found that the phosphorescent $C@Au_6Ag_2$ alloy cluster selectively stained the nucleolus of LO_2, Hela, and KB cells (Fig. 42b) with a much lower uptake in the nucleus and cytoplasm, and exhibited excellent photo-stability. Thus, $C@Au_6Ag_2$ alloy is a very attractive phosphorescent staining reagent for visualizing the nucleolus of living cells.[587]

Zan *et al*. synthesized a series of $Ag_{44-x}Au_x$ nanoclusters capped by tiopronin (abbrev. Tio, a thiol) and further modified these nanoclusters with doxorubicin (DOX, an anticancer drug for a wide range of malignancies).[644] The obtained $Ag_{44-x}Au_x$-Tio-DOX showed a red, intense emission at 595 nm, and could be used as a multifunctional cancer therapy platform with both imaging and therapy activities, and thus had potential in anti-cancer diagnosis.[644]

Yang *et al*. prepared $C@Au_6Ag_2$ alloy complex capped by 2-(diphenylphosphino)-5-pyridinecarboxaldehyde, and the terminal aldehyde groups on the surface were able to link the dissociative mono-amines in solution.[590] Significantly, the adsorption of chiral mono-amine induced the asymmetric torsion of the complex, and therefore, the *R*-Ag_2Au_6 and *S*-Ag_2Au_6 enantiomers were obtained and showed opposite CD signals (Fig. 42c, left).[590] Besides, a linear relationship was determined between the *e.e.* values of introduced chiral mono-amines (1-phenylethylamine, 1-cyclohexylethylamine, or 2-aminooctane) and the intensity of CD signals (Fig. 42c, right).[590]

9 Conclusions and Perspectives

Atom-precise alloying has shown its unique capability in dictating the electronic/geometrical structures and tuning the chemical/physical properties of mono-metal nanoclusters. To date, Au, Ag, Pt, Pd, Cu, Cd, Hg, Ir, *etc*., have been incorporated into the templates, resulting in bi-, tri-, and multi-metallic nanoclusters. Different metal atoms with distinct electronic configurations and physicochemical characteristics adopt different alloying modes, i.e., different heteroatom(s) follow unique doping preference. For example, based on $Au_{25}(SR)_{18}$, only one Pt/Pd can be doped into the central position,[216] whereas more than one Ag atoms can be incorporated, and they tend to be arranged on the icosahedral-kernel shell.[174] On the other hand, for the templates that are not electronic shell-closing, e.g., $Au_{21}(SR)_{15}$ and $Au_{23}(SR)_{16}$, structural transformation may be triggered by alloying.

Collectively, based on different types of heteroatoms, nanocluster templates, and doping modes, alloy nanoclusters have presented their explosive developments in terms of syntheses, characterizations, and structural determinations.

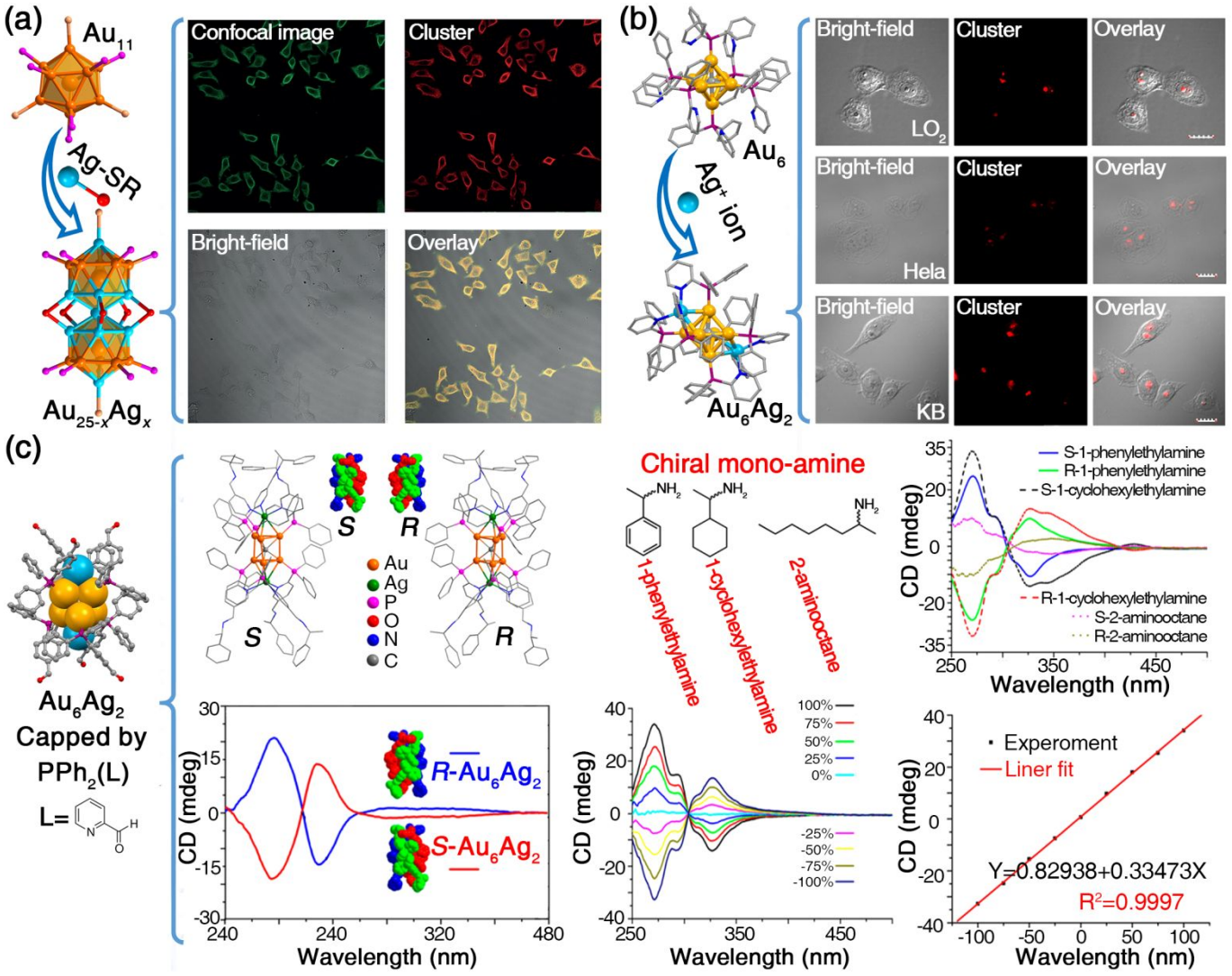

Fig. 42 Applications of alloy nanoclusters in cell labeling and chiral sensing. (a) Rod-like $Au_{25-x}Ag_x(PPh_3)_{10}(SR)_5Cl_2$ alloy nanoclusters used for labeling cancer cells (7402). Redrawn from ref. 368 with permission from Wiley-VCH, copyright 2014. (b) Fluorescent $C@Au_6Ag_2$ alloy complex used for labeling the LO_2, Hela, and KB cells. Redrawn from ref. 587 with permission from Elsevier Ltd., copyright 2013. (c) $C@Au_6Ag_2$ alloy complex used for sensing chiral mono-amines. Redrawn from ref. 590 with permission from American Chemical Society, copyright 2013.

Alloying is also able to tune the chemical/physical properties of homo-metal nanoclusters, including the optical, electrochemical, magnetic and chiral properties, as well as stability and reactivity. Owning to the inter-metallic synergistic effects, alloy nanoclusters often possess enhanced PL and catalytic activity compared to homo-metal counterparts. Furthermore, alloying effects on structures can be directly related to their properties at the atomic level, which further guides researchers to prepare more alloy nanoclusters with novel geometrical/electronic structures as well as desirable properties. Consequently, the enhanced properties endow alloy nanoclusters with potentials in many applications, such as catalysis, chemical sensing, bio-imaging, and so on.

Several perspectives are discussed herein.

1. Development of new alloying methods for novel alloy nanoclusters. Different synthetic methods have displayed their uniqueness in doping processes. For instance, Pt- and Pd-doped nanoclusters can only be prepared by the *in-situ* synthetic method;[63,204,258,262,435] and the Ir doping in $Au_{25}(SR)_{18}$ is only accomplished *via* the inter-nanocluster reaction method;[173] the metal-exchange method provides a facile approach for meticulously controlling the metal compositions of alloy nanoclusters.[174] The driving force of metal replacement (galvanic replacement, GR) in bulk metals is attributed to the difference in electrochemical potentials,[5,645] however, when the size of nanoparticles is below 3 nm (nanoclusters), anti-GR (AGR) reactions may occur.[80,186] Although many types of atoms have been used to prepare alloy nanoclusters, most of them are from groups 9-12, and introducing other types of atoms (*e.g.*, Fe, Mn, Co, W) remains challenging. Thus, new methods are still needed to prepare novel alloy nanoclusters.

2. Ligand-effected control over the composition of alloy nanoclusters. While there has been much work on the exploration of ligands (e.g., o-/m-/p-Me-Ph-SH for size control of homometal nanoclusters), their effects on alloy nanocluster composition remains elusive. Experimentally, it was found that the reduction of Au/Cu-SC_2H_4Ph precursors resulted in $Au_{25-x}Cu_x(SC_2H_4Ph)_{18}$ containing up to 4 Cu atoms only,[67] but selenolate-protected $Au_{25}(SePh)_{18}$ was found to be able to accommodate up to 9 Cu, and the resulting bimetallic nanoclusters are also more stable than $Au_{25-x}Cu_x(SC_2H_4Ph)_{18}$.[68] In another case, all Ag heteroatoms are on the icosahedral kernel's surface in $Au_{25-x}Ag_x(SC_2H_4Ph)_{18}$ nanoclusters,[66] while in the case of cyclic hexanethiolate protection, heavy-doping led to Ag atoms on the staple motifs of $Au_{25-x}Ag_x(SC_6H_{11})_{18}$ (x ~19) in addition to the kernel's surface.[179] These ligand-induced alterations in doping modes would help in completing the mechanisms for doped nanoclusters.

3. There is much room for improvement via alloying-triggered structural transformation. Although $Au_{23}(SR)_{16}$ can be subject to slight-doping without changing the structure, upon higher doping, the nanocluster undergoes transformations to form $Au_{19}Cd_2(SR)_{16}$, $Au_{20}Cd_4(SH)(SR)_{19}$, and $Au_{25-x}Ag_x(SR)_{18}$ of different structures. Based on precursors of different Au:Ag ratios, a correlated series of $Au_{21}(SR)_{15}$, $Au_{20}Ag_1(SR)_{15}$, $Au_{19}Ag_3(SR)_{15}$, and $Au_{23-x}Ag_x(SR)_{15}$ (x >4) of different structures can be obtained.[279] The starting homo-gold nanoclusters which do not have electronic shell-closing configurations might be responsible for the structural transformations, providing great potentials to achieve novel structures.

4. Asymmetric doping or alloying as a new "dimension". The preferences of heteroatom(s) in templates are symmetry-related, and for alloy nanoclusters of specific magic sizes, distributions of different atoms are corresponding to the structural symmetries as well. Under such circumstances, asymmetrically alloyed nanoclusters, e.g., $Au_{16}Ag_1(SR)_{13}$, $Au_{20}Ag_1(SR)_{15}$, $Au_{19}Ag_4(SR)_{15}$, $Au_{20}Cd_4(SH)(SR)_{19}$, become very informative, and their mechanisms require further elucidation *via* both experiment and calculation. Besides, asymmetric alloying generally results in more distorted structures, bringing about anisotropic properties to the nanoclusters which could be important but have not been discussed yet.

5. Shifting the "transition region" from plasmonic (or metallic) to non-metallic for nanoclusters by alloying. To date, the largest Au nanocluster with structure elucidation is $Au_{279}(SR)_{84}$,[418,419] and a sharp transition from plasmonic to molecular state occurs between $Au_{246}(SR)_{80}$ and $Au_{279}(SR)_{84}$.[419] On the other hand, the "transition region" of Ag nanoclusters moves to much smaller sizes.[427] Thus, alloying is expected to alter the boundary between metallic and non-metallic states. Alloy nanoclusters with large sizes, $Au_{130-x}Ag_x(SR)_{50}$ and $Au_{52}Cu_{72}(SR)_{55}$, still show non-metallic properties,[552,646] although Ag or Cu atoms outnumber Au in these cases. Whether $Au_{144}(SR)_{60}$ is metallic or non-metallic is still controversial based on femtosecond time-resolved transient absorption spectroscopy.[647,648] Upon doping, $Au_{144-x}Ag_x(SR)_{60}$ shows non-metallic optical peaks,[406] while that of $Au_{144-x}Cu_x(SR)_{60}$ is plasmon-like.[413] Therefore, doping/alloying on nanoclusters of large sizes is worth studying in the future.

6. Supplementary methods in addition to SC-XRD for more precise site-determination of heteroatoms. The alloying sites of different atoms in nanoclusters are of great significance for investigating the alloying mechanisms. The structural determination based on SC-XRD is the most precise way to identify the alloying sites no matter for template doping or for specific multi-metallic structures. However, due to the close atomic numbers and similar electron densities, SC-XRD can hardly distinguish Au from Pt/Hg, or Ag from Pd/Cd. Thus, other approaches are required; for example, EXAFS can be a useful approach and was demonstrated to identify the location of Pt in Pt_1Au_{24}.[215] NMR may also helpful in elucidating the alloying positions. New approaches remain to be developed.[176] A multi-approach analysis should be established for more precise determination of challenging cases of alloy nanoclusters at the atomic level.

7. Seeing the doping evolution process at the atomic-level. From crystal structures of mono-metallic nanoclusters and their doping counterparts, one can only gain the information of the final doping sites. However, the precise doping process remains a mystery. As to the mono- and central doping of Au in $Ag_{25}(SR)_{18}$,[69] Bakr *et al*. proposed that the introduced Au^+ was first reduced to Au(0), replacing one Ag on the icosahedral kernel shell, and then the Au(0) diffused to the center due to thermodynamic favorability.[69] Xie and coworkers further demonstrated this Au-doping process on the basis of alloying $Ag_{25}(MHA)_{18}$ into $Au_1Ag_{24}(MHA)_{18}$.[436] Future work is still necessary to provide more intuitive perspectives in many other doping processes. *In-situ* EXAFS may also provide precise information on this.

8. Applications of alloy nanoclusters. Alloy nanoclusters often display enhanced chemical/physical properties relative to their mono-metallic counterparts. As ongoing improvement is being done in terms of controlling over structures and compositions of nanoclusters, one future direction is to move on to precise tailoring of their properties for applications in various fields. For example, as some of the nanoclusters have been reported to have extraordinarily long (e.g. microsecond) carrier lifetimes,[274] promising applications such as $^1O_2$ generation, solar energy conversion, and photocatalysis can be expected.

On the whole, it is clear that alloying in atomically precise nanoclusters holds great potential in tailoring the material properties and achieving deep understanding of many fundamental issues, such as the alloying sites, evolution, and structure-property correlation. With the development of atomically precise nanocluster chemistry, the alloying strategies will open new opportunities for controlling the structure, properties, and applications of nanocluster materials.

Conflicts of interest

There are no conflicts to declare.

Acknowledgements

M.Z. acknowledges the financial support by NSFC (U1532141, 21631001, 21871001), the Ministry of Education, the Education Department of Anhui Province, 211 Project of Anhui University. R.J. acknowledges the US National Science Foundation (DMR-1808675) and Air Force Office of Scientific Research for financial support.

Notes and references

1 C-Z. Ning, L. Dou and P. Yang, *Nat. Rev. Mater.,* 2017, **2**, 17070.
2 M. Luo and Guo, S. *Nat. Rev. Mater.,* 2017, **2**, 17059.
3 C. T. Liu and J. O. Stiegler, *Science,* 1984, **226**, 636-642.
4 Y. Yao, Z. Huang, P. Xie, S. D. Lacey, R. J. Jacob, H. Xie, F. Chen, A. Nie, T. Pu, M. Rehwoldt, D. Yu, M. R. Zachariah, C. Wang, R. Shahbazian-Yassar, J. Li and L. Hu, *Science,* 2018, **359**, 1489-1494.
5 K. D. Gilroy, A. Ruditskiy, H.-C. Peng, D. Qin and Y. Xia, *Chem. Rev.,* 2016, **116**, 10414-10472.
6 Y.-J. Wang, N. Zhao, B. Fang, H. Li, X. T. Bi and H. Wang, *Chem. Rev.,* 2015, **115**, 3433-3467.
7 M. Sankar, N. Dimitratos, P. J. Miedziak, P. P. Wells, C. J. Kiely and G. J. Hutchings, *Chem. Soc. Rev.,* 2012, **41**, 8099-8139.
8 D. Hardt, C. Suling, C. Lindner and L. Morbitzer, *Angew. Chem., Int. Ed.,* 1982, **21**, 174-184.
9 H. Zhang, I. Hasa and S. Passerini, *Adv. Energy Mater.,* 2018, **8**, 1702582.
10 Y. E. Panfil, M. Oded and U. Banin, *Angew. Chem., Int. Ed.,* 2018, **57**, 4274-4295.
11 Y. Bing, H. Liu, L. Zhang, D. Ghosh and J. Zhang, *Chem. Soc. Rev.,* 2010, **39**, 2184-2202.
12 M. A. Z. G. Sial, M. A. U. Din and X. Wang, *Chem. Soc. Rev.,* 2018, **47**, 6175-6200.
13 T. Chen and V. O. Rodionov, *ACS Catal.,* 2016, **6**, 4025-4033.
14 L. Xu, H.-W. Liang, Y. Yang and S.-H. Yu, *Chem. Rev.,* 2018, **118**, 3209-3250.
15 U. R. Kortshagen, R. M. Sankaran, R. N. Pereira, S. L. Girshick, J. J. Wu and E. S. Aydil, *Chem. Rev.,* 2016, **116**, 11061-11127.
16 M. Sharma, N. Jung and S. J. Yoo, *Chem. Mater.,* 2018, **30**, 2-24.
17 H.-L. Liu, F. Nosheen and X. Wang, *Chem. Soc. Rev.,* 2015, **44**, 3056-3078.
18 F. Wang, K. Kusada, D. Wu, T. Yamamoto, T. Toriyama, S. Matsumura, Y. Nanba, M. Koyama and H. Kitagawa, *Angew. Chem., Int. Ed.,* 2018, **57**, 4505-4509.
19 K. Jiang, D. Zhao, S. Guo, X. Zhang, X. Zhu, J. Guo, G. Lu and X. Huang, *Sci. Adv.,* 2017, **3**, e1601705.
20 P.-C. Chen, X. Liu, J. L. Hedrick, Z. Xie, S. Wang, Q.-Y. Lin, M. C. Hersam, V. P. Dravid and C. A. Mirkin, *Science,* 2016, **352**, 1565-1569.
21 K. Sasaki, H. Naohara, Y. Choi, Y. Cai, W.-F. Chen, P. Liu and R. R. Adzic, *Nat. Commun.,* 2012, **3**, 1115.
22 Y. Xia, Y. Xiong, B. Lim and S. E. Skrabalak, *Angew. Chem., Int. Ed.,* 2009*,* **48***,* 60-103.
23 A. R. Tao, S. Habas and P. Yang, *Small,* 2008, **4**, 310-325.
24 N. E. Motl, A. F. Smith, C. J. DeSantis and S. E. Skrabalak, *Chem. Soc. Rev.,* 2014, **43**, 3823-3834.
25 K. Zhou and Y. Li, *Angew. Chem., Int. Ed.,* 2012, **51**, 602-613.
26 L. Zhang, Z. Xie and J. Gong, *Chem. Soc. Rev.,* 2016, **45**, 3916-3934.
27 J. F. Li, Y. F. Huang, Y. Ding, Z. L. Yang, S. B. Li, X. S. Zhou, F. R. Fan, W. Zhang, Z. Y. Zhou, D. Y. Wu, B. Ren, Z. L. Wang and Z. Q. Tian, *Nature,* 2010, **464**, 392-395.
28 S.-Y. Ding, J. Yi, J.-F. Li, B. Ren, D.-Y. Wu, R. Panneerselvam and Z.-Q. Tian, *Nat. Rev. Mater.,* 2016, **1**, 1-16.
29 J.-F. Li, Y.-J. Zhang, S.-Y. Ding, R. Panneerselvam and Z.-Q. Tian, *Chem. Rev.,* 2017, **117**, 5002-5069.
30 M. Haruta, *Catal. Today,* 1997, **36**, 153-166.
31 M. Valden, X. Lai and D. W. Goodman, *Science,* 1998, **281**, 1647-1650.
32 C. T. Campbell, S. C. Parker and D. E. Starr, *Science,* 2002, **298**, 811-814.
33 R. Narayanan and M. A. El-Sayed, *J. Phys. Chem. B,* 2005, **109**, 12663-12676.
34 A. Zecchina, E. Groppo and S. Bordiga, *Chem. Eur. J., 2007,* **13***,* 2440-2460*.*
35 Y. Xia, X. Xia and H.-C. Peng, *J. Am. Chem. Soc.,* 2015, **137**, 7947-7966.
36 A-C. Shi and R. I. Masel, *J. Catal.,* 1989, **120**, 421-431.
37 L. M. Falicov and G. A. Somorjai, *Proc. NatI. Acad. Sci. USA.,* 1985, **82**, 2207-2211.
38 J. A. Schuller, E. S. Barnard, W. Cai, Y. C. Jun, J. S. White and M. L. Brongersma, *Nat. Mater.,* 2010, **9**, 193-204.
39 X. Lu, M. Rycenga, S. E. Skrabalak, B. Wiley and Y. Xia, *Annu. Rev. Phys. Chem.,* 2009, **60**, 167-192.
40 M. R. Jones, K. D. Osberg, R. J. Macfarlane, M. R. Langille and C. A. Mirkin, *Chem. Rev.,* 2011, **111**, 3736-3827.
41 D. Wang and Y. Li, *Adv. Mater.,* 2011, **23**, 1044-1060.
42 R. G. Chaudhuri and S. Paria, *Chem. Rev.,* 2012, **112**, 2373-2433.
43 F. Zaera, *Chem. Soc. Rev.,* 2013, **42**, 2746-2762.
44 Z. Wei, J. Sun, Y. Li, A. K. Datye and Y. Wang, *Chem. Soc. Rev.,* 2012, **41**, 7994-8008.
45 F. Zereini and C. L. S. Wiseman, Platinum Metals in the Environment. *Springer-Verlag: Berlin, Heidelberg*., 2015.
46 R. Jin, *Nanoscale,* 2015, **7**, 1549-1565.
47 R. Jin, C. Zeng, M. Zhou and Y. Chen, *Chem. Rev.,* 2016, **116**, 10346-10413.
48 I. Chakraborty and T. Pradeep, *Chem. Rev.,* 2017, **117**, 8208-8271.
49 A. Fernando, M. D. K. L. Weerawardene, N. V. Karimova and C. M. Aikens, *Chem. Rev.,* 2015, **115**, 6112-6216.
50 Y. Lu and W. Chen, *Chem. Soc. Rev.,* 2012, **41**, 3594-3623.
51 W. Kurashige, Y. Niihori, S. Sharma and Y. Negishi, *Coord. Chem. Rev.,* 2016, **320**, 238-250.
52 P. Liu, R. Qin, G. Fu and N. Zheng, *J. Am. Chem. Soc.,* 2017, **139**, 2122-2131.
53 C. Zeng, Y. Chen, K. Kirschbaum, K. J. Lambright and R. Jin, *Science,* 2016, **354**, 1580-1584.
54 H. Yang, Y. Wang, X. Chen, X. Zhao, L. Gu, H. Huang, J. Yan, C. Xu, G. Li, J. Wu, A. J. Edwards, B. Dittrich, Z. Tang, D. Wang, L. Lehtovaara, H. Häkkinen and N. Zheng, *Nat. Commun.,* 2016, **7**, 12809.
55 C. Zeng, Y. Chen, A. Das and R. Jin, *J. Phys. Chem. Lett.,* 2015, **6**, 2976-2986.
56 Y. Chen, C. Zeng, D. R. Kauffman and R. Jin, *Nano Lett.,* 2015, **15**, 3603-3609.
57 S. Yamazoe, K. Koyasu and T. Tsukuda, *Acc. Chem. Res.,* 2014, **47**, 816-824.
58 G. Li and R. Jin, *Acc. Chem. Res.,* 2013, **46**, 1749-1758.
59 Y. Zhu, R. Jin and Y. Sun, *Catalysts,* 2011, **1**, 3-17.
60 S. Zhao, R. Jin and R. Jin, *ACS Energy Lett.,* 2018, **3**, 452-462.
61 A. Mathew and T. Pradeep, *Part. Part. Syst. Charact.,* 2014, **31**, 1017-1053.

62 A. Ghosh, O. F. Mohammed and O. M. Bakr, *Acc. Chem. Res.,* 2018, **51**, 3094-3103.
63 H. Qian, D.-e. Jiang, G. Li, C. Gayathri, A. Das, R. R. Gil and R. Jin, *J. Am. Chem. Soc.,* 2012, **134**, 16159-16162.
64 S. Xie, H. Tsunoyama, W. Kurashige, Y. Negishi and T. Tsukuda, *ACS Catal.,* 2012, **2**, 1519-1523.
65 Y. Negishi, T. Iwai and M. Ide, *Chem. Commun.,* 2010, **46**, 4713-4715.
66 C. Kumara, C. M. Aikens and A. Dass, *J. Phys. Chem. Lett.,* 2014, **5**, 461-466.
67 E. Gottlieb, H. Qian and R. Jin, *Chem. Eur. J.,* 2013, **19**, 4238-4243.
68 W. Kurashige, K. Munakata, K. Nobusada and Y. Negishi, *Chem. Commun.,* 2013, **49**, 5447-5449.
69 M. S. Bootharaju, C. P. Joshi, M. R. Parida, O. F. Mohammed and O. M. Bakr, *Angew. Chem., Int. Ed.,* 2016, **55**, 922-926.
70 G. Soldan, M. A. Aljuhani, M. S. Bootharaju, L. G. AbdulHalim, M. R. Parida, A.-H. Emwas, O. F. Mohammed and O. M. Bakr, *Angew. Chem., Int. Ed.,* 2016, **55**, 5749-5753.
71 L. Liao, S. Zhou, Y. Dai, L. Liu, C. Yao, C. Fu, J. Yang and Z. Wu, *J. Am. Chem. Soc.,* 2015, **137**, 9511-9514.
72 J. Fang, B. Zhang, Q. Yao, Y. Yang, J. Xie and N. Yan, *Coord. Chem. Rev.,* 2016, **322**, 1-29.
73 L. Nie, X. Xiao and H. Yang, *J. Nanosci. Nanotechnol.,* 2016, **16**, 8164-8175.
74 N. Goswami, Q. Yao, T. Chen and J. Xie, *Coord. Chem. Rev.,* 2016, **329**, 1-15.
75 T. C. W. Mak, X.-L. Zhao, Q.-M. Wang and G.-C. Guo, *Coord. Chem. Rev.,* 2007, **251**, 2311-2333.
76 A. W. Cook and T. W. Hayton, *Acc. Chem. Res.,* 2018, **51**, 2456-2464.
77 T. Udayabhaskararao and T. Pradeep, *J. Phys. Chem. Lett.,* 2013, **4**, 1553-1564.
78 R. R. Nasaruddin, T. Chen, N. Yan and J. Xie, *Coord. Chem. Rev.,* 2018, **368**, 60-79.
79 S. Wang, Q. Li, X. Kang and M. Zhu, *Acc. Chem. Res.,* 2018, **51**, 2784-2792.
80 Z. Gan, N. Xia and Z. Wu, *Acc. Chem. Res.,* 2018, **51**, 2774-2783.
81 S. Hossain, Y. Niihori, L. V. Nair, B. Kumar, W. Kurashige and Y. Negishi, *Acc. Chem. Res.,* 2018, **51**, 3114-3124.
82 B. Bhattarai, Y. Zaker, A. Atnagulov, B. Yoon, U. Landman and T. P. Bigioni, *Acc. Chem. Res.,* 2018, **51**, 3104-3113.
83 R. K. Krishnadas, G. Natarajan, Ananya. Baksi, A. Ghosh, E. Khatun and T. Pradeep, *Langmuir*, 2019, **35**, 11243-11254.
84 Q. Yao, T. Chen, X. Yuan and J. Xie, *Acc. Chem. Res.,* 2018, **51**, 1338-1348.
85 R. S. Dhayal, W. E. van Zyl and C. W. Liu, *Acc. Chem. Res.* 2016, **49**, 86-95.
86 N. A. Sakthivel and A. Dass, *Acc. Chem. Res.,* 2018, **51**, 1774-1783.
87 S. Sharma, K. K. Chakrahari, J.-Y. Saillard and C. W. Liu, *Acc. Chem. Res.,* 2018, **51**, 2475-2483.
88 H. Qian, M. Zhu, Z. Wu and R. Jin, *Acc. Chem. Res.,* 2012, **45**, 1470-1479.
89 R. Jin, S. Zhao, Y. Xing and R. Jin, *CrystEngComm,* 2016, **18**, 3996-4005.
90 T. Higaki, C. Zeng, Y. Chen, E. Hussain and R. Jin, *CrystEngComm,* 2016, **18**, 6979-6986.
91 Y. Niihori, S. Hossain, S. Sharma, B. Kumar, W. Kurashige and Y. Negishi, *Chem. Rec.,* 2017, **17**, 473-484.
92 Z. Lei, X.-K. Wan, S.-F. Yuan, Z.-J. Guan and Q.-M. Wang, *Acc. Chem. Res.,* 2018, **51**, 2465-2474.
93 L. H. Pignolet, M. A. Aubart, K. L. Craighead, R. A. T. Gould, D. A. Krogstad and J. S. Wiley, *Coord. Chem. Rev.,* 1995, **143**, 219-263.
94 C. Femoni, M. C. Iapalucci, S. Ruggieri and S. Zacchini, *Acc. Chem. Res.,* 2018, **51**, 2748-2755.
95 B. Li, H.-T. Fan, S.-Q. Zang, H.-Y. Li and L.-Y. Wang, *Coord. Chem. Rev.,* 2018, **377**, 307-329.
96 P. Chakraborty, A. Nag, A. Chakraborty and T. Pradeep, *Acc. Chem. Res.,* 2018, **52**, 2-11.
97 J. Yan, B. K. Teo and N. Zheng, *Acc. Chem. Res.,* 2018, **51**, 3084-3093.
98 X. Yuan, X. Dou, K. Zheng and J. Xie, *Part. Part. Syst. Charact.,* 2015, **32**, 613-629.
99 Y.-P. Xie, J.-L. Jin, G.-X. Duan, X. Lu and T. C. W. Mak, *Coord. Chem. Rev.,* 2017, **331**, 54-72.
100 K. R. Krishnadas, A. Baksi, A. Ghosh, G. Natarajan, A. Som, and T. Pradeep, *Acc. Chem. Res.,* 2017, **50**, 1988-1996.
101 Z. Lei and Q.-M. Wang, *Coord. Chem. Rev.,* 2017, **378**, 382-394.
102 S. Takano, S. Hasegawa, M. Suyama and T. Tsukuda, *Acc. Chem. Res.,* 2018, **51**, 3074-3083.
103 K. Konishi, M. Iwasaki and Y. Shichibu, *Acc. Chem. Res.,* 2018, **51**, 3125-3133.
104 Y. Pei, P. Wang, Z. Ma and L. Xiong, *Acc. Chem. Res.,* 2019, **52**, 23-33.
105 T. Chen, Q. Yao, R. R. Nasaruddin and J. Xie, *Angew. Chem., Int. Ed.,* 2019, **58**, 11967-11977.
106 X. Kang and M. Zhu, *Coord. Chem. Rev.,* 2019, **394**, 1-38.
107 X. Du, J. Chai, S. Yang, Y. Li, T. Higaki, S. Li and R. Jin, *Nanoscale,* 2019, **11**, 19158-19165.
108 P. Chakraborty and T. Pradeep, *NPG Asia Mater.,* 2019, **11**, 48.
109 S. Muramatsu and T. Tsukuda, *Chem. Asian J.,* 2019, **14**, 3763-3772.
110 Y. Ishida, R. D. Corpuz and T. Yonezawa, *Acc. Chem. Res.,* 2017, **50**, 2986-2995.
111 A. Cantelli, G. Guidetti, J. Manzi, V. Caponetti and M. Montalti, *Eur. J. Inorg. Chem.,* 2017, **44**, 5068-5084.
112 N. Goswami, Q. Yao, Z. Luo, J. Li, T. Chen and J. Xie, *J. Phys. Chem. Lett.,* 2016, **7**, 962-975.
113 H. Yu, B. Rao, W. Jiang, S. Yang and M. Zhu, *Coord. Chem. Rev.,* 2019, **378**, 595-617.
114 C. Zeng and R. Jin, *Chem. Asian J.,* 2017, **12**, 1839-1850.
115 S. H. Yau, O. Varnavski and T. Goodson, *Acc. Chem. Res.,* 2013, **46**, 1506-1516.
116 T. Zhao, P. J. Herbert, H. Zheng and K. L. Knappenberger, Jr. *Acc. Chem. Res.,* 2018, **51**, 1433-1442.
117 T. Higaki, Q. Li, M. Zhou, S. Zhao, Y. Li and S. Li, Jin, R. *Acc. Chem. Res.,* 2018, **51**, 2764-2773.
118 Q. Yao, X. Yuan, T. Chen, D. T. Leong and J. Xie, *Adv. Mater.,* 2018, **30**, 1802751.
119 B. Nieto-Ortega and T. Bürgi, *Acc. Chem. Res.,* 2018, **51**, 2811-2819.
120 M. Agrachev, M. Ruzzi, A. Venzo and F. Maran, *Acc. Chem. Res.,* 2019, **52**, 44-52.
121 K. Kwak and D. Lee, *Acc. Chem. Res.,* 2019, **52**, 12-22.
122 T. Higaki, Y. Li, S. Zhao, Q. Li, S. Li, X.-S. Du, S. Yang, J. Chai and R. Jin, *Angew. Chem., Int. Ed.,* 2019, **58**, 8291-8302.
123 X. Kang and M. Zhu, *Chem. Soc. Rev.,* 2019, **48**, 2422-2457.
124 Y. Du, H. Sheng, D. Astruc and M. Zhu, *Chem. Rev.,* 2020, **120**, 526-622.
125 C. A. Smith, M. R. Narouz, P. A. Lummis, I. Singh, A. Nazemi, C.-H. Li and C. M. Crudden, *Chem. Rev.,* 2019, **119**, 4986-5056.
126 N. V. Karimova and C. M. Aikens, *Part. Part. Syst. Charact.,* 2019, **36**, 1900043.
127 V. Bonačić-Koutecký and R. Antoine, *Nanoscale,* 2019, **11**, 12436-12448.
128 Q. Shi, Z. Qin, H. Xu and G. Li, *Nanomaterials,* 2019, **9**, 838.
129 X. Dou, X. Chen, H. Zhu, Y. Liu, D. Chen, X. Yuan, Q. Yao and J. Xie, *Dalton Trans.,* 2019, **48**, 10385-10392.

130 J. Zhao, L. Ge, H. Yuan, Y. Liu, Y. Gui, B. Zhang, L. Zhou and S. Fang, *Nanoscale,* 2019, **11**, 11429-11436.
131 B. Wang, M. Zhao, M. Mehdi, G. Wang, P. Gao and K.-Q. Zhang, *Mater. Chem. Front.,* 2019, **3**, 1722-1735.
132 X. Kang and M. Zhu, *Chem. Mater.,* 2019, **31**, 9939-9969.
133 Z. Wu, Q. Yao, S. Zang and J. Xie, *ACS Materials Lett.,* 2019, **1**, 237-248.
134 K. Hirata, R. Tomihara, K. Kim, K. Koyasu and T. Tsukuda, *Phys. Chem. Chem. Phys.,* 2019, **21**, 17463-17474.
135 S. Jin, S. Wang and M. Zhu, *Chem. Eur. J.,* 2019, **14**, 3222-3231.
136 X. Kang and M. Zhu, *Small,* 2019, **15**, 1902703.
137 S. Tian, Y. Cao, T. Chen, S. Zang and J. Xie, *Chem. Commun.,* 2020, **56**, 1163-1174.
138 J. Yang and R. Jin, *ACS Materials Lett.,* 2019, **1**, 482-489.
139 Y. Jia and Z. Luo, *Coord. Chem. Rev.,* 2019, **400**, 213053.
140 Y. Zhao, X. Wang, J. Mi, Y. Jiang and C. Wang, *Part. Part. Syst. Charact.,* 2019, **36**, 1900298.
141 T. Kawawaki, Y. Negishi and H. Kawasaki, *Nanoscale Adv.,* 2020, **2**, 17-36.
142 Y. Tao, M. Li, J. Ren and X. Qu, *Chem. Soc. Rev.,* 2015, **44**, 8636-8663.
143 N. Goswami, K. Zheng and J. Xie, *Nanoscale,* 2014, **6**, 13328-13347.
144 L. Zhang and E. Wang, *Nano Today,* 2014, **9**, 132-157.
145 R. W. Murray, *Chem. Rev.,* 2008, **108**, 2688-2720.
146 X. Yuan, Z. Luo, Y. Yu, Q. Yao and J. Xie, *Chem. Asian. J.,* 2013, **8**, 858-871.
147 N. Goswami, Z. Luo, X. Yuan, D. T. Leong and J. Xie, *Mater. Horiz.,* 2017, **4**, 817-831.
148 L.-Y. Chen, C.-W. Wang, Z. Yuan and H.-T. Chang, *Anal. Chem.,* 2015, **87**, 216-229.
149 X.-R. Song, N. Goswami, H.-H. Yang and J. Xie, *Analyst,* 2016, **141**, 3126-3140.
150 Z. Luo, K. Zheng and J. Xie, *Chem. Commun.,* 2014, **50**, 5143-5155.
151 X. Liu and D. Astruc, *Coord. Chem. Rev.,* 2018, **359**, 112-126.
152 P. Yu, X. Wen, Y.-R. Toh, X. Ma and J. Tang, *Part. Part. Syst. Charact.,* 2015, **32**, 142-163.
153 Y. Chen, M. L. Phipps, J. H. Werner, S. Chakraborty and J. S. Martinez, *Acc. Chem. Res.,* 2018, **51**, 2756-2763.
154 K. Zheng, M. I. Setyawati, D. T. Leong and J. Xie, *Coord. Chem. Rev.,* 2018, **357**, 1-17.
155 L. Shang, J. Xu and G. U. Nienhaus, *Nano Today,* 2019, **28**, 100767.
156 O. J. H. Chai, Z. Liu, T. Chen and J. Xie, *Nanoscale,* 2019, **11**, 20437-20448.
157 S. Maity, D. Bain and A. Patra, *Nanoscale,* 2019, **11**, 22685-22723.
158 H. Häkkinen, *Nat. Chem.,* 2012, **4**, 443-455.
159 H. Häkkinen, *Chem. Soc. Rev.,* 2008, **37**, 1847-1859.
160 Y. Pei and X. C. Zeng, *Nanoscale,* 2012, **4**, 4054-4072.
161 K. L. D. M. Weerawardene, H. Häkkinen and C. M. Aikens, *Annu. Rev. Phys. Chem.,* 2018, **69**, 205-229.
162 W. W. Xu, X. C. Zeng and Y. Gao, *Acc. Chem. Res.,* 2018, **51**, 2739-2747.
163 Q. Tang, G. Hu, V. Fung and D.-e. Jiang, *Acc. Chem. Res.,* 2018, **51**, 2793-2802.
164 C. M. Aikens, *Acc. Chem. Res.,* 2018, **51**, 3065-3073.
165 C. M. Aikens, *J. Phys. Chem. Lett.,* 2011, **2**, 99-104.
166 J. F. Parker, C. A. Fields-Zinna and R. W. Murray, *Acc. Chem. Res.,* 2010, **43**, 1289-1296.
167 X. Kang, H. Chong and M. Zhu, *Nanoscale,* 2018, **10**, 10758-10834.
168 G. Schmid, *Chem. Soc. Rev.,* 2008, **37**, 1909-1930.
169 Q.-F. Zhang, X. Chen and L.-S. Wang, *Acc. Chem. Res.,* 2018, **51**, 2159-2168.
170 T. G. Schaaff, G. Knight, M. N. Shafigullin, R. F. Borkman and R. L. Whetten, *J. Phys. Chem. B,* 1998, **102**, 10643-10646.
171 M. W. Heaven, A. Dass, P. S. White, K. M. Holt and R. W. Murray, *J. Am. Chem. Soc.,* 2008, **130**, 3754-3755.
172 M. Zhu, C. M. Aikens, F. J. Hollander, G. C. Schatz and R. Jin, *J. Am. Chem. Soc.,* 2008, **130**, 5883-5885.
173 S. Bhat, A. Baksi, S. K. Mudedla, G. Natarajan, V. Subramanian and T. Pradeep, *J. Phys. Chem. Lett.,* 2017, **8**, 2787-2793.
174 S. Wang, Y. Song, S. Jin, X. Liu, J. Zhang, Y. Pei, X. Meng, M. Chen, P. Li and M. Zhu, *J. Am. Chem. Soc.,* 2015, **137**, 4018-4021.
175 C. Yao, Y.-J. Lin, J. Yuan, L. Liao, M. Zhu, L-h. Weng, J. Yang and Z. Wu, *J. Am. Chem. Soc.,* 2015, **137**, 15350-15353.
176 W. Fei, S. Antonello, T. Dainese, A. Dolmella, M. Lahtinen, K. Rissanen, A. Venzo and F. Maran, *J. Am. Chem. Soc.,* 2019, **141**, 16033-16045.
177 R. Jin, S. Zhao, C. Liu, M. Zhou, G. Panapitiya, Y. Xing, N. L. Rosi, J. P. Lewis and R. Jin, *Nanoscale,* 2017, **9**, 19183-19190.
178 D. R. Kauffman, D. Alfonso, C. Matranga, H. Qian and R. Jin, *J. Phys. Chem. C,* 2013, **117**, 7914-7923.
179 Q. Li, S. Wang, K. Kirschbaum, K. J. Lambright, A. Das and R. Jin, *Chem. Commun.,* 2016, **52**, 5194-5197.
180 Y. Niihori, M. Eguro, A. Kato, S. Sharma, B. Kumar, W. Kurashige, K. Nobusada and Y. Negishi, *J. Phys. Chem. C,* 2016, **120**, 14301-14309.
181 W. Li, C. Liu, H. Abroshan, Q. Ge, X. Yang, H. Xu and G. Li, *J. Phys. Chem. C,* 2016, **120**, 10261-10267.
182 X. Dou, X. Yuan, Q. Yao, Z. Luo, K. Zheng and J. Xie, *Chem. Commun.,* 2014, **50**, 7459-7462.
183 J.-P. Choi, C. A. Fields-Zinna, R. L. Stiles, R. Balasubramanian, A. D. Douglas, M. C. Crowe and R. W. Murray, *J. Phys. Chem. C,* 2010, **114**, 15890-15896.
184 C. Yao, J. Chen, M. B. Li, L. Liu, J. Yang and Z. Wu, *Nano. Lett.,* 2015, **15**, 1281-1287.
185 X. Wei, X. Kang, S. Wang and M. Zhu, *Dalton Trans.,* 2018, **47**, 13766-13770.
186 Z. Wu, *Angew. Chem., Int. Ed.,* 2012, **51**, 2934-2938.
187 N. Xia, Z. Wu, *J. Mater. Chem. C,* 2016, **4**, 4125-4128.
188 R. Kazan, U. Müller and T. Bürgi, *Nanoscale,* 2019, **11**, 2938-2945.
189 K. R. Krishnadas, A. Ghosh, A. Baksi, I. Chakraborty, G. Natarajan and T. Pradeep, *J. Am. Chem. Soc.,* 2016, **138**, 140-148.
190 K. R. Krishnadas, A. Baksi, A. Ghosh, G. Natarajan and T. Pradeep, *Nat. Commun.,* 2016, **7**, 13447.
191 K. R. Krishnadas, D. Ghosh, A. Ghosh, G. Natarajan and T. Pradeep, *J. Phys. Chem. C,* 2017, **121**, 23224-23232.
192 K. R. Krishnadas, A. Baksi, A. Ghosh, G. Natarajan and T. Pradeep, *ACS Nano,* 2017, **11**, 6015-6023.
193 A. Ghosh, D. Ghosh, E. Khatun, P. Chakraborty and T. Pradeep, *Nanoscale,* 2017, **9**, 1068-1077.
194 Q. Li, J. C. Russell, T.-Y. Luo, X. Roy, N. L. Rosi, Y. Zhu and R. Jin, *Nat. Commun.,* 2018, **9**, 3871.
195 C. M. Aikens, *J. Phys. Chem. C,* 2008, **112**, 19797-19800.
196 S. E. Skrabalak, J. Chen, Y. Sun, X. Lu, L. Au, C. M. Cobley and Y. Xia, *Acc. Chem. Res.,* 2008, **41**, 1587-1595.
197 X. Wang, J. Feng, Y. Bai, Q. Zhang and Y. Yin, *Chem. Rev.,* 2016, **116**, 10983-1060.
198 M. B. Cortie and A. M. McDonagh, *Chem. Rev.,* 2011, **111**, 3713-3735.
199 M. Walter, J. Akola, O. Lopez-Acevedo, P. D. Jadzinsky, G. Calero, C. J. Ackerson, R. L. Whetten, H. Grönbeck and H. Häkkinen, *Proc. Natl. Acad. Sci. USA,* 2008, **105**, 9157-9162.

200 M. Zhu, P. Wang, N. Yan, X. Chai, L. He, Y. Zhao, N. Xia, C. Yao, J. Li, H. Deng, Y. Zhu, Y. Pei and Z. Wu, *Angew. Chem., Int. Ed.,* 2018, **57**, 4500-4504.
201 Y. Negishi, K. Munakata, W. Ohgake and K. Nobusada, *J. Phys. Chem. Lett.,* 2012, **3**, 2209-2214.
202 S. Yamazoe, W. Kurashige, K. Nobusada, Y. Negishi and T. Tsukuda, *J. Phys. Chem. C,* 2014, **118**, 25284-25290.
203 C. A. Fields-Zinna, M. C. Crowe, A. Dass, J. E. Weaver and R. W. Murray, *Langmuir,* 2009, **25**, 7704-7710.
204 Y. Negishi, W. Kurashige, Y. Niihori, T. Iwasa and K. Nobusada, *Phys. Chem. Chem. Phys.,* 2010, **12**, 6219-6225.
205 Y. Niihori, W. Kurashige, M. Matsuzaki and Y. Negishi, *Nanoscale,* 2013, **5**, 508-512.
206 Y. Niihori, Y. Kikuchi, A. Kato, M. Matsuzaki and Y. Negishi, *ACS Nano,* 2015, **9**, 9347-9356.
207 S. Hossain, Y. Imai, D. Suzuki, W. Choi, Z. Chen, T. Suzuki, M. Yoshioka, T. Kawawaki, D. Lee and Y. Negishi, *Nanoscale*, 2019, **11**, 22089-22098.
208 A. Sels, N. Barrabes, S. Knoppe and T. Bürgi, *Nanoscale,* 2016, **8**, 11130-11135.
209 Y. Negishi, W. Kurashige, Y. Kobayashi, S. Yamazoe, N. Kojima, M. Seto and T. Tsukuda, *J. Phys. Chem. Lett.,* 2013, **4**, 3579-3583.
210 M. A. Tofanelli, T. W. Ni, B. D. Phillips and C. J. Ackerson, *Inorg. Chem.,* 2016, **55**, 999-1001.
211 K. Kwak, Q. Tang, M. Kim, D.-e. Jiang and D. Lee, *J. Am. Chem. Soc.,* 2015, **137**, 10833-10840.
212 M. A. Tofanelli and C. J. Ackerson, *J. Am. Chem. Soc.*, 2012, **134**, 16937-16940.
213 A. Sels, G. Salassa, S. Pollitt, C. Guglieri, G. Rupprechter, N. Barrabés and T. Bürgi, *J. Phys. Chem. C,* 2017, **121**, 10919-10926.
214 H. Qian, B. Ellen, Y. Zhu and R. Jin, *Acta Phys.-Chim. Sin.,* 2011, **27**, 513-519.
215 S. L. Christensen, M. A. MacDonald, A. Chatt, P. Zhang, H. Qian and R. Jin, *J. Phys. Chem. C,* 2012, **116**, 26932-26937.
216 S. Tian, L. Liao, J. Yuan, C. Yao, J. Chen, J. Yang and Z. Wu, *Chem. Commun.,* 2016, **52**, 9873-9876.
217 K. Kwak, W. Choi, Q. Tang, M. Kim, Y. Lee, D.-e. Jiang and D. Lee, *Nat. Commun.,* 2017, **8**, 14723.
218 G. Hu, Q. Tang, D. Lee, Z. Wu and D.-e. Jiang, *Chem. Mater.,* 2017, **29**, 4840-4847.
219 K. Kwak, W. Choi, Q. Tang, D.-e. Jiang and D. Lee, *J. Mater. Chem. A,* 2018, **6**, 19495-19501.
220 M. Zhou, H. Qian, M. Y. Sfeir, K. Nobusada and R. Jin, *Nanoscale,* 2016, **8**, 7163-7171.
221 M. Zhou, C. Yao, M. Y. Sfeir, T. Higaki, Z. Wu and R. Jin, *J. Phys. Chem. C,* 2018, **122**, 13435-13442.
222 M. Suyama, S. Takano, T. Nakamura and T. Tsukuda, *J. Am. Chem. Soc.,* 2019, **141**, 14048-14051.
223 S. Takano, S. Ito and T. Tsukuda, *J. Am. Chem. Soc.,* 2019, **141**, 15994-16002.
224 J.-J. Li, Z.-J. Guan, Z. Lei, F. Hu and Q.-M. Wang, *Angew. Chem., Int. Ed.,* 2019, **58**, 1083-1087.
225 M. Walter and M. Moseler, *J. Phys. Chem. C,* 2009, **113**, 15834-15837.
226 D.-e. Jiang and S. Dai, *Inorg. Chem.,* 2009, **48**, 2720-2722.
227 K. A. Kacprzak, L. Lehtovaara, J. Akola, O. Lopez-Acevedo and H. Häkkinen, *Phys. Chem. Chem. Phys.,* 2009, **11**, 7123-7129.
228 E. B. Guidez, V. Mäkinen, H. Häkkinen and C. M. Aikens, *J. Phys. Chem. C,* 2012, **116**, 20617-20624.
229 G. J. Camacho and A. Muñoz-Castro, *J. Phys. Chem. C,* 2016, **120**, 27019-27026.
230 G. Panapitiya, H. Wang, Y. Chen, E. Hussain, R. Jin and J. P. Lewis, *Phys. Chem. Chem. Phys.,* 2018, **20**, 13747-13756.
231 M. G. Taylor and G. Mpourmpakis, *J. Phys. Chem. Lett.,* 2018, **9**, 6773-6778.
232 H. Qian, W. T. Eckenhoff, Y. Zhu, T. Pintauer and R. Jin, *J. Am. Chem. Soc.,* 2010, **132**, 8280-8281.
233 Y. Pei, Y. Gao and X. C. Zeng, *J. Am. Chem. Soc.,* 2008, **130**, 7830-7832.
234 L. Cheng, C. Ren, X. Zhang and J. Yang, *Nanoscale*, 2013, **5**, 1475-1478.
235 M. Rambukwella, S. Burrage, M. Neubrander, O. Baseggio, E. Aprà, M. Stener, A. Fortunelli and A. Dass, *J. Phys. Chem. Lett.,* 2017, **8**, 1530-1537.
236 W. Kurashige, S. Yamazoe, K. Kanehira, T. Tsukuda and Y. Negishi, *J. Phys. Chem. Lett.,* 2013, **4**, 3181-3185
237 Q. Yao, X. Yuan, V. Fung, Y. Yu, D. T. Leong, D-e. Jiang and J. Xie, *Nat. Commun.,* 2017, **8**, 927.
238 M. S. Devadas, S. Bairu, H. Qian, E. Sinn, R. Jin and G. Ramakrishna, *J. Phys. Chem. Lett.,* 2011, **2**, 2752-2758.
239 T. D. Green, C. Yi, C. Zeng, R. Jin, S. McGill and K. L., Knappenberger, *J. Phys. Chem. A,* 2014, **118**, 10611-10621.
240 R. D. Senanayake, E. B. Guidez, A. J. Neukirch, O. V. Prezhdo and C. M. Aikens, *J. Phys. Chem. C,* 2018, **122**, 16380-16388.
241 M. Hesari, M. S. Workentin and Z. Ding, *ACS Nano,* 2014, **8**, 8543-8553.
242 S. Knoppe, R. Azoulay, A. Dass and T. Bürgi, *J. Am. Chem. Soc.,* 2012, **134**, 20302-20305.
243 S. Knoppe, I. Dolamic and T. Bürgi, *J. Am. Chem. Soc.,* 2012, **134**, 13114-13120.
244 I. Dolamic, S. Knoppe, A. Dass and T. Bürgi, *Nat. Commun.,* 2012, **3**, 798.
245 I. Dolamic, B. Varnholt and T. Bürgi, *Nat. Commun.,* 2015, **6**, 7117.
246 S. Tian, Y.-Z. Li, M.-B. Li, J. Yuan, J. Yang, Z. Wu and R. Jin, *Nat. Commun.,* 2015, **6**, 8667.
247 C. Liu, T. Li, G. Li, K. Nobusada, C. Zeng, G. Pang, N. L. Rosi and R. Jin, *Angew. Chem., Int. Ed.,* 2015, **54**, 9826-9829.
248 X.-K. Wan, J.-Q. Wang, Z.-A. Nan and Q.-M. Wang, *Sci. Adv.,* 2017, **3**, e1701823.
249 C. Kumara, K. J. Gagnon and A. Dass, *J. Phys. Chem. Lett.,* 2015, **6**, 1223-1228.
250 C. Kumara and A. Dass, *Nanoscale,* 2012, **4**, 4084-4086.
251 B. Zhang, G. Salassa and T. Bürgi, *Chem. Commun.,* 2016, **52**, 9205-9207.
252 B. Zhang, O. V. Safonova, S. Pollitt, G. Salassa, A. Sels, R. Kazan, Y. Wang, G. Rupprechter, N. Barrabes and T. Bürgi, *Phys. Chem. Chem. Phys.,* 2018, **20**, 5312-5318.
253 B. Zhang and T. Bürgi, *J. Phys. Chem. C,* 2016, **120**, 4660-4666.
254 Y. Niihori, S. Hashimoto, Y. Koyama, S. Hossain, W. Kurashige and Y. Negishi, *J. Phys. Chem. C,* 2019, **123**, 13324-13329.
255 J. Chai, Y. Lv, S. Yang, Y. Song, X. Zan, Q. Li, H. Yu, M. Wu and M. Zhu, *J. Phys. Chem. C,* 2017, **121**, 21665-21669.
256 X. Kang, C. Silalai, Y. Lv, G. Sun, S. Chen, H. Yu, F. Xu and M. Zhu, *Eur. J. Inorg. Chem.,* 2017, 1414-1419.
257 R. Kazan, B. Zhang and T. Bürgi, *Dalton Trans.,* 2017, **46**, 7708-7713.
258 Y. Negishi, K. Igarashi, K. Munakata, W. Ohgake and K. Nobusada, *Chem. Commun.,* 2012, **48**, 660-662.
259 N. Barrabés, B. Zhang and T. Bürgi, *J. Am. Chem. Soc.,* 2014, **136**, 14361-14364.
260 B. Zhang, S. Kaziz, H. Li, D. Wodka, S. Malola, O. Safonova, M. Nachtegaal, C. Mazet, I. Dolamic, J. Llorca, E. Kalenius, L. M. L. Daku, H. Häkkinen, T. Bürgi and N. Barrabés, *Nanoscale,* 2015, **7**, 17012-17019.
261 D. Toffoli, O. Baseggio, G. Fronzoni, M. Stener, A. Fortunelli and L. Sementa, *Phys. Chem. Chem. Phys.,* 2019, **21**, 3585-3596.
262 M. Kim, Q. Tang, A. V. N. Kumar, K. Kwak, W. Choi, D.-e. Jiang and D. Lee, *J. Phys. Chem. Lett.,* 2018, **9**, 982-989.

263 A. Muñoz-Castro, *Chem. Commun.,* 2019, **55**, 7307-7310.
264 T. Dainese, S. Antonello, S. Bogialli, W. Fei, A. Venzo and F. Maran, *ACS Nano,* 2018, **12**, 7057-7066.
265 A. Das, C. Liu, H. Y. Byun, K. Nobusada, S. Zhao, N. Rosi and R. Jin, *Angew. Chem., Int. Ed.,* 2015, **54**, 3140-3144.
266 S. Chen, S. Wang, J. Zhong, Y. Song, J. Zhang, H. Sheng, Y. Pei and M. Zhu, *Angew. Chem., Int. Ed.,* 2015, **54**, 3145-3149.
267 J. Xiang, P. Li, Y. Song, X. Liu, H. Chong, S. Jin, Y. Pei, X. Yuan and M. Zhu, *Nanoscale,* 2015, **7**, 18278-18283.
268 Y. Yu, Q. Yao, T. Chen, G. X. Lim and J. Xie, *J. Phys. Chem. C,* 2016, **120**, 22096-22102.
269 B. Molina and A. Tlahuice-Flores, *Phys. Chem. Chem. Phys.,* 2016, **18**, 1397-1403.
270 S. Chen, L. Xiong, S. Wang, Z. Ma, S. Jin, H. Sheng, Y. Pei and M. Zhu, *J. Am. Chem. Soc.,* 2016, **138**, 10754-10757.
271 X. Kang, L. Xiong, S. Wang, Y. Pei and M. Zhu, *Inorg. Chem.,* 2018, **57**, 335-342.
272 X. Dou, X. Yuan, Y. Yu, Z. Luo, Q. Yao, D. T. Leong and J. Xie, *Nanoscale,* 2014, **6**, 157-161.
273 R. Ho-Wu, P. K. Sahu, N. Wu, T. K. Chen, C. Yu, J. Xie and T. Goodson, *J. Phys. Chem. C,* 2018, **122**, 24368-24379.
274 M. Zhou, T. Higaki, G. Hu, M. Y. Sfeir, Y. Chen, D.-e. Jiang and R. Jin, *Science,* 2019, **364**, 279-282.
275 Y. Chen, C. Liu, Q. Tang, C. Zeng, T. Higaki, A. Das, D.-e. Jiang, N. L. Rosi and R. Jin, *J. Am. Chem. Soc.*, 2016, **138**, 1482-1485.
276 S. Yang, J. Chai, Y. Song, J. Fan, T. Chen, S. Wang, H. Yu, X. Li and M. Zhu, *J. Am. Chem. Soc.,* 2017, **139**, 5668-5671.
277 T. C. Jones, L. Sementa, M. Stener, K. J. Gagnon, V. D. Thanthirige, G. Ramakrishna, A. Fortunelli and A. Dass, *J. Phys. Chem. C,* 2017, **121**, 10865-10869.
278 A. Fortunelli, L. Sementa, V. D. Thanthirige, T. C. Jones, M. Stener, K. J. Gagnon, A. Dass and G. Ramakrishna, *J. Phys. Chem. Lett.,* 2017, **8**, 457-462.
279 Y. Li, T.-Y. Luo, M. Zhou, Y. Song, N. L. Rosi and R. Jin, *J. Am. Chem. Soc.,* 2018, **140**, 14235-14243.
280 A. Das, T. Li, K. Nobusada, C. Zeng, N. L. Rosi and R. Jin, *J. Am. Chem. Soc.,* 2013, **135**, 18264-18267.
281 Q. Li, T.-Y. Luo, M. G. Taylor, S. Wang, X. Zhu, Y. Song, G. Mpourmpakis, N. L. Rosi and R. Jin, *Sci. Adv.,* 2017*,* **3***,* e1603193.
282 Q. Li, M. G. Taylor, K. Kirschbaum, K. J. Lambright, X. Zhu, G. Mpourmpakis and R. Jin, *J. Colloid. Interface. Sci.,* 2017, **505**, 1202-1207.
283 Q. Li, K. J. Lambright, M. G. Taylor, K. Kirschbaum, T. Y. Luo, J. Zhao, G. Mpourmpakis, S. Mokashi-Punekar, N. L. Rosi and R. Jin, *J. Am. Chem. Soc.,* 2017, **139**, 17779-17782.
284 A. Das, T. Li, G. Li, K. Nobusada, C. Zeng, N. L. Rosi and R. Jin, *Nanoscale,* 2014, **6**, 6458-6462.
285 T. Higaki, C. Liu, Y. Chen, S. Zhao, C. Zeng, R. Jin, S. Wang, N. L. Rosi and R. Jin, *J Phys. Chem. Lett.,* 2017, **8**, 866-870.
286 L. Tang, X. Kang, S. Wang and M. Zhu, *Langmuir,* 2019, **35**, 12350-12355.
287 D. R. Kauffman, D. Alfonso, C. Matranga, G. Li and R. Jin, *J. Phys. Chem. Lett.*, 2013, **4**, 195-202.
288 C. Zeng, H. Qian, T. Li, G. Li, N. L. Rosi, B. Yoon, R. N. Barnett, R. L. Whetten, U. Landman and R. Jin, *Angew. Chem., Int. Ed.,* 2012, **51**, 13114-13118.
289 P. R. Nimmala, S. Knoppe, V. R. Jupally, J. H. Delcamp, C. M. Aikens and A. Dass, *J. Phys. Chem. B,* 2014, **118**, 14157-14167.
290 A. Das, C. Liu, C. Zeng, G. Li, T. Li, N. L. Rosi and R. Jin, *J. Phys. Chem. A,* 2014, *118*, 8264-8269.
291 P. R. Nimmala and A. Dass, *J. Am. Chem. Soc.* 2011, **133**, 9175-9177.
292 C. Zeng, C. Liu, Y. Pei and R. Jin, *ACS Nano,* 2013, **7**, 6138-6145.
293 M. Rambukwella and A. Dass, *Langmuir,* 2017, **33**, 10958-10964
294 A. Dass, T. C. Jones, S. Theivendran, L. Sementa and A. Fortunelli, *J. Phys. Chem. C,* 2017, **121**, 14914-14919.
295 M. Rambukwella, L. Chang, A. Ravishanker, A. Fortunelli, M. Stener and A. Dass, *Phys. Chem. Chem. Phys.,* 2018, **20**, 13255-13262.
296 D. M. Chevrier, A. Chatt, P. Zhang, C. Zeng and R. Jin, *J. Phys. Chem. Lett.,* 2013, **4**, 3186-3191.
297 D. J. Morris, R. Yang, T. Higaki, M. J. Ward, R. Jin and P. Zhang, *J. Phys. Chem. C,* 2018, **122**, 23414-23419.
298 A. Kim, C. Zeng, M. Zhou and R. Jin, *Part. Part. Syst. Charact.,* 2017, **34**, 1600388.
299 M. Zhou, C. Zeng, M. Y. Sfeir, M. Cotlet, K. Iida, K. Nobusada and R. Jin, *J. Phys. Chem. Lett.,* 2017, **8**, 4023-4030.
300 S. Yang, J. Chai, Y. Song, X. Kang, H. Sheng, H. Chong and M. Zhu, *J. Am. Chem. Soc.,* 2015, **137**, 10033-10035.
301 X.-K. Wan, Z.-J. Guan and Q.-M. Wang, *Angew. Chem., Int. Ed.,* 2017, **56**, 11494-11497.
302 S. Theivendran, L. Chang, A. Mukherjee, L. Sementa, M. Stener, A. Fortunelli and A. Dass, *J. Phys. Chem. C,* 2018, **122**, 4524-4531
303 N. A. Sakthivel, M. Stener, L. Sementa, M. Medves, G. Ramakrishna, A. Fortunelli, A. G. Oliver and A. Dass, *J. Phys. Chem. C*, 2019, **123**, 29484-29494.
304 S. Wang, L. Xiong, G. Sun, L. Tang, J. Zhang, Y. Pei and M. Zhu, *Nanoscale Adv.*, 2020, **2**, 664-668.
305 B. Rao, T. Zhao, S. Yang, J. Chai, Y. Pan, S. Weng, H. Yu, X. Li and M. Zhu, *Dalton Trans.,* 2018, **47**, 475-480.
306 L. Cheng, Y. Yuan, X. Zhang and J. Yang, *Angew. Chem., Int. Ed.*, 2013, **52**, 9035-9039.
307 L. Xiong, S. Yang, X. Sun, J. Chai, B. Rao, L. Yi, M. Zhu and Y. Pei, *J. Phys. Chem. C,* 2018, **122**, 14898-14907.
308 D. M. P. Mingos, *Chem. Soc. Rev.*, 1986, **15**, 31-61.
309 P. L. Bellon, F. Cariati, M. Manassero, L. Naldini and M. Sansoni, *Chem. Commun.,* 1971, 1423-1424.
310 K. P. Halp, B. R. C. Theobald, D. I. Gilmour, D. M. P. Mingos and A. I. Welch, *J. Chem. Soc., Chem. Commun.,* 1982, 528-530.
311 C. E. Briant, K. P. Hall and D. M. P. Mingos, *J. Chem. Soc., Chem. Commun.,* 1982, 290-291.
312 M. Schulz-Dobrick and M. Jansen, *Eur. J. Inorg. Chem*., 2006, 4498-4502.
313 F. Wen, U. Englert, B. Gutrath and U. Simon, *Eur. J. Inorg. Chem.,* 2008, 106-111.
314 L. N. Ito, B. J. Johnson, A. M. Mueting and L. H. Pignolet, *Inorg. Chem.,* 1989, **28**, 2026-2028.
315 S. Matsuo, S. Takano, S. Yamazoe, K. Koyasu and T. Tsukuda, *Chemelectrochem,* 2016, **3**, 1206-1211.
316 S. Yamazoe, S. Matsuo, S. Muramatsu, S. Takano, K. Nitta and T. Tsukuda, *Inorg. Chem.,* 2017, **56**, 8319-8325.
317 K. Hirata, P. Chakraborty, A. Nag, S. Takano, K. Koyasu, T. Pradeep and T. Tsukuda, *J. Phys. Chem. C,* 2018, **122**, 23123-23128.
318 S. Takano, H. Hirai, S. Muramatsu and T. Tsukuda, *J. Am. Chem. Soc.,* 2018, **140**, 8380-8383.
319 S. Takano, H. Hirai, S. Muramatsu and T. Tsukuda, *J. Am. Chem. Soc.,* 2018, **140**, 12314-12317.
320 M. F. J. Schoondergang, J, J. Bour, G. P. F. van Strijdonck, P. P. J. Schlebos, W. P. Bosman, J. M. M. Smits, P. T. Beurskens and J. J. Steggerda, *Inorg. Chem.,* 1991, **30**, 2048-2052.
321 J. G. M. van der Linden, A. M. Roelofsen and G. H. W. Ipskamp, *Inorg. Chem.,* 1989, **28**, 967-970.

322 V. G. Albano, P. L. Bellon, M. Manassero and M. Sanso, *Chem. Commun.,* 1970, 1210-1211.
323 R. C. B. Copley and D. M. P. Mingos, *J. Chem. Soc., Dalton Trans.,* 1996, 479-489.
324 B. S. Gutrath, U. Englert, Y. Wang and U. Simon, *Eur. J. Inorg. Chem.,* 2013, **12**, 2002-2006.
325 L. C. McKenzie, T. O. Zaikova and J. E. Hutchison, *J. Am. Chem. Soc.,* 2014, **136**, 13426-13435.
326 X. Kang, Y. Song, H. Deng, J. Zhang, B. Liu, C. Pan and M. Zhu, *RSC Adv.,* 2015, **5**, 66879-66885.
327 C. E. Briant, B. R. C. Theobald, J. W. White, L. K. Bell and D. M. P. Mingo, *J. Chem. Soc., Chem. Commun.,* 1981, 201-202.
328 J. W. A. van der Velden, F. A. Vollenbroek, J. J. Bour, P. T. Beurskens, J. M. M. Smits and W. P. Bosman, *Recueil, J. Royal Neth. Chem. Soc.,* 1981, **100**, 148-152.
329 Y. Shichibu and K. Konishi, *Small,* 2010, **6**, 1216-1220.
330 Y-Z. Li, R. Ganguly, K. Y. Hong, Y. Li, M. E. Tessensohn, R. Webster and W. K. Leong, *Chem. Sci.,* 2018, **9**, 8723-8730.
331 S.-S. Zhang, L. Feng, R. D. Senanayake, C. M. Aikens, X.-P. Wang, Q.-Q. Zhao, C. H. Tung and D. Sun, *Chem. Sci.,* 2018, **9**, 1251-1258.
332 W. Kurashige and Y. Negishi, *J. Clust. Sci.,* 2012, **23**, 365-374.
333 T. G. M. M. Kappen, P. P. J. Schlebos, J. J. Bour, W. P. Bosman, G. Beurskens, J. M. M. Smits, P. T. Beurskens and J. J. Steggerda, *Inorg. Chem.,* 1995, **34**, 2121-2132.
334 T. G. M. M. Kappen, P. P. J. Schlebos, J. J. Bour, W. P. Bosman, G. Beurskens, J. M. M. Smits, P. T. Beurskens and J. J. Steggerda, *Inorg. Chem.,* 1995, **34**, 2133-2142.
335 R. C. B. Copley and D. M. P. Mingos, *J. Chem. Soc., Dalton Trans.,* 1992, 1755-1756.
336 R. C. B. Copley and D. M. P. Mingos, *J. Chem. Soc., Dalton Trans.,* 1996, 491-500.
337 Z. Qin, D. Zhao, L. Zhao, Q. Xiao, T. Wu, J. Zhang, C. Wan and G. Li, *Nanoscale Adv.,* 2019, **1**, 2529-2536.
338 Y. Lv, X. Kang, S. Yang, T. Chen, A. Liu, H. Yu and M. Zhu, *RSC Adv.,* 2017, **7**, 51538-51545.
339 B. K. Teo and H. Zhang, *Inorg. Chim. Acta,* 1988, **144**, 173-176.
340 B. K. Teo, *Polyhedron,* 1988, **7**, 2317-2320.
341 B. K. Teo and H. Zhang, *Polyhedron,* 1990, **9**, 1985-1999.
342 B. K. Teo and H. Zhang, *J. Clust. Sci.,* 1990, **1**, 155-187.
343 B. K. Teo and H. Zhang, *J. Clust. Sci.,* 1990, **1**, 223-228.
344 B. K. Teo and H. Zhang, *Proc. Natl. Acad. Sci. USA,* 1991, **88**, 5067-5071.
345 B. K. Teo and H. Zhang, *Coord. Chem. Rev.,* 1995, **143**, 611-636.
346 H. Feld, A. Leute, D. Rading and A. Benninghoven, *J. Am. Chem. Soc.,* 1990, **112**, 8166-8167.
347 D.-e. Jiang, K. Nobusada, W. Luo and R. L. Whetten, *ACS Nano,* 2009, **3**, 2351-2357.
348 F. K. Sheong, J.-X. Zhang and Z. Lin, *Inorg. Chem.,* 2016, **55**, 11348-11353.
349 Y. Shichibu, Y. Negishi, T. Watanabe, N. K. Chaki, H. Kawaguchi and T. Tsukuda, *J. Phys. Chem. C,* 2007, **111**, 7845-7847.
350 Bond Energies, Encyclopedia of Inorganic Chemistry, 2006; DOI: 10.1002/0470862106.id098.
351 M.-B. Li, S.-K. Tian, Z. Wu and R. Jin, *Chem. Mater.,* 2016, **28**, 1022-1025.
352 H. Qian, M. Zhu, E. Lanni, Y. Zhu, M. E. Bier and R. Jin, *J. Phys. Chem. C,* 2009, **113**, 17599-17603.
353 H. Qian, W. T. Eckenhoff, M. E. Bier, T. Pintauer and R. Jin, *Inorg. Chem.,* 2011, **50**, 10735-10739.
354 S. Park and D. Lee, *Langmuir,* 2012, **28**, 7049-7054.
355 Y. Song, S. Jin, X. Kang, J. Xiang, H. Deng, H. Yu and M. Zhu, *Chem. Mater.,* 2016, **28**, 2609-2617.
356 M. Y. Sfeir, H. Qian, K. Nobusada and R. Jin, *J. Phys. Chem. C,* 2011, **115**, 6200-6207.
357 M. S. Devadas, V. D. Thanthirige, S. Bairu, E. Sinn and G. Ramakrishna, *J. Phys. Chem. C,* 2013, **117**, 23155-23161.
358 K. Katsiev, N. Lozova, L. Wang, K. S. Krishna, R. Li, W.-N. Mei, S. E. Skrabalak, C. S. R. Kumar and Y. Losovyj, *Nanoscale,* 2016, **8**, 14711-14715.
359 V. D. Thanthirige, E. Sinn, G. P. Wiederrecht and G. Ramakrishn, *J. Phys. Chem. C,* 2017, **121**, 3530-3539.
360 B. K. Teo and K. Keating, *J. Am. Chem. Soc.,* 1984, **106**, 2224-2226.
361 B. K. Teo, H. Zhang and X. Shi, *Inorg. Chem.,* 1990, **29**, 2083-2091.
362 B. K. Teo, X. Shi and H. Zhang, *J. Am. Chem. Soc.,* 1991, **113**, 4329-4331.
363 B. K. Teo and H. Zhang, *Inorg. Chem.,* 1991, **30**, 3115-3116.
364 B. K. Teo, X. Shi and H. Zhang, *J. Chem. Soc., Chem. Commun.,* 1992, 1195-1196.
365 B. K. Teo and H. Zhang, *Angew. Chem., Int. Ed.,* 1992, **104**, 445-447.
366 L. Liu, Y. Song, H. Chong, S. Yang, J. Xiang, S. Jin, X. Kang, J. Zhang, H. Yu and M. Zhu, *Nanoscale,* 2016, **8**, 1407-1412.
367 K. Nunokawa, M. Ito, T. Sunahara, S. Onaka, T. Ozeki, H. Chiba, Y. Funahashi, H. Masuda, T. Yonezawa, H. Nishihara, M. Nakamoto and M. Yamamoto, *Dalton Trans.,* 2005, 2726-2730.
368 S. Wang, X. Meng, A. Das, T. Li, Y. Song, T. Cao, X. Zhu, M. Zhu and R. Jin, *Angew. Chem., Int. Ed.,* 2014, **53**, 2376-2380.
369 F. Muniz-Miranda, M. C. Menziani and A. Pedone, *J. Phys. Chem. C,* 2015, **119**, 10766-10775.
370 M. Zhou, J. Zhong, S. Wang, Q. Guo, M. Zhu, Y. Pei and A. Xia, *J. Phys. Chem. C,* 2015, **119**, 18790-18797.
371 D. Mishra, S. Wang, Z. Jin, Y. Xin, E. Lochner and H. Mattoussi, *Phys. Chem. Chem. Phys.,* 2019, **21**, 21317-21328.
372 S. Wang, H. Abroshan, C. Liu, T. Y. Luo, M. Zhu, H. J. Kim, N. L. Rosi and R. Jin, *Nat. Commun.,* 2017, **8**, 848.
373 A. Das, T. Li, K. Nobusada, Q. Zeng, N. L. Rosi and R. Jin, *J. Am. Chem. Soc.,* 2012, **134**, 20286-20289.
374 J.-Q. Goh, S. Malola, H. Häkkinen and J. Akola, *J. Phys. Chem. C,* 2013, **117**, 22079-22086.
375 S. Yang, J. Chai, T. Chen, B. Rao, Y. Pan, H. Yu and M. Zhu, *Inorg. Chem.,* 2017, **56**, 1771-1774.
376 L. V. Nair, S. Hossain, S. Takagi, Y. Imai, G. Hu, S. Wakayama, B. Kumar, W. Kurashige, D.-e. Jiang and Y. Negishi, *Nanoscale,* 2018, **10**, 18969-18979.
377 X. Kang, J. Xiang, Y. Lv, W. Du, H. Yu, S. Wang and M. Zhu, *Chem. Mater.,* 2017, **29**, 6856-6862.
378 X. Kang, L. Xiong, S. Wang, H. Yu, S. Jin, Y. Song, T. Chen, L. Zheng, C. Pan, Y. Pei and M. Zhu, *Chem. Eur. J.,* 2016, **22**, 17145-17150.
379 B. K. Teo, H. Zhang and X. Shi, *J. Am. Chem. Soc.,* 1993, **115**. 8489-8490.
380 B. K. Teo, H. Zhang and X. Shi, *Inorg. Chem.,* 1994, **33**, 4086-4097.
381 T. G. M. M. Kappen, P. P. J. Schlebos, J. J. Bour, W. P. Bosnian, J. M. M. Smits, P. T. Beurskens and J. J. Steggerda, *Inorg. Chem.,* 1994, **33**, 754-758.
382 T. Iwasa, K. Nobusada and A. Nakajima, *J. Phys. Chem. C,* 2013, **117**, 24586-24591.
383 M. S. Bootharaju, S. M. Kozlov, Z. Cao, M. Harb, N. Maity, A. Shkurenko, M. R. Parida, M. N. Hedhili, M. Eddaoudi, O. F. Mohammed, O. M. Bakr, L. Cavallo and J.-M. Basset, *J. Am. Chem. Soc.,* 2017, **139**, 1053-1056.
384 S. Weng, Y. Lv, H. Yu and M. Zhu, *ChemPhysChem,* 2019, **20**, 1822-1829.

385 S. Chen, H. Ma, J. W. Padelford, W. Qinchen, W. Yu, S. Wang, M. Zhu and G. Wang, *J. Am. Chem. Soc.,* 2019, **141**, 9603-9609.
386 B. K. Teo, M. C. Hong, H. Zhang and D. B. Huang, *Angew. Chem., Int. Ed.,* 1987, **26**, 897-899.
387 R. Jin, C. Liu, S. Zhao, A. Das, H. Xing, C. Gayathri, Y. Xing, N. L. Rosi, R. R. Gil and R. Jin, *ACS Nano,* 2015, **9**, 8530-8536.
388 K. Nobusada and T. Iwasa, *J. Phys. Chem. C,* 2007, **111**, 14279-14282.
389 O. Palacios-Álvarez and A. Tlahuice-Flores, *J. Raman. Spectrosc.,* 2019, **50**, 52-62.
390 Y. Song, F. Fu, J. Zhang, J. Chai, X. Kang, P. Li, S. Li, H. Zhou and M. Zhu, *Angew. Chem., Int. Ed.,* 2015, **54**, 8430-8434.
391 B. K. Teo, K. Keating and Y.-H. Kao, *J. Am. Chem. Soc.,* 1987, **109**, 3494-3495.
392 B. K. Teo, H. Zhang and X. Shi, *J. Am. Chem. Soc.,* 1990, **112**, 8552-8562.
393 B. K. Teo, M. Hong, H. Zhang, D. Huang and X. Shi, *J. Chem. Soc., Chem. Commun.,* 1988, 204-206.
394 B. K. Teo, X. Shi and H. Zhang, *Inorg. Chem.,* 1993, **32**, 3987-3988.
395 N. K. Chaki, Y. Negishi, H. Tsunoyama, Y. Shichibu and T. Tsukuda, *J. Am. Chem. Soc.,* 2008, **130**, 8608-8610.
396 H. Qian and R. Jin, *Nano Lett.,* 2009, **9**, 4083-4087.
397 C. A. Fields-Zinna, R. Sardar, C. A. Beasley and R. W. Murray, *J. Am. Chem. Soc.,* 2009, **131**, 16266-16271.
398 T. Dainese, M. Agrachev, S. Antonello, D. Badocco, D. M. Black, A. Fortunelli, J. A. Gascón, M. Stener, A. Venzo, R. L. Whetten and F. Maran, *Chem. Sci.,* 2018, **9**, 8796-8805.
399 N. Bodappa, H. Ren, J.-C. Dong, D.-Y. Wu, Z.-Q. Tian and J.-F. Li, *ChemElectroChem,* 2019, **6**, 101-105.
400 R. L. Whetten, H.-C. Weissker, J. J. Pelayo, S. M. Mullins, X. López-Lozano and I. L. Garzón, *Acc. Chem. Res.,* 2019, **52**, 34-43.
401 O. Lopez-Acevedo, J. Akola, R. L. Whetten, H. Grönbeck and H. Häkkinen, *J. Phys. Chem. C,* 2009, **113**, 5035-5038.
402 D. Bahena, N. Bhattarai, U. Santiago, A. Tlahuice, A. Ponce, S. B. H. Bach, B. Yoon, R. L. Whetten, U. Landman and M. Jose-Yacaman, *J. Phys. Chem. Lett.,* 2013, **4**, 975-981.
403 M. Azubel, A. L. Koh, K. Koyasu, T. Tsukuda and R. D. Kornberg, *ACS Nano,* 2017, **11**, 11866-11871.
404 N. Yan, N. Xia, L. Liao, M. Zhu, F. Jin, R. Jin and Z. Wu, *Sci. Adv.,* 2018, **4**, eaat7259.
405 Z. Lei, J. J. Li, X.-K. Wan, W.-H. Zhang and Q.-M. Wang, *Angew. Chem., Int. Ed.,* 2018, **57**, 8639-8643.
406 C. Kumara and A. Dass, *Nanoscale,* 2011, **3**, 3064-3067.
407 J. Koivisto, S. Malola, C. Kumara, A. Dass, H. Häkkinen and M. Pettersson, *J. Phys. Chem. Lett.,* 2012, **3**, 3076-3080.
408 S. Malola, L. Lehtovaara and H. Häkkinen, *J. Phys. Chem. C,* 2014, **118**, 20002-20008.
409 J. Liu, K. S. Krishna, C. Kumara, S. Chattopadhyay, T. Shibata, A. Dass and C. S. S. R. Kumar, *RSC Adv.,* 2016, **6**, 25368-25374.
410 H. Zheng, M. A. Tofanelli, C. J. Ackerson and K. L. Knappenberger, *Phys. Chem. Chem. Phys.,* 2017, **19**, 14471-14477.
411 V. R. Jupally and A. Dass, *Phys. Chem. Chem. Phys.,* 2014, **16**, 10473-10479.
412 C. Kumara, X. Zuo, D. A. Cullen and A. Dass, *J. Phys. Chem. Lett.,* 2015, **6**, 3320-3326.
413 A. C. Dharmaratne and A. Dass, *Chem. Commun.,* 2014, **50**, 1722-1724.
414 S. Malola, M. J. Hartmann and H. Häkkinen, *J. Phys. Chem. Lett.,* 2015, **6**, 515-520.
415 N. Kothalawala, C. Kumara, R. Ferrando and A. Dass, *Chem. Commun.,* 2013, **49**, 10850-10852.
416 S. Vergara, D. A. Lukes, M. W. Martynowycz, U. Santiago, G. Plascencia-Villa, S. C. Weiss, M. J. de la Cruz, D. M. Black, M. M. Alvarez, X. López-Lozano, C. O. Barnes, G. Lin, H.-C. Weissker, R. L. Whetten, T. Gonen, M. J. Yacaman and G. Calero, *J. Phys. Chem. Lett.,* 2017, **8**, 5523-5530.
417 M. Zhou, C. Zeng, Y. Song, J. W. Padelford, G. Wang, M. Y. Sfeir, T. Higaki and R. Jin, *Angew. Chem., Int. Ed.,* 2017, **56**, 16257-16261.
418 N. A. Sakthivel, S. Theivendran, V. Ganeshraj, A. G. Oliver and A. Dass, *J. Am. Chem. Soc.,* 2017, **139**, 15450-15459.
419 T. Higaki, M. Zhou, K. J. Lambright, K. Kirschbaum, M. Y. Sfeir and R. Jin, *J. Am. Chem. Soc.,* 2018, **140**, 5691-5695.
420 N. A. Sakthivel, M. Stener, L. Sementa, A. Fortunelli, G. Ramakrishna and A. Dass, *J. Phys. Chem. Lett.,* 2018, **9**, 1295-1300.
421 L. Sumner, N. A. Sakthivel, H. Schrock, K. Artyushkova, A. Dass and S. Chakraborty, *J. Phys. Chem. C,* 2018, **122**, 24809-24817.
422 H. Qian, Y. Zhu and R. Jin, *Proc. Natl. Acad. Sci. USA,* 2012, **109**, 696-700.
423 C. Kumara, X. Zuo, J. Ilavsky, K. W. Chapman, D. A. Cullen and A. Dass, *J. Am. Chem. Soc.,* 2014, **136**, 7410-7417.
424 C. Kumara, X. Zuo, D. A. Cullen and A. Dass, *ACS Nano,* 2014, **8**, 6431-6439.
425 C. Kumara, M. M. Hoque, X. Zuo, D. A. Cullen, R. L. Whetten and A. Dass, *J. Phys. Chem. Lett.,* 2018, **9**, 6825-6832.
426 S. Vergara, U. Santiago, C. Kumara, D. Alducin, R. L. Whetten, M. J. Yacaman, A. Dass and A. Ponce, *J. Phys. Chem. C,* 2018, **122**, 26733-26738.
427 Y. Song, K. Lambright, M. Zhou, K. Kirschbaum, J. Xiang, A. Xia, M. Zhu and R. Jin, *ACS Nano,* 2018, **12**, 9318-9325.
428 I. Chakraborty, A. Govindarajan, J. Erusappan, A. Ghosh, T. Pradeep, B. Yoon, R. L. Whetten and U. Landman, *Nano Lett.,* 2012, **12**, 5861-5866.
429 J. Yan, J. Zhang, X. Chen, S. Malola, B. Zhou, E. Selenius, X. Zhang, P. Yuan, G. Deng, K. Liu, H. Su, B. K. Teo, H. Häkkinen, L. Zheng and N. Zheng, *Natl. Sci. Rev.,* 2018, **5**, 694-702.
430 Q. Zhou, S. Kaappa, S. Malola, H. Lu, D. Guan, Y. Li, H. Wang, Z. Xie, Z. Ma, H. Häkkinen, N. Zheng, X. Yang and L. Zheng, *Nat. Commun.,* 2018, **9**, 2948.
431 I. Chakraborty, J. Erusappan, A. Govindarajan, K. S. Sugi, T. Udayabhaskararao, A. Ghosh and T. Pradeep, *Nanoscale,* 2014, **6**, 8024-8031.
432 C. P. Joshi, M. S. Bootharaju, M. J. Alhilaly and O. M. Bakr, *J. Am. Chem. Soc.,* 2015, **137**, 11578-11581.
433 M. S. Bootharaju, C. P. Joshi, M. J. Alhilaly and O. M. Bakr, *Chem. Mater.,* 2016, **28**, 3292-3297.
434 E. Khatun, A. Ghosh, D. Ghosh, P. Chakraborty, A. Nag, B. Mondal, S. Chennu and T. Pradeep, *Nanoscale,* 2017, **9**, 8240-8248.
435 J. Yan, H. Su, H. Yang, S. Malola, S. Lin, H. Häkkinen and N. Zheng, *J. Am. Chem. Soc.,* 2015, **137**, 11880-11883.
436 K. Zheng, V. Fung, X. Duan, D.-e. Jiang and J. Xie, *J. Am. Chem. Soc.,* 2019, **141**, 18977-18983.
437 X. Liu, J. Yuan, C. Yao, J. Chen, L. Li, X. Bao, J. Yang and Z. Wu, *J. Phys. Chem. C,* 2017, **121**, 13848-13853.
438 K. L. D. M. Weerawardene and C. M. Aikens, *J. Phys. Chem. C,* 2018, **122**, 2440-2447.
439 Q. Yuan, X. Kang, D. Hu, C. Qin, S. Wang and M. Zhu, *Dalton Trans.,* 2019, **48**, 13190-13196.
440 Y. Liu, X. Chai, X. Cai, M. Chen, R. Jin, W. Ding and Y. Zhu, *Angew. Chem., Int. Ed.,* 2018, **57**, 9775-9779.
441 X. Kang, S. Chen, S. Jin, Y. Song, Y. Xu, H. Yu, H. Sheng and M. Zhu, *ChemElectroChem,* 2016, **3**, 1261-1265.
442 M. S. Bootharaju, L. Sinatra and O. M. Bakr, *Nanoscale,* 2016, **8**, 17333-17339.

443 M. S. Bootharaju, R. Dey, L. E. Gevers, M. N. Hedhili, J.-M. Basset and O. M. Bakr, *J. Am. Chem. Soc.,* 2016, **138**, 13770-13773.
444 X. Kang, L. Xiong, S. Wang, Y. Pei and M. Zhu, *Chem. Commun.,* 2017, **53**, 12564-12567.
445 S. Yang, J. Chai, Y. Lv, T. Chen, S. Wang, H. Yu and M. Zhu, *Chem. Commun.,* 2018, **54**, 12077-12080.
446 L. G. AbdulHalim, M. S. Bootharaju, Q. Tang, S. D. Gobbo, R. G. AbdulHalim, M. Eddaoudi, D.-e. Jiang and O. M. Bakr, *J. Am. Chem. Soc.,* 2015, **137**, 11970-11975.
447 X. Kang, M. Zhou, S. Wang, S. Jin, G. Sun, M. Zhu and R. Jin, *Chem. Sci.,* 2017, **8**, 2581-2587.
448 X. Kang, X. Wei, S. Jin, Q. Yuan, X. Luan, Y. Pei, S. Wang, M. Zhu and R. Jin, *Proc. Natl. Acad. Sci. USA,* 2019, **116**, 18834-18840.
449 X. Lin, C. Liu, K. Sun, R. Wu, X. Fu and J. Huang, *Nano Res.,* 2019, **12**, 309-314.
450 X. Kang, S. Wang and M. Zhu, *Chem. Sci.,* 2018, **9**, 3062-3068.
451 A. Nag, P. Chakraborty, M. Bodiuzzaman, T. Ahuja, S. Antharjanam and T. Pradeep, *Nanoscale,* 2018, **10**, 9851-9855.
452 S. M. Aly, L. G. AbdulHalim, T. M. D. Besong, G. Soldan, O. M. Bakr and O. F. Mohammed, *Nanoscale,* 2016, **8**, 5412-5416.
453 E. Khatun, A. Ghosh, P. Chakraborty, P. Singh, M. Bodiuzzaman, P. Ganesan, G. Nataranjan, J. Ghosh, S. K. Pal and T. Pradeep, *Nanoscale,* 2018, **10**, 20033-20042.
454 G. H. Ahmed, M. R. Parida, A. Tosato, L. G. AbdulHalim, A. Usman, Q. A. Alsulami, B. Murali, E. Alarousu, O. M. Bakr and O. F. Mohammed, *J. Mater. Chem. C,* 2016, **4**, 2894-2900.
455 A. A. Almansaf, M. R. Parida, T. M. D. Besong, P. Maity, M. S. Bootharaju, O. M. Bakr and O. F. Mohammed, *Chem. Phys. Lett.,* 2017, **683**, 393-397.
456 P. Chakraborty, A. Nag, G. Paramasivam, G. Natarajan and T. Pradeep, *ACS Nano,* 2018, **12**, 2415-2425.
457 K. S. Sugi, G. Mallikarjunachari, A. Som, P. Ghosh and T. Pradeep, *ChemNanoMat,* 2018, **4**, 401-408.
458 P. Chakraborty, A. Baksi, E. Khatun, A. Nag, A. Ghosh and T. Pradeep, *J. Phys. Chem. C,* 2017, **121**, 10971-10981.
459 A. Nag, P. Chakraborty, G. Paramasivam, M. Bodiuzzaman, G. Natarajan and T. Pradeep, *J. Am. Chem. Soc.,* 2018, **140**, 13590-13593.
460 X. Wei, X. Kang, Q. Yuan, C. Qin, S. Jin, S. Wang and M. Zhu, *Chem. Mater.,* 2019, **31**, 4945-4952.
461 E. Khatun, P. Chakraborty, B. R. Jacob, G. Paramasivam, M. Bodiuzzaman, W. A. Dar and T. Pradeep, *Chem. Mater.*, 2020, **32**, 611-619.
462 P. Chakraborty, A. Baksi, S. K. Mudedla, A. Nag, G. Paramasivam, V. Subramanian and T. Pradeep, *Phys. Chem. Chem. Phys.,* 2018, **20**, 7593-7603.
463 P. Chakraborty, A. Nag, K. S. Sugi, T. Ahuja, B. Varghese and T. Pradeep, *ACS Materials Lett.*, 2019, **1**, 534-540.
464 M. S. Bootharaju, S. M. Kozlov, Z. Cao, M. Harb, M. R. Parida, M. N. Hedhili, O. F. Mohammed, O. M. Bakr, L. Cavallo and J.-M. Basset, *Nanoscale,* 2017, **9**, 9529-9536.
465 M. S. Bootharaju, S. M. Kozlov, Z. Cao, A. Shkurenko, A. M. El-Zohry, O. F. Mohammed, M. Eddaoudi, O. M. Bakr, L. Cavallo and J.-M. Basset, *Chem. Mater.,* 2018, **30**, 2719-2725.
466 R. Juarez-Mosqueda, S. Malola and H. Häkkinen, *Phys. Chem. Chem. Phys.,* 2017, **19**, 13868-13874.
467 X.-Y. Xie, P. Xiao, X. Cao, W.-H. Fang, G. Cui and M. Dolg, *Angew. Chem., Int. Ed.,* 2018, **57**, 9965-9969.
468 X. Kang, H. Abroshan, S. Wang and M. Zhu, *Inorg. Chem.,* 2019, **58**, 11000-11009.
469 M. A. H. Muhammed, F. Aldeek, G. Palui, L. Trapiella-Alfonso and H. Mattoussi, *ACS Nano,* 2012, **6**, 8950-8961.
470 I. Russier-Antoine, F. Bertorelle, R. Hamouda, D. Rayane, P. Dugourd, Ž. Sanader, V. Bonačić-Koutecký, P.-F. Brevet and R. Antoine, *Nanoscale,* 2016, **8**, 2892-2898.
471 M. van der Linden, A. Barendregt, A. J. van Bunningen, P. T. Chin, D. Thies-Weesie, F. M. F. de Groot and A. Meijerink, *Nanoscale,* 2016, **8**, 19901-19909.
472 D. M. Black, G. Robles, P. Lopez, S. B. H. Bach, M. Alvarez and R. L. Whetten, *Anal. Chem.,* 2018, **90**, 2010-2017.
473 P. Lopez, H. H. Lara, S. M. Mullins, D. M. Black, H. M. Ramsower, M. M. Alvarez, T. L. Williams, X. Lopez-Lozano, H.-C. Weissker, A. P. García, I. L. Garzón, B. Demeler, J. L. Lopez-Ribot, M. J. Yacamán and R. L. Whetten, *ACS Appl. Nano. Mater.,* 2018, **1**, 1595-1602.
474 D. Mishra, V. Lobodin, C. Zhang, F. Aldeek, E. Lochner and H. Mattoussi, *Phys. Chem. Chem. Phys.,* 2018, **20**, 12992-13007.
475 O. M. Bakr, V. Amendola, C. M. Aikens, W. Wenseleers, R. Li, L. D. Negro, G. C. Schatz and F. Stellacci, *Angew. Chem., Int. Ed.,* 2009, **48**, 5921-5926.
476 A. Desireddy, B. E. Conn, J. Guo, B. Yoon, R. N. Barnett, B. M. Monahan, K. Kirschbaum, W. P. Griffith, R. L. Whetten, U. Landman and T. P. Bigioni, *Nature,* 2013, **501**, 399-402.
477 H. Yang, Y. Wang, H. Huang, L. Gell, L. Lehtovaara, S. Malola, H. Häkkinen and N. Zheng, *Nat. Commun.,* 2013, **4**, 2422.
478 L. G. AbdulHalim, S. Ashraf, K. Katsiev, A. R. Kirmani, N. Kothalawala, D. H. Anjum, S. Abbas, A. Amassian, F. Stellacci, A. Dass, I. Hussain and O. M. Bakr, *J. Mater. Chem. A,* 2013, **1**, 10148-10154.
479 B. Bhattarai, I. Chakraborty, B. E. Conn, A. Atnagulov, T. Pradeep and T. P. Bigioni, *J. Phys. Chem. C,* 2017, **121**, 10964-10970.
480 B. E. Conn, A. Desireddy, A. Atnagulov, S. Wickramasinghe, B. Bhattarai, B. Yoon, R. N. Barnett, Y. Abdollahian, Y. W. Kim, W. P. Griffith, S. R. J. Oliver, U. Landman and T. P. Bigioni, *J. Phys. Chem. C,* 2015, **119**, 11238-11249.
481 Y. Cao, J. Guo, R. Shi, G. I. N. Waterhouse, J. Pan, Z. Du, Q. Yao, L.-Z. Wu, C.-H. Tung, J. Xie and T. Zhang, *Nat. Commun.,* 2018, **9**, 2379.
482 K. M. Harkness, Y. Tang, A. Dass, J. Pan, N. Kothalawala, V. J. Reddy, D. E. Cliffel, B. Demeler, F. Stellacci, O. M. Bakr and J. A. McLean, *Nanoscale,* 2012, **4**, 4269-4274.
483 L. G. AbdulHalim, N. Kothalawala, L. Sinatra, A. Dass and O. M. Bakr, *J. Am. Chem. Soc.,* 2014, **136**, 15865-15868.
484 I. Chakraborty, W. Kurashige, K. Kanehira, L. Gell, H. Häkkinen, Y. Negishi and T. Pradeep, *J. Phys. Chem. Lett.,* 2013, **4**, 3351-3355.
485 I. Chakraborty and T. Pradeep, *Nanoscale,* 2014, **6**, 14190-14194.
486 B. Yoon, W. D. Luedtke, R. N. Barnett, J. Gao, A. Desireddy, B. E. Conn, T. Bigioni and U. Landman, *Nat. Mater.,* 2014, **13**, 807-811.
487 Q. Yao, Y. Yu, X. Yuan, Y. Yu, D. Zhao, J. Xie and J. Y. Lee, *Angew. Chem., Int. Ed.,* 2015, **54**, 184-189.
488 A. Chakraborty, A. C. Fernandez, A. Som, B. Mondal, G. Natarajan, G. Paramasivam, T. Lahtinen, H. Häkkinen, Nonappa and T. Pradeep, *Angew. Chem., Int. Ed.,* 2018, **57**, 6522-6526.
489 H. Su, Y. Wang, L. Ren, P. Yuan, B. K. Teo, S. Lin, L. Zheng and N. Zheng, *Inorg. Chem.,* 2019, **58**, 259-264.
490 L. Gell and H. Häkkinen, *J. Phys. Chem. C,* 2015, **119**, 10943-10948.
491 C. Morera-Boado, F. Hidalgo and C. Noguez, *J. Phys. Chem. C*, 2019, **43**, 26633-26643.
492 B. E. Conn, A. Atnagulov, B. Bhattarai, B. Yoon, U.

Landman and T. P. Bigioni, *J. Phys. Chem. C,* 2018, **122**, 13166-13174.
493 Q. Yao, Y. Feng, V. Fung, Y. Yu, D.-e. Jiang, J. Yang and J. Xie, *Nat. Commun.,* 2017, **8**, 1555.
494 M. A. Tofanelli, K. Salorinne, T. W. Ni, S. Malola, B. Newell, B. Phillips, H. Häkkinen and C. J. Ackerson, *Chem. Sci.,* 2016, **7**, 1882-1890.
495 M. Zhu, W. T. Eckenhoff, T. Pintauer and R. Jin, *J. Phys. Chem. C,* 2008, **112**, 14221-14224.
496 W. Du, S. Jin, L. Xiong, M. Chen, J. Zhang, X. Zou, Y. Pei, S. Wang and M. Zhu, *J. Am. Chem. Soc.,* 2017, **139**, 1618-1624.
497 R. S. Dhayal, J.-H. Liao, Y.-C. Liu, M. H. Chiang, S. Kahlal, J.-Y. Saillard and C. W. Liu, *Angew. Chem., Int. Ed.,* 2015, **54**, 3702-3706.
498 R. S. Dhayal, Y. R. Lin, J.-H. Liao, Y. J. Chen, Y. C. Liu, M.-H. Chiang, S. Kahlal, J.-Y. Saillard and C. W. Liu, *Chem. Eur. J.,* 2016, **22**, 9943-9947.
499 W.-T. Chang, P.-Y. Lee, J.-H. Liao, K. K. Chakrahari, S. Kahlal, Y.-C. Liu, M.-H. Chiang, J.-Y. Saillard and C. W. Liu, *Angew. Chem., Int. Ed.,* 2017, **56**, 10178-10182.
500 Y.-R. Lin, P. Kishore, J. H. Liao, S. Kahlal, Y.-C. Liu, M.-H. Chiang, J.-Y. Saillard and C. W. Liu, *Nanoscale,* 2018, **10**, 6855-6860.
501 W.-T. Chang, S. Sharma, J. H. Liao, S. Kahlal, Y.-C. Liu, M.-H. Chiang, J.-Y. Saillard and C. W. Liu, *Chem. Eur. J.,* 2018, **24**, 14352-14357.
502 J.-H. Liao, S. Kahlal, Y.-C. Liu, M.-H. Chiang, J.-Y. Saillard and C. W. Liu, *J. Clust. Sci.,* 2018, **29**, 827-835.
503 S. K. Barik, T.-H. Chiu, Y.-C. Liu, M.-H. Chiang, F. Gam, I. Chantrenne, S. Kahlal, J.-Y. Saillard and C. W. Liu, *Nanoscale,* 2019, **11**, 14581-14586.
504 T.-H. Chiu, J.-H. Liao, F. Gam, I. Chantrenne, S. Kahlal, J.-Y. Saillard and C. W. Liu, *J. Am. Chem. Soc.,* 2019, **141**, 12957-12961.
505 J. Yan, H. Su, H. Yang, C. Hu, S. Malola, S. Lin, B. K. Teo, H. Häkkinen and N. Zheng, *J. Am. Chem. Soc.,* 2016, **138**, 12751-12754.
506 M. S. Bootharaju, H. Chang, G. Deng, S. Malola, W. Baek, H. Häkkinen, N. Zheng and T. Hyeon, *J. Am. Chem. Soc.,* 2019, **141**, 8422-8425.
507 H. Yang, Y. Wang, J. Lei, L. Shi, X. Wu, V. Makinen, S. Lin, Z. Tang, J. He, H. Häkkinen, L. Zheng and N. Zheng, *J. Am. Chem. Soc.,* 2013, **135**, 9568-9571.
508 G. Deng, S. Malola, J. Yan, Y. Han, P. Yuan, C. Zhao, X. Yuan, S. Lin, Z. Tang, B. K. Teo, H. Häkkinen and N. Zheng, *Angew. Chem., Int. Ed.,* 2018, **57**, 3421-3425.
509 C. Zhou, H. Li, Y. Song, F. Ke, W. W. Xu and M. Zhu, *Nanoscale,* 2019, **11**, 19393-19397.
510 Y. Song, Y. Lv, M. Zhou, T. Y. Luo, S. Zhao, N. L. Rosi, H. Yu, M. Zhu and R. Jin, *Nanoscale,* 2018, **10**, 12093-12099.
511 H. Yang, Y. Wang, J. Yan, X. Chen, X. Zhang, H. Häkkinen and N. Zheng, *J. Am. Chem. Soc.,* 2014, **136**, 7197-7200.
512 L. He, J. Yuan, N. Xia, L. Liao, X. Liu, Z. Gan, C. Wang, J. Yang and Z. Wu, *J. Am. Chem. Soc.,* 2018, **140**, 3487-3490.
513 L. He, Z. Gan, N. Xia, L. Liao and Z. Wu, *Angew. Chem., Int. Ed.,* 2019, **58**, 9897-9901.
514 X. Kang, L. Huang, W. Liu, L. Xiong, Y. Pei, Z. Sun, S. Wang, S. Wei and M. Zhu, *Chem. Sci.,* 2019, **10**, 8685-8693.
515 X. Kang, S. Jin, L. Xiong, X. Wei, M. Zhou, C. Qin, Y. Pei, S. Wang and M. Zhu, *Chem. Sci.,* 2020, **11**, 1691-1697.
516 X. Kang, F. Xu, X. Wei, S. Wang and M. Zhu, *Sci. Adv.,* 2019, **5**, eaax7863.
517 K. K. Chakrahari, J.-H. Liao, S. Kahlal, Y.-C. Liu, M.-H. Chiang, J.-Y. Saillard and C. W. Liu, *Angew. Chem., Int. Ed.,* 2016, **55**, 14704-14708.
518 R. P. B. Silalahi, K. K. Chakrahari, J.-H. Liao, S. Kahlal, Y.-C. Liu, M.-H. Chiang, J.-Y. Saillard and C. W. Liu, *Chem. Asian J.,* 2018, **13**, 500-504.
519 K. K. Chakrahari, R. P. B. Silalahi, J.-H. Liao, S. Kahlal, Y.-C. Liu, J.-F. Lee, M.-H. Chiang, J.-Y. Saillard and C. W. Liu, *Chem. Sci.,* 2018, **9**, 6785-6795.
520 S. Yang, S. Wang, S. Jin, S. Chen, H. Sheng and M. Zhu, *Nanoscale,* 2015, **7**, 10005-10007.
521 N. Yan, L. Liao, J. Yuan, Y.-j. Lin, L.-h. Weng, J. Yang and Z. Wu, *Chem. Mater.,* 2016, **28**, 8240-8247.
522 S. Sharma, W. Kurashige, K. Nobusada and Y. Negishi, *Nanoscale,* 2015, **7**, 10606-10612.
523 S. Sharma, S. Yamazoe, T. Ono, W. Kurashige, Y. Niihori, K. Nobusada, T. Tsukuda and Y. Negishi, *Dalton Trans.,* 2016, **45**, 18064-18068.
524 S. Hossain, T. Ono, M. Yoshioka, G. Hu, M. Hosoi, Z. Chen, L. V. Nair, Y. Niihori, W. Kurashige, D.-e. Jiang and Y. Negishi, *J. Phys. Chem. Lett.,* 2018, **9**, 2590-2594.
525 A. Puls, P. Jerabek, W. Kurashige, M. Forster, M. Molon, T. Bollermann, M. Winter, C. Gemel, Y. Negishi, G. Frenking and R. A. Fischer, *Angew. Chem., Int. Ed.,* 2014, **53**, 4327-4331.
526 Y. Wang, H. Su, L. Ren, S. Malola, S. Lin, B. K. Teo, H. Häkkinen and N. Zheng, *Angew. Chem., Int. Ed.,* 2016, **55**, 15152-15156.
527 H. Hirai, S. Takano and T. Tsukuda, *ACS Omega,* 2019, **4**, 7070-7075.
528 S. Jin, W. Liu, D. Hu, X. Zou, X. Kang, W. Du, S. Chen, S. Wei, S. Wang and M. Zhu, *Chem. Eur. J.,* 2018, **24**, 3712-3715.
529 Z. Lei, Z.-J. Guan, X.-L. Pei, S. F. Yuan, X.-K. Wan, J.-Y. Zhang and Q.-M. Wang, *Chem. Eur. J.,* 2016, **22**, 11156-11160.
530 Z.-R. Wen, Z.-J. Guan, Y. Zhang, Y.-M. Lin and Q.-M. Wang, *Chem. Commun.,* 2019, **55**, 12992-12995.
531 S. Wickramasinghe, A. Atnagulov, B. E. C. Conn, B. Yoon, R. N. Barnett, W. P. Griffith, U. Landman and T. P. Bigioni, *J. Am. Chem. Soc.,* 2015, **137**, 11550-11553.
532 B. E. Conn, A. Atnagulov, B. Yoon, R. N. Barnett, U. Landman and T. P. Bigioni, *Sci. Adv.,* 2016, **2**, e1601609.
533 T. Chen, S. Yang, J. Chai, Y. Song, J. Fan, B. Rao, H. Sheng, H. Yu and M. Zhu, *Sci. Adv.,* 2017, **3**, e1700956.
534 T. Han, X. Feng, D. Chen and Y. Dong, *J. Mater. Chem. C,* 2015, **3**, 7446-7454.
535 L. Qian, B. Tong, J. Shen, J. Shi, J. Zhi, Y. Dong, F. Yang, Y. Dong, J. W. Y. Lam, Y. Liu and B. Z. Tang, *J. Phys. Chem. B,* 2009, **113**, 9098-9103.
536 S. Jin, W. Du, S. Wang, X. Kang, M. Chen, D. Hu, S. Chen, X. Zou, G. Sun and M. Zhu, *Inorg. Chem.,* 2017, **56**, 11151-11159.
537 S. Jin, F. Xu, W. Du, X. Kang, S. Chen, J. Zhang, X. Li, D. Hu, S. Wang and M. Zhu, *Inorg. Chem.,* 2018, **57**, 5114-5119.
538 Y. Li, M. Zhou, S. Jin, L. Xiong, Q. Yuan, W. Du, Y. Pei, S. Wang and M. Zhu, *Chem. Commun.,* 2019, **55**, 6457-6460.
539 Y. Du, Z.-J. Guan, Z.-R. Wen, Y.-M. Lin and Q.-M. Wang, *Chem. Eur. J.,* 2018, **24**, 16029-16035.
540 X.-J. Xi, J.-S. Yang, J.-Y. Wang, X.-Y. Dong and S.-Q. Zang, *Nanoscale,* 2018, **10**, 21013-21018.
541 Z.-J. Guan, F. Hu, S.-F. Yuan, Z.-A. Nan, Y.-M. Lin and Q.-M. Wang, *Chem. Sci.,* 2019, **10**, 3360-3365.
542 W. Du, X. Kang, S. Jin, D. Liu, S. Wang and M. Zhu, *Inorg. Chem.*, 2020, **59**, 1675-1681.
543 Z. Wang, R. Senanayake, C. M. Aikens, W. M. Chen, C.-H. Tung and D. Sun, *Nanoscale,* 2016, **8**, 18905-18911.
544 Y. Wang, H. Su, C. Xu, G. Li, L. Gell, S. Lin, Z. Tang, H. Häkkinen and N. Zheng, *J. Am. Chem. Soc.,* 2015, **137**, 4324-4327.

545 L. Huang, J. Yan, L. Ren, B. K. Teo and N. Zheng, *Dalton Trans.,* 2017, **46**, 1757-1760.
546 H. Li, Y. Song, Y. Lv, Y. Yun, X. Lv, H. Yu and M. Zhu, *Inorg. Chem.,* 2019, **58**, 1724-1727.
547 S. Jin, X. Zou, L. Xiong, W. Du, S. Wang, Y. Pei and M. Zhu, *Angew. Chem., Int. Ed.,* 2018, **57**, 16768-16772.
548 Y. Wang, X.-K. Wan, L. Ren, H. Su, G. Li, S. Malola, S. Lin, Z. Tang, H. Häkkinen, B. K. Teo, Q.-M. Wang and N. Zheng, *J. Am. Chem. Soc.,* 2016, **138**, 3278-3281.
549 S. Wang, S. Jin, S. Yang, S. Chen, Y. Song, J. Zhang and M. Zhu, *Sci. Adv.,* 2015, **1***,* e1500441.
550 J.-L. Zeng, Z.-J. Guan, Y. Du, Z.-A. Nan, Y.-M. Lin and Q.-M. Wang, *J. Am. Chem. Soc.,* 2016, **138**, 7848-7851.
551 Z.-J. Guan, J.-L. Zeng, S.-F. Yuan, F. Hu, Y.-M. Lin and Q.-M. Wang, *Angew. Chem., Int. Ed.,* 2018, **57**, 5703-5707.
552 T. Higaki, C. Liu, D. J. Morris, G. He, T.-Y. Luo, M. Y. Sfeir, P. Zhang, N. L. Rosi and R. Jin, *Angew. Chem., Int. Ed.,* 2019, **58**, 18798-18802.
553 J. Yan, S. Malola, C. Hu, J. Peng, B. Dittrich, B. K. Teo, H. Häkkinen, L. Zheng and N. Zheng, *Nat. Commun.,* 2018, **9**, 3357.
554 E. G. Mednikov, M. C. Jewell and L. F. Dahl, *J. Am. Chem. Soc.,* 2007, **129**, 11619-11630.
555 X. Kang, S. Wang, Y. Song, S. Jin, G. Sun, H. Yu and M. Zhu, *Angew. Chem., Int. Ed.,* 2016, **55**, 3611-3614.
556 X. Kang, X. Li, H. Yu, Y. Lv, G. Sun, Y. Li, S. Wang and M. Zhu, *RSC Adv.,* 2017, *7*, 28606-28609.
557 W. Yu, D. Hu, L. Xiong, Y. Li, X. Kang, S. Chen, S. Wang, Y. Pei and M. Zhu, *Part. Part. Syst. Charact.,* 2019, **36**, 1800494.
558 Y. Song, S. Weng, H. Li, H. Yu and M. Zhu, *Inorg. Chem.,* 2019, **58**, 7136-7140.
559 T.-A. D. Nguyen, Z. R. Jones, B. R. Goldsmith, W. R. Buratto, G. Wu, S. L. Scott and T. W. Hayton, *J. Am. Chem. Soc.,* 2015, **137**, 13319-13324.
560 A. Chen, X. Kang, S. Jin, W. Du, S. Wang and M. Zhu, *J. Phys. Chem. Lett.,* 2019, **10**, 6124-6128.
561 J. Chai, S. Yang, Y. Lv, H. Chong, H. Yu and M. Zhu, *Angew. Chem., Int. Ed.,* 2019, **58**, 15671-15674.
562 X.-K. Wan, X.-L. Cheng, Q. Tang, Y.-Z. Han, G. Hu, D.-e. Jiang and Q.-M. Wang, *J. Am. Chem. Soc.,* 2017, **139**, 9451-9454.
563 P. I. Silvestri, F. Andemarian, G. N. Khairallah, S. W. Yap, T. Quach, S. Tsegay, C. M. Williams, R. A. J. O'Hair, P. S. Donnelly and S. J. Williams, *Org. Biomol. Chem.,* 2011, **9**, 6082-6088.
564 T. U. Connell, S. Sandanayake, G. N. Khairallah, J. M. White, R. A. J. O'Hair, P. S. Donnelly and S. J. Williams, *Dalton Trans.,* 2013, **42**, 4903-4907.
565 X. Zou, S. Jin, S. Wang, M. Zhu and R. Jin, *Nano Futures,* 2018, **2**, 045004.
566 H. Yang, Y. Wang and N. Zheng, *Nanoscale,* 2013, **5**, 2674-2677.
567 X. Zou, S. Jin, W. Du, Y. Li, P. Li, S. Wang and M. Zhu, *Nanoscale,* 2017, **9**, 16800-16805.
568 S. Yang, J. Chai, H. Chong, Y. Song, H. Yu and M. Zhu, *Chem. Commun.,* 2018, **54**, 4314-4316.
569 S. Yang, S. Chen, L. Xiong, C. Liu, H. Yu, S. Wang, N. L. Rosi, Y. Pei and M. Zhu, *J. Am. Chem. Soc.,* 2018, **140**, 10988-10994.
570 E. S. Shibu and T. Pradeep, *Chem. Mater.,* 2011, **23**, 989-999.
571 Y. Yu, X. Chen, Q. Yao, Y. Yu, N. Yan and J. Xie, *Chem. Mater.,* 2013, **25**, 946-952.
572 Q. Yao, Y. Yu, X. Yuan, Y. Yu, J. Xie and J. Y. Lee, *Small,* 2013, **9**, 2696-2701.
573 D.-e. Jiang, S. H. Overbury and S. Dai, *J. Am. Chem. Soc.,* 2013, **135**, 8786-8789.
574 K. K. Chakrahari, R. P. B. Silalahi, T.-H. Chiu, X. Wang, N. Azrou, S. Kahlal, Y.-C. Liu, M.-H. Chiang, J.-Y. Saillard and C. W. Liu, *Angew. Chem., Int. Ed.,* 2019, **58**, 4943-4947.
575 W. Zhang, S. Zhuang, L. Liao, H. Dong, N. Xia, J. Li, H. Deng and Z. Wu, *Inorg. Chem.,* 2019, **58**, 5388-5392.
576 H. Shen and T. Mizuta, *Chem. Asian. J.,* 2017, **12**, 2904-2907.
577 E. G. Mednikov, S. A. Ivanov and L. F. Dahl, *Inorg. Chem.,* 2015, **54**, 6157-6168.
578 J. Weβing, C. Ganesamoorthy, S. Kahlal, R. Marchal, C. Gemel, O. Cador, A. C. H. Da Silva, J. L. F. Da Silva, J.-Y. Saillard and R. A. Fischer, *Angew. Chem., Int. Ed.,* 2018, **57**, 14630-14634.
579 S. Sarkar, I. Chakraborty, M. K. Panwar and T. Pradeep, *J. Phys. Chem. Lett.,* 2014, **5**, 3757-3762.
580 T. U. B. Rao and T. Pradeep, *Angew. Chem., Int. Ed.,* 2010, **49**, 3925-3929.
581 T. Udayabhaskararao, Y. Sun, N. Goswami, S. K. Pal, K. Balasubramanian and T. Pradeep, *Angew. Chem., Int. Ed.,* 2012, **51**, 2155-2159.
582 S. Hayashi, R. Ishida, S. Hasegawa, S. Yamazoe and T. Tsukuda, *Top. Catal.,* 2018, **61**, 136-141.
583 S. Hasegawa, S. Takano, S. Yamazoe and T. Tsukuda, *Chem. Commun.,* 2018, **54**, 5915-5918.
584 F. Alkan, P. Pandeya and C. M. Aikens, *J. Phys. Chem. C,* 2019, **123**, 9516-9527.
585 F. Scherbaum, A. Grohmann, B. Huber, C. Kruger and H. Schmidbaur, *Angew. Chem., Int. Ed.,* 1988, ***27***, 1544-1546.
586 J.-H. Jia and Q.-M. Wang, *J. Am. Chem. Soc.,* 2009, **131**, 16634-16635.
587 M. Chen, Z. Lei, W. Feng, C. Li, Q. M. Wang and F. Li, *Biomaterials,* 2013, **34**, 4284-4295.
588 M. Zhou, Z. Lei, Q. Guo, Q.-M. Wang and A. Xia, *J. Phys. Chem. C,* 2015, **119**, 14980-14988.
589 J.-F. Greisch, A. Ballester-Caudet, S. V. Kruppa, Z. Lei, Q.-M. Wang, C. Riehn and F. Remacle, *J. Phys. Chem. A,* 2018, **122**, 5799-5810.
590 Y. Yang, X.-L. Pei and Q.-M. Wang, *J. Am. Chem. Soc.,* 2013, **135**, 16184-16191.
591 X.-Y. Liu, Y. Yang, Z. Lei, Z.-J. Guan and Q.-M. Wang, *Chem. Commun.,* 2016, **52**, 8022-8025.
592 J.-H. Jia, J.-X. Liang, Z. Lei, Z.-X. Cao and Q.-M. Wang, *Chem. Commun.,* 2011, **47**, 4739-4741.
593 Z. Lei, X.-L. Pei, Z.-G. Jiang and Q.-M. Wang, *Angew. Chem., Int. Ed.,* 2014, **53**, 12771-12775.
594 Z. Lei, X.-L. Pei, Z.-J. Guan and Q.-M. Wang, *Angew. Chem., Int. Ed.,* 2017, **56**, 7117-7120.
595 K. Kim, K. Hirata, K. Nakamura, H. Kitazawa, S. Hayashi, K. Koyasu and T. Tsukuda, *Angew. Chem., Int. Ed.,* 2019, **58**, 11637-11641.
596 M. van der Linden, A. J. van Bunningen, L. Amidani, M. Bransen, H. Elnaggar, P. Glatzel, A. Meijerink and F. M. F. de Groot, *ACS Nano,* 2018, **12**, 12751-12760.
597 J. Jana, T. Aditya and T. Pal, *New J. Chem.,* 2019, **43**, 7074-7082
598 V. D. Thanthirige, M. Kim, W. Cho, K. Kwak, D. Lee and G. Ramakrishna, *J. Phys. Chem. C,* 2016, **120**, 23180-23188.
599 D. Lee, R. L. Donkers, G. L. Wang, A. S. Harper and R. W. Murray, *J. Am. Chem. Soc.,* 2004, **126**, 6193-6199.
600 K. Kwak and D. Lee, *J. Phys. Chem. Lett.,* 2012, **3**, 2476-2481.
601 A. H. Holm, M. Ceccato, R. L. Donkers, L. Fabris, G. Pace and F. Maran, *Langmuir,* 2006, **22**, 10584-10589.
602 S. Antonello, N. V. Perera, M. Ruzzi, J. A. Gascón and F. Maran, *J. Am. Chem. Soc.,* 2013, **135**, 15585-15594.
603 T. Dainese, S. Antonello, J. A. Gascón, F. Pan, N. V. Perera, M. Ruzzi, A. Venzo, A. Zoleo, K. Rissanen and F. Maran, *ACS Nano,* 2014, **8**, 3904-3912.

604 M. Rambukwella, L. Sementa, G. Barcaro, A. Fortunelli and A. Dass, *J. Phys. Chem. C,* 2015, **119**, 25077-25084.
605 M. Hesari and Z. Ding, *Acc. Chem. Res.,* 2017, **50**, 218-230.
606 K. N. Swanick, M. Hesari, M. S. Workentin and Z. Ding, *J. Am. Chem. Soc.,* 2012, **134**, 15205-15208.
607 M. Hesari, Z. Ding and M. S. Workentin, *Organometallics,* 2014, **33**, 4888-4892.
608 M. Hesari, M. S. Workentin and Z. Ding, *Chem. Sci.,* 2014, **5**, 3814-3822.
609 M. Hesari, M. S. Workentin and Z. Ding, *RSC Adv.,* 2014, **4**, 29559-29562.
610 M. Hesari, M. S. Workentin and Z. Ding, *Chem. Eur. J.,* 2014, **20**, 15116-15121.
611 K. Wang, X. Wei and Y. Tu, *Microchim Acta,* 2014, **181**, 1223-1230.
612 Y. Tang, J. Xu, C. Xiong, Y. Xiao, X. Zhang and S. Wang, *Analyst,* 2019, **144**, 2643-2648.
613 Q. Zhai, H. Xing, X. Zhang, J. Li and E. Wang, *Anal. Chem.,* 2017, **89**, 7788-7794.
614 P. Crespo, R. Litrán, T. C. Rojas, M. Multigner, J. M. de la Fuente, J. C. Sanchez-López, M. A. García, A. Hernando, S. Penadés and A. Fernández, *Phys. Rev. Lett.,* 2004, **93**, 087204.
615 Y. Negishi, H. Tsunoyama, M. Suzuki, N. Kawamura, M. M. Matsushita, K. Maruyama, T. Sugawara, T. Yokoyama and T. Tsukuda, *J. Am. Chem. Soc.,* 2006, **128**, 12034-12035.
616 J. de la Venta, A. Pucci, E. F. Pinel, M. A. García, C. de Julian Fernández, P. Crespo, P. Mazzoldi, G. Ruggeri and A. Hernando, *Adv. Mater.,* 2007, **19**, 875-877.
617 Z. Wu, J. Chen and R. Jin, *Adv. Funct. Mater.,* 2011, **21**, 177-183.
618 M. Zhu, C. M. Aikens, M. P. Hendrich, R. Gupta, H. Qian, G. C. Schatz and R. Jin, *J. Am. Chem. Soc., 2009,* **131***, 2*490-2492.
619 S. Antonello, N. V. Perera, M. Ruzzi, J. A. Gascon and F. Maran, *J. Am. Chem. Soc.,* 2013, **135**, 15585-15594.
620 K. S. Krishna, P. Tarakeshwar, V. Mujica and C. S. S. R. Kumar, *Small,* 2014, **10**, 907-911.
621 N. Fedik, A. Boldyrev and A. Muñoz-Castro, *Phys. Chem. Chem. Phys.,* 2019, **21**, 25215-25219.
622 R. Kobayashi, Y. Nonoguchi, A. Sasaki and H. Yao, *J. Phys. Chem. C,* 2014, **118**, 15506-15515.
623 H. Yao, R. Kobayashi and Y. Nonoguchi, *J. Phys. Chem. C,* 2016, **120**, 1284-1292.
624 S. Malola and H. Häkkinen, *J. Am. Chem. Soc.,* 2019, **141**, 6006-6012.
625 J. Zhao and R. Jin, *Nano Today,* 2018, **18**, 86-102.
626 W. Zhou, Y. Fang, J. Ren and S. Dong, *Chem. Commun.,* 2019, **55**, 373-376.
627 M.-B. Li, S.-K. Tian and Z. Wu, *Chin. J. Chem.,* 2017, **35**, 567-571.
628 J. Chai, H. Chong, S. Wang, S. Yang, M. Wu and M. Zhu, *RSC Adv.,* 2016, **6**, 111399-111405.
629 L. Sun, K. Shen, H. Sheng, Y. Yun, Y. Song, D. Pan, Y. Du, H. Yu, M. Chen and M. Zhu, *J. Catal.,* 2019, **378**, 220-225.
630 X. L. Du, X. L. Wang, Y. H. Li, Y. L. Wang, J. J. Zhao, L. J. Fang, L. R. Zheng, H. Tong and H. G. Yang, *Chem. Commun.,* 2017, **53**, 9402-9405.
631 H. Chong, G. Gao, J. Chai, S. Yang, B. Rao, G. Li and M. Zhu, *ChemNanoMat,* 2018, **4**, 482-486.
632 W. Choi, G. Hu, K. Kwak, M. Kim, D.-e. Jiang, J.-P. Choi and D. Lee, *ACS Appl. Mater. Interfaces,* 2018, **10**, 44645-44653.
633 M. Frey, *ChemBioChem,* 2002, **3**, 153-160.
634 F. A. Armstrong and J. Hirst, *Proc. Natl. Acad. Sci. USA,* 2011, **108**, 14049-14054.
635 C. Madden, M. D. Vaughn, I. Díez-Pérez, K. A. Brown, P. W. King, D. Gust, A. L. Moore and T. A. Moore, *J. Am. Chem. Soc.,* 2012, **134**, 1577-1582.
636 Y. Lu, C. Zhang, X. Li, A. R. Frojd, W. Xing, A. Z. Clayborne and W. Chen, *Nano Energy,* 2018, **50**, 316-322.
637 W. Kurashige, R. Hayashi, H. Wakamatsu, Y. Kataoka, S. Hossain, A. Iwase, A. Kudo, S. Yamazoe and Y. Negishi, *ACS Appl. Energy Mater.,* 2019, **2**, 4175-4187.
638 Y. Wongnongwa, S. Namuangruk, N. Kungwan and S. Jungsuttiwong, *New J. Chem.,* 2018, **42**, 14120-14127.
639 L. Sun, Y. Yun, H. Sheng, Y. Du, Y. Ding, P. Wu, P. Li and M. Zhu, *J. Mater. Chem. A,* 2018, **6**, 15371-15376.
640 G. Panapitiya, G. Avendaño-Franco, P. Ren, X. Wen, Y. Li and J. P. Lewis, *J. Am. Chem. Soc.,* 2018, **140**, 17508-17514.
641 W. Jiang, B. Rao, Q. Li, J. Chai, S. Yang, Y. Du, H. Yu and M. Zhu, *Anal. Methods*, 2018, **10**, 5181-5187.
642 T.-Y. Zhou, L.-P. Lin, M.-C. Rong, Y.-Q. Jiang and X. Chen, *Anal. Chem.,* 2013, **85**, 9839-9844.
643 A. Sannigrahi, S. Chowdhury, I. Nandi, D. Sanyal, S. Chall and K. Chattopadhyay, *Nanoscale Adv.,* 2019, **1**, 3660-3669.
644 X. Zan, Q. Li, Y. Pan, D. J. Morris, P. Zhang, P. Li, H. Yu and M. Zhu, *ACS Appl. Nano Mater.,* 2018, **1**, 6773-6781.
645 Y. Sun and Y. Xia, *J. Am. Chem. Soc.,* 2004*,* **126***,* 3892-3901.
646 Y. Song, Y. Li, H. Li, F. Ke, J. Xiang, C. Zhou, P. Li, M. Zhu and R. Jin, *Nat. Commun.,* 2020, **11**, 478.
647 C. Yi, M. A. Tofanelli, C. J. Ackerson and K. L. Knappenberger, Jr., *J. Am. Chem. Soc.,* 2013*,* **135***,* 18222-18228.
648 M. Zhou, T. Higaki, Y. Li, C. Zeng, Q. Li, M. Y. Sfeir and R. Jin, *J. Am. Chem. Soc.,* 2019*,* **141***,* 19754-19764.

Table of Contents Graphic

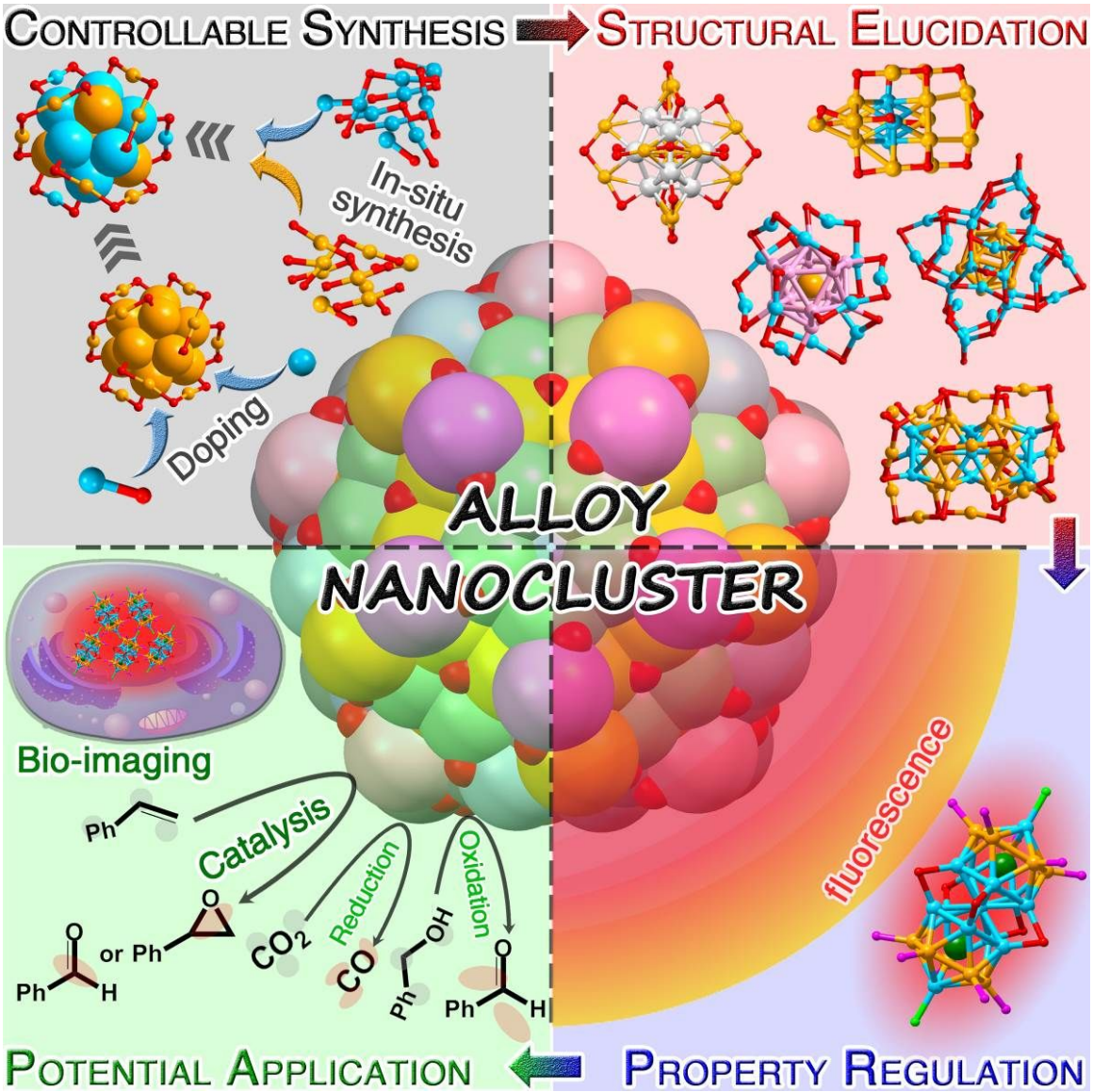

Atomically precise alloy nanoclusters have been continuously appealing to scientists owing to their capability in tuning the electronic/geometric structures and enriching the physicochemical properties of nanoclusters.